

UNIVERSITÀ
DEGLI STUDI
DI BRESCIA

DOTTORATO DI RICERCA IN INGEGNERIA CIVILE, AMBIENTALE, DELLA COOPERAZIONE INTERNAZIONALE E DI MATEMATICA

XXXVIII CICLO

Ph.D. Thesis

Mathematical and numerical models for entomology

SSD: MAT/08 — Analisi numerica

AGR/11 — Entomologia generale e applicata

Supervisor:
Prof. Paola Gervasio

Co-supervisor:
Prof. Gianni Gilioli

Ph.D. candidate:
Enrico Bertoldi

Id. number:
744525

Contents

Summary **5**

Sommario **6**

1 Introduction **7**
1.1 Main contributions 9

2 Mathematical and entomological background **11**
2.1 Mathematical background 11
2.1.1 Sobolev spaces 11
2.1.2 Bochner spaces 12
2.1.3 Schauder Fixed Point Theorem 12
2.1.4 Aubin–Lions Compactness Theorem 12
2.1.5 Lions–Magenes Theorem 13
2.1.6 Dominated convergence theorem 13
2.1.7 Kolmogorov system for insect stage-structured population dynamics 14
2.1.8 Compartmental models 15
2.1.9 Physiologically based demographic models 16
2.2 Entomological Background 17
2.2.1 Spodoptera frugiperda 17
2.2.2 Erasmoneura vulnerata 18
2.2.3 Philaenus spumarius 20
2.2.4 Xylella fastidiosa 21
Xf–Olive pathosystem 22
Xf–Grapevine pathosystem 22

3 Entomonlib: a MATLAB library for entomology **24**
3.1 Real problems and stage-structured population models 24
3.2 Useful models for entomologists 25
3.2.1 Demographic model 25
3.2.2 Phenological model 25
3.2.3 Demographic and Phenological models with optimisation processes 26
3.2.4 Demographic and Phenological models with optimisation processes - multisite. 27
3.3 Diapause 27
3.4 Numerical discretisation 28
3.4.1 Discretisation of the core system for a single stage 28

3.4.2 Discretisation of the Multistage Problem . . . 32
3.5 Description of the Entomonlib code logic structure . . . 33
3.5.1 Input, related checks, and determination of the Input folder . . . 33
3.5.2 Data loading . . . 34
3.5.3 Functions settings . . . 37
3.5.4 Discretisation settings . . . 45
3.5.5 Solution step . . . 47
3.5.6 Plotting solutions and functions . . . 48
3.5.7 Computing errors . . . 48
3.6 Technicalities . . . 49
3.7 Entomonlib applications . . . 50
3.7.1 Development of a phenological model for *Erasmoneura vulnerata* . 50
3.7.2 A model describing population dynamics of *P. spumarius* . . . 51
3.7.3 Entomonlib as a satellite model . . . 53

4 Physiologically-based eco-epidemiological model of *Xylella fastidiosa* infection in olive groves 54
4.1 The BeXyl project . . . 54
4.2 Introduction . . . 56
4.3 Material and Methods . . . 58
4.3.1 Model definitions . . . 58
4.3.2 Model assumptions . . . 62
4.3.3 Case study . . . 63
4.3.4 Model calibration and validation . . . 67
4.3.5 Results . . . 67
Simulated dynamics across all olive groves . . . 68
4.3.6 Herbaceous vegetation (H) and Non-susceptible shrubs and trees (N) . . . 69
Reservoir plants . . . 70
Insect vectors . . . 70
Epidemiological dynamic in olive trees . . . 71
4.4 Discussion . . . 72
4.5 Conclusion . . . 76
4.6 Model functions and parameter estimation . . . 77
4.6.1 Monod equation . . . 77
4.6.2 Vector–plant contact function (n^j) . . . 77
4.6.3 Preimaginal vector stage (P) . . . 79
Emergence function (ε^P) . . . 80
Preimaginal mortality function (m^P) . . . 80
4.6.4 Adult vector stage (V_S and V_I) . . . 81
Adult mortality function (m^V) . . . 82

4.6.5 Olive trees ($C_S, C_0 - C_5$) . . . 83
Disease progression function (d^{C_i}) . . . 84
Bacterial mortality rate ($b_m^{C_i}$) . . . 86
Temperature-dependent disease recovery function ($r_T^{C_i}$) . . . 86
Non-systemic infection recovery function (r_n^C) . . . 86
4.6.6 Herbaceous vegetation (H) . . . 87
4.6.7 Non-susceptible shrubs and trees (N) . . . 87
4.6.8 Reservoir plants (R_S and R_I) . . . 89
4.7 Model calibration and meteorological data . . . 90

5 Two simplified mathematical models for the spread of *Xf* in olive trees 93
5.1 Background Theorems and Definitions . . . 93
5.1.1 Lyapunov stability and its first criterion . . . 93
5.1.2 Lyapunov's theorem . . . 95
5.1.3 Fixed Point Method . . . 96
5.2 First simplified Model . . . 97
5.2.1 Introduction . . . 97
5.2.2 Model #1: structure and derivation . . . 98
5.2.3 Analysis of Model #1 . . . 100
5.2.4 Local existence and uniqueness of solution . . . 103
5.2.5 Global existence and uniqueness of the solution of Model #1 . . . 108
5.2.6 Equilibrium points and Jacobian analysis . . . 109
Vector equilibria and the regime $m_X \geq g_X$. . . . 113
5.3 Second simplified Model . . . 115
5.3.1 Introduction . . . 115
5.3.2 Model #2: structure and derivation . . . 115
5.3.3 Local existence and uniqueness of solutions . . . 118
5.3.4 Global existence and uniqueness of the solution of Model #2 . . . 119
5.3.5 Equilibrium points and Jacobian analysis . . . 122
5.3.6 A visual–numerical validation . . . 124

6 A mathematical model with host preference for the spread of *Xf* in olive trees 127
6.1 Introduction . . . 128
6.2 Model structure and derivation . . . 129
6.2.1 Reservoir plant dynamics . . . 130
6.2.2 Crop plant dynamics . . . 130
6.2.3 Vector dynamics . . . 131
6.3 Analysis of the system with preferences . . . 132
6.3.1 Local existence and uniqueness of the solutions . . . 132
6.3.2 Global existence and uniqueness of the solutions . . . 135

6.3.3 State variable bounds induced by initial data 137
6.3.4 Equilibrium points and Jacobian analysis 140
6.4 Model Applications 141
6.5 Numerical Simulations 144
6.6 Discussion and conclusion 146

7 Coupled Kolmogorov model for bacterial spread in grapevine 151
7.1 The mathematical model 152
7.2 Existence and Uniqueness (decoupled case, branches) 153
7.3 Analysis of the non-linear coupled problem 162
7.3.1 Existence of a solution via Schauder's fixed-point theorem 167
7.4 The S–ϕ relationship — two options 167
7.5 Discretisation 170
7.5.1 Positivity correction (post–processing) 172
7.5.2 Special case: pruning 173
7.6 Epidemiological model of *Xylella fastidiosa* infection in vineyards 174

Summary

In the realm of biology, the integration of mathematics has become increasingly indispensable, even within the field of entomology (the scientific study of insects, hence a branch of zoology). Moreover, the ongoing climate changes are poised to induce shifts in the habitats of invasive insect species. This phenomenon presents a critical challenge as indigenous flora often struggle to defend themselves against these new "predators". Consequently, the application of mathematical models to predict the dynamics of these biological processes has never been more helpful to entomologists in developing reliable and accurate models.

Indeed, the intricate interplay between climate change and insect behaviour necessitates a multidisciplinary approach to understanding and mitigating potential negative ecological consequences. Mathematics provides a powerful toolset for researchers and scientists to develop models that simulate and forecast the complex interactions between invasive insect species and native plant populations, and the life cycle processes of the insects themselves, allowing for proactive measures to be taken. Consequently, informed strategies can be programmed to protect vulnerable ecosystems and native plant species from the threats posed by invasive insects.

Hence, it becomes increasingly important for mathematics to serve entomology, improving and testing the models that analyse and forecast the behavioural structures and physiological mechanisms through which insects interact with each other and with the surrounding ecosystem. This thesis, which is part of this particular scientific research branch, after a background introduction (Chapter 2), opens its list of results and analyses by introducing Entomonlib: a MATLAB library that unifies demographic and phenological modelling and the estimation of physiological function parameters from datasets taken from one or more biological sites (Chapter 3). The thesis then continues describing the works carried out for the BeXyl international project: (i) a comprehensive compartmental eco-epidemiological plant–vector model (case study: *Xylella fastidiosa* in olive trees), calibrated on Apulian data and used to design and assess management strategies (Chapter 4); (ii) two exploratory reduced models (Chapter 5) that lead to (iii) a reduced, compartmental model that focuses on host-choice mechanisms driven by vector preferences and that can be rigorously analysed (Chapter 6). Finally (Chapter 7), we present our most recent work: a coupled Kolmogorov system for trees that describes within-plant diffusion of bacteria, together with a stable numerical scheme and first qualitative insights (case study: *Xylella fastidiosa* in vineyards).

Sommario

Nell'ambito della biologia, l'integrazione della matematica è diventata sempre più indispensabile, anche nel campo dell'entomologia (lo studio scientifico degli insetti, dunque un ramo della zoologia). Inoltre, i cambiamenti climatici in corso sono destinati a indurre spostamenti negli habitat delle specie di insetti invasive. Questo fenomeno rappresenta un'importante sfida poiché la flora indigena spesso fatica a difendersi da questi nuovi "predatori". Di conseguenza, l'applicazione di modelli matematici per prevedere le dinamiche di questi processi biologici non è mai stata così importante per gli entomologi nello sviluppo di modelli affidabili e accurati.

Inoltre, l'intricato intreccio tra cambiamento climatico e comportamento degli insetti richiede un approccio multidisciplinare per comprendere e mitigare le potenziali conseguenze ecologiche negative. La matematica fornisce a ricercatori e scienziati un potente insieme di strumenti per sviluppare modelli che simulano e prevedono le complesse interazioni tra specie di insetti invasive e popolazioni di piante native, nonché i processi del ciclo vitale degli stessi insetti, permettendo di adottare misure proattive. Di conseguenza, si possono programmare strategie informate per proteggere gli ecosistemi vulnerabili e le specie vegetali native dalle minacce poste dagli insetti invasivi.

Diventa quindi sempre più importante che la matematica dia il suo contributo nel ramo scientifico dell'entomologia, migliorando e testando i modelli che analizzano e prevedono le strutture comportamentali e i meccanismi fisiologici attraverso i quali gli insetti interagiscono tra loro e con l'ecosistema circostante. Questa tesi, che si inserisce in questo quadro di ricerca scientifica, dopo una breve introduzione composta da definizioni e teoremi utili da richiamare (Capitolo 2), apre il suo elenco di risultati e analisi introducendo Entomonlib: una libreria MATLAB che unifica la modellistica demografica e fenologica e la stima di parametri di funzioni fisiologiche da dataset presi da uno o più siti biologici (Capitolo 3). La tesi prosegue descrivendo i lavori svolti per il progetto internazionale BeXyl: (i) un modello compartimentale eco-epidemiologico piante–vettori completo (caso di studio: *Xylella fastidiosa* in oliveti), questo modello è stato calibrato su dati provenienti dalla Puglia e utilizzato per progettare e valutare strategie di gestione (Capitolo 4); (ii) due modelli esplorativi (Capitolo 5) che portano ad (iii) un modello compartimentale ridotto che si concentra sui meccanismi di scelta della pianta-ospite guidati da parametri che quantificano le preferenze dei vettori verso le singole tipologie di piante, il modello ridotto è stato rigorosamente analizzato matematicamente (Capitolo 6). Infine (Capitolo 7), presentiamo il nostro lavoro più recente: un sistema di Kolmogorov accoppiato che descrive la diffusione dei batteri all'interno dei vasi xilematici delle piante, insieme a uno schema numerico stabile e a primi spunti qualitativi sull'affidabilità matematica del modello (caso di studio: *Xylella fastidiosa* nei vigneti).

1
Introduction

In the ever-evolving landscape of biological research, the integration of mathematics has become indispensable for gaining a deeper understanding of complex phenomena. The field of entomology, which explores the complex world of insects, benefits significantly from applying mathematical methodologies. Note, indeed, the fact that ecosystems where insects live are extremely complex, with intricate interactions among insects, plants, other organisms, and all the surrounding environment. Mathematical models help simulate these complex interactions, aiding scientists in making predictions and better understanding how insects influence and are influenced by their surroundings.

Mathematical models provide a means to elucidate and simulate intricate biological processes, allowing researchers to explore the dynamics of insect populations and interactions. From population ecology to the study of insect behaviour, mathematical models offer a quantitative lens through which to analyse patterns and predict trends.

Moreover, the vast amount of data generated in modern biological research necessitates advanced analytical tools. Mathematics plays a pivotal role in extracting meaningful patterns from data. In entomology, where observations can range from individual behaviour to ecosystem-level dynamics, optimisation methods enable researchers to discern trends, validate hypotheses, and make informed decisions based on empirical evidence. In this thematic framework, the specific objectives addressed in this thesis are linked to:
(i) demographic and phenological mathematical models for stage-structured insect populations;
(ii) compartmental models supporting the management of the spread of the bacterium *Xylella fastidiosa*, a growing threat to olive groves, e.g., throughout Italy (with already incalculable damage in Apulia);
(iii) coupled models analysing modes and dynamics of bacterial spread within olive trees.

All of these models have been tested and validated as well in contexts beyond the single case study. More concretely, this thesis is articulated into three main strands.

Chapter 3 addresses demographic and phenological problems for stage–structured insect populations. Starting from real case studies (the invasive leafhopper *Erasmoneura vulnerata* and the spittlebug *Philaenus spumarius*), I formulate the dynamics in terms of Kolmogorov-type Partial Differential Equations in physiological age, describing their development, mortality and fecundity. These equations are discretised by second–order finite-volumes in physiological age and a semi-implicit Euler scheme in time, and mapped into a general MATLAB library, called Entomonlib, that I have designed and coded. Within this framework, I calibrate the physiological functions against field data, validate the resulting phenological predictions across multiple sites, and analyse how parameter

changes and environmental forcing affect population peaks and specific physiological events, both analytically and numerically.

The second strand (Chapters 4–6) focuses on models supporting the management of *Xylella fastidiosa* epidemics in olive agro-ecosystems. In Chapter 4, within the BeXyl project, I contribute to the construction and implementation of a mechanistic eco–epidemiological model formulated as a system of Ordinary Differential Equations and Delayed Differential Equations that link vegetation dynamics, vector demography and phenology, and olive disease classes. I implemented the simulation and calibration code, linked the model to Entomonlib to generate vector emergence functions, and used adaptive Runge–Kutta solvers to explore control scenarios and their impact on epidemic outcomes. In Chapter 5, simplified compartmental models from this framework are analysed: Model #1 models vector preferences for different types of trees and shrubs but neglects the pathogen. Model #2 models both infection and vector preferences. In Chapter 6, a more comprehensive epidemiological ODE model is formulated and analysed. Here, vector transmission is explicitly driven by host preference and depends on the current availability and infection status of reservoir, crop and non-susceptible plants. For all these three systems I carried out the full mathematical analysis (local and global existence and uniqueness, positivity and bounds induced by initial data, equilibrium points and Jacobian-based stability, including closed-form solutions in special parameter regimes) and performed targeted numerical simulations that illustrate and confirm the analytical results, with particular attention to how vector preferences and non-susceptible vegetation shape infection levels in crops and vectors.

The third strand (Chapter 7) investigates the modes and dynamics of bacterial spread within individual plants and their epidemiological consequences. I consider a coupled Kolmogorov model for the within-host distribution of bacterial load in roots and branches of grapevine. The PDE system and its coupling structure are analysed; I prove existence and uniqueness results (first for a linear decoupled problem, then for the coupled system via Schauder's fixed-point theorem), and design a finite–volume / upwind scheme with implicit time-stepping.

This PDE framework is then applied to an eco-epidemiological case study of *Xylella fastidiosa* infection in vineyards. Exploiting published laboratory and field data from a Southern European outbreak, I calibrated the parameters, implemented the numerical scheme in MATLAB, and used it to explore how temperature forcing, root–branch feedbacks and pruning strategies affect the evolution of bacterial load profiles and the associated infection risk at vineyard scale.

Across these three strands, my personal contributions lie in the formulation of the models, the design of the discretisation schemes, the MATLAB implementations, and, whenever feasible, the analytical and numerical studies of the resulting systems; these contributions are outlined in the following lines and positioned with respect to the current state of the art.

1.1 Main contributions

C1. A unified MATLAB library for stage-structured insect models.
(Chapter 3) I designed and implemented *Entomonlib*, a new reusable MATLAB library that unifies demographic and phenological models for stage-structured insects within a Kolmogorov/Fokker–Planck framework, including temperature-driven development, mortality and fecundity functions, and a flexible architecture with pluggable model components. *Advance beyond the state of the art:* rather than relying on case-specific scripts, the library consolidates and generalises models and calibrations into a single, documented platform, including optimisation routines and multisite calibration capabilities to fit physiological parameters simultaneously across multiple field locations.

C2. Mechanistic eco-epidemiological models for *X. fastidiosa* management.
(Chapter 4) Within the BeXyl project, I contributed to the construction and implementation of a mechanistic eco-epidemiological model linking vegetation dynamics, vector demography and phenology, and host disease classes, formulated as an ODE/DDE system and calibrated on Apulian data. I implemented the simulation and calibration code and linked the epidemiological model to Entomonlib outputs (vector emergence functions) to assess management scenarios. *Advance:* the resulting framework integrates stage-structured vector phenology with landscape/host components in a single mechanistic platform for scenario exploration and decision support.

C3. Reduced models that isolate vector preference mechanisms.
(Chapter 5) I derived and analysed two simplified compartmental models that formalize dynamic vector preference and progressively reintroduce infection dynamics, in order to identify key parameter regimes and drivers of asymptotic infection prevalence in crops and vectors. *Advance:* these reduced systems provide analytical transparency that is often unreachable in large mechanistic models, and they inform the structure and interpretation of the full preference-driven model in Chapter 6.

C4. A preference-driven plant–vector epidemiological model with rigorous analysis. (Chapter 6) I formulated a deterministic compartmental ODE model in which disease transmission is explicitly driven by host choice through dynamically updated weight functions that respond to host availability and vector preferences. I established well-posedness under biologically meaningful assumptions, derived invariant bounds for the state variables, and performed equilibrium and Jacobian-based local stability analyses, complemented by targeted numerical simulations and management-motivated scenarios. *Advance:* while many ODE models assume homogeneous mixing or static contact rates, the proposed formulation incorporates adaptive, behaviour-driven contact frequencies, providing a mechanistic and analytically tractable framework to quantify how host preference and non-susceptible vegetation reshape epidemic trajectories and equilibrium infection levels.

C5. A coupled within-host model for bacterial load redistribution in crops.

(Chapter 7) I analysed a coupled Kolmogorov PDE system describing the within-host distribution of bacterial load in roots and branches, and proved existence results for the coupled non-linear problem. I then designed an upwind implicit finite-volume discretisation of the system and proposed conservative post-processing tools and a consistent representation of impulsive pruning events. *Advance:* the model moves beyond rough within-host scalar descriptions by resolving bacterial load distributions and root-branch feedbacks, while maintaining numerical robustness and biological consistency (e.g., mass conservation and non-negativity) required for reliable simulations.

2

Mathematical and entomological background

2.1 Mathematical background

In this section, we summarize the mathematical background and the numerical models employed in this thesis.

2.1.1 Sobolev spaces

Standard definitions from [32].

Definition 2.1 (First-order weak derivative)**.** Let $\Omega \subset \mathbb{R}^n$ be open and let $u \in L^1_{\mathrm{loc}}(\Omega)$. For $i = 1, \dots, n$, a function $v_i \in L^1_{\mathrm{loc}}(\Omega)$ is called the (partial) weak derivative $\partial_i u$ of u if

$$\int_\Omega u\, \partial_i \varphi \, dx \;=\; -\int_\Omega v_i\, \varphi \, dx \qquad \text{for every } \varphi \in C_c^\infty(\Omega).$$

In this case we write $\partial_i u = v_i$ and set $\nabla u := (\partial_1 u, \dots, \partial_n u)$.

Definition 2.2 (Sobolev spaces $W^{1,p}(\Omega)$ and $H^1(\Omega)$)**.** For $1 \le p \le \infty$ we define

$$W^{1,p}(\Omega) := \big\{\, u \in L^p(\Omega) \,:\, \partial_i u \in L^p(\Omega) \text{ for } i = 1, \dots, n \,\big\}.$$

This is a Banach space with norm

$$\|u\|_{W^{1,p}(\Omega)} := \begin{cases} \big(\|u\|_{L^p(\Omega)}^p + \|\nabla u\|_{L^p(\Omega)}^p\big)^{1/p}, & 1 \le p < \infty, \\ \max\big\{\|u\|_{L^\infty(\Omega)},\, \|\nabla u\|_{L^\infty(\Omega)}\big\}, & p = \infty. \end{cases}$$

For $p = 2$ we write $H^1(\Omega) := W^{1,2}(\Omega)$; it is a Hilbert space with inner product

$$\langle u, v \rangle_{H^1(\Omega)} := \int_\Omega uv \, dx + \int_\Omega \nabla u \cdot \nabla v \, dx.$$

We denote by $W_0^{1,p}(\Omega)$ the closure of $C_c^\infty(\Omega)$ in $W^{1,p}(\Omega)$.

2.1.2 Bochner spaces

Standard definitions from: [33].

Definition 2.3 (Bochner spaces $L^p(0,T;X)$)**.** Let $(0,T)$ be a finite time interval and let X be a separable Banach space. A (strongly) measurable map $u : (0,T) \to X$ belongs to $L^p(0,T;X)$, $1 \le p < \infty$, if

$$\int_0^T \|u(t)\|_X^p \, dt < \infty,$$

with norm $\|u\|_{L^p(0,T;X)} := \Big(\int_0^T \|u(t)\|_X^p \, dt \Big)^{1/p}$. For $p = \infty$ we set

$$L^\infty(0,T;X) := \left\{ u : \operatorname*{ess\,sup}_{t\in(0,T)} \|u(t)\|_X < \infty \right\}, \quad \|u\|_{L^\infty(0,T;X)} := \operatorname*{ess\,sup}_{t\in(0,T)} \|u(t)\|_X.$$

2.1.3 Schauder Fixed Point Theorem

Following [2] (compact convex subsets), we use the equivalent Banach-space form below.

Theorem 2.4. *Let $(X, \|\cdot\|)$ be a Banach space and let $S \subset X$ be nonempty, closed, bounded, and convex. If $A : S \to S$ is a compact mapping (i.e., A is continuous and $A(S)$ is relatively compact in X), then A has at least one fixed point; that is, there exists $u \in S$ such that $A(u) = u$.*

Remark 2.5. In particular, it is sufficient to assume that A is continuous and maps S into a compact subset of X.

2.1.4 Aubin–Lions Compactness Theorem

From [5].

Theorem 2.6. *Let B_0, B, B_1 be Banach spaces with continuous embeddings $B_0 \hookrightarrow B \hookrightarrow B_1$, assume that the embedding $B_0 \hookrightarrow B$ is compact and that B_1 is reflexive. For $1 < p_0, p_1 < \infty$, set*

$$W := \{\, v \in L^{p_0}(0,T;B_0) \ : \ \partial_t v \in L^{p_1}(0,T;B_1) \,\}.$$

Then the embedding $W \hookrightarrow L^{p_0}(0,T;B)$ is compact.

2.1.5 Lions–Magenes Theorem

From [32].

Theorem 2.7. *Assume $u \in L^2(0,T;H^1(\Omega))$ and $\partial_t u \in L^2(0,T;H^{-1}(\Omega))$. Then:*

1. *$u \in C([0,T];L^2(\Omega))$;*
2. *the map $t \mapsto \|u(t)\|^2_{L^2(\Omega)}$ is absolutely continuous and, for a.e. $t \in [0,T]$,*

$$\frac{d}{dt}\|u(t)\|^2_{L^2(\Omega)} = 2\,\langle \partial_t u(t), u(t)\rangle_{H^{-1},H^1};$$

3. *there exists $C = C(T,\Omega) > 0$ such that*

$$\max_{0\le t\le T} \|u(t)\|_{L^2(\Omega)} \le C\Big(\|u\|_{L^2(0,T;H^1(\Omega))} + \|\partial_t u\|_{L^2(0,T;H^{-1}(\Omega))}\Big).$$

2.1.6 Dominated convergence theorem

From [37, Thm. 1.4.49], specialised to Lebesgue spaces on domains of $\mathbb{R}^k$.

Theorem 2.8 (Dominated convergence)**.** *Let $D \subset \mathbb{R}^k$ be a measurable set and let $\{f_n\}_{n\in\mathbb{N}}$ be a sequence of measurable functions on D. Assume that*

1. *$f_n(x) \to f(x)$ for a.e. $x \in D$;*
2. *there exists $g \in L^1(D)$ such that $|f_n(x)| \le g(x)$ for all n and for a.e. $x \in D$.*

Then $f \in L^1(D)$ and

$$\int_D |f_n - f|\,dx \longrightarrow 0 \qquad \text{as } n \to \infty,$$

in particular

$$\int_D f_n\,dx \longrightarrow \int_D f\,dx.$$

Moreover, if $1 \le p < \infty$ and $g \in L^p(D)$, then $f \in L^p(D)$ and

$$\|f_n - f\|_{L^p(D)} \longrightarrow 0 \qquad \text{as } n \to \infty.$$

2.1.7 Kolmogorov system for insect stage-structured population dynamics

Throughout this thesis, we will often refer to a standard PDE system widely used for insect stage-structured population dynamics (see, e.g., [86]). It originates from the classical Von Foerster transport equation for the density $\varphi^s : (0,T) \times (0,1) \to \mathbb{R}_{\geq 0}$ in stage $s = 1, \ldots, \mathcal{S}$:

$$\begin{cases} \partial_t \varphi^s(t,x) + \partial_x \varphi^s(t,x) = -\, M^s\, \varphi^s(t,x), & (t,x) \in (0,T) \times (0,1), \\ \varphi^s(t,0) = \displaystyle\int_0^1 G^s(y)\, \varphi^s(t,y)\, dy, & t \in (0,T), \\ \varphi^s(0,x) = \varphi_0^s(x), & x \in (0,1). \end{cases} \tag{2.1}$$

Kolmogorov's adaptation replaces the unit drift by a (time–dependent) development rate $S^s \geq 0$, introduces a stochastic diffusion term $b^s \geq 0$, and works with the flux

$$H^s(t,x) = S^s\, \varphi^s(t,x) - b^s\, \partial_x \varphi^s(t,x),$$

leading to the forward (Fokker–Planck–type) equation

$$\begin{cases} \partial_t \varphi^s(t,x) + \partial_x \big(S^s\, \varphi^s(t,x) - b^s\, \partial_x \varphi^s(t,x) \big) = -\, M^s\, \varphi^s(t,x), & \text{in } (0,T) \times (0,1), \\ \big(S^s \varphi^s - b^s \partial_x \varphi^s \big)\big|_{x=0} = \mathcal{F}^s(t), & \text{for } t \in (0,T), \\ \big(- b^s \partial_x \varphi^s \big)\big|_{x=1} = 0, & \text{for } t \in (0,T), \\ \varphi^s(0,x) = \varphi_0^s(x), & \text{for } x \in (0,1). \end{cases} \tag{2.2}$$

with stage–inflow terms

$$\mathcal{F}^1(t) = F \int_0^1 G(y)\, \varphi^{\mathcal{S}}(t,y)\, dy, \qquad \mathcal{F}^s(t) = S^{s-1}\, \varphi^{\,s-1}(t,1), \quad s = 2, \ldots, \mathcal{S}. \tag{2.3}$$

Here the unknown function φ^s is the stage–s density function, S^s the development non-negative rate coefficient, b^s the diffusion positive term, M^s the mortality non-negative rate coefficient, while F and G specify reproduction terms. The boundary condition at $x = 0$ injects new individuals into each stage, and the zero diffusive flux at $x = 1$ makes the advective outflow $S^s \varphi^s(t,1)$ the transition to the next stage.

Remark 2.9 (Non-linear and non-local mortality term and time-dependent development and fertility functions). In some applications, including [86] and [11], the stage–specific mortality M^s term is assumed to depend on time and also on the total abundance of individuals in the same stage. This leads to a non-linear and non-local modification of the mortality rate of the form:

$$\mathcal{M}^s(t,\varphi^s) = M^s(t)\Big(1 + a^s\big(N^s(t)\big)^2\Big)^{d^s}, \qquad N^s(t) := \int_0^1 \varphi^s(t,y)\,dy, \tag{2.4}$$

where $a^s, d^s > 0$ are prescribed parameters (this lets us write that with these choices $\mathcal{M}^s(t,\varphi^s) \geq 0$). The quantity $N^s(t)$ represents the total abundance in stage s, so the above expression strengthens mortality when the stage population becomes large. Substituting M^s with $\mathcal{M}^s$ in (2.2) yields a Kolmogorov equation with a non-linear (and non-local) reaction term, a structure frequently used in density-regulated stage–structured models. Finally, we note that in many formulations the development rates S^s and the reproduction term F may also depend explicitly on time, allowing the model to incorporate environmental forcing (e.g. temperature or seasonal drivers). With these implementations the final *Kolmogorov system with non-linear and non-local density-dependent mortality term* becomes:

$$\partial_t\varphi^s(t,x) + \partial_x\left(S^s(t)\varphi^s(t,x) - b^s\partial_x\varphi^s(t,x)\right) = -\varphi^s(t,x)\mathcal{M}^s(t,\varphi^s), \tag{2.5}$$

$$\left(S^s(t)\varphi^s(t,x) - b^s\partial_x\varphi^s(t,x)\right)_{x=0} = \mathcal{F}^s(t), \tag{2.6}$$

$$\left(-b^s\partial_x\varphi^s(t,x)\right)_{x=1} = 0, \tag{2.7}$$

$$\varphi^s(0,x) = \varphi_0^s(x), \tag{2.8}$$

$$\mathcal{F}^1(t) = F(t)\int_0^1 G(y)\varphi^{\mathcal{S}}(t,y)dy, \tag{2.9}$$

$$\mathcal{F}^s(t) = S^{s-1}(t)\varphi^{s-1}(t,1), \quad s = 2,\ldots,\mathcal{S}. \tag{2.10}$$

For later use, we introduce the notation:

$$H^s(t,x) = S^s(t)\,\varphi^s(t,x) - b^s\,\partial_x\varphi^s(t,x). \tag{2.11}$$

2.1.8 Compartmental models

Compartmental models describe the time evolution of populations partitioned into homogeneous classes ("compartments") and linked by prescribed flows (infection, recruitment, removal, *etc.*). They are widely used in mathematical epidemiology and population dynamics for their transparency, analytical tractability, and ease of extension. These models originated in the early twentieth century through pioneering epidemiological work by several mathematicians (e.g., Kermack–McKendrick [1], [3]). Most implementations use ordinary differential equations (ODEs), which yield deterministic and mathematically tractable dynamics; stochastic formulations incorporate randomness and can be more realistic at the cost of added analytical complexity.

Two illustrative examples: SIR and SEIR

We present two of the simplest compartmental models, comprising three and four ODEs, respectively.

SIR. A closed population $N = S + I + R$ is partitioned into susceptibles S, infectives I, and removed (recovered/immune) R individuals:

$$\begin{cases} \dot{S}(t) = -\beta \dfrac{S(t)\, I(t)}{N}, \\ \dot{I}(t) = \beta \dfrac{S(t)\, I(t)}{N} - \gamma I(t), \\ \dot{R}(t) = \gamma I(t), \\ S(0) = S_0,\ I(0) = I_0,\ R(0) = R_0. \end{cases} \tag{2.12}$$

Parameters: $\beta > 0$ (transmission/contact rate), $\gamma > 0$ (removal/recovery rate; mean infectious period $= 1/\gamma$). Non-negative initial data preserve $S, I, R \geq 0$ and conserve N. The *basic reproduction number* (a fundamental threshold parameter in epidemiology) is, for the SIR model,

$$R_0 = \frac{\beta}{\gamma}.$$

If $R_0 > 1$ and $S(0) \approx N$, the infected class initially increases.

SEIR. Adding an exposed class E (infected but not yet infectious) yields $N = S + E + I + R$:

$$\begin{cases} \dot{S}(t) = -\beta \dfrac{S(t) I(t)}{N}, \\ \dot{E}(t) = \beta \dfrac{S(t) I(t)}{N} - \sigma E(t), \\ \dot{I}(t) = \sigma E(t) - \gamma I(t), \\ \dot{R}(t) = \gamma I(t), \\ S(0) = S_0, \quad E(0) = E_0, \quad I(0) = I_0, \quad R(0) = R_0. \end{cases} \tag{2.13}$$

Here $\sigma > 0$ is the progression rate from exposed to infectious (mean latent period $= 1/\sigma$). Again, solutions remain non-negative and N is conserved. With standard incidence, the threshold remains

$$R_0 = \frac{\beta}{\gamma},$$

while the latent period (via σ) slows early growth and shifts epidemic timing.

2.1.9 Physiologically based demographic models

Various living and non-living factors influence the presence and number of insect species that harm crops, forests, or livestock (species commonly known as pests). These factors

are often challenging to separate and measure over different regions and periods. However, we can understand the biological processes and behaviours of these species, as well as their interactions with other relevant species in their environment, by using mechanistic models called "physiologically based demographic models" (PBDMs). These models can be integrated into a geographic information system to predict where these species might be found and how abundant they might be under different weather conditions, including observed and potential future climate changes.

PBDMs, when influenced by weather patterns, can forecast things like the timing of life cycle events, the age distribution of the species, and how their numbers change over time at one or multiple locations. This helps in predicting the distribution of these species across large geographical areas. PBDMs are effective at capturing the complexity of ecosystems using a small number of measurable factors because they apply the same ecological models to understand how resources are acquired and allocated at different levels of the food chain. Using these models makes parameter estimation easier when we already know the functions that model the physiology of the specific insect. This is particularly helpful, especially when there is limited biological data available.

Thus, a PBDM can be defined as a temperature–driven, stage–structured demographic model in which the population dynamics are governed by mechanistic development, mortality and reproduction functions.

2.2 Entomological Background

We specify here some background knowledge from a biological and entomological perspective. Some of the insects discussed and researched must be understood at a physiological level and in relation to the surrounding environment. The same applies to a bacterium that has caused considerable damage worldwide and also in our Italian region of Puglia.

2.2.1 Spodoptera frugiperda

The *Fall Armyworm* (Spodoptera frugiperda) belongs to the order Lepidoptera and is identified as one of the species of Fall Armyworm moths, specifically during their larval stage. The term "armyworm" is a general reference to various species, typically denoting the widespread invasive behaviour exhibited by the larvae. Recognized as a destructive pest, the Fall Armyworm poses a significant threat to a diverse range of crops, leading to substantial economic losses. Its scientific name, derived from the ancient Latin term "frugiperda" which means "lost fruits", highlights its capability to devastate crops. Due to its destructive nature, extensive research has been conducted on the Fall Armyworm's habits and potential methods of crop protection. Additionally, it serves as a notable subject for studying sympatric speciation[1].

[1]In evolutionary biology, sympatric speciation is the evolution of a new species from a surviving ancestral species while both continue to inhabit the same geographic region.



Figure 1: Spodoptera frugiperda - Larva.
Source: website *www.agro.genica.com.*

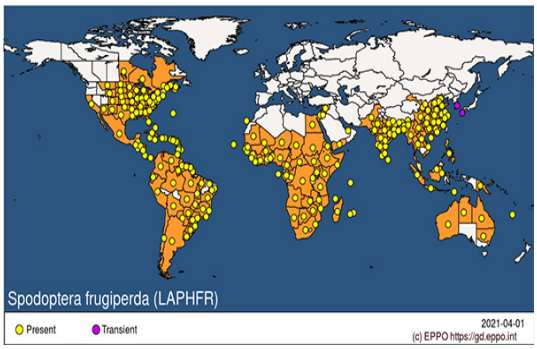


Figure 2: Spodoptera frugiperda States Distribution Map - 2021.
Source: website *www.eppo.int.*

The Fall Armyworm has a broad distribution spanning eastern and central North America, as well as South America. Its ability to endure winter is limited, as it cannot withstand below-freezing temperatures. Consequently, it only persists through the winter in the southernmost regions of the United States, specifically Texas and Florida. This characteristic makes the Fall Armyworm a more prevalent pest in the southeastern states. Nevertheless, during certain seasons, it extends its reach across the eastern United States, reaching as far north as southern Canada, colonizing regions with adequate food resources.

The armyworm primarily feeds on grasses and grain crops, such as corn, making it a significant agricultural pest. Interestingly, it has been observed to consume over 80 different plants, encompassing both non-economic and economic varieties.

Larvae exhibit cannibalistic behaviour, particularly targeting smaller larvae when food resources are scarce. Despite its potential negative impact on their own fitness, the larvae engage in cannibalism whenever possible. One damaging aspect of cannibalism for the Fall Armyworm is the transmission of diseases among individuals. However, in natural settings, the disadvantage of cannibalism may be offset by its role in eliminating competitors, thereby enhancing resource availability and indirectly improving the fitness of Fall Armyworm populations. A comprehensive picture of this insect biology, host range, invasion and larval cannibalism emerges from classic and recent syntheses: Sparks' (1979) [8] review on biology, Montezano et al.(2018) [57] on host plants, Goergen et al.(2016) [49] on the African invasion, and Chapman et al.(1999) [16] on the consequences of cannibalism.

2.2.2 Erasmoneura vulnerata

Erasmoneura vulnerata, as it can be seen in Figure 5, is a species of leafhopper (the common name for any species from the family Cicadellidae) native to North America.

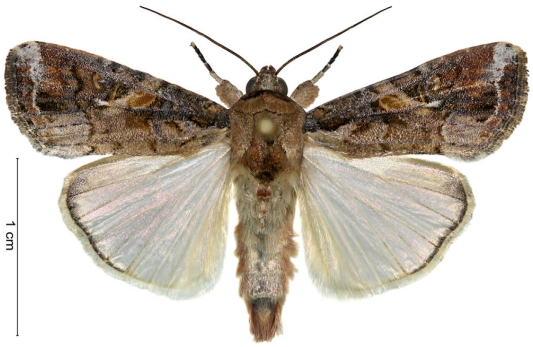


Figure 3: Spodoptera frugiperda - Adult. Source: website *www.defrentealcampo.com.*



Figure 4: Spodoptera frugiperda damage. Source: website *www.entomologytoday.org.*

The species was found to be in Europe in 2004 where it causes significant economic damage to vineyards. Erasmoneura vulnerata is commonly found on wild and cultivated grapes from both continents.

About its life cycle and reproduction, it must be mentioned that leafhoppers develop through five nymphal instars [2]. Within their native range, adults overwinter near vineyard margins where there is adequate canopy cover, inside plant structures, or organic material. Similarly, it was observed in Italy that buildings near vineyards seem to be important for their overwintering. Common overwintering species can include the canopy of Vitis labrusca and Vitis vinifera. Adults usually will move away from their overwintering sites towards vineyards beginning in April. In their natural habitat, female leafhoppers lay their eggs in the clusters of tubes within the leaf's main vein, as well as on the upper surface of the leaf.

Early instar nymphs can be first detected in late May while older nymph populations peak in June. The time for egg development is 16-20 days whereas overall development for adults requires 35-38 days. Two generations of Erasmoneura vulnerata per year are detected in their native range. However, three peaks are recorded in nymph densities in Europe suggesting the species is capable of three generations a year. It is additionally found that the 2nd generation is the most abundant.

Speaking about its plant hosts and the damage it can create, it is known that Erasmoneura vulnerata's exoskeletons are commonly observed on host leaves' undersides whereas both nymph instars and adults will mainly inhabit the upper leaf surfaces.

[2]Nymph (from Ancient Greek: meaning "bride") is the juvenile form of some invertebrates, particularly insects, which undergoes gradual metamorphosis (hemimetabolism) before reaching its adult stage. Unlike a typical larva, a nymph's overall shape already is very similar to that of the adult, except for a lack of wings (in winged species) and the emergence of genitalia. In addition, while a nymph moults, it never enters a pupal stage. Instead, the final moult results in an adult insect. Nymphs undergo multiple stages of development called instars.



Figure 5: Erasmoneura vulnerata.
Source: website *www.BugGuide.net.*



Figure 6: Foliage lesions (light green stains) and Erasmoneura vulnerata excrement (black spots).
Source: website *www.alpineentomology.net.*

Both the nymph and adult Erasmoneura vulnerata eat the leaf causing speckled white lesions on the leaf surface as can be seen in Fig. 6. If the damage is significant the lesions can fuse, causing large portions of discoloured tissue. The leaf has potential to prematurely fall at this point.

The leafhopper is commonly found in Vitis vinifera (the common grape vine) vineyards in Europe, infesting various crops equally. Vitis labrusca and the Judas tree are also attractive host plants for the adults. Additionally, Erasmoneura vulnerata has been recorded on many other host plants such as Aesculus, Rubus, and Salix species although the frequency of their collection on these plants is significantly lower than on Vitis species.

For European introduction, spread and vineyard-focused phenology/management, see the integrative review and field investigations by Duso and colleagues [65].

2.2.3 Philaenus spumarius

The meadow spittlebug, *Philaenus spumarius*, is a highly polyphagous xylem-feeding and widely distributed insect and the primary vector of *Xylella fastidiosa* in southern Europe. Under Mediterranean conditions the life cycle is typically univoltine (only one generation a year): eggs laid in late summer–autumn on low vegetation overwinter in diapause; in early spring they hatch and five nymphal instars develop on the herbaceous layer, each encased in a protective spittle mass that protects against desiccation and predators. Adult emergence peaks in late spring; as ground cover senesces, *P. spumarius* shifts from herbaceous hosts to shrubs and trees (including olive canopies), increasing contact with crops. Females enter an ovarian parapause that suppresses oviposition during the hottest months; reproduction resumes toward late summer/early autumn, and newly laid eggs re-enter diapause, closing the annual cycle. The species disperses by hopping and



Figure 7: Adult *Philaenus spumarius* (meadow spittlebug) on a leaf, dorsal view. Source: website *www.idtools.dpi.nsw.gov.*

short flights, yet can traverse tens to hundreds of meters across fragmented landscapes, shaping the spatial scale of transmission. Management relies on these phenological traits: control targets nymphs in spring (mechanical weeding/mowing, habitat manipulation) and newly emerged adults around the host shift, while surveillance relies on ground-cover inspections and canopy sampling. Phenology, dispersal and management in southern European olive systems are reviewed/quantified by Bodino et al., while Cornara et al. provide a broader synthesis of spittlebugs as *Xf* vectors ([83], [52]).

2.2.4 Xylella fastidiosa

Xylella fastidiosa is a bacterium that thrives aerobically (it needs oxygen for surviving) within the genus Xylella. Functioning as a plant pathogen, it flourishes within the water-conducting tissues of plants and spreads exclusively through xylem sap-feeding insects, i.e. insects that feed on the fluid transported in the xylem of plants, called xylem sap. Xylem is the vascular tissue of plants that carries water and nutrients from the roots to other parts of the plant.

Numerous plant diseases stem from Xylella fastidiosa infections. Although major outbreaks of Xylella fastidiosa-related diseases have predominantly occurred in the Americas and Europe, this pathogen has also been identified in other regions worldwide, including Taiwan, Israel, and a few other countries.

Xylella fastidiosa displays a remarkable capacity to infect an extensive set of plants, with many remaining asymptomatic. Disease manifestation arises in plant species susceptible to water flow blockages in the xylem vessels, attributed to factors such as bacterial obstruction, an exaggerated plant immune response, and the creation of air embolisms. A particular variant of *Xylella fastidiosa*, responsible for citrus variegated chlorosis, holds

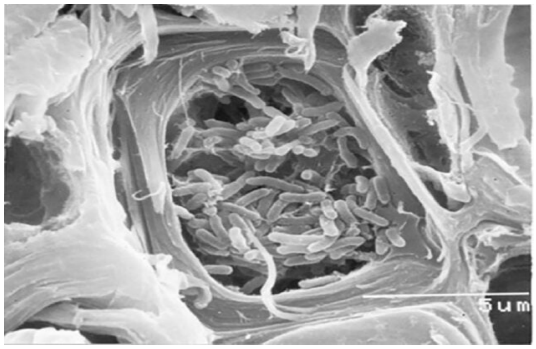


Figure 8: *Xylella fastidiosa* under the electron microscope.
Source: *www.denia.com.*



Figure 9: *Xylella fastidiosa* damage in Puglia - Italy.
Source: *www.terraevita.edagricole.it.*

the distinction of being the first bacterial plant pathogen to undergo genome sequencing, underscoring its significance in agriculture. Given the substantial global impact of this pathogen on agricultural crops, significant investments are being made in scientific research pertaining to Xylella fastidiosa and the associated diseases it brings.

Xf–Olive pathosystem In olive (*Olea europaea*), *X. fastidiosa* subsp. *pauca* is the causal agent of the olive quick decline syndrome (OQDS) in Apulia. After inoculation by xylem sap–feeding vectors (chiefly *Philaenus spumarius*), the bacterium colonizes xylem vessels forming biofilms and spreading systemically, which impairs hydraulic conductivity and produces canopy desiccation and decline ([54], [71], [52]). Vector phenology and host seasonal physiology tightly constrain the transmission window; in particular, the emergence and feeding dynamics of *P. spumarius* modulate the force of infection at the landscape scale ([104], [96], [80]). Within-host multiplication is temperature dependent and interacts with plant water status; water deficit can reshape symptom progression and carbohydrate allocation, thereby affecting detectable titres and disease trajectories [92]. In Chapter 4 we model these mechanisms with a stage-structured eco-epidemiological system of ODEs/DDEs that links vegetation dynamics, vector demography and phenology, and olive-tree disease classes, where infection is driven by acquisition and inoculation functions, disease progression is modulated by temperature and water stress (including superinfection), and recovery arises from thermal stress functions and non-systemic abortive infection functions. Foundational evidence on olive infection in Apulia, vector ecology and the role of water stress is synthesized in Saponari et al. (2017 [54]; 2019 [71]), Cornara et al. (2017) [52], and De Pascali et al. (2022) [92].

Xf–Grapevine pathosystem In grapevine (*Vitis vinifera*), *X. fastidiosa* subsp. *fastidiosa* causes Pierce's disease. Transmission is mediated by sharpshooters; infection

probability over a feeding event is well described by a Poisson model linking successful inoculations to vector number and feeding duration [21]. Efficient acquisition by vectors requires a minimum bacterial load in planta, establishing an epidemiologically relevant threshold for infectiousness [13]. Disease expression reflects xylem occlusions and vascular dysfunction [39], while temperature modulates both transmission efficiency and within-host dynamics, including the well-known cold-curing phenomenon in winter [35]. These features underpin the seasonal forcing and risk patterns of Pierce's disease considered in Chapter 7, in line with recent modelling and risk-mapping studies [94, 58]. In Chapter 7, indeed, we present a Grapevine Infection Model (GIM) that analyses and predicts the seasonal amplification/decline of *Xf* and its bidirectional redistribution between roots and branches within a cohort of vines, as driven by temperature, exogenous vector–borne inoculations, root-to-branches infection during spring regrowth, and the feedback whereby infections in the branches raise bacterial load in the roots.

3
Entomonlib: a MATLAB library for entomology

In this chapter we present *Entomonlib*, a MATLAB library we have written and used to simulate insect population dynamics modelled by the Kolmogorov equation (See subsection 2.1.7). We first frame the real-world problems that motivate its design, then formalize them into stage-structured population models. Next, we describe the numerical scheme adopted to solve these models, and finally we map these choices to the MATLAB implementation. Throughout, a fixed and reusable core is combined with pluggable components.

One of the first purposes of Entomonlib is to integrate key concepts in ecological modelling. It features physiologically based demographic models and phenological models, providing, among other things, a comprehensive understanding of how physiological processes intricately influence the growth or decline of populations under examination. The library numerically solves systems of partial differential equations to precisely describe interconnections between physiological processes.

One of Entomonlib's strengths lies in the generalization and optimisation of preexisting codes, consolidating them into a unified platform. This approach improves the library's versatility and usability.

The available models within Entomonlib, so far, cover a spectrum, including demographic models, phenological models, a demographic model with an optimised representation of two parameters linked to density-dependent mortality terms, demographic and phenological models with a set of different parameters to be optimised if requested. Moreover, every optimisation-enabled model can also run in a multisite mode: it fits the parameters using field and temperature data from several locations at once, so the estimates are based on a wider area and better reflect the species' biology rather than a possible response from a single site. All of this makes Entomonlib a powerful tool for researchers and practitioners engaged in ecological and population studies, offering a robust and flexible platform for exploring and simulating diverse ecological scenarios.

3.1 Real problems and stage-structured population models

Entomonlib has a multiplicity of objectives that can be chosen according to the individual needs of the user. Three illustrative examples follow.

The first real problem consists in predicting, in the months or years to come, the

population density of specific insect species. The second problem is related to defining how a particular insect group moves from one stage (for example: egg, larva, pupa, adult) to the next one. The third one consists in finding the parameters that best characterize the physiological functions of a particular insect population (information regarding the physiological functions will be given later in Subsection 3.5.3).

To solve these problems we need to model the dynamics of insect populations as a function of time and physiological age; furthermore the life cycle of these insects can be divided into stages that depend on this internal age variable. Since we adopt physiological age as the spatial variable, a suitable class of PDEs for this purpose is given by the Kolmogorov equations already presented in Subsection 2.1.7.

3.2 Useful models for entomologists

We now turn to a more detailed analysis of the different types of models that Entomonlib provides to entomologists, among those of greatest interest to them.

The selectable options on Entomonlib are:

1. demographic model,
2. phenological model,
3. demographic and phenological models with optimisation processes,
4. demographic and phenological models with optimisation processes - multisite modality.

3.2.1 Demographic model

Demographic models predict, months or even years in advance, how the population density and the relative abundance of a specific insect population will vary by solving the system of differential equations modelling the entomological problem.

3.2.2 Phenological model

Phenological models for insects predict the timing of characteristic events of their life, like emergence or, in general, transitions from a life stage to the next one. In this model, the target data are usually those related to the emergence of the adult phase, meaning the function that informs us about the changing percentage of insects transitioning from the pre-adult stage (e.g., larva) to the adult phase.

Another peculiarity of phenological models is that they analyse the insect life cycles basing their analysis even on various generations, as can be observed in Fig. 10, where we have three different generations with their emergence functions as output solutions

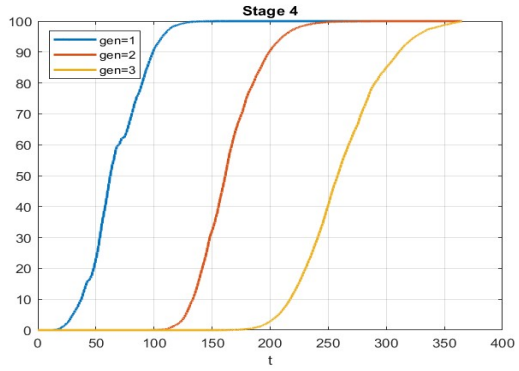


Figure 10: Example of output solution from Entomonlib for a phenological model in which emergence functions are defined over a one-year time span for 3 consecutive generations. The 4th stage is the adult one.
Source: Entomonlib.

from Entomonlib. The fact that the first generation emerges a few days from the initial time of the model is due to the fact that all insects were initially "placed" in the pre-adult phase as initial data. A multi-generation analysis can also be performed with the demographic model; however, knowing which generation a given insect belongs to at the time under consideration is of lesser importance, since the focus is on the total number of insects—regardless of generation—at that same moment.

3.2.3 Demographic and Phenological models with optimisation processes

Demographic and phenological models have been combined with an optimisation model to find the parameters that best approximate the physiological functions of insects. Currently, in Entomonlib, having target data to reference related to the model's solution function (usually abundance/density for the demographic models, emergence function for the phenological models), you can calculate the parameters that will best approximate the model's solution to the data you have. This is done through dedicated functions that are created on a case-by-case set based on the set of parameters you want to optimize. These can range from a single parameter of a single function, to potentially a much higher number, and even across separate functions (one related to development and one to mortality, for example), always remembering that "With four parameters I can fit an elephant, and with five I can make him wiggle his trunk" (John Von Neumann). Optimised parameters may not be tied to a specific physiological function; however, Entomonlib can calculate, e.g., the end-of-diapause day (the hibernation of insects), typically in early spring, which best approximates the emergence function of adults in late spring or summer. Obviously, using these models requires a large amount of target data; otherwise, the optimisation process may be inefficient. Now we report a summary of the

logic behind the Entomonlib optimisation process.

Given the data $(t_i, y_{\text{data},i})$, for $i = 1, \ldots, N$, we look for a parameter vector $\theta \in \mathbb{R}^p$ that minimizes the *loss function*

$$J(\theta) = \sum_{i=1}^{N} \left(y_{\text{model}}(t_i; \theta) - y_{\text{data},i} \right)^2 \tag{3.1}$$

where y_{model} is the solution provided by Entomonlib using the current occurrence of θ, and $y_{\text{data},i}$ are the data target corresponding to t_i. Prior knowledge is encoded as bounds and (possibly) linear/non-linear constraints (given by the user). The bounds are expressed by $\ell \in \mathbb{R}^p$ and $u \in \mathbb{R}^p$ such that

$$\ell_i \leq \theta_i \leq u_i, \quad \forall i = 1, \ldots, p,$$

they keep the search in physically/biologically meaningful regions and reduce the effective search space. To minimize the loss function, we have used the MATLAB function `fmincon`[3], which is a local and gradient-based optimizer; it hence requires a starting point (given by the user too) $\theta^{(0)}$. A good $\theta^{(0)}$ (from prior knowledge, coarse scans, or simpler fits) speeds convergence and improves the chance of finding the minimum of J. Having this information, `fmincon`, using algorithms such as interior-point, SQP, or trust region, iteratively updates θ to reduce J while satisfying constraints. Whenever the loss function is non-convex, the returned solution is generally a *local* minimum, not guaranteed to be global, especially in high dimension.

3.2.4 Demographic and Phenological models with optimisation processes - multisite.

It is quite common for the data collected to come from different sites. The optimisation process, described in Sect. 3.2.3, can be applied simultaneously to more than one site, or geographical zone. Having target data and temperature data for different sites can refine the process and increase the sensitivity of our search for parameters that make the solutions approximate, from site to site, the data target of their specific site. In this case, too, functions must be created specifically for the specific optimisation problem at hand, and, of course, Entomonlib must be provided with all the data necessary for the optimisation process.

3.3 Diapause

Diapause is a programmed, hormonally mediated state of suppressed development and metabolism that synchronizes the life cycle with predictable periods of adversity (e.g.,

[3] `fmincon` is a MATLAB function for constrained non-linear optimisation: given an objective function, an initial point/guess, and a set of equality/inequality bound constraints, it searches for a local minimum by using gradient–based algorithms (e.g. interior-point, SQP, active-set).

winter cold or summer drought). Unlike *quiescence*—a reversible slowdown that occurs directly in response to immediate unfavourable conditions—diapause is anticipatory: it is induced in advance by environmental cues and proceeds through distinct phases even if conditions temporarily improve. During diapause, growth, molting, or reproduction are paused, metabolic rate declines, and physiological adjustments increase tolerance to cold, desiccation, and food scarcity. The process typically includes induction, preparation, maintenance, termination, and post-diapause development. Diapause can occur at embryonic, larval/nymphal, pupal, or adult stages; it may be obligate (every generation) or facultative (triggered only under certain conditions), with both winter and summer forms. Photoperiod may be the primary cue, modulated by temperature, food quality, and crowding; in many species, maternal photoperiod or temperature can program diapause in the offspring. Ecologically, diapause aligns active development with resource availability and suitable climate windows, trading immediate growth or reproduction for survival and long-term fitness. In modelling work, diapause is often represented as a stage-dependent switch governed by photoperiod/temperature thresholds for induction and by termination rules such as chilling requirements or degree-day accumulation; this switch modifies development, mortality, and fecundity during maintenance and reverts them upon termination (see [70] or [50]). Entomonlib allows, in each of its models, the option to include an insect diapause period. This requires specifying the rules for diapause induction and termination and, where appropriate, adjusting (recalibrating) the physiological functions during and after the diapause interval. By default, during diapause the development rate is markedly reduced, mortality is increased, and fecundity is set to zero. In the post-diapause period, the model can either revert to the pre-diapause physiological functions or adopt alternative ones. The user can also choose which generations may enter diapause and which may not, as well as which specific stages are selectable.

3.4 Numerical discretisation

We now move from the mathematical models to numerical methods. The PDE system is discretised by second-order centered Finite Volumes in physiological age and by (semi-implicit) backward Euler in time. We first present the single-stage scheme, then extend it to the multistage coupling used in applications.

3.4.1 Discretisation of the core system for a single stage

We begin with a single stage and derive its Finite Volume semi-discretisation. Then we apply a semi-implicit Euler scheme. The latter choice allows us to avoid strong nonlinearity due to the, possibly, non-local nature of both mortality and fecundity functions.

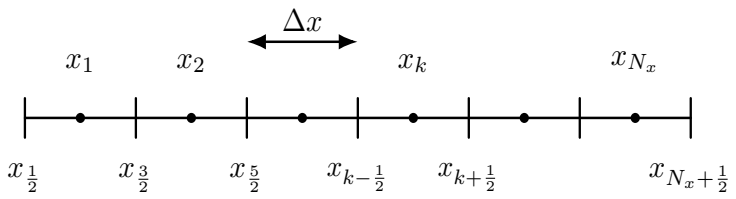


Figure 11: Nodes and control volumes in the interval [0,1].

Let us consider the system (2.5)-(2.10). Given a positive integer N_x, let $\Delta x = \frac{1}{N_x}$, let us define the nodes

$$x_k = (k - 0.5) \cdot \Delta x \text{ for } k = 1, \dots, N_x, \tag{3.2}$$

and consider the partition of the interval $[0, 1]$ into control volumes

$$I_k = \left[x_k - \frac{\Delta x}{2}, x_k + \frac{\Delta x}{2} \right], \quad \text{for } k = 1, \dots, N_x. \tag{3.3}$$

Subsequently, for $k = 1, \dots, N_x$, let us define $x_{k-\frac{1}{2}}$ and $x_{k+\frac{1}{2}}$ as the left and right endpoints, respectively, of the volume I_k (see Fig. 11).

For each $t \in (0, T)$, we restrict the differential equation (2.5) to each control volume I_k and integrate it by parts: we have

$$\begin{gathered} \partial_t \int_{I_k} \varphi(t,x)dx + H(t,x)|_{x=x_{k+\frac{1}{2}}} - H(t,x)|_{x=x_{k-\frac{1}{2}}} + \\ \mathcal{M}^s(t,\varphi) \int_{I_k} \varphi(t,x)dx = 0, \end{gathered} \tag{3.4}$$

where $H(t, x)$ has been defined in (2.11).

Then, for each $t \in (0, T)$ let $\varphi_{\Delta x}(t, x)$ be a function that is constant with respect to x on each control volume I_k and set

$$\varphi_k(t) = \varphi_{\Delta x}(t, \cdot)|_{I_k} \quad \text{for } k = 1, \dots, N_x \text{ and } \boldsymbol{\varphi}(t) = \begin{bmatrix} \varphi_1(t) \\ \varphi_2(t) \\ \vdots \\ \varphi_{N_x}(t) \end{bmatrix}. \tag{3.5}$$

$\varphi_k(t)$ is an approximation of the mean over I_k of the unknown function $\varphi(t, x)$.

Note that

$$\int_0^1 \varphi_{\Delta x}(t,x)dx = \Delta x \sum_{k=1}^{N_x} \varphi_k(t). \tag{3.6}$$

From now on, for clarity, we set

$$\mathcal{M}_{\Delta x}(t, \boldsymbol{\varphi}(t)) = \mathcal{M}(t, \varphi_{\Delta x}), \tag{3.7}$$

for example, if $\mathcal{M}$ is chosen as in (2.4), then

$$\mathcal{M}_{\Delta x}(t, \boldsymbol{\varphi}(t)) = M(t) \left(1 + a \left(\int_0^1 \varphi_{\Delta x}(t, x) dx \right)^2 \right)^d.$$

Let us define $|I_k|$ as the measure of the k-th control volume I_k. The discretisation of the Finite Volumes on (3.4) reads

$$|I_k| \frac{d\varphi_k(t)}{dt} + H_k^+(t) - H_k^-(t) + \mathcal{M}_{\Delta x}(t, \boldsymbol{\varphi}(t)) |I_k| \varphi_k(t) = 0, \tag{3.8}$$

where $H_k^-(t)$ and $H_k^+(t)$ are suitable approximations of $H(t,x)|_{x=x_{k-\frac{1}{2}}}$ and $H(t,x)|_{x=x_{k+\frac{1}{2}}}$, respectively, obtained by applying second-order centered finite difference schemes (with respect to Δx).

More precisely, after defining

$$\mathcal{G}_{\Delta x}(\boldsymbol{\varphi}(t)) = \Delta x \sum_{k=1}^{N_x} G(x_k) \varphi_k(t) \tag{3.9}$$

(indeed $\mathcal{G}_{\Delta x}(\boldsymbol{\varphi}(t))$ is the approximation of the integral $\int_0^1 G(x)\varphi(t,x)dx$ using the composite midpoint method), and considering both (2.11) and the boundary conditions (2.6)-(2.7), we have:

$$\begin{aligned}
&H_1^-(t) = F(t)\mathcal{G}_{\Delta x}(t) \\
&H_k^-(t) = S(t)\frac{\varphi_k(t) + \varphi_{k-1}(t)}{2} - b\frac{\varphi_k(t) - \varphi_{k-1}(t)}{\Delta x}, \quad k = 2, \dots, N_x, \\
&H_k^+(t) = S(t)\frac{\varphi_{k+1}(t) + \varphi_k(t)}{2} - b\frac{\varphi_{k+1}(t) - \varphi_k(t)}{\Delta x}, \quad k = 1, \dots, N_x - 1, \\
&H_{N_x}^+(t) = S(t)\varphi_{N_x}(t).
\end{aligned} \tag{3.10}$$

Writing (3.8) for each $k = 1, \dots, N_x$ and recalling that $|I_k| = \Delta x$ for $k = 1, \dots, N_x$, the semi-discrete approximation of the system (2.5)-(2.10) reads:

given $\varphi_k(0) = \varphi_0(x_k)$ for $k = 1, \dots, N_x$, for each $t \in (0, T)$ we seek the functions $\varphi_1(t), \dots, \varphi_{N_x}(t)$ such that

$$
\begin{cases}
\dfrac{d\varphi_1}{dt}(t) + \left[\dfrac{S(t)}{2\Delta x} + \dfrac{b}{(\Delta x)^2} + \mathcal{M}_{\Delta x}(\boldsymbol{\varphi}(t))\right]\varphi_1(t) + \\
\qquad\qquad + \left[\dfrac{S(t)}{2\Delta x} - \dfrac{b}{(\Delta x)^2}\right]\varphi_2(t) = \dfrac{F(t)}{\Delta x}\mathcal{G}_{\Delta x}(\boldsymbol{\varphi}(t)), \\
\dfrac{d\varphi_k}{dt}(t) - \left[\dfrac{S(t)}{2\Delta x} + \dfrac{b}{(\Delta x)^2}\right]\varphi_{k-1}(t) + \left[\dfrac{2b}{(\Delta x)^2} + \mathcal{M}_{\Delta x}(\boldsymbol{\varphi}(t))\right]\varphi_k(t) + \\
\qquad\qquad + \left[\dfrac{S(t)}{2\Delta x} - \dfrac{b}{(\Delta x)^2}\right]\varphi_{k+1}(t) = 0, \text{ for } k = 2, \ldots, N_x - 1 \\
\dfrac{d\varphi_{N_x}}{dt}(t) - \left[\dfrac{S(t)}{2\Delta x} + \dfrac{b}{(\Delta x)^2}\right]\varphi_{N_x-1}(t) \\
\qquad\qquad + \left[\dfrac{S(t)}{2\Delta x} + \dfrac{b}{(\Delta x)^2} + \mathcal{M}_{\Delta x}(\boldsymbol{\varphi}(t))\right]\varphi_{N_x}(t) = 0.
\end{cases}
\tag{3.11}
$$

Setting $\boldsymbol{\varphi}^0 = \begin{bmatrix} \varphi_0(x_1) \\ \varphi_0(x_2) \\ \vdots \\ \varphi_0(x_{N_x}) \end{bmatrix}$,

$$
A(t) = \begin{bmatrix}
\beta_1(t) & \gamma_1(t) & 0 & \cdots & 0 & 0 \\
\alpha_2(t) & \beta_2(t) & \gamma_2(t) & \cdots & 0 & 0 \\
0 & \alpha_3(t) & \beta_3(t) & \cdots & 0 & 0 \\
\cdots & \cdots & \cdots & \cdots & \cdots & \cdots \\
\cdots & \cdots & \cdots & \cdots & \cdots & \cdots \\
0 & 0 & 0 & \cdots & \alpha_{N_x}(t) & \beta_{N_x}(t)
\end{bmatrix},
\tag{3.12}
$$

with

$$
\begin{aligned}
&\beta_1(t) = \frac{S(t)}{2\Delta x} + \frac{b}{(\Delta x)^2}, \quad \gamma_1(t) = \frac{S(t)}{2\Delta x} - \frac{b}{(\Delta x)^2}; \\
&\quad \text{for } k = 2, \ldots, N_x - 1 \\
&\alpha_k(t) = -\left(\frac{S(t)}{2\Delta x} + \frac{b}{(\Delta x)^2}\right), \beta_k(t) = \frac{2b}{(\Delta x)^2}, \gamma_k(t) = \frac{S(t)}{2\Delta x} - \frac{b}{(\Delta x)^2}; \\
&\alpha_{N_x}(t) = -\left(\frac{S(t)}{2\Delta x} + \frac{b}{(\Delta x)^2}\right), \quad \beta_{N_x}(t) = \frac{S(t)}{2\Delta x} + \frac{b}{(\Delta x)^2},
\end{aligned}
$$

and denoting by $\mathbf{e}_1 \in \mathbb{R}^{N_x \times 1}$ the vector whose first term is 1 and all others are 0, the semi-discrete algebraic form of (3.11) reads

$$
\begin{cases}
\frac{d\boldsymbol{\varphi}}{dt}(t) + A(t)\boldsymbol{\varphi}(t) + \mathcal{M}_{\Delta x}(\boldsymbol{\varphi}(t))\boldsymbol{\varphi}(t) = \frac{F(t)}{\Delta x}\mathcal{G}_{\Delta x}(\boldsymbol{\varphi}(t))\mathbf{e}_1, \quad t \in (0, T) \\
\boldsymbol{\varphi}(0) = \boldsymbol{\varphi}^0.
\end{cases}
\tag{3.13}
$$

The complete discretisation of the system (2.5)-(2.8) is achieved by applying the Implicit Euler method to (3.13). To do this, we define a positive integer N_T, denote by $\Delta t = T/N_T$ the time discretisation step, set $t^n = n\Delta t$, and denote by $\boldsymbol{\varphi}^n$ the approximation of $\boldsymbol{\varphi}(t^n)$. It reads: given $\boldsymbol{\varphi}^0$ as in (3.13), for $n = 1, \ldots, N_T$, we seek $\boldsymbol{\varphi}^n$ such that

$$\frac{\boldsymbol{\varphi}^n - \boldsymbol{\varphi}^{n-1}}{\Delta t} + A(t^n)\,\boldsymbol{\varphi}^n + \mathcal{M}_{\Delta x}(\boldsymbol{\varphi}^n)\,\boldsymbol{\varphi}^n = \frac{F(t^n)}{\Delta x}\mathcal{G}_{\Delta x}(\boldsymbol{\varphi}^n)\,\mathbf{e}_1. \tag{3.14}$$

To overcome the non-linearity in (3.14) (and to avoid a large computational cost at each time step t^n), we replace the term $\mathcal{M}_{\Delta x}(\boldsymbol{\varphi}^n)$ with $\mathcal{M}_{\Delta x}(\boldsymbol{\varphi}^{n-1})$, which means taking into account a delay of Δt in the mortality function. Consequently, even though the right-hand side of (3.14) is linear with respect to $\boldsymbol{\varphi}^n$, we apply the same delay to it by substituting $\mathcal{G}_{\Delta x}(\boldsymbol{\varphi}^n)$ with $\mathcal{G}_{\Delta x}(\boldsymbol{\varphi}^{n-1})$, aiming to not alter the tridiagonality of the matrix $A(t)$. Indeed, solving a tridiagonal system of size N_x is very inexpensive as only $\mathcal{O}(N_x)$ floating-point operations are required. Conversely, if we were to consider $\mathcal{G}_{\Delta x}(\boldsymbol{\varphi}^n)$ instead of $\mathcal{G}_{\Delta x}(\boldsymbol{\varphi}^{n-1})$, the small bandwidth of the matrix $A(t^n)$ would be lost, leading to a matrix fill-in case, and the computational cost to compute $\boldsymbol{\varphi}^n$ would increase to $\mathcal{O}(N_x^3)$ floating-point operations.

Therefore, instead of (3.14), which is non-linear, we solve the linearized problem (indeed, we are applying a semi-implicit version of the Implicit Euler method): given $\boldsymbol{\varphi}^0$ as in (3.12), for $n = 1, \ldots, N_T$, we seek $\boldsymbol{\varphi}^n$ such that

$$\frac{\boldsymbol{\varphi}^n - \boldsymbol{\varphi}^{n-1}}{\Delta t} + A(t^n)\,\boldsymbol{\varphi}^n + \mathcal{M}_{\Delta x}\left(\boldsymbol{\varphi}^{n-1}\right)\boldsymbol{\varphi}^n = \frac{F(t^n)}{\Delta x}\mathcal{G}_{\Delta x}\left(\boldsymbol{\varphi}^{n-1}\right)\mathbf{e}_1. \tag{3.15}$$

Let $\tilde{\varphi}(t,x)$ denote the numerical approximation of the solution $\varphi(t,x)$ of (2.5)-(2.8) obtained so far. $\tilde{\varphi}(t,x)$ is a piecewise constant function in both t and x. More precisely, defining $\boldsymbol{\varphi}_k^n$ as the k-th component of the vector $\boldsymbol{\varphi}^n$ (for $k = 1, \ldots, N_x$), we have

$$\tilde{\varphi}(t,x) = \boldsymbol{\varphi}_k^n \quad \forall (t,x) \in \left[t^n, t^{n+1}\right) \times I_k. \tag{3.16}$$

It can be shown that $\tilde{\varphi}(t,x)$ is an approximation of $\varphi(t,x)$ accurate to second order with respect to Δx and first order with respect to Δt, provided that both Δx and Δt are sufficiently small.

3.4.2 Discretisation of the Multistage Problem

We now couple stages by adding the boundary influx from reproduction (from stage $\mathcal{S}$ to stage 1) and the fluxes between consecutive stages.

For each stage s, indeed, we proceed as done in the previous section. Let $(\boldsymbol{\varphi}^s)^n$ denote the fully discretised solution of the function φ^s at time t^n and similarly, let $A^s(t^n)$ denote the Finite Volume matrix at stage s and time t^n, and similarly with other variables.

The approximation of the multistage system (2.5)-(2.8) with the second-order centered Finite Volume method in space and the semi-implicit Euler method in time reads:

$$
\begin{aligned}
&\text{given } (\boldsymbol{\varphi}^1)^0, \dots, (\boldsymbol{\varphi}^{\mathcal{S}})^0,\\
&\text{for } n = 1, \dots, N_T, \text{ seek } (\boldsymbol{\varphi}^1)^n, \dots, (\boldsymbol{\varphi}^{\mathcal{S}})^n \text{ such that}\\
&\qquad \frac{(\boldsymbol{\varphi}^1)^n - (\boldsymbol{\varphi}^1)^{n-1}}{\Delta t} + A^1(t^n)(\boldsymbol{\varphi}^1)^n + \mathcal{M}^1_{\Delta x}\big((\boldsymbol{\varphi}^1)^{n-1}\big)(\boldsymbol{\varphi}^1)^n\\
&\qquad = \frac{F^1(t^n)}{\Delta x}\, \mathcal{G}_{\Delta x}\big((\boldsymbol{\varphi}^{\mathcal{S}})^{n-1}\big)\, \mathbf{e}_1, \qquad (3.17)\\
&\qquad \text{for } s = 2, \dots, \mathcal{S},\\
&\qquad\qquad \frac{(\boldsymbol{\varphi}^s)^n - (\boldsymbol{\varphi}^s)^{n-1}}{\Delta t} + A^s(t^n)(\boldsymbol{\varphi}^s)^n + \mathcal{M}^s_{\Delta x}\big((\boldsymbol{\varphi}^s)^{n-1}\big)(\boldsymbol{\varphi}^s)^n\\
&\qquad\qquad = S^{s-1}(t^n)\, (\boldsymbol{\varphi}^{s-1})^n_{N_x}\, \mathbf{e}_1.
\end{aligned}
$$

We recall that the superscript n and subscript N_x in $(\boldsymbol{\varphi}^{s-1})^n_{N_x}$ denote the time step and Finite Volume, respectively.

3.5 Description of the Entomonlib code logic structure

Finally, we map the numerical method to the MATLAB implementation. We walk through the execution process on a minimal single-site demographic model without optimisation, illustrating inputs, function setup, discretisation, solver loop, outputs, and (where applicable) error computation. This serves as a minimal working example among those implemented in Entomonlib.

3.5.1 Input, related checks, and determination of the Input folder

The run starts from the user-editable input file containing the problem's data. *Entomonlib* validates sizes, types, and required fields, reports inconsistencies, and resolves the absolute path to the input folder to make the data discoverable at runtime.

So the first thing Entomonlib does in a run is to read the MATLAB file of the input data creating the MATLAB structure[4] called *prob_data*. The file in question is the only one that can be modified directly by the user and concerns the various choices which will be described in more detail later. There are diverse MATLAB input files for the various mathematical models that can be used, e.g. *Demographic_Set_Data_Input, Phenological_Set_Data_Input*, etc.

[4]A MATLAB structure is a data type that allows you to organize and group related data into a single variable. It can contain several fields, each of which can be an array, matrix, string, scalar value, or another structure.

Immediately afterwards Entomonlib checks the input data just chosen. The fact that many inputs must have the correct size, or must necessarily be MATLAB strings (or arrays, or cells, etc), or whether or not they must actually be defined: these facts make it necessary to check all these different situations to avoid errors in the execution of the code. When Entomonlib finds an inconsistency it displays it on the screen to the user, making the inconsistent parameter explicit, so that the user can return to the Input file in order to fix what is incorrect. The MATLAB file in question is called *Arrays_Check*.

After this, there is a brief part of the code that ensures that the complete path to the folder containing input data is correctly identified and added to MATLAB's path, enabling the code to access this data during its execution.

3.5.2 Data loading

Subsequently, we find the part of Entomonlib code dedicated to data loading: named e.g. *Demographic_Load_Data*. Basically, three types of data can be inserted where necessary:

Box 3.1: Abiotic Drivers in Insect Biology

Insects live, thrive, die, and reproduce according to some biotic and other abiotic drivers. Among the abiotic drivers are:

1. Temperature: plays a crucial role in influencing the metabolic activity of insects. It can affect development rate, survival, reproduction, and other aspects of insect biology.
2. Humidity: environmental humidity can influence insect survival, especially concerning their ability to regulate water loss.
3. Light: can influence the behaviour, activity, and rhythm of insects.
4. Quality and quantity of food: the availability and composition of food can impact the development, survival, and reproduction of insects.
5. Substrate and habitat: characteristics of the substrate or habitat where insects live can significantly impact their biology. For example, soil type can influence egg deposition and larval survival.
6. Environmental pollution: such as pesticides, heavy metals, and other contaminants can have negative effects on insect health, influencing development and survival.
7. Atmospheric pressure: variations in atmospheric pressure can influence the flight of insects, especially for those that rely on flight as a means of locomotion.

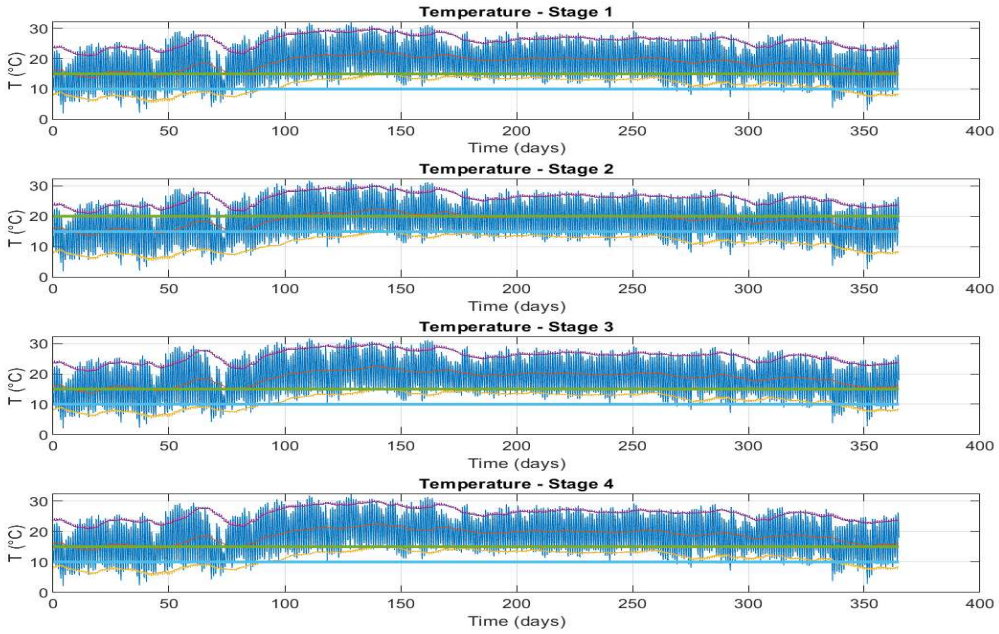


Figure 12: An example of temperature plots.
Source: Entomonlib.

• The first input data we have to give Entomonlib are the temperature data, the only chosen abiotic driver so far for Entomonlib.

Temperature data are mandatory for the program to function. They can be stored in .txt or .csv files. The file must consist of two columns. The first contains the times of the various measurements and the second contains the actual temperatures (in degrees Celsius) measured at the time relative to the same row. As we can see in Fig. 12 the temperatures can be different from one stage of the insect to another. This is because the main driver of an insect's physiological and metabolic processes can vary from the place where the insect lives most: the possibilities at the moment are: soil, air, and water. Depending on where, in the specific stage, the insect spends most of its time, we will use some data rather than others.

• The second type of input data is not necessary if you already have parameters that can define the physiological functions of the insect (development rate, mortality rate, temperature-dependent fertility rate, and physiological age-dependent rate function). If these parameters are not available, Entomonlib can search, starting from a chosen reference function (this topic will be discussed in more detail later), the best, in the sense of least squares, function that approximates the data provided by the user. This

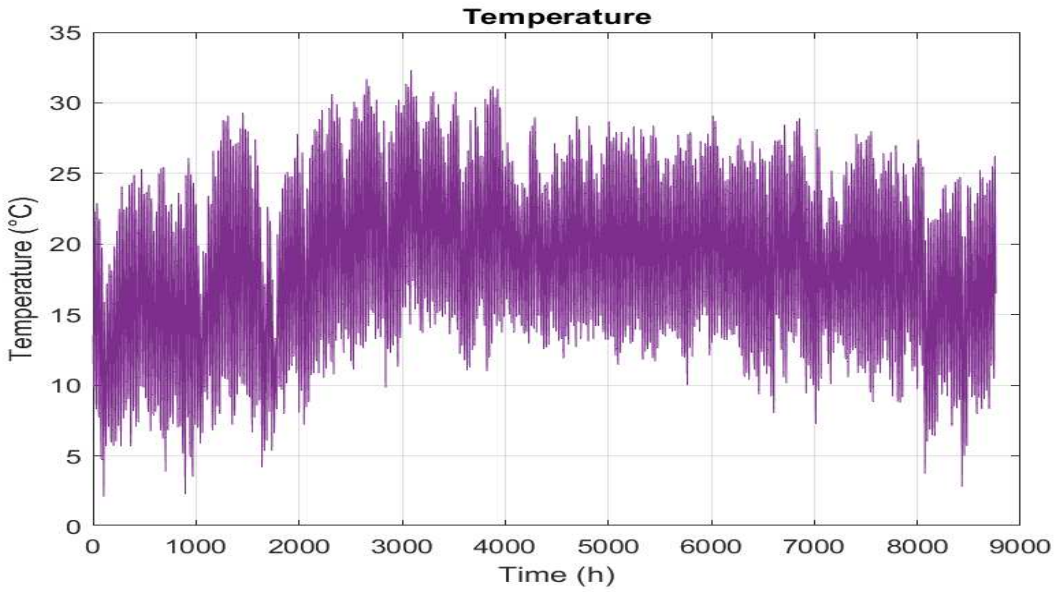


Figure 13: Another example of a temperature plot.
Source: Entomonlib.

data, if required, is uploaded at this time. An example of what this process may output can be seen in Fig. 14. The red asterisks are the data taken in the field or in the laboratory by researchers. In this case, Entomonlib has found the Brière-type function that best approximates these data to be able to have a function that can relate to all the temperatures in the range chosen by the user. Like the temperature data, these data must also be input in a .txt or .csv file and must consist of two columns: but this time the first will contain the various temperatures at which the measurement was taken, and the second one the rate of the function in question relative to the temperature on the same row.

• The third type of input data is the so-called "target data". They are the only data that can be used to validate the reliability of the model. In the demographic model for example, in which the population density of a specific insect is a function of time, the target data are precisely the measurements of population densities or the abundance taken in the field. The target data are necessary to define the two types of errors that can be evaluated between the solution and the target data itself. This evaluation is needed in all those series of models with an optimisation that allow us to find the parameters that best approximate the physiological functions of the specific insect.

If you do not have these data, Entomonlib will still work, unless a model is used that is based on an optimisation process starting from the target data, or is asked to plot the data on the screen together with the solutions found. Also in this case the data must be

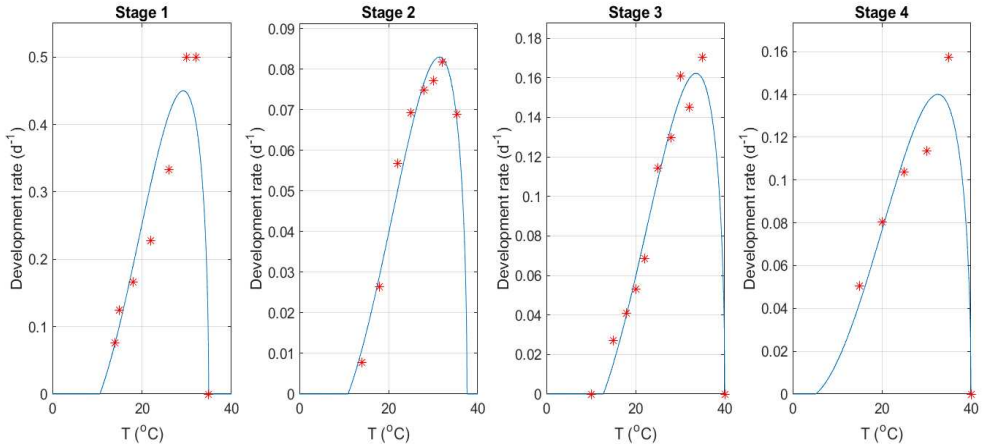


Figure 14: Development rate functions determined from data (chosen function type: Brière).
Source: Entomonlib.

contained in .txt or .csv files, in two columns: in the first one, we have time instants, and in the second one the measured values of the specific physical quantity under analysis, related to the corresponding time instant, in the same row.

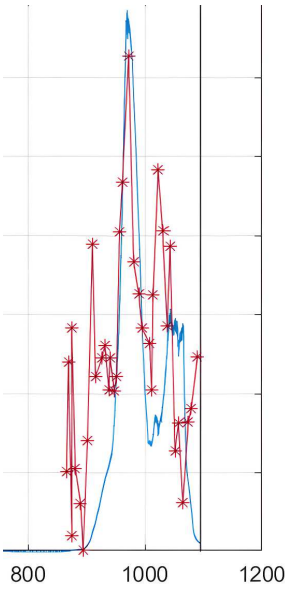


Figure 15: A visual comparison of an Entomonlib abundance solution (blue line) and the related target data (red asterisks).
Source: Entomonlib.

3.5.3 Functions settings

The third main step taken by Entomonlib is the setting of the physiological functions of the insect population. They are as follows: development rate functions, mortal-

ity rate functions, temperature-dependent fertility rate function, and physiological-age-dependent fertility rate function. To these are also added any modifications of the first two typologies in the possible diapause and post-diapause periods of the insect. Each stage of the insect has its specific development and mortality rate function (with possible variations linked to diapause). The adult stage is the only one to have fertility functions, being the only one that can procreate.

Now follows a list of the possible basic functions from which the user can choose for each type of rate function. It is necessary to remember that Entomonlib was born with the idea of always being improved and further assembled with more possible functions and choices. The following list consists of the choices that can be used during the month of October 2025.

We also remember that the various functions can be defined either starting from parameters, entered by the user, or through an optimisation process, in the sense of least squares, starting from data taken in the field or in the laboratory. A separate modality is linked to the fertility function dependent on physiological age, this will be discussed extensively in due course.

1. Development rate function

The development rate function, temperature-dependent, models how temperature experienced by an insect affects its rate of development. The development rate could be interpreted as the speed at which the physiological age of the insect progresses from the initial value to the final value of the particular stage it is undergoing at that time. Therefore, the development rate could be considered as the inverse of the time the insect takes to complete the stage it is undergoing. This function indicates how temperature influences key biological processes such as growth and maturation. By modelling the impact of temperature on the development rate, scientists gain insights into the temporal dynamics of an organism's life cycle. This function is crucial for understanding how environmental temperatures shape the progression of developmental stages within a population, providing valuable information for ecological and population studies.

The following functions map temperature expressed in degrees Celsius as $T[^{\circ}C]$ to the daily development rate of the insect $y[d^{-1}]$.

1. Constant $y = a$
2. Linear $y = aT + b$
3. Quadratic $y = aT^2 + bT + c$
4. Brière $y = aT(T - b)\sqrt{c - T}$

   Since the Brière-type function is less known than the others, we also report it in a graph in Fig. 16. Generalized Brière functions, depending on more than

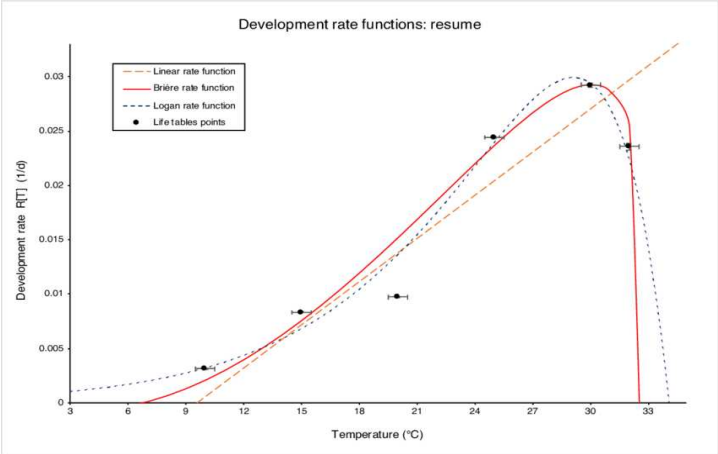


Figure 16: A Brière function cut in its negative values.
Source: [78].

three parameters, are largely used in the literature. Here we have chosen classical Brière functions depending on three parameters and they are: a scale multiplicative coefficient a, and two other parameters b, c that define where the function will be positive (for $b < T < c$).

Each function is modified by nullifying its possible negative values. Furthermore, it is set to zero outside a suitable interval chosen by the user (*Set_Data_Input* script).

2. Mortality rate function

The temperature-dependent mortality rate function describes how temperature affects the rate at which individuals within a population die. This function captures how temperature influences various physiological processes affecting an organism's survival. By modelling the mortality rate as a function of temperature, researchers can gain insights into the impact of environmental conditions on population dynamics.

The following functions map temperature expressed in degrees Celsius $T[°C]$, to the daily rate of mortality of the insect as the dependent variable $y[d^{-1}]$.

Also in this case, each function is modified by nullifying its possible negative values. Furthermore, it is set to zero outside a suitable interval previously decided by the user.

1. Constant $y = a$
2. Linear $y = aT + b$
3. Quadratic with constant exterior branches $y = aT^2 + bT + c$

   This type of function is simply a parabola nullified in its possible negative values and equalized to a certain value (decided by the user) if the latter is exceeded by the values of the parabola. (Fig. 17)

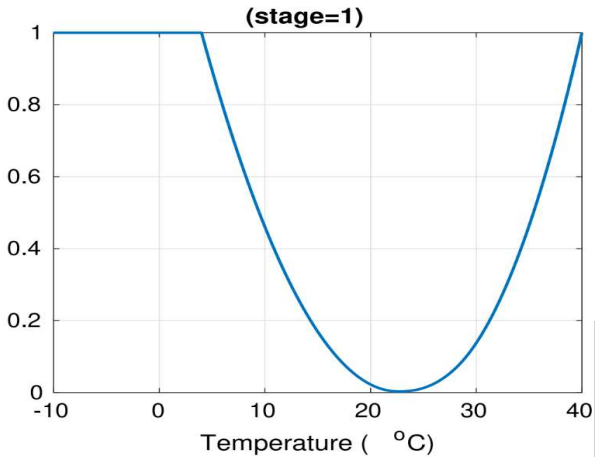


Figure 17: The quadratic with constant exterior branches function.
Source: Entomonlib.

4. 3branches

This mortality rate function has a very laborious and non-trivial definition (Fig. 18). Another similar piecewise function is defined in [9], albeit for the development rate and not the mortality rate.

We first define the average proportional mortality function $\mu(T)$, modelled with a convex and continuous function, namely $\mu(T) = \max\left(\tilde{\mu}(T), 0\right)$ with

$$\tilde{\mu}(T) = \begin{cases} k, & T < T_k^{\text{inf}} \\ AT^2 + BT + C, & T_k^{\text{inf}} \leq T \leq T_k^{\text{sup}} \\ k, & T > T_k^{\text{sup}} \end{cases} \tag{3.18}$$

With the fixed cut-off threshold $k \in [0, +\infty]$ chosen by the user, Entomonlib can find T_k^{sup} and T_k^{inf} to guarantee that $\mu(T)$ is globally continuous.

Then, set

$$m(T) = \begin{cases} c_{1l}\left(T - \bar{T_\nabla}\right)^2 + c_{2l}\left(T - \bar{T_\nabla}\right) + c_{3l}, & T < \bar{T_\nabla}, \\ -S(T)\ln\left(1 - \mu(T)\right), & \bar{T_\nabla} \leq T \leq \bar{T_\Delta}, \\ c_{1r}\left(T - \bar{T_\Delta}\right)^2 + c_{2r}\left(T - \bar{T_\Delta}\right) + c_{3r}, & T > \bar{T_\Delta}, \end{cases} \tag{3.19}$$

where $S(T)$ is the development rate function of the related stage, previously defined, while the values $\bar{T_\nabla}$ and $\bar{T_\Delta}$ are set within an interval previously decided by the user, and are, respectively, the first point where the central branch of the function is positive, decreasing and convex and the last point where the function is

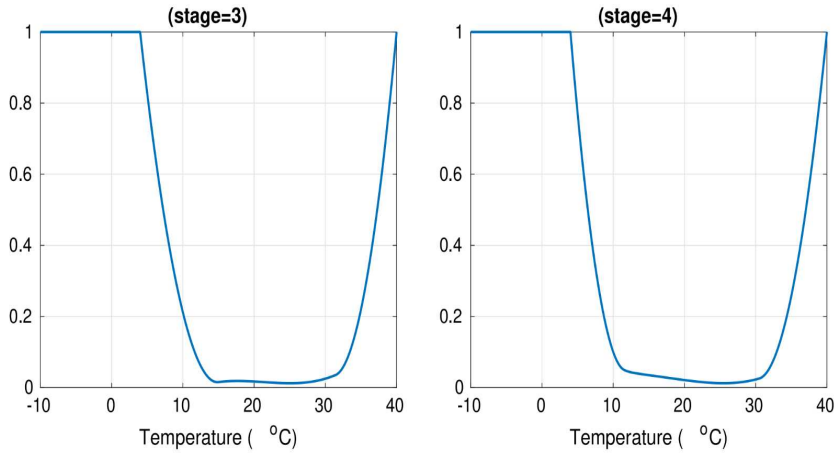


Figure 18: The 3branches function.
Source: Entomonlib.

positive, increasing and convex. The parameters c_{il} and $c_{ir}, i = 1, 2, 3$, are inferred imposing, in order to guarantee that $m(T)$ is globally C^1, the following conditions:

A) the passage of the lateral parabolic branch through the point with abscissa $\bar{T_\nabla}$ ($\bar{T_\Delta}$, resp.) if we are evaluating the parameters of the left (right, resp.) parabolic branch,

B) differentiability at $\bar{T_\nabla}$ ($\bar{T_\Delta}$, resp.)

C) the passage through a point P (P', resp.), defined by the user, if we are evaluating the parameters of the left (right, resp.) parabolic branch. The point P (P', resp.) is the interface point between the parabolic branch and the constant cutoff branch.

Finally, we define the 3branches temperature-dependent mortality rate function as

$$M(T) = max(\tilde{M}(T), 0), \tag{3.20}$$

where

$$\tilde{M}(T) = \begin{cases} \min\left(m(T), y_P\right), & T < \bar{T_\nabla}, \\ m(T), & \bar{T_\nabla} \leq T \leq \bar{T_\Delta}, \\ \min\left(m(T), y_{P'}\right), & T > \bar{T_\Delta}. \end{cases} \tag{3.21}$$

5. Power function (symmetric around an optimum)

$$y(T) \;=\; \min\left\{ \left(\frac{|T - T_{\text{opt}}|}{s} \right)^{2b}, 1 \right\}, \qquad b > 0.$$

This function is zero at the optimal temperature T_{opt}, increases with the distance $|T - T_{\text{opt}}|$, and saturates at the value 1 for $|T - T_{\text{opt}}| \geq s$. The exponent b controls the curvature/steepness: larger b makes the function flatter near T_{opt} and steeper near the saturation. By construction it is non-negative; as for the other cases, it can be set to zero outside the user-defined interval $[T_{\min}, T_{\max}]$.

3. Fertility rate function
The fertility function is defined as

$$y(T, x) = \varphi(T) \cdot \vartheta(x), \tag{3.22}$$

where $\varphi(T)$ is a temperature-dependent fertility function and $\vartheta(x)$ is a physiological-age-dependent fertility rate function.

Temperature-dependent fertility rate function
The temperature-dependent fertility rate function models the fertility of an insect in its adult stage as a function of temperature. This mathematical expression captures the impact of temperature on the insect's reproductive capabilities. As temperature influences biological processes crucial for reproduction, such as development and metabolism, the fertility rate function provides valuable insights into how environmental conditions may shape the insect population dynamics in its adult life stage.

The following functions map temperature, expressed in degrees Celsius $T[^\circ C]$, to the number of eggs produced per female insect per day $\varphi(T)$ [eggs female^{-1} d^{-1}].

1. Constant $y = a$
2. Linear $y = aT + b$
3. Quadratic $y = aT^2 + bT + c$
4. Brière $y = aT(T - b)\sqrt{c - T}$

Each function is modified by nullifying its possible negative values. Furthermore, it is set to zero outside the interval whose extremes are previously decided by the user.

Physiological-age-dependent fertility rate function
The physiological-age-dependent fertility rate function models the fertility of an insect, as a function of its physiological age. Physiological age measures the internal biological

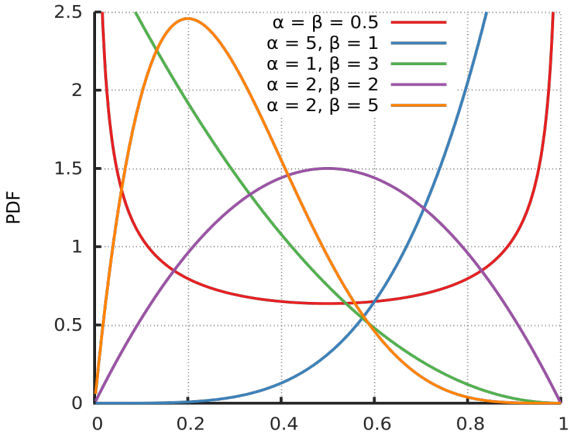


Figure 19: The Euler beta distribution.
Source: www.en.wikipedia.org.

state of an individual, accounting for factors like maturation and aging. This mathematical expression reflects how an organism's reproductive capacity changes over its life span. Understanding this function is essential for comprehending the intricate interplay between an individual's physiological state and its reproductive capabilities in population dynamics.

The following functions map physiological age (usually having values between 0 and 1) expressed with a pure number that identifies the passing of the insect's life in the adult stage x[pure number]; to the distribution of the daily egg production of the insect $\vartheta(x)$[pure number].

1. Constant $y = a$

2. Linear $y = ax + b$

3. Quadratic $y = ax^2 + bx + c$

4. Euler Beta distribution $y = x^{\alpha-1}(1-x)^{\beta-1}$

   The probability density function (PDF) of the Beta distribution (Fig. 19) for $0 \leq x \leq 1$, and shape parameters $\alpha, \beta > 0$, is a power function of the variable x and of its reflection $(1-x)$.

5. Bieri distribution $y = \frac{x-a}{e^{b(x-a)}}$

   The Bieri distribution (Fig. 20) is a mathematical function in which a is a location parameter, and b is a sort of scale parameter. This distribution is characterized by the presence of an exponential term in the denominator, influencing the shape of the curve.

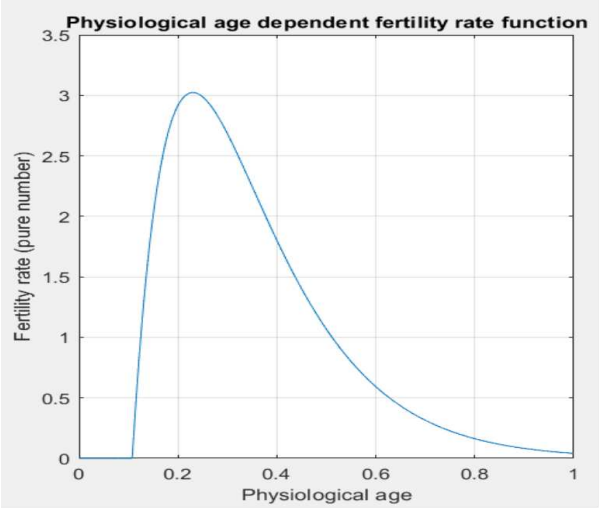


Figure 20: A Bieri distribution.
Source: Entomonlib.

6. Gamma distribution $y = x^{k-1}e^{-\frac{x}{\vartheta}}$

   This function is a simplified, real-input version, of the well-known Euler Gamma Function (Fig. 21).

   In Entomonlib the parameter $1/\vartheta$ is defined as a numerator parameter $b = 1/\vartheta$. The Gamma distribution is often used to model processes involving time or duration and can be applied in various fields, including obviously ecology and entomology.

   Here is a reason why the Gamma distribution might be chosen to model the physiological-age-dependent fertility rate function of an insect: since this type of distribution is commonly used to model time, it can be applied to variables involving duration, such as the reproductive lifespan of an insect or the duration of a specific phase of its life cycle.

Each function is modified by nullifying its possible negative values. Furthermore, it is set to zero outside the interval whose extremes are previously decided by the user.

As regards the physiological age–dependent fertility function, Entomonlib includes a method to identify its parameters (α and β in the Beta distribution, a and b in the Bieri distribution, k and θ in the Gamma distribution) directly from physiological information, rather than from fitted empirical data. In fact, not having data from the field or laboratory, given the impossibility of being able to define the physiological age of an insect (abscissas of these functions), we look for the parameters (α, β), (a, b), and (k, θ) regarding the Euler Beta, Bieri, or Gamma distribution, respectively, starting from 3 values that are now explained.

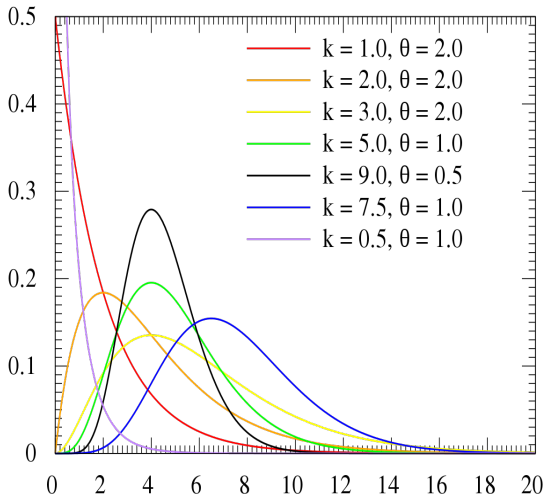


Figure 21: The Gamma distribution.
Source: www.en.wikipedia.org.

• $p_{opt} \in (0, 1)$ is the value of the physiological age at which we have the maximum value of eggs laid per day.

• $p_{end} \in (0, 1)$ is the value of the physiological age at which the insect has oviposited a determined percentage K of its eggs.

• $K \in (0, 1)$ is the percentage referred to in the previous point.

Having set these parameters (remember that you can directly insert the functional parameters in Entomonlib, if you have them) in the input file, Entomonlib can calculate the parameters (α, β), (a, b), and (k, θ) that ensure the age-dependent fertility function reflects the given information.

After this process we have a final step in which the function is normalized: that is, it is divided, pointwise, by its integral. So as to make the final integral of the function equal to 1 in the chosen integration domain.

A double-entry fertility function (temperature and physiological age dependent) is shown in Fig. 22 (right panel).

3.5.4 Discretisation settings

Starting from the inputs given by the user, the next step in Entomonlib is the setting of the various parameters defining the discretisation of the problem. We recall that the Kolmogorov system is discretised by a centered second-order finite-volumes scheme in "space" (the component relating to physiological age), and the semi-implicit Euler method in time, on an equally spaced grid for both variables. The eventual non-linear mortality term, which will be discussed in the next subsection, is treated semi-implicitly

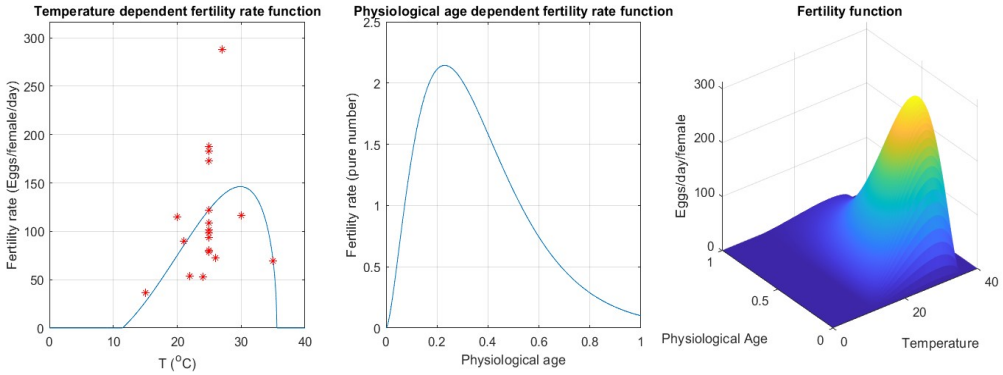


Figure 22: Source: Entomonlib.

(density is calculated at the previous time step). In order to guarantee stability to the scheme, the "space"-step Δx_s, for each stage, must satisfy the relation

$$\Delta x_s \ < \ \frac{2b^s}{\max\limits_t |S^s(t)|}, \qquad s = 1, \ldots, \mathcal{S}. \tag{3.23}$$

related to the Péclet number

$$Pe^s = \frac{\max\limits_t |S^s(t)| \cdot \Delta x_s}{2b^s}, \tag{3.24}$$

(see Box 3.5.4), where $S^s(t)$ is the development rate function and b^s the stochastic diffusion coefficient of the stage s, with $s = 1, \ldots, S$.

Basically, the Entomonlib function *Set_Discretisation* creates a MATLAB structure, named *data_discr*, containing:

- the time-step dt of the problem, eventually divided by a power of two (defined by the user) whenever greater precision is desired at the expense of the model's computational times,
- the total number Nt of time-steps, according even to the number of years decided for the simulation,
- the temperature stored in a MATLAB cell, containing the temperature vectors, one for each stage, directly taken from the main problem structure (*prob_data*),
- the Péclet numbers (3.24), one for every stage (see the next grey box).
- the number N^s of space-steps for the stage s,
- the length of the single space-step dx^s defined as the reciprocal of N^s,

- the MATLAB cell called *space* that contains a grid for each stage, with respect to the physiological age discretisation.

Box 3.2: Péclet number (Pe)

The Péclet number (Pe) (see, e.g., [26]) is a dimensionless parameter commonly used in the modelling of transport phenomena, such as the diffusion of substances, heat transfer, and mass movement. It commonly represents the ratio between the advection time scale (convective transport) and the diffusion time scale.
The decision-making process regarding the subdivision of the spatial span (physiological age in our problems) into elements of the vector formed by all spatial steps is crucially influenced by the Péclet number. By placing the convective term at the numerator and the diffusive term at the denominator, the Péclet number encapsulates the relative influence of advection and diffusion in the system. This ratio guides the determination of spatial discretisation by highlighting the dominance of convective or diffusive transport mechanisms. For instance, a high Péclet number signifies the prevalence of advection, necessitating smaller spatial intervals to capture rapid convective changes accurately. Conversely, a low Péclet number indicates diffusion dominance, suggesting larger spatial intervals may be sufficient to represent the system adequately. Stability of the numerical discretisation is guaranteed if $\mathrm{Pe} < 1$. Typically, the Péclet numbers associated with the tests carried out using Entomonlib were rather large, since the transport term, namely the development rate $S^s(t)$, takes values in $[0, 1)$, in particular, values of order 10^{-1}–10^{-2} , whereas b^s is of order 10^{-3} or 10^{-4}.

3.5.5 Solution step

After the discretisation step, the function that solves the system of differential equations operates as follows.

After renaming some arrays and useful parameters for brevity, the function named Solve_Demographic_System computes the values of development and mortality functions for each stage of the insect population, the temperature-dependent and physiological-age-dependent fertility functions for the stage $\mathcal{S}$. It is worth noting that even the development and mortality rate functions are temperature-dependent.

The initial conditions provided by the user on physiological age are defined: these consist of a normalized (by Entomonlib) distribution on a specific chosen stage, defining how the physiological ages of the insects are distributed along the axis of physiological ages at the initial time.

The next step is the most expensive one from the computational point of view. Two nested loop cycles are opened, the first one ranges over each time step, and the

second, internal to the previous one, ranges over the various stages of the insect's life (see algorithm 3.17).

After assembling the matrix $A^s(t^n)$ and the corresponding right-hand side, the tridiagonal linear system is solved by the Thomas algorithm (see, e.g., [26]). The resulting solution $(\boldsymbol{\varphi}^s)^n$ is used to compute the right-hand side for the next stage. The right-hand side of the first stage depends on the fecundity computed at the previous time step. At the end of each time step, the population abundance of stage s is computed as

$$N^s(t^n) \;=\; \Delta x \sum_{k=1}^{N_x} \big(\varphi_k^s\big)^n.$$

The function returns an array of length Nt (total number of time-steps) containing the computed abundances for each time step and the solution arrays $(\boldsymbol{\varphi}^s)^n$ for each stage and each time–step.

3.5.6 Plotting solutions and functions

Once the numerical solution has been computed, Entomonlib proceeds to create and/or save (based on the user's choices) the images containing a selection of graphs from a list that varies on the model's type. Common choices for all models include the plot of the development rate functions, mortality rate functions, temperature-dependent fertility rate functions, age-dependent fertility rate functions, temperature functions, the initial conditions functions, and the abundance function.

3.5.7 Computing errors

Whenever target values for the abundances are provided, Entomonlib computes the errors between the target data and the computed abundances. Typically, data on the adult stage are used. Obviously, only the values of the solutions at the time instants for which data are available are selected. Subsequently, based on user choices, two different types of errors can be calculated: the squared L2-norm error and the Root Mean Squared Error (RMSE).

If y_i are the values of the solution computed numerically and $\hat{y}_i$ the related target values, Entomonlib computes

$$\text{Squared L2-norm} = \sum_{i=1}^{n} (\hat{y}_i - y_i)^2 \tag{3.25}$$

$$\text{RMSE} = \sqrt{\frac{1}{n} \sum_{i=1}^{n} (\hat{y}_i - y_i)^2}. \tag{3.26}$$

Finally, Entomonlib terminates the execution displaying on-screen all the images containing the requested plots and the numerical values of the requested errors.

3.6 Technicalities

Entomonlib is a library available for the entomology research group of the University of Brescia. Through a process of encryption in MATLAB, Entomonlib allows the modification and visualization of only the scripts related to the parameters and input choices discussed in the first part of Subsection 3.5.1. By downloading Entomonlib, one will also have access to a series of manuals written to enable its efficient and knowledgeable use. These manuals provide brief theoretical insights and explanations of each parameter that the user can modify within the input-related script. In each model, the number of parameters exceeds a hundred, so it is easy to understand how necessary a guide is in this intricate labyrinth of parameters, functional choices, and folders to define.

3.7 Entomonlib applications

One of the main peculiarities of *Entomonlib* lies in its versatility. We report here two very different studies, among the various ones in which it took part, in which it made a very substantial contribution.

The first one concerns a temperature-driven, stage-structured phenological model for the Nearctic leafhopper *Erasmoneura vulnerata* in Franciacorta vineyards, presented as a poster at the XXVIII Congresso Nazionale Italiano di Entomologia (Siena, 16–20 June 2025). Built from 14 months of field monitoring (adult traps with automated recognition, juvenile counts) and local weather data, the workflow uses a recursive calibration to infer development curves without individual-level rearing.

The second one focuses on a demographic model for *Philaenus spumarius*—vector of *Xylella fastidiosa*—in Apulian olive landscapes, coupling temperature-dependent development and mortality with diapause/parapause and density regulation to explore surveillance and management scenarios.

The two conference abstracts are reported below.

3.7.1 Development of a phenological model for *Erasmoneura vulnerata*

The present work, developed in collaboration with Andrea De Francesco, Igor Daniel Weber, Fabio Gatti, Kevyllen Moreira Barbosa Borges, Anna Simonetto, and Gianni Gilioli, of the University of Brescia, has been presented as a poster at the XXVIII Congresso Nazionale Italiano di Entomologia (Siena, 16–20 June 2025).

Erasmoneura vulnerata is an alien leafhopper of Nearctic origin, first reported in Europe in Italy in 2004, when it was found in some vineyards in the Veneto region. Although it is not particularly harmful in its native range, significant infestations in commercial vineyards have been reported in Italy since 2016. In vineyards, the pest reduces the photosynthetic capacity of plants, potentially affecting grape quality and the plant's vegetative recovery at the beginning of the following season.

The leafhopper overwinters as an adult in reproductive diapause within vegetation at vineyard margins, recolonizing the vineyards as soon as temperatures allow and food resources become available. During the growing season in northern Italy, *Erasmoneura vulnerata* completes up to three highly overlapping generations, making it difficult to determine the optimal timing for monitoring and control interventions.

The objective of this study is to develop a phenological model for *Erasmoneura vulnerata* populations in vineyards to provide guidance on optimal timing for monitoring and planning control measures.

The phenological model was developed based on intensive sampling of leafhopper population dynamics in five vineyards of the Franciacorta DOCG area over a continuous

14-month period, including the winter season.

Monitoring focused on both adult and preimaginal stages. Adults were sampled using chromotropic traps with weekly replacements, placed both in vineyards and in the surrounding vegetation. Captures were counted using an automatic recognition system based on neural networks trained to detect the leafhopper. Juvenile stages were monitored by collecting leaves and counting individuals in the laboratory.

The leafhopper's phenology was described using a physiologically based population dynamics model with temperature-dependent developmental functions (cfr. more precisely, the Kolmogorov system (2.5)–(2.11)). The model was initially calibrated using the dataset obtained from field sampling. Based on the field data, abundance curves were defined for different stages and generations. Temperature data were collected from meteorological stations near the experimental vineyards.

In the absence of individual-level developmental rate data, the application of a recursive calibration procedure allowed estimation of the development curve functions. This procedure identified the parameter combination that best approximated the observed population dynamics across all the studied vineyards. Preliminary evaluation highlighted the model's ability to estimate with adequate precision the timing of different life stages across generations.

The implementation of the recursive calibration procedure helped compensate for the lack of experimental data required for parameterizing the leafhopper's developmental functions. The analysis of simulated dynamics can help identify critical time windows for monitoring and for implementing control actions, allowing intervention planning in relation to the population dynamics of other vineyard pests as well. Further evaluation phases are needed for model application, which will be conducted in subsequent monitoring campaigns

3.7.2 A model describing population dynamics of *P. spumarius*

The present work, developed in collaboration with Igor Daniel Weber, Anna Simonetto, Paola Gervasio, Andrea De Francesco, Gianni Gilioli, of University of Brescia, DICATAM; Crescenza Dongiovanni of Istituto per la Protezione Sostenibile delle Piante (IPSP), CNR, Bari, Italy; and Vincenzo Cavalieri, of Centro di Ricerca, Formazione e Sperimentazione in Agricoltura "Basile Caramia" (CRSFA), Locorotondo, Bari, Italy, has been presented at XXVIII Congresso Nazionale Italiano di Entomologia (Siena, 16–20 June 2025).

The meadow spittlebug, *Philaenus spumarius* L. (Hemiptera: Aphrophoridae), is a highly polyphagous and abundant species widely distributed across the Palearctic and Nearctic regions. It is considered as the main vector of *Xf* in European outbreaks, an

invasive bacterial plant pathogen native to the Americas that poses a serious threat to numerous economically important crops, including olives, grapevine, almonds, plums, and citrus.

The control of vector population is one of the key strategies for the effective containment of Xf outbreaks. Vector management efforts primarily target juvenile stages in the herbaceous layer and newly emerged adults to prevent their migration to the canopy of cultivated trees, thereby disrupting transmission dynamics. The development of accurate demographic models that describe *P. spumarius* phenology and abundance in agroecosystems is essential for supporting rational decision-making for the efficient management of the vector population.

In this study, we developed a temperature-driven demographic model to describe the population dynamics of *P. spumarius*. The model integrates key biological and environmental factors through a physiologically based framework that simulates species life history processes. The phenological dynamics and abundance of *P. spumarius* are simulated through a stage-structured population model based on the system of Kolmogorov partial differential equations ((2.5)–(2.11)). Seven development stages were considered: eggs, five nymphal instars, and adult stage. The development rates are described by stage-specific temperature-dependent functions. Mortality is modelled through a combination of intrinsic temperature-dependent mortality and stage-specific extrinsic mortality, such as natural enemies and other biotic factors. Additionally, a density-dependent mortality term is applied to nymphal stages to account for resource competition. After emergence, females undergo ovarian parapause, with its termination regulated by environmental conditions. The model also incorporates fecundity dynamics.

Overwintering dynamics and diapause breakage process are included into the model to perform multi-year simulations. Biodemographic functions were estimated from the literature and calibrated using population dynamics datasets from Apulia (Italy) and additional published studies. Model accuracy was evaluated through validation with an independent dataset. As an illustrative example, Figure 23 shows the simulated seasonal dynamics of *P. spumarius* life stages in a Ligurian olive grove, superimposed to field monitoring data for nymphs ($N3$–$N5$) and adults. The good agreement between simulated and observed abundances supports the suitability of the proposed model structure and parameter set for describing *P. spumarius* population dynamics under field conditions.

The proposed framework for simulating *P. spumarius* population dynamics under varying environmental conditions provides essential support for the design and implementation of effective vector control and monitoring strategies. The model allows for evaluating the impact of additional mortality factors on *P. spumarius* population abundance, enabling the exploration of integrated control strategies for efficient pest management. Furthermore, it serves as a valuable tool for studying the epidemiology of diseases transmitted by *P. spumarius*, providing insights to enhance our understanding of its

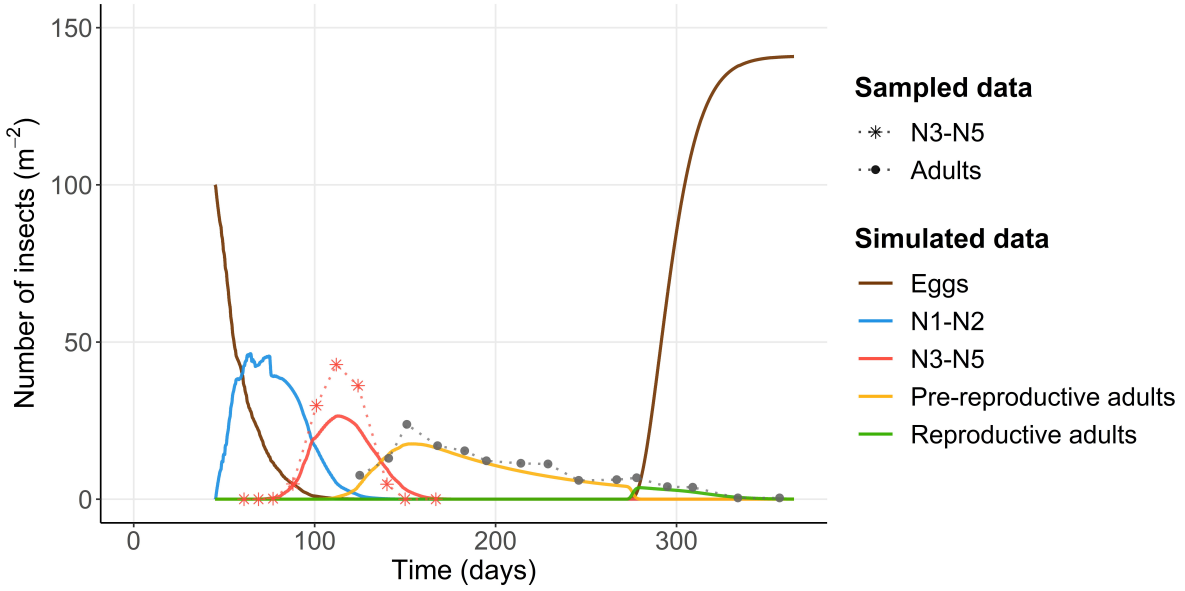


Figure 23: Simulated population dynamics (insects $/m^2$) of *P. spumarius* life stages in Liguria, Northern Italy, used as an example of model validation. Red asterisks represent field monitoring data for $N3$–$N5$ nymphal stages, and grey dots represent field monitoring data for adult stages, converted to insects per square meter.

role in Xf outbreaks and helping to optimize surveillance strategies and improve disease management approaches.

3.7.3 Entomonlib as a satellite model

We have shown that Entomonlib, together with the models it encompasses, can support a wide range of entomological studies. It can also serve as an auxiliary component within models of a very different nature. We have used Entomonlib as a satellite module to compute adult vector emergence functions inside an eco-epidemiological model to study the diffusion of *Xylella fastidiosa* in Apulia olive plants (see Chapter 4).

4

Physiologically-based eco-epidemiological model of *Xylella fastidiosa* infection in olive groves

The content of this chapter has been written in collaboration with Igor Daniel Weber, Anna Simonetto, Paola Gervasio, Gianni Gilioli of the University of Brescia; Maria Saponari of the Institute for Sustainable Plant Protection, National Research Council (CNR), Bari, Italy; Crescenza Dongiovanni of Centro di Ricerca, Formazione e Sperimentazione in Agricoltura "Basile Caramia" (CRSFA), Locorotondo, Bari, Italy; and Juan Antonio Navas-Cortés of Institute for Sustainable Agriculture (IAS), Spanish National Research Council (CSIC), Avda, Spain. It has been submitted to *Bulletin of Mathematical Biology* in October 2025.

The model presented was developed for the international BeXyl project, which is described in the next subsection.

4.1 The BeXyl project

BeXyl (Beyond Xylella, Integrated Management Strategies for Mitigating *Xylella fastidiosa* impact in Europe) is a research project funded by the EU that brings together top scientists from around the world and stakeholder demands to address the impact of *Xylella fastidiosa*, one of the most harmful plant pathogens for agriculture, landscapes, and ecosystems in the European Union.

From 2022 to 2026, the EU supports BeXyl with approximately 7 million euros from the Horizon Europe research program. The goal is to promote a multidisciplinary approach and innovative solutions to move beyond emergency measures and develop new strategies for the sustainable control of *Xylella fastidiosa* in Europe. BeXyl directly involves 31 partners from 14 countries, with the United Kingdom and Australia as associate partners, and a stakeholder council with the active participation of over 40 scientific institutions, NGOs, companies, government agencies, farmer associations, and nurseries worldwide.

Main goals of the project:

- Understanding the triggers of *Xf* epidemics, including climate change;

- New strategies and improved methods for surveillance, early diagnosis, and disease monitoring;
- Use of heat treatments for plant sanitation and the production/trade of Xf-free nursery material;
- Development of genomics tools related to Xf resistance and their application for screening germplasm in genomics-assisted breeding;
- Environmentally and economically viable solutions for effective control of Xf vectors and interruption of Xf transmission;
- Economically and environmentally safe solutions for effective Xf control and increased plant resilience to Xf infection;
- Tools to support the design and implementation of tactics and strategies to mitigate the impacts of Xf infections;
- Ecological, social, and economic impacts of Xf and management approaches to epidemic control;
- Stakeholder engagement, dissemination, communication, and technology transfer.

The project fills gaps in research, dedicating substantial analysis to the socio-economic and environmental impact of the pathogen under climate change scenarios. Stakeholders' involvement is another distinctive characteristic. More than 40 research institutions, government agencies, nurseries and farmer's associations, NGOs, and "operational groups" of the EU-funded European Innovation Partnership, participate in the project. The goal is to create a community of scientists, citizens, economic operators, and policymakers to shorten the distance between research and on-field applications.

BeXyl will support studies on both basic research and technological innovation. In the first group, there is work on the drivers of *Xylella fastidiosa* epidemics in the EU, considering climate change. Scientists will also be modelling the impact and sustainability of different practical tactics to contrast the pathogen's spread in different agroecosystems and landscapes. In the second group, we find improved detection methods for the bacterium and its vectors, with tools ranging from remote sensing technology to dogs' sense of smell. BeXyl will also establish a global network of "sentinel plots" acquiring data from a wide range of latitudes and conditions.

Other research lines include thermal treatment to secure safe plant material exchange. To support specific plant breeding programs, scientists will improve the understanding of genetic mechanisms leading to resistance to *Xylella fastidiosa*. Findings in the studies carried out in former research projects encourage exploring beneficial bacteria (bacteriophages), innovative compounds, and formulations that reduce the spread of *Xylella*

fastidiosa within plants. BeXyl will also outline new solutions for helping farmers to use integrated pest management to control the bacterium and its vectors. We now introduce the main topic of this chapter.

4.2 Introduction

Xylella fastidiosa (*Xf*) Wells (1987) (Proteobacteria: Xanthomonadaceae) is a xylem-limited, Gram-negative bacterium that infects over 700 plant species (EFSA, 2025 [66]). It is the causal agent of economically significant diseases, including Pierce's disease of grapevine, citrus variegated chlorosis, almond leaf scorch, and olive quick decline syndrome, and poses a substantial threat to agriculture worldwide (EFSA PLH Panel, 2019 [66]). The pathogenic process of *Xf* begins with the colonization of the xylem vessels of the host plants, where it progressively multiplies and spreads, inducing xylem occlusions (i.e., tyloses, callose-like structures, and gums/pectin gels) that impair plant hydraulic conductivity (Rapicavoli et al., 2018 [58] ; Sicard et al., 2018 [59]; Sun et al., 2013 [39]). As a result, *Xf* infection induces symptoms primarily associated with water stress, such as marginal leaf necrosis and scorching, progressing to twigs and branch dieback until plant death (Rapicavoli et al., 2018 [58]). The successful establishment of infection and disease progression depends on multiple factors, such as pathogen genotype, host susceptibility, plant–pathogen interaction dynamics, environmental conditions (e.g., temperature, water availability), as well as vector population dynamics, abundance, dispersal capacity and transmission efficiency (Bodino et al., 2023 [96]; EFSA PLH Panel, 2019 [66]; Sicard et al., 2018 [59]).

Native to the Americas, *Xf* is currently present in Europe, Middle East and Asia. The first severe European outbreak was documented in 2013, when *Xf* subspecies *pauca* triggered a devastating epidemic in olive groves in Apulia, Italy (Saponari et al., 2013, 2019 [38][71]). Since then, the three major *Xf* subspecies (*fastidiosa*, *multiplex*, and *pauca*) have been reported in several countries across Europe, where they have caused significant outbreaks in diverse agroecosystems (Schneider et al. 2020 [79]; Sicard et al. 2018 [59]). Xf is transmitted by xylem-feeding insects, with the spittlebug *Philaenus spumarius* L. (1758) (Hemiptera: Aphrophoridae) recognized as the primary vector in European outbreaks up to date (Cornara et al., 2018 [55]; EFSA PLH Panel, 2019 [66]). In the vector, the bacterium colonizes and multiplies in the foregut, enabling persistent transmission without a latency period (Almeida et al. 2005 [21]).

Several modelling frameworks have been developed to investigate the epidemiology of *Xf*. A common approach for analysing transmission processes between vectors and plants uses compartmental models, such as the Susceptible-Infected-Removed (SIR) framework (Soubeyrand et al., 2018 [60]) and extensions that incorporate temperature-dependent variables to predict the global distribution of *Xf* (Giménez-Romero et al., 2022 [94]). Some studies have further refined these models, e.g., Susceptible-Exposed-Infected-

Removed (SEIR) models, by including host infection stages and explicitly accounting for an asymptomatic phase to better represent disease progression (Jeger and Bragard, 2018 [69]; White et al., 2020 [80]).

Spatially explicit models have been developed to represent the spatio-temporal dynamics of *Xf* outbreaks across different spatial scales and outbreak scenarios. These include reaction-diffusion equations (Aniţa et al., 2021 [81]; Gilioli et al., 2023 [99]; Martin et al., 2021 [88]), ordinary differential equation systems (Cendoya et al., 2024 [102]), and lattice-based framework (Fierro et al., 2019 [67]). Models that explicitly integrate vector population dynamics provide a more comprehensive and mechanistic representation of vector-driven transmission processes (Fierro et al., 2019 [67]; Gilioli et al., 2023 [99]; Giménez-Romero et al., 2023 [100]). Additionally, studies have explored the influence of ground cover plants on the *Xf* pathosystem, considering their potential role in disease persistence and vector ecology (Aniţa et al., 2021 [81]; Brunetti et al., 2020 [72]; Fierro et al., 2019 [67]).

These modelling frameworks have provided valuable insights into *Xf* epidemiology, and some are already employed as tools to support Pest Risk Assessment (PRA) and pest risk management. Nonetheless, there remains a need for models that can inform the design and implementation of effective management strategies under the Integrated Pest Management (IPM) framework to achieve effective and sustainable control of *Xf*-associated diseases in infected scenarios. Such models must mechanistically integrate the key physiological and bioecological processes underlying vector and bacterial population dynamics, including vector–host plant interactions, disease transmission and symptom progression, to accurately simulate *Xf* epidemiology.

Our study presents a novel physiologically-based eco-epidemiological model for *Xf* in olive agro-ecosystems. The model adopts a mechanistic framework that explicitly incorporates the influences of environmental and meteorological variables on vector phenology, mortality, and disease dynamics within the host plants, as well as the seasonality of vector–host interactions and vector preferences on transmission. The model captures population dynamics and disease progression through a compartmental model, where compartments represent both vector life stages and host health status classes. The eco-epidemiological system is formulated as a system of ordinary and delayed differential equations, allowing for a detailed and dynamic representation of the plant–vector–bacterium interactions.

While the model is calibrated using the *Xf* outbreak in Apulia as a case study, its mechanistic representation of disease dynamics in olive agro-ecosystems is designed to be generalisable across diverse contexts and environments. The results, based on this calibration, provide novel insights into infection dynamics and demonstrate the potential of the approach for broader applications to advance understanding and management of *Xf* epidemiology.

This chapter follows the structure of the pre-print submitted to the scientific journal *Ecological Modelling*.

In Section 4.3.1 we present the physiological model and its mathematical formulation. Details on the several functions included in the mathematical equations will be given in Section 4.6. Always in Section 4.3.1, we present a case study, the model calibration and its validation. Sections 4.4 and 4.5 are dedicated to the discussion of numerical results and conclusions, respectively. Finally, Section 4.7 includes supplementary material for the model calibration.

4.3 Material and Methods

4.3.1 Model definitions

A physiologically-based eco-epidemiological model was developed to simulate the dynamics of *Xf* in olive agroecosystems. The model provides a mechanistic representation of *Xf* epidemiology (Figure 24) by integrating key bioecological processes, including vector population dynamics, vector–plant interactions, disease transmission, growth of non-crop vegetation, and disease progression in infected olive trees. It is formulated as a compartmental system of ordinary and delayed differential equations that explicitly incorporates vector life stages, host infection status, and environmental drivers. The vector population is structured into three compartments: preimaginal stages (P), non-infected adults (V_S), and infected adults (V_I). Vegetation is structured into different groups: i) non-susceptible plants, composed of herbaceous vegetation (H) and non-susceptible shrubs and trees (N); ii) reservoir plants, divided into susceptible non-infected (R_S) and infected (R_I) compartments; and iii) olive trees (crops), represented by seven compartments corresponding to successive stages of disease progression ($C_S, C_0, \ldots, C_5$) (Table 1). Seven ordinary differential equations (ODEs) describe the dynamics of non-crop plants and vectors (i.e., H, N, R_S, R_I, P, V_S, and V_I). Delay differential equations (DDEs) were used to represent the progression of olive trees through consecutive disease stages. This approach incorporates minimum delay period (τ^{C_i}, with $i \in \{0, 1, \ldots, 4\}$) for the infected olive tree compartments ($C_0, \ldots, C_4$), ensuring that trees remain in each stage at least the specified duration before progressing to the next. The term $C_i^*(t, \tau^{C_i})$ denotes the number of olive trees at time t that have persisted in stage i for at least the corresponding delay period τ^{C_i}.

Overall, the eco-epidemiological model consists of 14 differential equations, one corresponding to each compartment. For clarity, the functions are presented below as a system of equations without explicit parameters definitions, except for time and delay terms:

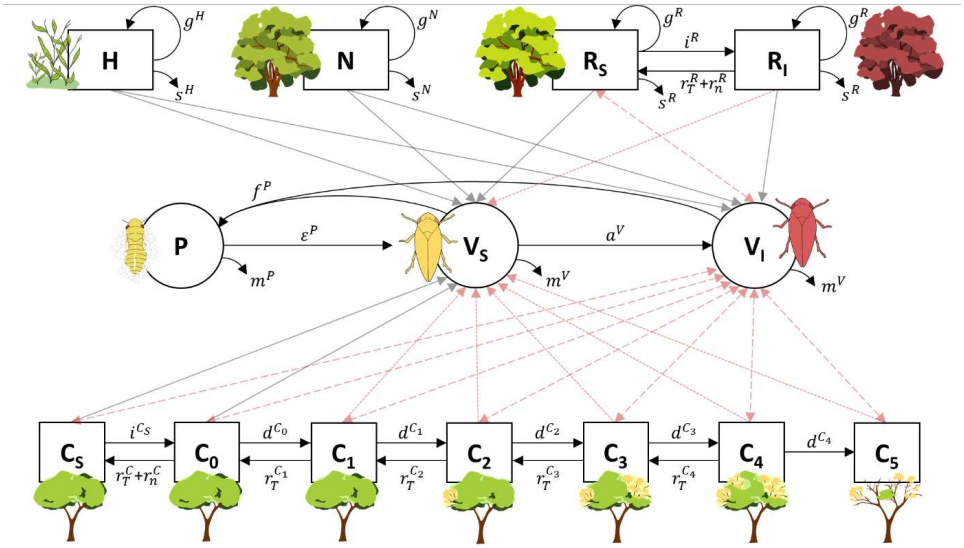


Figure 24: Schematic representation of the eco-epidemiological model framework. Rectangles represent vegetation compartments, while circles denote vector compartments. Solid black arrows denote vegetation dynamics, demographic processes, and transitions between compartments. Red arrows depict vector—host plant interactions that determine vector acquisition (dotted arrows) from infectious plants and inoculation events (dashed arrows) by infected vectors. Grey arrows are vector–host plant interactions that do not involve pathogen transmission. Definitions of model compartments and functions are provided in Table 1.

$$
\begin{aligned}
&\text{a)}\ \frac{dH}{dt}(t) = g^H(t) - s^H(t)\,H(t),\\
&\text{b)}\ \frac{dN}{dt}(t) = g^N(t)\,N(t) - s^N(t)\,N(t),\\
&\text{c)}\ \frac{dR_S}{dt}(t) = g^R(t)\,R_S(t) + s^R(t)\,R_S(t) + r_T^R(t)\,R_I(t) + r_n^R(t) - i^R(t)\,R_S(t),\\
&\text{d)}\ \frac{dR_I}{dt}(t) = g^R(t)\,R_I(t) + i^R(t)\,R_S(t) + s^R(t)\,R_I(t) - r_T^R(t)\,R_I(t) - r_n^R(t),\\
&\text{e)}\ \frac{dP}{dt}(t) = f^P(t)\left(V_S(t) + V_I(t)\right) - \varepsilon^P(t)\,P(t) - m^P(t)\,P(t),\\
&\text{f)}\ \frac{dV_S}{dt}(t) = \varepsilon^P(t)\,P(t) - a^V(t)\,V_S(t) - m^V(t)\,V_S(t),\\
&\text{g)}\ \frac{dV_I}{dt}(t) = a^V(t)\,V_S(t) - m^V(t)\,V_I(t),\\
&\text{h)}\ \frac{dC_S}{dt}(t) = r_T^{C^0}(t)\,C_0^*(t,\tau^{C^0}) + r_n^C(t) - i^{C_S}(t)\,C_S(t),\\
&\text{i)}\ \frac{dC_0}{dt}(t) = i^{C_S}(t)\,C_S(t) + r_T^{C^1}(t)\,C_1^*(t,\tau^{C^1}) - d^{C^0}(t)\,C_0^*(t,\tau^{C^0}) - r_T^{C^0}(t)\,C_0^*(t,\tau^{C^0}) - r_n^C(t),\\
&\text{j)}\ \frac{dC_1}{dt}(t) = d^{C^0}(t)\,C_0^*(t,\tau^{C^0}) + r_T^{C^2}(t)\,C_2^*(t,\tau^{C^2}) - d^{C^1}(t)\,C_1^*(t,\tau^{C^1}) - r_T^{C^1}(t)\,C_1^*(t,\tau^{C^1}),\\
&\text{k)}\ \frac{dC_2}{dt}(t) = d^{C^1}(t)\,C_1^*(t,\tau^{C^1}) + r_T^{C^3}(t)\,C_3^*(t,\tau^{C^3}) - d^{C^2}(t)\,C_2^*(t,\tau^{C^2}) - r_T^{C^2}(t)\,C_2^*(t,\tau^{C^2}),\\
&\text{l)}\ \frac{dC_3}{dt}(t) = d^{C^2}(t)\,C_2^*(t,\tau^{C^2}) + r_T^{C^4}(t)\,C_4^*(t,\tau^{C^4}) - d^{C^3}(t)\,C_3^*(t,\tau^{C^3}) - r_T^{C^3}(t)\,C_3^*(t,\tau^{C^3}),\\
&\text{m)}\ \frac{dC_4}{dt}(t) = d^{C^3}(t)\,C_3^*(t,\tau^{C^3}) - d^{C^4}(t)\,C_4^*(t,\tau^{C^4}) - r_T^{C^4}(t)\,C_4^*(t,\tau^{C^4}),\\
&\text{n)}\ \frac{dC_5}{dt}(t) = d^{C^4}(t)\,C_4^*(t,\tau^{C^4}).
\end{aligned}
\tag{4.1}
$$

The state variables presented in (4.1) are summarised in Tab. 1. A detailed description of the model's functions and parameters is provided in Section 4.6. The temporal resolution of the model is set at 1 hour.

Table 1: Summary of model state variables and functions of the overall Eco-epidemiological model.

Symbol	**Description**	**Units**
State variables		
H	Herbaceous vegetation	kg ha^{-1}
N	Non-susceptible shrubs and trees	kg ha^{-1}
R_S	Susceptible (non-infected) reservoirs	kg ha^{-1}
R_I	Infected reservoirs	kg ha^{-1}
P	Preimaginal vector stage	insects ha^{-1}
V_S	Susceptible (non-infected) adults	insects ha^{-1}
V_I	Infected adults	insects ha^{-1}
C_S	Susceptible (non-infected) olive trees	plants ha^{-1}
C_0	Infected but non-infectious asymptomatic olive trees	plants ha^{-1}
C_1	Infectious asymptomatic olive trees	plants ha^{-1}
C_2	Initial severity, with >0 to 25% canopy with desiccated branches	plants ha^{-1}
C_3	Medium severity, with >25 to 50% canopy with desiccated branches	plants ha^{-1}
C_4	High severity, with >50 to 75% canopy with desiccated branches	plants ha^{-1}
C_5	Very high severity, with >75% canopy with desiccated branches or fully desiccated trees	plants ha^{-1}
C_i^*	Number of olive trees that have persisted in infection stage i (with $i \in \{0, 1, \ldots, 4\}$) for at least the corresponding delay period	plants ha^{-1}
	Functions or parameters	
Herbaceous vegetation		
g^H	Growth function of herbaceous vegetation	–
s^H	Senescence function of herbaceous vegetation	–
Non-susceptible shrubs and trees		
g^N	Growth rate function of non-susceptible shrubs and trees	–
s^N	Senescence function of the deciduous biomass of non-susceptible shrubs and trees	–
Reservoir plants		

Symbol	Description	Units
g^R	Growth rate function of infected and susceptible reservoir plants	–
s^R	Senescence rate function of the deciduous reservoir biomass during autumn	–
i^R	Infection rate function of non-infected reservoir plants by infected vectors	–
r_T^R	Temperature-dependent disease recovery rate function of infected reservoir plants due to low winter temperatures	–
r_n^R	Non-systemic infection recovery rate function of infected reservoir plants	–
Insect vectors		
f^P	Fecundity rate function of adult vectors	–
ε^P	Emergence rate function of adult vectors	–
m^P	Mortality rate function of preimaginal vectors	–
m^V	Mortality rate function of adult vectors	–
a^V	Acquisition rate function of non-infected vectors from infectious vegetation compartments	–
Crop – Olive trees		
i^{C_S}	Infection rate function of non-infected olive trees by infected vectors	–
d_i^C	Disease progression rate function describing the transition rate of olive trees from disease stage i to the next disease stage	–
$r_T^{C_i}$	Temperature-dependent disease recovery rate function of infected olive trees of disease stage i	–
r_n^C	Non-systemic infection recovery rate function of infected olive trees of disease stage C_0	–

4.3.2 Model assumptions

The vector population considered in this model refers to *P. spumarius*, which follows a univoltine life cycle. It is structured into three compartments: preimaginal stages (P), non-infected adults (V_S), and infected adults (V_I), all constrained within $[0, K^P]$, where K^P (insects ha^{-1}) denotes the carrying capacity for preimaginal vectors. The development of preimaginal stage (ε^P) is determined by a temperature-dependent model adapted from the *P. spumarius* phenological model developed by Gilioli et al. (2024) [104]. We refer to Section 4.6.3 for a deeper analysis of this step. Mortality of preimaginal stages

and adult vectors are modelled using temperature-dependent functions, and fecundity is defined by a fixed rate (see Sections 4.6.3 and 4.6.4).

Olive trees are represented as the number of trees per unit area, determined by the planting density of the olive grove, and constitute the crop compartment. They are classified into seven categories according to infection status and percentage of canopy desiccation: susceptible non-infected olive trees (C_S), infected but non-infectious asymptomatic trees (C_0), infectious asymptomatic trees (C_1), and symptomatic trees with $]0\%, 25\%]$ (C_2), $]25\%, 50\%]$ (C_3),$]50\%, 75\%]$ (C_4), and $]75\%, 100\%]$ (C_5) canopy desiccation (Table 1). Symptomatic classes follow the definitions of Hornero et al. (2020)[75]. The total number of olive trees remains constant throughout the simulations. Disease progression dynamics are described by functions depending on temperature, soil water availability, the density of infected vectors, and vector feeding preferences (see Section 4.6.5).

Herbaceous vegetation (H) non-host to *Xf* is assumed to uniformly cover the field and is modelled as biomass per area unit, constrained to non-negative values. Biomass varies over time and is limited by suboptimal air temperature (T_{AD}), limited incident solar radiation (I_{AD}), and reduced proportion of soil water content (W) (see Section 4.6.6).

Non-susceptible shrubs and trees (N) serve as a food source for the vector, with biomass constrained within the range $[0, K^N]$, where K^N (kg ha^{-1}) represents the field's carrying capacity for the N vegetation compartment. Reservoir plants (shrubs and trees susceptible to *Xf*) are divided into susceptible non-infected (R_S) and infected (R_I) reservoirs, with their combined biomass constrained within $[0, K^R]$, where K^R (kg ha^{-1}) is the field's carrying capacity for reservoir plants. The biomass of both non-susceptible shrubs and trees and reservoir plants varies over time and is described by a temperature-dependent function (see Sections 4.6.7 and 4.6.8). A proportion of these woody plants consists of deciduous species that shed their foliage in autumn.

The simulated landscape represents a one-hectare olive grove, structured into four vegetation compartments: ground cover vegetation, non-susceptible shrubs and trees, reservoir plants, and olive trees. Given the small spatial scale, spatial constraints are neglected, and the landscape is considered isolated with no inflow or outflow of vectors, allowing only local epidemiological dynamics.

4.3.3 Case study

The case study was designed to represent the outbreak of *Xf* in olive groves of Apulia, southern Italy. To this end, the model (Sys. (4.1)) was applied to capture the dynamics of disease in naturally infected olive trees from 16 olive groves in the *Xf*-infected area of Lecce province (Zarco-Tejada et al., 2018 [61], 2021 [90]). Between 2016 and 2019, a total of 3,099 olive trees were monitored for 1 to 3 years, with disease severity visually

assessed up to four times per year and *Xf* presence confirmed by qPCR[5] . Most groves consisted of old trees (over 50 years old) of the highly susceptible cultivars Ogliarola Salentina and Cellina di Nardò, within a landscape dominated by olive groves.

The study area is characterized by a Mediterranean climate (C_S according to the Köppen-Geiger classification), with mild, wet winters and hot-dry summers (Kottek et al., 2006 [24]). Meteorological data were retrieved from Visual Crossing Corporation (2025) and interpolated using the Inverse Distance Weighting (IDW) method implemented in the gstat R package (Pebesma, 2004 [20]). The dataset included hourly temperature, daily precipitation (Figures 25–26, Section 4.6), solar radiation, and daylight duration.

[5]qPCR (quantitative Polymerase Chain Reaction, also known as real-time PCR) is a molecular technique that amplifies specific DNA fragments and monitors the accumulation of amplified product in real time using a fluorescent signal, allowing both detection and approximate quantification of the pathogen in the sample.

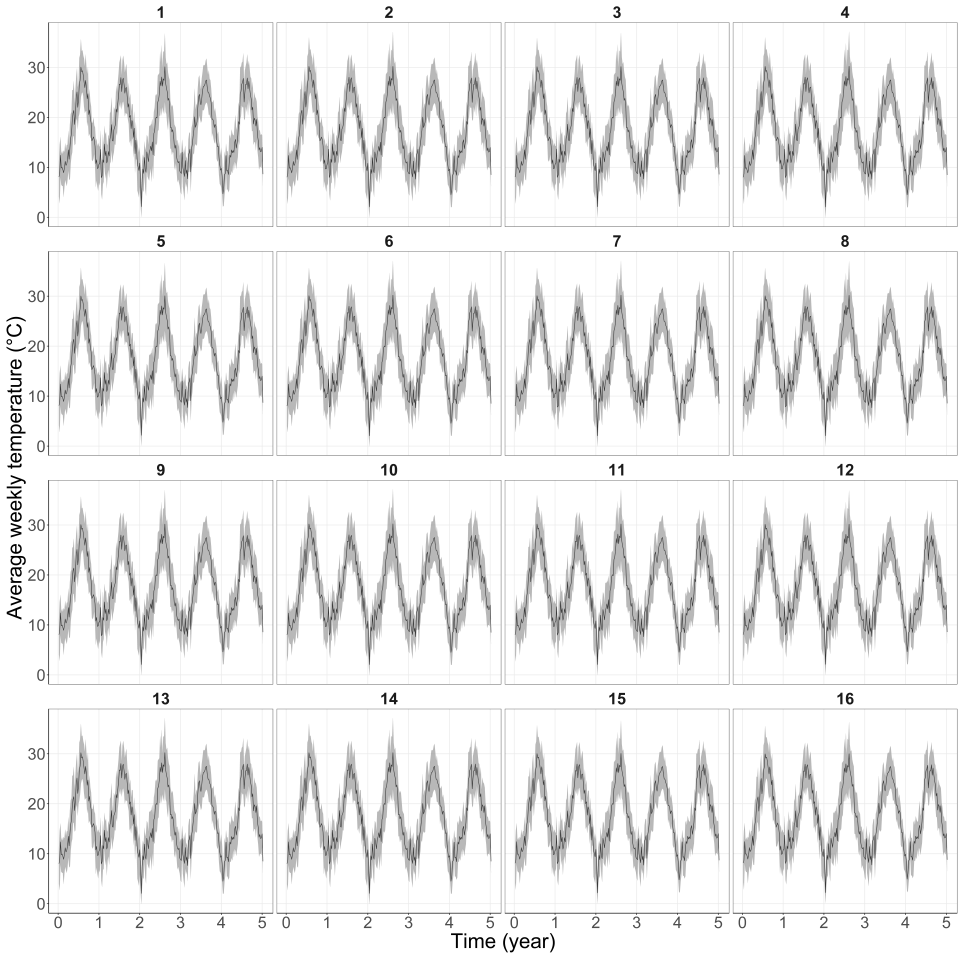


Figure 25: Average weekly temperatures (°C) over the five-year simulation period (2015–2019) in olive groves used for model calibration and validation in the Apulia region, Italy. Each panel corresponds to a different calibration site. The black lines represent the mean weekly temperatures, while the shaded grey areas indicate the range between average weekly maximum and minimum temperatures.

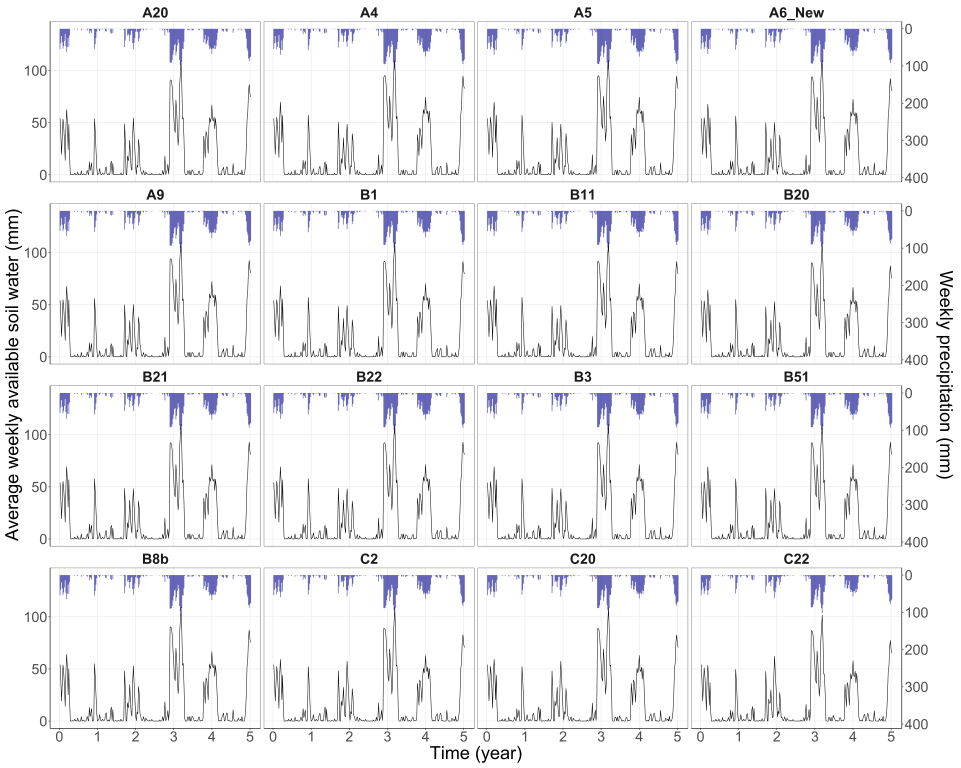


Figure 26: Average weekly available soil water (mm, black lines, left y-axis) and weekly cumulative precipitation (mm, blue bars, right y-axis) over the five-year simulation period (2015-2019) in olive groves used for model calibration and validation in the Apulia region, Italy.

4.3.4 Model calibration and validation

The eco-epidemiological model was calibrated using disease severity data from five olive groves. Calibration focused on two key parameters: host susceptibility to *Xf* infection (i_{sp}^{C} and i_{sp}^{R}) and the non-systemic infection recovery rate (r_{np}^{C} and r_{np}^{R}), both assumed equal for olive trees and reservoir plants. The landscape composition of each monitored grove was reproduced in simulations by defining olive tree density and the carrying capacities of non-susceptible shrubs and trees (K^N) and reservoir plants (K^R) based on high-resolution satellite imagery (Google Earth Pro, Google Inc.© 2024) and biomass estimates (Pasalodos-Tato et al., 2015 [44]). Initial conditions were set to reflect realistic field situations, including herbaceous biomass, woody vegetation cover, reservoir infection levels, and vector population density. A detailed description of parameter values and initial conditions is provided in Section 4.6.

Simulations were initialized starting from January 1, 2015, as the baseline date for the model to account for transmission history and disease progression. They were run over a 5-year period to capture long-term epidemic dynamics. Model performance was assessed using the root mean square error (RMSE) between simulated and observed cumulative numbers of olive trees in each disease stage, with the best-fitting parameter set selected for calibration.

For model validation, disease severity data from 11 additional olive groves, monitored for periods ranging from 1 to 3 years, were used to test the model's predictive capacity.

4.3.5 Results

Model calibration

The model was calibrated to accurately reproduce the observed dynamics of disease progression across the study fields. Despite the complexity of the system, the simulations successfully captured the overall trends, reproducing both the timing of increases and subsequent declines in the proportions of trees at each disease stage (Figure 27). Calibration performance, expressed as total RMSE, ranged from 7.86 in field 5 to 21.81 in field 4. Nonetheless, the model was less effective in reproducing certain complex patterns observed in the field, such as multi-peaked dynamics across years (e.g., stages C_2 and C_3 in fields 1 and 5) and rapid, large fluctuations in the proportion of trees within disease stages. These discrepancies are partly attributable to sampling variability, particularly the inherent uncertainty associated with visual classification of disease stages over time.

Model validation

The simulated epidemiological dynamics of olive trees showed good agreement with the observed data across most validation fields (Figure 28). Similar to the calibration fields, the model effectively reproduced the overall patterns of disease progression across all stages, capturing the timing and general trends of increase and decrease in the proportions of trees at each disease stage. Accuracy was generally higher for asymptomatic

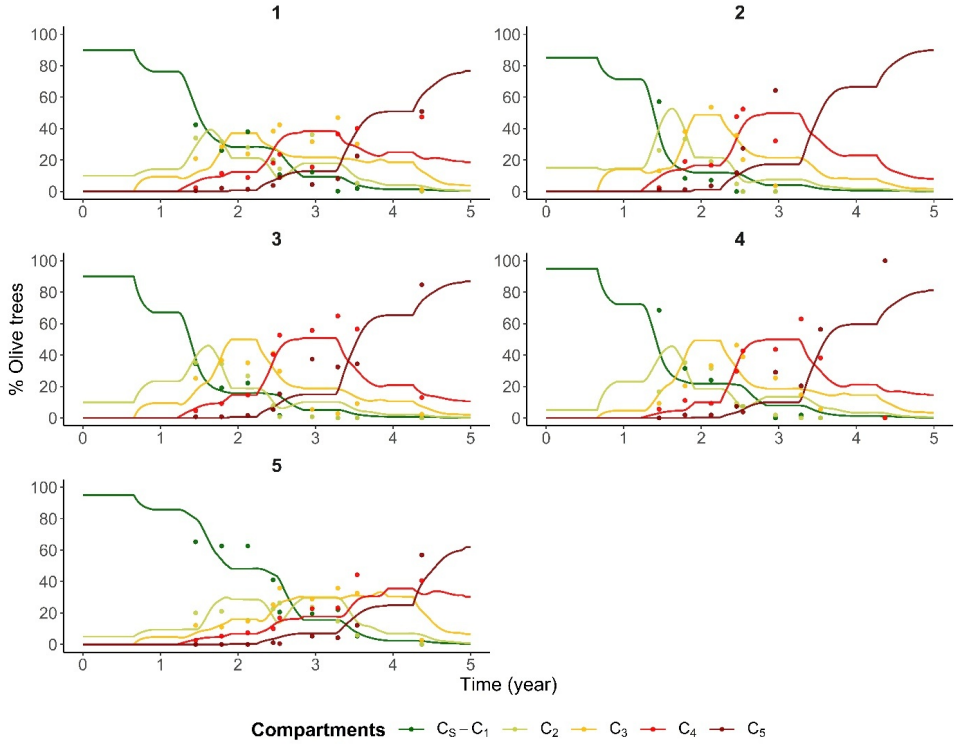


Figure 27: Trends of infection over five years (2015–2019) at the five calibration sites. Lines represent the simulated percentage of olive trees in each disease stage, while points indicate observed field data in the *Xf*-infected area of Lecce province (Zarco-Tejada et al., 2018 [61], 2021 [90]). C_S–C_1: Asymptomatic olives; C_2: $>$ 0–25% canopy with desiccated branches; C_3: $>$ 25–50%; C_4: $>$ 50–75%; and C_5: $>$ 75% canopy with desiccated branches or fully desiccated trees.

trees (C_S–C_1) and fully desiccated trees (C_5), while the intermediate stages were less precisely reproduced, reflecting more variable dynamics in the field. Total RMSE values ranged from 3.88 in field 11 to 45.03 in field 14, highlighting some variability in model performance across validation sites.

Simulated dynamics across all olive groves To illustrate the main simulation outcomes, results for one representative olive grove are presented in Figure 29. Corresponding simulations, for all 16 groves included in the model calibration and validation, are available in Section 4.7.

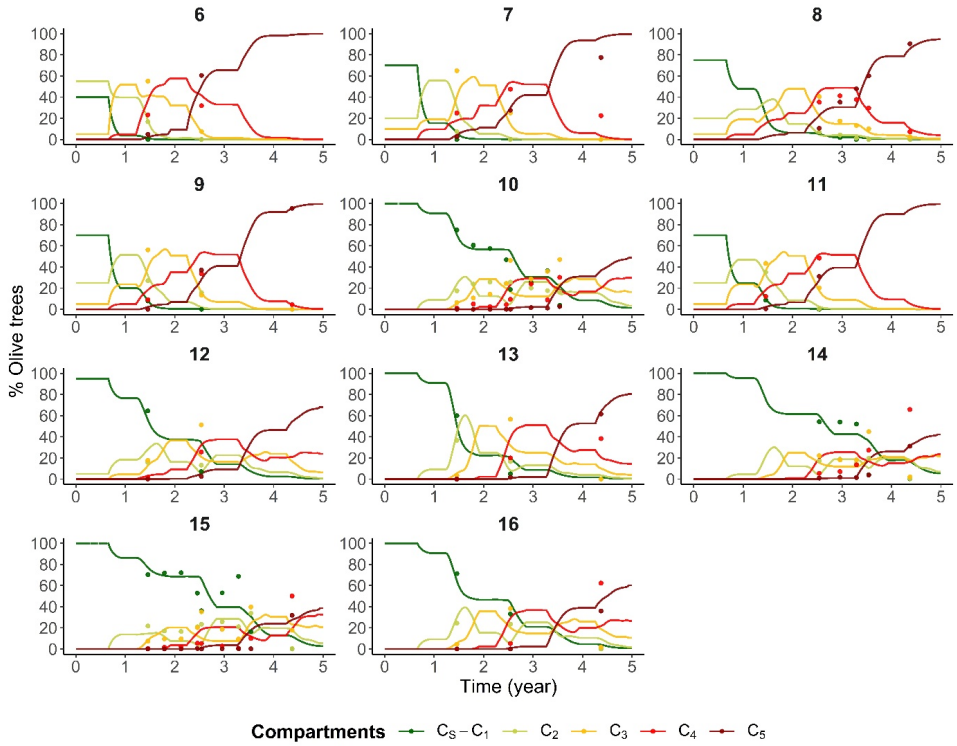


Figure 28: Trends of infection over five years (2015–2019) at the validation sites. Lines represent the simulated percentage of olive trees in each disease stage, while points indicate observed field data in the *Xf*-infected area of Lecce province (Zarco-Tejada et al., 2018 [61], 2021 [90]). C_S–C_1: Asymptomatic olives; C_2: > 0–25% canopy with desiccated branches; C_3: > 25–50%; C_4: > 50–75%; and C_5: > 75% canopy with desiccated branches or fully desiccated trees.

4.3.6 Herbaceous vegetation (H) and Non-susceptible shrubs and trees (N)

The H biomass showed a consistent temporal pattern across all olive groves during the 5-year simulation (Figure 29a for an illustrative case; Figure 30 in Section 4.6 for all groves). Significant growth occurred from late autumn to mid-spring, followed by a marked decline in late spring and summer. Across all fields, the mean H biomass (± standard error) ranged from a maximum of 3584.83 ± 29.93 kg ha^{-1} in the spring of the fourth year to a minimum of 5.56 ± 0.02 kg ha^{-1} in the summer of the fourth year. Notably, lower biomass peaks were observed during the winter and spring of the second year, with an average maximum of 627.55 ± 6.65 kg ha^{-1}, due to the reduced precipitation that constrained the growth rate.

The biomass of N presented a consistent temporal pattern across all olive groves during the five-year simulation (Figures 29b and 31), gradually progressing towards the

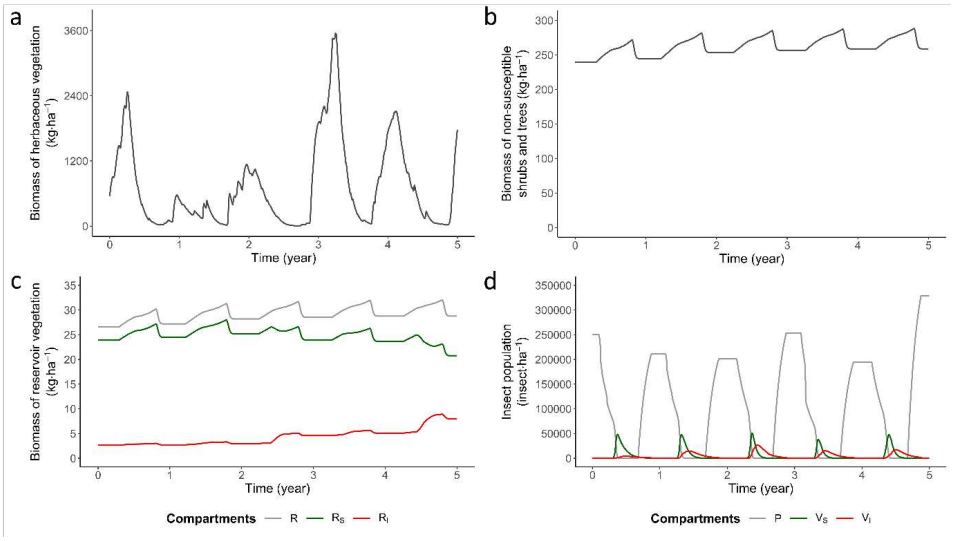


Figure 29: Simulated dynamics of non-crop vegetation and vectors over a five-year period in one of the 16 simulated olive groves in the Apulia region, Italy. Panels show (a) herbaceous vegetation biomass, (b) biomass of non-susceptible shrubs and trees, (c) biomass of the reservoir vegetation (R_S – susceptible, R_I – infected; R– overall), and (d) vector populations (P – preimaginal insects, V_S – non-infected adults; V_I – infected adults).

carrying capacity defined for each field. Periods of highest biomass growth were observed during the period from spring to early summer and again in early autumn, when temperature conditions were close to the estimated optimum temperature for woody biomass growth (i.e., 17.5 ℃).

Reservoir plants The temporal dynamics of total reservoir plant biomass ($R_S + R_I$) followed a pattern similar to that observed for N (Figures 29c and 32). Throughout the simulation period, the biomass of R_I plants steadily increased in all fields, with a more pronounced rise during the second half of the simulation. By the end of the simulation period, the average percentage of R_I biomass reached $23.08\% \pm 1.46\%$, with highest percentage recorded in field 6 (31.83%), while field 14 presented the lowest value (13.47%), starting from an initial R_I percentage of approximately 10% at all fields.

Insect vectors *P. spumarius* showed marked interannual variability in population abundance across all fields during the 5-year simulation period (Figures 29d and 33). The temporal dynamics of insect population followed a similar pattern among all olive groves. The infection prevalence in vector population varied notably across fields and years (Figure 34). Within each year, the simulated percentage of V_I gradually increased until mid-November, marking the end of adult longevity. In most fields, the lowest

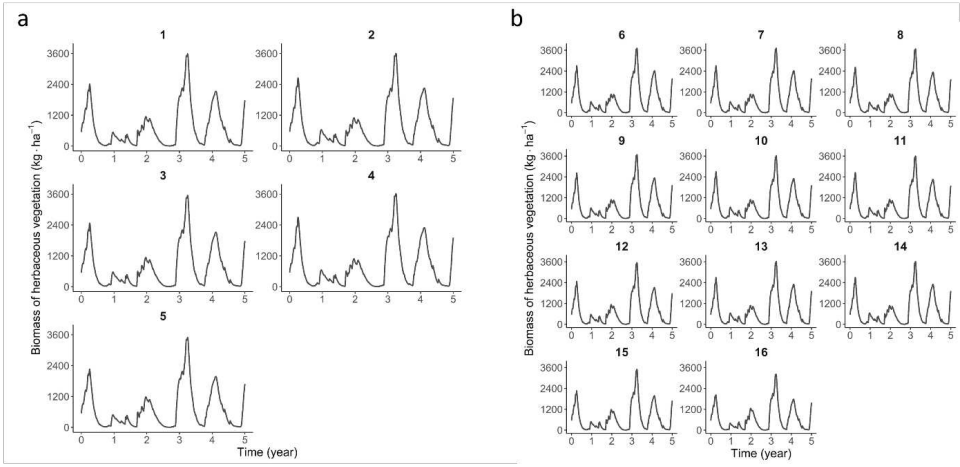


Figure 30: Simulated herbaceous biomass dynamics (H) (kg ha^{-1}) over five-year period (2015-2019) in olive groves used for model calibration (a) and validation (b) in the Apulia region, Italy.

annual peak of V_I prevalence occurred in the first simulation year, with values ranging from 23.44% in field 14 to 78.01% in field 2, and highest prevalence typically observed between the third and fifth years, with peaks reaching approximately 100%. These peaks coincided with periods of higher prevalence of infective olive trees at intermediate disease stages, representing still suitable hosts for the vectors and thus more likely to transmit the pathogen (Figure 24).

Epidemiological dynamic in olive trees In most fields, the majority of trees were either non-infected (C_S) or in the early stages of infection (C_0 and C_1) during the first simulation year, indicating the early phases of *Xf* outbreaks (Figures 27 and 28). In these fields, approximately half of trees transitioned to symptomatic stages by the end of the second year and the third year, with full prevalence of symptomatic trees generally reached by the fourth or fifth year. In contrast, fields with advanced initial infection (i.e., 6, 7, 9, and 11) showed a rapid decline in asymptomatic stages toward the end of the first year, with the entire tree population becoming symptomatic by the second year of simulation (Figures 27 and 28). The dynamics of stages C_S, C_0, and C_1, along with the aggregated symptomatic stage dynamics, are shown in Figure 35.

The estimated curves for symptomatic stages displayed a consistent progression within each field. The dynamics of each stage followed those of the preceding stage, with a temporal offset reflecting the stage-specific delay and the seasonal interruption of disease progression during winter months. Bacterial mortality ($b_{msp}^{C_i}$) had a minor influence on overall disease dynamics, as extreme temperatures were rarely reached within the climatic range for the simulation study.

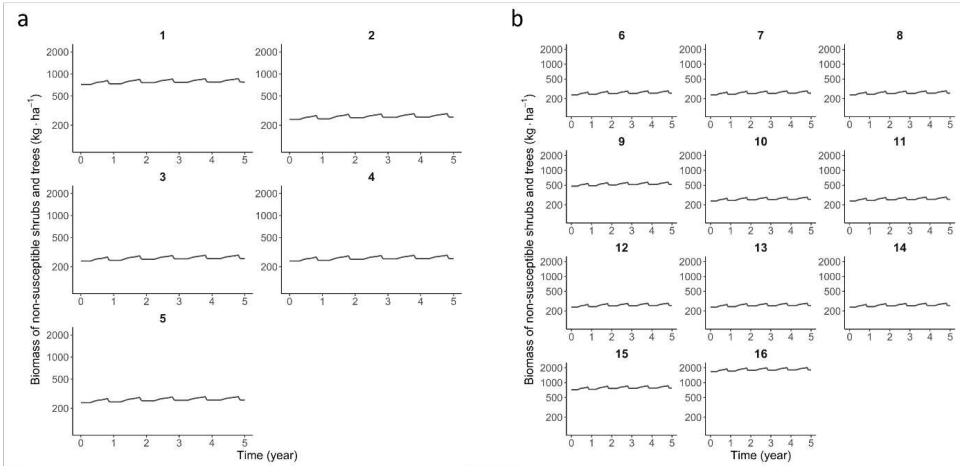


Figure 31: Simulated biomass dynamics of non-susceptible shrubs and trees (N) (kg ha^{-1}) over five-year period (2015-2019) in olive groves used for model calibration (a) and validation (b) in the Apulia region, Italy.

Progression to the final disease stage (C_5) typically began at the start of the third simulation year, with a marked increase during the fourth year. Significant accumulation of trees in stage C_5 occurred approximately 2.5 years after the first appearance of symptoms. By the end of the simulation period, the proportion of trees in stage C_5 ranged from 38.60% to 94.78%.

4.4 Discussion

The eco-epidemiological modelling framework developed in this study effectively captures the key biological processes and abiotic drivers underlying the dynamics of the *Xf* pathosystem in olive agroecosystems. A major strength of the model is its mechanistic representation of disease progression in olive trees, structured into compartments corresponding to distinct infection stages and symptom severity levels. Transitions between stages are described as physiologically based processes linked to within-host bacterial dynamics and symptom development, modulated by biotic factors such as host phenology, susceptibility, and superinfection events, as well as abiotic variables including temperature and soil moisture. The explicit incorporation of vector population dynamics and seasonal patterns, further enhanced the realism and predictive power of the simulated *Xf* epidemiology.

Climatic conditions in southern Apulia, Italy, during the simulation period were characterized by warm-hot temperatures and mild winters, which are favourable for the development and persistence of *Xf* subspecies *pauca* infection in olive trees (EFSA PLH Panel, 2019 [66]; Godefroid et al., 2022 [95]). The consistently suitable temperatures

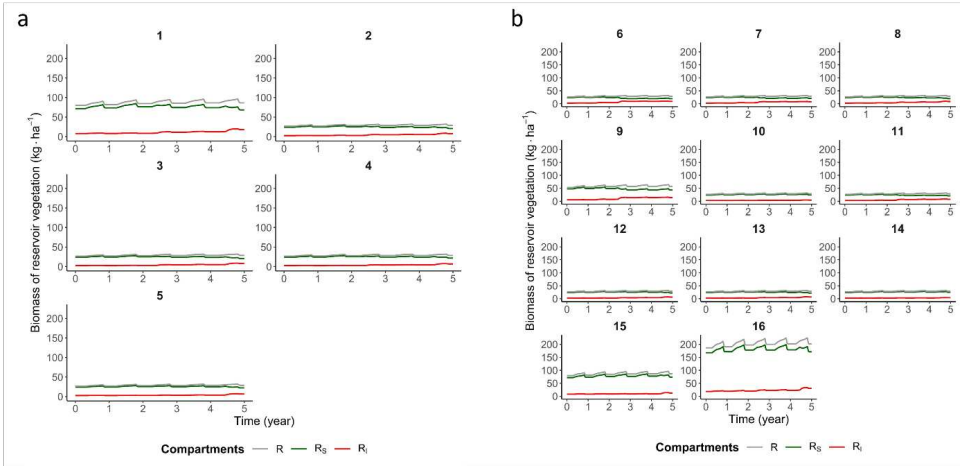


Figure 32: Simulated biomass dynamics of non-infected (R_S), infected (R_I) and total reservoir (R) (kg ha^{-1}) over five-year period (2015-2019) in olive groves used for model calibration (a) and validation (b) in the Apulia region, Italy.

from late spring through mid-autumn supported the effective establishment and rapid disease progression, while the absence of cold-induced recovery mechanisms limits natural disease regression under the estimated model parameters. Future climate change scenarios are expected to increase the frequency and intensity of heat stress events, which may potentially reduce the environmental suitability of the region for *Xf* infection (Bosso et al., 2016 [47]; Giménez-Romero et al., 2022 [94]).

Symptom progression in olive trees was further influenced by seasonal water stress, particularly during summer months. Prolonged drought periods accelerated symptom expression, while increased rainfall and cooler temperatures during autumn tend to mitigate disease progression, consistent with previous findings (De Pascali et al., 2022 [92]; Wallis and Gorman, 2024 [105]). However, the role of water stress in disease dynamics remains unclear, as it may also affect bacterial proliferation and vector behaviour (Godefroid et al., 2022 [95]), warranting further investigation.

The average duration of the asymptomatic period in our model was consistent with empirical and model-based estimates of approximately 1 year (EFSA PLH Panel, 2019 [66]; Saponari et al., 2017 [54]). Model simulations estimated that disease progression from the initial phase of *Xf* outbreak to the point where the entire population exhibited maximum disease severity averaged approximately 5 years, aligning with estimates reported by White et al. (2020)[80] and Giménez-Romero et al. (2023)[100].

The results show that the abundance of infected adult vectors peaked during summer, in agreement with previous modelling studies (Gilioli et al., 2023 [99]; Giménez-Romero et al., 2023 [100]). The prevalence of infected vectors gradually increased until mid-November, often exceeding 90% of the total vector population during most of the

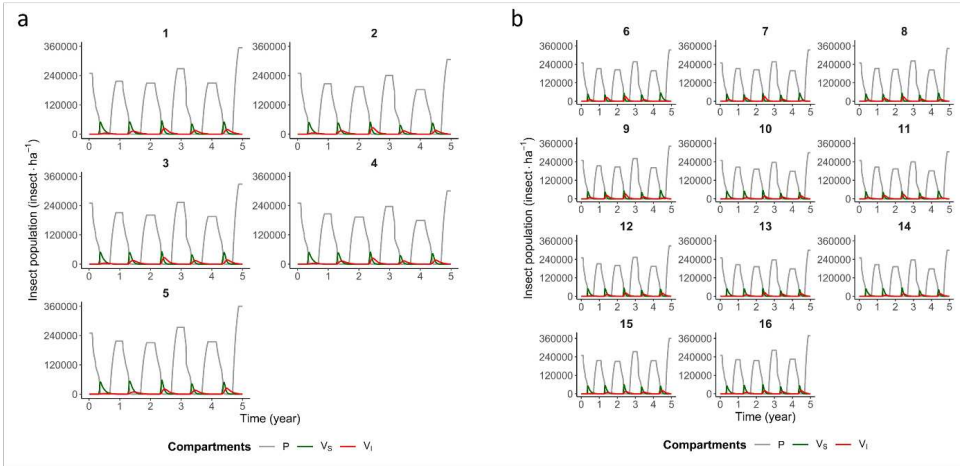


Figure 33: Simulated number of preimaginal stage (P), and non-infected (V_S) and infected (V_I) adult stages of *Philaenus spumarius* over five-year period (2015-2019) in olive groves used for model calibration (a) and validation (b) in the Apulia region, Italy.

simulated years. Field observations, however, show more variable and non-linear seasonal patterns, with infection prevalence in vectors rarely surpassing 70% (Ben Moussa et al., 2016 [46]; Cavalieri et al., 2019 [63]; Cornara et al., 2017 [52]). These differences may reflect influence of spatial and temporal heterogeneity in host plant infection, climate variability, and the seasonal movements of vector among host compartments, all of which can also affect the estimates of prevalence of infected vectors derived from field sampling.

Vector infectivity was highest when olive trees in intermediate disease stages were most prevalent, subsequently declining as trees advanced to severe disease stages, which are less attractive to vectors (Daugherty et al., 2011 [34]). This pattern has also been documented in Apulia in recent years (Bodino et al., 2023 [96]), where widespread tree desiccation and the introduction of resistant cultivars (characterized by lower bacterial loads even when infected) are believed to have contributed to declining vector infection rates. High vector infection levels observed in model simulations also reflect the predominance of susceptible olive trees in the simulated landscape, mirroring the typical host composition in the Apulian outbreak zone. The limited presence of non-host woody vegetation likely contributed to sustained transmission, highlighting the role of host plant composition in shaping epidemic dynamics (Cornara et al., 2018 [55]).

Reservoir plants in the simulations exhibited a slow increase in infection prevalence over time, likely due to their lower abundance compared to other vegetation compartments. This resulted in reduced contact rates with infected vectors and limited transmission events. While their contribution to *Xf* spread appears marginal under the simulated conditions, further research is essential to clarify the role of reservoir plants in *Xf*

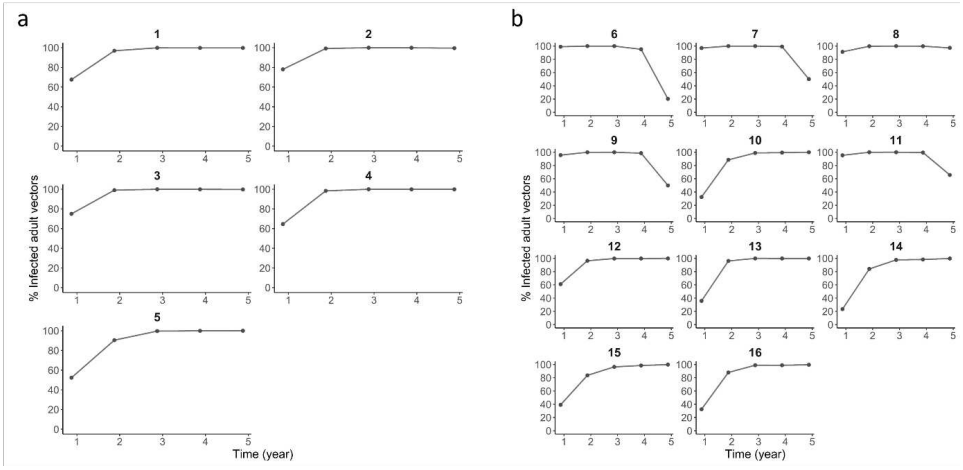


Figure 34: Peak prevalence (%) of infected *P. spumarius* adults over five-year period (2015-2019) in olive groves used for model calibration (a) and validation (b) in the Apulia region, Italy.

epidemiology. Specifically, experimental data on their transmission efficiency, latency period, and symptom expression are needed to better inform risk assessments and support effective management strategies.

Model parameterisation presented several challenges due to the limited empirical data on the bioecological processes governing disease progression and vector dynamics. Despite these constraints, the calibration produced a coherent and biologically plausible parameter set, with simulated outputs consistent with field observations. However, both calibration and validation relied on data from a geographically restricted area with relatively homogeneous environmental and landscape conditions. Initial distribution of disease stage was inferred due to the absence of field data, and vector populations were assumed uniform across sites, a reasonable assumption given the spatial proximity of fields and similar landscape contexts, but still a source of uncertainty.

Future enhancements could incorporate spatially explicit network modelling to more accurately capture landscape-level disease spread and the influence of management practices. Overall, this framework not only advances scientific understanding of *Xf* epidemiology but also directly supports decision-making for effective disease containment and sustainable management in affected olive-growing regions. This mechanistic, stage-structured model provides a valuable tool for both pest risk assessment (PRA) and integrated pest management (IPM). For PRA, it enables simulation of disease spread under varying environmental and host conditions, supporting risk evaluation and contingency planning. For IPM, it allows assessment of intervention strategies targeting different system components (i.e., trees, vectors, or reservoirs) by incorporating intervention-induced mortality or delay effects.

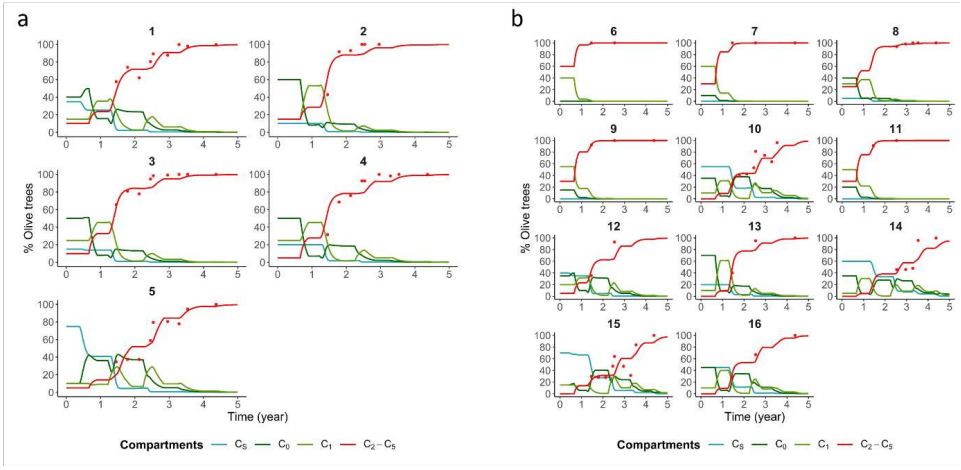


Figure 35: Percentage (%) of olive trees in each disease stage over a five-year period (2015-2019) in olive groves used for model calibration (a) and validation (b) in the Apulia region, Italy. Lines represent the simulated dynamics, while points represent the observed dynamics from field data in the *Xf*-infected area of Lecce province. C_S: non-infected olive trees;C_0: infected but non-infectious asymptomatic trees; C_1: infectious asymptomatic trees; and C_2–C_5: symptomatic trees.

4.5 Conclusion

This study presents a robust, mechanistic model for simulating the eco-epidemiological dynamics of *Xf* in olive systems. By capturing key biological interactions and their modulation by climate, the model enhances realism and adaptability to diverse agroecosystems. Furthermore, it offers a valuable tool for assessing the effectiveness of individual and combined control strategies targeting different components of *Xf* pathosystem, through the incorporation of intervention-induced mortality factors to the model. The integration of a spatially explicit network modelling approach in future developments could provide additional insights into the spatial spread of *Xf* epidemics and the influence of landscape configuration and management practices on disease containment. Overall, this modelling framework offers a powerful platform for advancing risk assessment, optimizing surveillance design, and the development of integrated management strategies for *Xf* outbreaks.

Although this model is very accurate from a biological point of view and takes into account the multiple interactions among the different components, it turns out it is very complex to study its well–posedness from a mathematical point of view. In Chapters 5 and 6 we will study analytically a simplified case of this model. In the following sections we report all the functions that come into play in this model and the parameters used.

4.6 Model functions and parameter estimation

4.6.1 Monod equation

The Monod equation [4] is a mathematical model widely used in microbiology and biochemistry to describe the growth of organisms in relation to the concentration of a limiting nutrient. It is particularly known for modelling microbial growth, where growth rate is influenced by the availability of a key nutrient.

The Monod equation reads:

$$\mu(S) = \mu_{\max} \frac{S}{K_s + S}$$

where:

- $\mu(S)$ is the microbial growth rate,
- $\mu_{\max}$ is the maximum growth rate,
- S is the concentration of the substrate (limiting nutrient),
- K_s is the half-saturation constant, representing the substrate concentration at which the growth rate is half of $\mu_{\max}$.

The Monod equation is employed to model various biological processes beyond microbial growth, such as nutrient uptake and enzymatic degradation. It allows predictions on how resource availability affects the rate of these processes.

The biological significance of the K_s constant is particularly important. It indicates an organism's ability to access nutrients at low concentrations. Organisms with a low K_s value can thrive in environments where the nutrient is scarce, whereas a higher value suggests that the organism requires greater concentrations of the nutrient to achieve the same growth rate.

The Monod equation is a cornerstone in environmental and biological sciences for studying the dynamics of microbial populations. Its simplicity and ability to adapt to many real-world scenarios make it a valuable tool in scientific research.

4.6.2 Vector–plant contact function (n^j)

Adult movement among vegetation compartments is modelled through a vector–plant contact function (n^j) described by a modified Monod functional response, which depends on vegetation abundance (J) and vector preference (p^j) for different vegetation compartments (j) (definition of Monod function in Subsec. 4.6.1). This preference follows a seasonal pattern influenced by temperature and host plant suitability (Bodino et al., 2023 [96]), and is further affected by the health status of olive trees, with highly

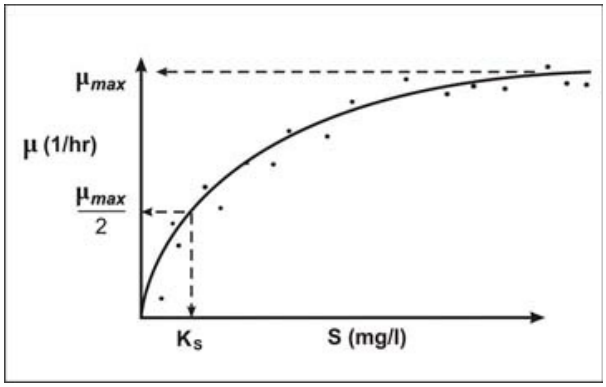


Figure 36: The Monod equation (the unit of measure could vary depending on the application topic.
Source: www.cs.montana.edu.

symptomatic trees being less attractive to the insects (Daugherty et al., 2011 [34]). The vector–plant contact function is defined as:

$$n^j(\lambda^j, p^j, J) = \frac{p^j \cdot J}{\lambda^j + J} \tag{4.2}$$

where λ^j is the j-th semi-saturation constant of the functional response (with the same unit as the corresponding vegetation compartment). To obtain the proportion of vectors feeding on a given vegetation compartment per time unit ($\hat{n}^j$), the Eq. (4.2) is normalized:

$$\hat{n}^j(\lambda^j, p^j, J) = \frac{n^j(\lambda^j, p^j, J)}{\sum_j n^j(\lambda^j, p^j, J)}. \tag{4.3}$$

The seasonal dynamics of *P. spumarius* among the vegetation compartments in the Apulia were described using preference values that varied across two distinct periods of the year: i) higher preferences for olive trees and for non-cultivated shrubs and trees, in the warm season (early June to late September in Apulia), ii) higher preference for herbaceous vegetation during the rest of the year. For each preference period, the average percentage of adults in each vegetation compartment was estimated from monitoring data of *P. spumarius* adults (unpublished data). The transitions between the two preference periods were parametrized based on thermal and chilling requirements. The first transition, occurring in late spring, is determined by the accumulation of critical degree-days (DD_p) above a temperature threshold ($T_{p\,inf}$), starting from the date when the cumulative emergence rate function of preimaginal vectors (ε, Eq. (4.5)) reaches 10%. The second transition, occurring in late summer, is driven by the accumulation of critical chilling degree-days (CDD_p) below a temperature threshold ($T_{p\,sup}$), starting

from August 1st. These parameters were estimated for the Apulian context through simulation studies, resulting in optimal values of $DD_p = 451$ degree-days, $T_{p\,inf} = 3$℃, $CDD_p = 20.4$ degree-days, and $T_{p\,sup} = 22$℃.

Preference values estimated for the non-cultivated shrubs and trees compartment were applied to non-susceptible shrubs and trees (N), and reservoir plants (R_S and R_I). Infected reservoir plants were assumed to display only mild symptoms, which did not affect vector preference. Preference values estimated for the olive trees compartment were applied for non-symptomatic olive trees (C_S, C_0 and C_1). Symptomatic olive trees at stages C_2, C_3, and C_4 were assumed to experience a reduction in vector preference by 25%, 50%, and 75%, respectively. Severely symptomatic olives trees (C_5) were assumed to be completely avoided by the vectors.

The semi-saturation parameters for herbaceous vegetation (λ^H) and non-cultivated shrubs and trees compartments (λ^N, λ^{R_S},λ^{R_I}) were estimated based on foliage and above-ground biomass of olive trees, set at 610 kg ha^{-1} for λ^H and 18,920 kg ha^{-1} for λ^N, λ^{R_S}, and λ^{R_I} (Brunori et al., 2017 [51]). Semisaturation parameters for olive stages (λ^{C_S} to λ^{C_5}) were estimated based on half the density of olive trees per hectare for each simulated landscape, considering areas occupied exclusively by olive trees; as these values are specific to the simulated context, they are reported in Table 4.

4.6.3 Preimaginal vector stage (P)

The dynamics of preimaginal vector stage defined in Eq. (4.1e) is governed by the fecundity function (f^P), the emergence function (ε^P), and the mortality function (m^P).

Fecundity function (f^P)

We assumed a piecewise constant oviposition rate function described as:

$$f^P(D_{\mathrm{OY}}) = \begin{cases} f^P_{0R} \cdot f^P_{SR}, & \text{if } f^P_{\mathrm{DOYmin}}(D_{\mathrm{DL}}) \leq D_{\mathrm{OY}} \leq f^P_{\mathrm{DOYmax}}, \\ 0, & \text{otherwise,} \end{cases} \tag{4.4}$$

where:

- f^P_{0R}: oviposition rate per female vector, set equal to 0.076 h^{-1} (Di Serio et al., 2019 [64]; Silva et al., 2015 [45]);
- f^P_{SR}: average sex ratio of *P. spumarius* population during the oviposition period, set equal to 0.65 (Bodino et al., 2023 [96]);
- $f^P_{\mathrm{DOYmin}}(D_{\mathrm{DL}})$: onset of oviposition period corresponding to the day of the year when daylight duration (D_{DL}) drops below a critical threshold (D^P_f), set at 13 hours (Avosani et al., 2021 [82]; Morente et al., 2021 [89]; Witsack, 1973 [6]);

- f^P_{DOYmax}: end of the oviposition period and maximum adult longevity after which adult populations are rarely observed in the field, set at November 15 considering Apulian conditions (Bodino et al., 2023 [96]).

Emergence function (ε^P) The emergence function of the preimaginal stage (ε^P) is determined by a satellite model (developed with Entomonlib - Ch: 3) from the *P. spumarius* phenological model developed by Gilioli et al. (2024)[104]. This stage-structured population model is formulated as a system of Kolmogorov PDEs that accounts for both chronological time and the physiological age of insect stages. The relative cumulative emergence curve generated by this phenological model is integrated into the eco-epidemiological framework through the emergence function ε^P defined as:

$$\varepsilon^P = Kolmogorov(T_{AH}), \tag{4.5}$$

where *Kolmogorov* represents the operator that, by solving the PDE system defining the phenological model in Gilioli et al. (2024) [104], maps the average hourly temperature (T_{AH}) to the function ε^P. The simulation of the phenological model begins on January 1st, when preimaginal individuals are assumed to be in diapause. Diapause ends when preimaginals accumulate a critical degree-day threshold ($DD^P_e = 120DD$) above a minimum temperature threshold ($T^P_e = 6.5\,℃$) from January 1 onward (Gilioli et al., 2024 [104]). Development rate $z^P(T_{AH})(h^{-1})$ of post-diapausing preimaginal stage is determined by the temperature-based Brière function:

$$z^P(T_{\text{AH}}) = \begin{cases} z^P_a\, T_{\text{AH}} \left(T_{\text{AH}} - T^P_{z\,\text{inf}}\right) \sqrt{T^P_{z\,\text{sup}} - T_{\text{AH}}}\,, & \text{if } T^P_{z\,\text{inf}} \le T_{\text{AH}} \le T^P_{z\,\text{sup}}, \\ 0, & \text{otherwise,} \end{cases} \tag{4.6}$$

where z^P_a is an empirical constant fixed at 2.36×10^{-5}, $T^P_{z\,\text{inf}}$ and $T^P_{z\,\text{sup}}$ are the lower and the upper development temperature thresholds, set at 5.5 ℃ and 33 ℃, respectively, according to the optimisation procedure described by Gilioli et al. (2024)[104].

Preimaginal mortality function (m^P) The mortality function of preimaginal stage (m^P) combines intrinsic temperature-dependent mortality (abiotic) with extrinsic mortality related to natural control factors. The function is defined as:

$$m^P(T_{\text{AH}},\, D_{\text{OY}},\, P) = \begin{cases} m^P_T(T_{\text{AH}}) \left[1 + \left(\frac{P}{K^P}\right)^2\right], & \text{if } D_{\text{OY}} \ge m^P_{\text{DOY}}(T_{\text{AH}})\,, \\ 0, & \text{otherwise,} \end{cases} \tag{4.7}$$

where $m^P_T(T_{\text{AH}})$ represents the temperature-dependent mortality function, incorporating both abiotic and extrinsic factors. This term is modulated by a density-dependent

mortality component linked to the maximum insect abundance sustained in the landscape (K^P), set at 1,000 nymphs per ha (Yurtsever, 2000 [17]) and the abundance of preimaginal insects (P). Preimaginal mortality is considered only after diapause termination, which occurs once the degree-day threshold $m^P_{DOY}(T_{AH})$ is reached in emergence model (see Section 4.6.3). Accordingly, preimaginal mortality is neglected from oviposition in the previous year until diapause termination of following year.

Temperature-dependent mortality is modelled using a function adapted from Gilioli et al. (2016)[48], and is expressed as:

$$m^P_T(T_{\mathrm{AH}}) = \begin{cases} m^P_n \cdot \left[\left(T^P_{z\,\mathrm{inf}} - T_{\mathrm{AH}}\right)^2 + 1\right], & \text{if } T_{\mathrm{AH}} < T^P_{z\,\mathrm{inf}}, \\ -\, z^P(T_{\mathrm{AH}}) \cdot \ln\Big(1 - \mu^P_T(T_{\mathrm{AH}})\Big) \;+\; m^P_n, & \text{if } T^P_{z\,\mathrm{inf}} \le T_{\mathrm{AH}} \le T^P_{z\,\mathrm{sup}}, \\ m^P_n \cdot \left[\left(T_{\mathrm{AH}} - T^P_{z\,\mathrm{sup}}\right)^2 + 1\right], & \text{if } T_{\mathrm{AH}} > T^P_{z\,\mathrm{sup}}. \end{cases} \tag{4.8}$$

where:

- m^P_n: extrinsic mortality due to natural control factors (h^{-1}), set to 3.77×10^{-4} h^{-1} based on monitoring data of *P. spumarius* nymphal stages collected in 10 olive groves in the Apulian region in 2019 (unpublished data);
- z^P: development rate function (4.6);
- $T^P_{z\,\mathrm{inf}}$ and $T^P_{z\,\mathrm{sup}}$ are the minimum and maximum, respectively, development temperature thresholds;
- $\mu^P_T(T_{\mathrm{AH}})$: average stage proportional mortality of P defined as:

$$\mu^P_T(T_{\mathrm{AH}}) = \begin{cases} 0.75 \cdot \left(\dfrac{T^P_{z\,\mathrm{inf}}}{T^P_{\mu\,\mathrm{opt}}} - 1\right)^{-2} \cdot \left(\dfrac{T_{\mathrm{AH}} - T^P_{\mu\,\mathrm{opt}}}{T^P_{\mu\,\mathrm{opt}}}\right)^2 + 0.1, & \text{if } T^P_{z\,\mathrm{inf}} \le T_{\mathrm{AH}} \le T^P_{z\,\mathrm{sup}}, \\ 0.85 & \text{otherwise,} \end{cases} \tag{4.9}$$

where:

$$T^P_{\mu\,\mathrm{opt}} = \frac{T^P_{z\,\mathrm{inf}} + T^P_{z\,\mathrm{sup}}}{2}.$$

4.6.4 Adult vector stage (V_S and V_I)

The dynamics of adult vector stages, defined in Eqs. (4.1f) and (4.1g), are regulated by the acquisition function (α^V), the adult mortality function (m^V), and the emergence function (ε^P).

Acquisition function (α^V)

Vector acquisition is assumed to depend on the bacterium titre within the infected plant and the daily duration of feeding activity by the vector (Gilioli et al., 2023 [99]). Assuming that each vector feeds on one host plant per time unit, the acquisition rate is defined as:

$$\begin{aligned} a^V(\hat{n}^j) \; = & \; \hat{n}^{R_I}\big(\lambda^{R_I},\, p^{R_I},\, R_I\big) \cdot a^{R_I} + \hat{n}^{C_1}\big(\lambda^{C_1},\, p^{C_1},\, C_1\big) \cdot a^{C_1} \\ & + \hat{n}^{C_2}\big(\lambda^{C_2},\, p^{C_2},\, C_2\big) \cdot a^{C_2} + \hat{n}^{C_3}\big(\lambda^{C_3},\, p^{C_3},\, C_3\big) \cdot a^{C_3} \\ & \hat{n}^{C_4}\big(\lambda^{C_4},\, p^{C_4},\, C_4\big) \cdot a^{C_4}. \end{aligned} \tag{4.10}$$

where the acquisition rate corresponds to the proportion of insects feeding on infectious vegetation (given by $\hat{n}^j$, (4.3)) per time unit, weighted by the probability of acquiring the bacterium from the respective vegetation compartment (a^j, h^{-1}).

The bacterium titres for each olive stage were assigned based on literature data (De Pascali et al., 2022 [92]; Hill and Purcell, 1997 [13]; Saponari et al., 2017 [54], 2019 [71]) and are presented in Table 2. For non-infectious symptomatic olive trees (C_0), the same bacterium threshold level for effective acquisition observed in grapevines by Hill and Purcell (1997)[13] was assumed. Considering a maximum acquisition rate at 0.1206 (EFSA PLH Panel, 2019 [66]), the acquisition probabilities (a^j) were estimated from literature (Bodino et al., 2021 [84]; Cavalieri et al., 2019 [63]; Cornara et al., 2017 [52]). The acquisition rate from infected reservoir plants (a^{R_I}) was set at $1.53 \cdot 10^{-3}$ h^{-1}, assuming the same rate as for mild symptomatic olive trees (C_2) (Table 2).

Table 2: Intervals of bacterium titre [$\log(B^j)$, CFU(Colony Forming Units) ml^{-1}] for each compartment of infected olive trees (C_0–C_5), and the central values of bacterium titre intervals assumed for estimating the vector acquisition rates.

Variable	**Bacterium titre** $\log(B^j)$	**Central value of bacterium titre** $\log(B^j)$	**Acquisition rate** (α^j) h^{-1}
C_0	(0; 4]	2.00	0.00
C_1	(4; 4.97]	4.49	0.33×10^{-3}
C_2	(4.97; 5.43]	5.20	1.53×10^{-3}
C_3	(5.43; 5.90]	5.67	3.37×10^{-3}
C_4	(5.90; 6.37]	6.14	5.08×10^{-3}
C_5	(6.37; 7]	6.69	5.35×10^{-3}

Adult mortality function (m^V) The mortality of adult stage (m^V) is defined by:

$$m^V(T_{\mathrm{AH}},\, D_{\mathrm{OY}}) = 1 - \Big[1 - m_T^V(T_{\mathrm{AH}})\Big] \cdot \Big[1 - m_a^V(D_{\mathrm{OY}})\Big], \tag{4.11}$$

where $m_a^V(D_{\mathrm{OY}})$ describes the mortality rate due to aging process (h^{-1}), set at $2.46 \times 10^{-4}\mathrm{h}^{-1}$ assuming an average adult longevity in Apulian conditions of 170 days (Bodino

et al., 2023 [96]), and $m_T^V(T_{\mathrm{AH}})$ denotes a temperature-dependent mortality function that incorporates extrinsic mortality related to natural control factors (h^{-1}). The function $m_T^V(T_{\mathrm{AH}})$ is defined as:

$$m_T^V(T_{\mathrm{AH}}) = \begin{cases} m_n^V \cdot \left[\left(T_{m\,\mathrm{inf}}^V - T_{\mathrm{AH}}\right)^2 + 1\right], & \text{if } T_{\mathrm{AH}} < T_{m\,\mathrm{inf}}^V, \\ m_{T_a}^V \cdot \left(m_{T_b}^V\right)^{T_{\mathrm{AH}}} + m_n^V, & \text{if } T_{\mathrm{AH}} \geq T_{m\,\mathrm{inf}}^V. \end{cases} \tag{4.12}$$

where:

- m_n^V: extrinsic mortality due to natural control factors (h^{-1}), estimated as 5.82×10^{-4};
- $T_{m\,\mathrm{inf}}^V$: lower temperature threshold (in °C) at which the mortality formula changes, set at 5 °C;
- $m_{T_a}^V$, $m_{T_b}^V$: dimensionless parameters shaping the temperature-dependent mortality; estimated as 9.10×10^{-11} and 1.73, respectively.

4.6.5 Olive trees ($C_S, C_0 - C_5$)

The dynamics of olive tree compartments, defined in Eqs. (4.1h) and (4.1n), are governed by an infection function (i^{C_S}), a disease progression function (d^{C_i}), a climate-dependent disease recovery function (r_T^C), and a non-systemic infection recovery function (r_n^C). The olive tree compartments are represented by a system of Delayed Differential Equations (DDEs), where the disease progression and recovery functions act on the number of olive trees that have remained in the disease stage i (with $i \in \{0, 1, \ldots, 4\}$) for at least corresponding delay period τ^{C_i}, indicated by $C_i^*(t, \tau^{C_i})$. The delay periods were set at:

- τ^{C_0}: 7.5 months (τ^{C_0} = 5,400 h; Saponari et al., 2017)
- τ^{C_1}: 3 months (τ^{C_1} = 2,160 h; EFSA PLH Panel, 2019 [66]; Saponari et al., 2017 [54]; White et al., 2020 [80])
- τ^{C_2}: 4 months (τ^{C_2} = 2,880 h; EFSA PLH Panel, 2019 [66]; expert knowledge)
- τ^{C_3}: 6 months (τ^{C_3} = 4,320 h; EFSA PLH Panel, 2019 [66]; expert knowledge)
- τ^{C_4}: 7.5 months (τ^{C_4} = 5,400 h; EFSA PLH Panel, 2019 [66]; expert knowledge)

Infection function (i^{C_S})

Non-infected olive trees (C_S) may become infected through contact with infected vectors (V_I). The probability of infection depends on the number of V_I feeding on

a susceptible tree and follows a non-linear pattern derived from the Poisson infection probability model described by Daugherty and Almeida (2009)[28]:

$$i^{C_S}\big(\hat{n}^{C_S},\, C_S,\, V_I\big) = 1 - e^{-\,i^C_{sp}\, i^C_{ip}\, \frac{\hat{n}^{C_S}\, V_I}{C_S}} \tag{4.13}$$

where:

- i^C_{sp}: index of susceptibility of olive trees to *Xf* (real value in $[0, 1]$), assumed $i^C_{sp} = 2.50 \times 10^{-2}$;
- i^C_{ip}: vector inoculation rate (in insect$^{-1} \cdot$ h^{-1}, range $[0, 1]$), equivalent to the probability that an infected vector transmits the bacterium to host plants; based on Cornara et al. (2017)[52] we assumed $i^C_{ip} = 1.45 \times 10^{-3}$;
- $\hat{n}^{C_S}$: fraction of V_I feeding on C_S (in $[0, 1]$).

Disease progression function (d^{C_i}) The disease progression function of infected olive trees is modelled through an implicit representation of the bacterium growth and spread within the plant, as well as the resulting symptom development in olive canopy. Disease progression is influenced by temperature (affecting bacterial replication), soil water availability (reflecting the impact of water stress on symptom severity), and the density of infected vectors (capturing the effect of superinfection events on disease dynamics) (Godefroid et al., 2019 [68]; Sicard et al., 2018 [59]; Sun et al., 2013 [39]). Extreme temperatures can reduce bacterial populations within the plant, allowing for partial disease recovery, except in advanced disease stages where trees exhibit severe symptoms throughout most of the canopy or are desiccated. The disease progression combines the effects of temperature on bacterium growth and water stress, and is defined as:

$$d^{C_i}\big(b^{C_i}_{TS},\, Ws^{C_i},\, b^{C_i}_m\big) = \max\Big\{ b^{C_i}_{TS}\big(D_{\mathrm{OY}},\, b^{C_i}_T,\, b^{C_i}_S\big)\, Ws^{C_i}\big(AW\big) - b^{C_i}_m(TF),\; 0 \Big\}. \tag{4.14}$$

where:

- $b^{C_i}_{TS}\big(D^C_{\mathrm{OY}},\, b^{C_i}_T,\, b^{C_i}_S\big)$: disease progression rate (see (4.15)) due to cumulated bacterium growth, driven by temperature and superinfection events;
- $Ws^{C_i}\big(AW\big)$: disease progression factor (see (4.16)) due to water stress (dimensionless);
- $b^{C_i}_m(TF)$: disease regression rate due to bacterium mortality by adverse temperature factor (see (4.18)) TF(h^{-1}).

The disease progression rate ($b^{C_i}_{TS}$) due to cumulated bacterium growth is defined as:

$$b_{TS}^{C_i}\Big(D_{\mathrm{OY}},\, b_T^{C_i},\, b_S^{C_i}\Big) = \begin{cases} b_{TS\,sp}^{C_i} \cdot b_T^{C_i}(T_{\mathrm{AH}},\, D_{\mathrm{OY}}) \\ \qquad \cdot\Big[1 + b_S^{C_i}\big(\hat{n}^{\,C_i},\, C_i,\, V_I\big)\Big], & \text{if } b^{C}_{\mathrm{DOYmin}}(T_{\mathrm{AH}}) \le D_{\mathrm{OY}} \le b^{C}_{\mathrm{DOYmax}}(T_{\mathrm{AH}})\,, \\ 0, & \text{otherwise.} \end{cases} \tag{4.15}$$

where $b_{TS\,sp}^{C_i}$ is the stage-specific shape parameter estimated from Saponari et al.(2017)[54]: $b_{TS\,sp}^{C_0} = 5.50 \times 10^{-6}$, $b_{TS\,sp}^{C_1}$ 1.44×10^{-5}, $b_{TS\,sp}^{C_2} = 1.24 \times 10^{-5}$, $b_{TS\,sp}^{C_3} = 1.04 \times 10^{-5}$, and $b_{TS\,sp}^{C_4} = 6.90 \times 10^{-6}$. The temperature-dependent growth function ($b_T^{C_i}$), which defines the cumulated bacterium growth rate during the delay period for each disease stage (C_i), was modelled using the function proposed by Analytis (1977). Bacterium growth is assumed to start at the onset of the sprouting phase in spring and is arrested at the onset of dormancy in late autumn. The sprouting phase in olive trees is defined by a chilling and forcing model adapted from Didevarasl et al. (2023)[98]. The onset of dormancy phase is defined by the accumulation of chilling hours according to the model proposed by López-Bernal et al. (2020)[77]. The cumulative bacterium growth in infected olive trees can be accelerated by superinfection events ($b_S^{C_i}$), which occur when infected vectors transmit *Xf* to the infected plants during the delay period.

The disease progression rate due to water stress ($Ws^{Ci}(AW)$) was adapted from the water stress coefficient defined by Allen et al. (1998)[14] and is expressed as:

$$Ws^{C_i}(AW) = 1 - \frac{1}{\tau^{Ws}} \int_{t-\tau^{Ws}}^{t} \min\left\{ Ws_k^{C_i} \cdot \frac{AW}{AWC - RAW},\ 1 \right\} ds \tag{4.16}$$

where:

- τ^{Ws}: water stress accumulation period, set to 30 days ($\tau^{Ws} = 720$ h);
- AW: soil available water (mm) (Allen et al., 1998 [14]);
- AWC: soil available water capacity at field capacity (mm) for olive trees, set to 122.5 mm based on Castellini et al. (2020)[73];
- RAW: readily available water (mm), set to 79.6 mm based on the reference water stress coefficient for olive trees defined by FAO (Allen et al., 1998 [14]);
- $Ws_k^{C_i}$: water stress parameter (dimensionless), describing the effect of *Xf* infection on olive-tree susceptibility to water stress (De Pascali et al., 2022 [92]).

Bacterial mortality rate ($b_m^{C_i}$) The bacterial mortality rate ($b_m^{C_i}$), adapted from Giménez-Romero et al. (2022)[94], provides a temperature-dependent mortality function that integrates the combined effects of cold and heat stress on bacterial survival. It is defined as:

$$b_m^{c_i}(CF) = 1 - \frac{b_{m\,sp}^{C_i}}{b_{m\,sp}^{C_i} + TF^3(T_{\mathrm{AH}})}\,. \tag{4.17}$$

where $b_{m\,sp}^{C_i}$ is a shape parameter (dimensionless) specific for disease class C_i, and $TF(T_{\mathrm{AH}})$ represents the temperature factor accounting for the effects of cold and hot temperatures on bacterial mortality. $TF(T_{\mathrm{AH}})$ is defined as:

$$TF(T_{\mathrm{AH}}) = \frac{1}{24}\int_{t-\tau^{C_i}}^{t} f(s)\,ds, \qquad \text{with} \qquad f(s) = \begin{cases} T_{b\,\mathrm{cold}}^{C} - T_{\mathrm{AH}}(s), & \text{if } T_{\mathrm{AH}}(s) < T_{b\,\mathrm{cold}}^{C}, \\ 15.4\left(T_{\mathrm{AH}}(s) - T_{b\,\mathrm{hot}}^{C}\right), & \text{if } T_{\mathrm{AH}}(s) > T_{b\,\mathrm{hot}}^{C}, \\ 0, & \text{otherwise,} \end{cases} \tag{4.18}$$

where $T_{b\,cold}^{C}$ is the lower temperature threshold for cold stress accumulation, set to 6℃ (Lieth et al., 2011 [35]), and $T_{b\,hot}^{C}$ is the upper threshold for heat stress, set to 36℃. The parameterisation of $b_m^{C_i}(CF)$ was derived from $TF(T_{AH})$ values calculated between November 1 and March 31 in the northernmost commercial olive-growing regions in Europe (i.e., provinces of Sondrio and Trento in northern Italy; Gambella et al., 2011 [85]) and climatic suitability estimated by species distribution models (EFSA PLH Panel, 2019 [66]; Godefroid et al., 2019 [68]): $b_{m\,sp}^{C_0} = 2.62\times10^{10}$, $b_{m\,sp}^{C_1} = 8.94\times10^{9}$, $b_{m\,sp}^{C_2} = 7.10\times10^{10}$, $b_{m\,sp}^{C_3} = 8.00\times10^{10}$, and $b_{m\,sp}^{C_4} = 1.06\times10^{11}$.

Temperature-dependent disease recovery function ($r_T^{C_i}$) Infected olive trees can recover to the previous disease stage due to the negative effects of cold and hot temperatures on the bacterial population within plants during the delay period. The recovery rate function due to temperature is defined as:

$$r_T^{C_i}\big(b_{TS}^{C_i},\, WS^{C_i},\, b_m^{c_i}\big) = \Big|\min\Big\{b_{TS}^{C_i}\big(D_{\mathrm{OY}},\, b_T^{C_i},\, b_{SI}^{C_i}\big)\, Ws^{C_i}\big(Ws_f^{C_i}\big) - b_m^{C_i}(TF)\,,\; 0\Big\}\Big|. \tag{4.19}$$

Non-systemic infection recovery function (r_n^C) In addition to the temperature-driven recovery function, newly infected olive trees can recover due to the unsuccessful establishment of bacterium infection within the xylem following new inoculations. This process is described by:

$$r_n^C\big(t,\, i^C,\, C_S,\, C_0\big) = \min\Big\{\, r_{np}^C \cdot C_0(t),\; i^C\big(t,\, \hat{n}^{C_S},\, C_S,\, V_I\big)\cdot C_S(t)\Big\}. \tag{4.20}$$

The non-systemic infection recovery parameter (r_{np}^{C}) was set at 4.19×10^{-4} h^{-1} based on preliminary simulations, with the constraint that the number of recovered plants cannot exceed the number of new infected plants occurring during the same time unit.

4.6.6 Herbaceous vegetation (H)

Herbaceous vegetation dynamics defined in Eq. (4.1a) are governed by a growth function (g^H) and a senescence function (s^H).

Growth follows the model of McCall and Bishop-Hurley (2003)[19], refined by Romera et al. (2009)[29], selected for its simplicity and effectiveness in simulating herbage production under diverse environmental conditions. The growth function g^H is defined as:

$$g^H(T_{\mathrm{AD}},\, I_{\mathrm{AD}},\, P_{\mathrm{DA}},\, \mathrm{PET},\, W,\, H) = 10\,\alpha \cdot (I_{\mathrm{AD}}) \cdot I_{\mathrm{AD}} \cdot g_T^H(T_{\mathrm{AD}}) \cdot g_W^H(P_{\mathrm{DA}},\, \mathrm{PET},\, W) \cdot g_l^H(H) \quad (4.21)$$

where:

- $\alpha(I_{\mathrm{AD}})$: net photosynthesis efficiency function (g DM MJ^{-1});
- T_{AD}: average daily temperature (°C);
- I_{AD}: incident solar radiation (MJ m^{-2} day^{-1});
- P_{DA}: daily precipitation (mm day^{-1});
- PET: potential evapotranspiration (mm day^{-1});
- W: proportion of soil water content;
- H: biomass of herbaceous vegetation (kg ha^{-1}).

The senescence rate of herbaceous vegetation is described by the temperature-dependent function s^H, which accounts for the leaf lifespan (LLS, °C) expressed in degree days and a remobilization coefficient (rem) that represents the proportion of leaf content reabsorbed during senescence:

$$s^H(T_{\mathrm{AD}}) = \max\left\{ \frac{T_{\mathrm{AD}}}{LLS}\,(1 - rem),\ 0 \right\}. \quad (4.22)$$

4.6.7 Non-susceptible shrubs and trees (N)

The dynamics of non-susceptible shrubs and trees defined in Eq. (4.1b) are governed by a logistic growth function (g^N) and a senescence function (s^N).

Biomass growth of non-susceptible shrubs and trees is assumed to occur from spring to autumn, coinciding with the period of active vegetative growth and reproductive tissue development. The growth rate function (g^N) is defined as:

$$g^N(N,\, T_{\mathrm{AH}},\, D_{\mathrm{DL}},\, D_{\mathrm{OY}}) = g_T^N(T_{\mathrm{AH}},\, D_{\mathrm{DL}},\, D_{\mathrm{OY}}) \left(1 - \frac{N}{K^N}\right). \tag{4.23}$$

where K^N is the field's carrying capacity for the vegetation compartment (kg ha^{-1}), and g_T^N is the temperature-dependent growth term adapted from Yan and Wallace (1996)[12]:

$$g_T^N\,(T_{\mathrm{AH}},\, D_{\mathrm{DL}},\, D_{\mathrm{OY}}) = \begin{cases} \max\Big\{\, g_{\max}^N - g_{sp}^N\,(T_{\mathrm{AH}} - T_{g\,\mathrm{opt}}^N)^2,\; 0\Big\}, & \text{if } g_{\mathrm{DOYmin}}^N(T_{\mathrm{AH}}) \le D_{\mathrm{OY}} \le g_{\mathrm{DOYmax}}^N(H,\, D_{\mathrm{DL}})\,, \\ 0, & \text{otherwise.} \end{cases} \tag{4.24}$$

Parameters are set as follows:

- $g_{\max}^N = 1.95 \times 10^{-4}$ h^{-1} (Pasalodos Tato et al., 2015 [44]);
- $g_{sp}^N = 1.25 \times 10^{-6}$ (dimensionless, analytically defined);
- $T_{g\,\mathrm{opt}}^N = 17.5\,$°C, the optimal growth temperature, corresponding to the average between 5 °C and 30 °C thresholds (Rossi et al., 2007 [25]; Dombrowski et al., 2022 [93]).

The parameters g_{DOYmin}^N and g_{DOYmax}^N define the start and end of the active vegetative growth period, corresponding to bud break at spring and the onset of foliage senescence at autumn, respectively. Bud break is assumed to occur simultaneously with olive trees (see Sec. 4.6.5). Following Jeong and Medvigy (2014)[40], autumnal senescence (g_{DOYmax}^N) occurs when the accumulation of cold degree-days ($CDD_{s1,critic}^N$) reaches 1348. Cold degree-day accumulation, calculated relative to a threshold temperature $T_S^N = 36.03$°C, begins once daylight duration (D_{DL}) drops below a critical value ($D_S^N = 14.4$ h) (Liu et al., 2020)[76].

At the onset of autumnal senescence, biomass growth stops, and the deciduous fraction of the vegetation begins to lose foliage. Senescence is described as (adapted from Dufrêne et al., 2005 [22]):

$$s^N(D_{\mathrm{DL}}) = \left[\left(\frac{D_{\mathrm{DL}} - D_{\min}^N}{D_{\mathrm{ts}}^N - D_{\min}^N}\right)^{S_\ell^N} - 1\right] \cdot \left(1 - s_e^N\right) \cdot \max\left\{\frac{N - N_e}{N_{\mathrm{ts}} - N_e},\, 0\right\} \tag{4.25}$$

where:

- $D_{\min}^N$: daylight duration of the shortest day of the year (hours);
- D_{ts}^N: daylight duration of the day of senescence onset (hours);
- S_ℓ^N: leaf ageing parameter (set equal to 0.4);

- s_e^N: fraction of evergreen biomass within the N vegetation compartment (set at 0.9);
- considering that most of the biomass consists of trunks, branches, and twigs, and that the majority of species in the study area are evergreen. N_e denotes the biomass of the evergreen non-susceptible shrubs and trees, and N_{ts} is the N biomass at the time of onset of senescence (ts) of the current year.

This formulation prevents evergreen biomass from reduction during senescence.

4.6.8 Reservoir plants (R_S and R_I)

The dynamics of susceptible (R_S) and infected (R_I) reservoir compartments defined in equations (4.1-c) and (4.1-d) are governed by a logistic growth function (g^R) and a senescence function (S^R).

The biomass growth rate (g^R) of R_S and R_I vegetation compartments is modelled using a function similar to that given in (4.23):

$$g^R(R_S,\, R_I,\, T_{\text{AH}},\, D_{\text{DL}},\, D_{\text{OY}}) = g_T^R(T_{\text{AH}},\, D_{\text{DL}},\, D_{\text{OY}})\, \Big(1 - \frac{R_S + R_I}{K^R}\Big). \tag{4.26}$$

where g_T^R is defined analogously to (4.24). The senescence rate function s^R is modelled similarly to (4.25):

$$s^R(D_{\text{DL}}) = \left[\left(\frac{D_{\text{DL}} - D_{\text{min}}^R}{D_{\text{ts}}^R - D_{\text{min}}^R}\right)^{S_\ell^R} - 1\right] \cdot \big(1 - s_e^R\big) \cdot \max\left\{\frac{R_S + R_I - R_e}{R_{\text{ts}} - R_e},\, 0\right\} \tag{4.27}$$

where:

- R_e: biomass of the evergreen reservoir plants (kg ha^{-1});
- R_{ts}: total biomass of reservoir vegetation at the time of senescence onset (kg ha^{-1});
- D_{min}^R, D_{ts}^R, S_ℓ^R, and s_e^R are set equal to the corresponding parameters defined in Section 4.6.7.

The transfer from R_S to R_I is modelled by an infection function (i^R), originally developed for olive trees (see Section 4.6.5) and assumed applicable to reservoir plants as well.

The recovery process of reservoir plants accounts for two components: a temperature-dependent disease recovery function (r_T^R) and a non-systemic infection recovery function (r_n^R). Infected reservoir biomass can recover from infection due to the negative effects of

cold temperatures on the bacterial population within plants during winter. The recovery rate is defined as (Giménez-Romero et al., 2022 [94]):

$$r_T^R(t,\, T_{\mathrm{AH}},\, D_{\mathrm{OY}}) = \begin{cases} 1 - \dfrac{r_{sp}^R}{r_{sp}^R + \mathrm{CDD}^3(T_{\mathrm{AH}})}, & \text{if } D_{\mathrm{OY}} = \text{April 1}, \\ 0, & \text{otherwise} \end{cases} \tag{4.28}$$

where r_{sp}^R is a dimensionless shape parameter, and $CDD(T_{AH})$ represents the cumulative cold degree-days, calculated as the sum of hourly temperatures below the threshold $T_{b\,cold}^R$. Cumulative cold degree-days are calculated from November 1 of the year preceding the simulation until March 31 of the simulation year. For modelling purposes, recovery is assumed to occur instantaneously at the end of winter, on April 1. Parameters are assumed equal to those used for olive trees at the C_2 stage (see Section 4.6.5): $r_{sp}^R = 7.94 \times 10^{10}$, and $T_{b\,cold}^R = 6$℃.

In addition to the temperature-driven recovery function, newly infected reservoir plants can recover due to the unsuccessful establishment of bacterium infection within the xylem following new inoculations. This process is described by:

$$r_n^R\big(t,\, i^R,\, R_S,\, R_I\big) = \min\Big\{ r_{np}^R \cdot R_I(t),\; i^R\big(t,\, \hat{n}^{\,R_S},\, R_S,\, V_I\big) \cdot R_S(t) \Big\}. \tag{4.29}$$

The local recovery rate (r_{np}^R) was set at 4.19×10^{-4} h^{-1} based on preliminary simulations, with the constraint that the recovered biomass cannot exceed the new infected biomass occurring during the same time unit.

4.7 Model calibration and meteorological data

Given the low prevalence of *Xf*-susceptible plants in the region, 90% of the non-olive woody vegetation was assumed to consist of non-susceptible species. Olive tree density reflected that of the corresponding monitored groves. The resulting values of K^N and K^R, and olive tree populations are reported in Table 3. Herbaceous vegetation was assumed to uniformly cover all simulated fields. All simulations were performed at a spatial resolution of one hectare.

Initial conditions were set to reflect realistic field conditions. Herbaceous biomass (H) was fixed at 550 kg ha^{-1}, while non-susceptible shrubs and trees (N), and reservoir plants (R_S and R_I) started at 80% of their carrying capacities, accounting for deciduous biomass loss from the previous autumn. Infected reservoir plants (R_I) were assumed to constitute 10% of the initial reservoir biomass. The initial distribution of olive trees across disease stages was estimated based on historical data of prevalence (Table 4). The initial preimaginal population of *P. spumarius* (P) was set at 2.5×10^5 insects per hectare (≈ 25 insects m^{-2}), based on nymphal and adult monitoring data collected in 2019 within 4 km of the surveyed groves.

The susceptibility of olive trees to *Xf* infection (i_{sp}^{C}), resulted from model calibration, was estimated at 0.01, indicating a 100-fold reduction in the infection rate of individual infected vectors estimated in the model. The non-systemic disease recovery rate of newly infected olive trees (r_{np}^{C}) was set at 2.09×10^{-4} h^{-1}, meaning that up to 0.5% of early-stage infections (within disease stage C_0) failed to become established in host every day. This recovery rate was also applied to reservoir plants (r_{np}^{R}). Figures 25 and 26 show the meteorological conditions used for model calibration and validation.

Table 3: Carrying capacities of non-susceptible shrubs and trees (K^N) and reservoir plants (K^R), total number of olive trees, and semi-saturation of the Monod functional response (λ^H, $\lambda^N, \lambda^{R_S}, \lambda^{R_I}$, and λ^{C_S} to λ^{C_5}) assumed for each host plant compartment across all simulated olive groves.

Olive field	K^N (kg ha^{-1})	K^R (kg ha^{-1})	Number of olive trees per ha	λ^H (kg ha^{-1})	λ^N, λ^{R_S}, λ^{R_I} (kg ha^{-1})	λ^{C_S} *to* λ^{C_5} (trees ha^{-1})
Calibration fields						
1	1000	110	78	610	18920	39
2	332	37	89	610	18920	45
3	332	37	84	610	18920	42
4	332	37	93	610	18920	47
5	332	37	64	610	18920	32
Validation fields						
6	332	37	98	610	18920	49
7	332	37	90	610	18920	46
8	332	37	111	610	18920	56
9	665	74	97	610	18920	49
10	332	37	137	610	18920	69
11	332	37	74	610	18920	37
12	332	37	107	610	18920	54
13	332	37	114	610	18920	57
14	332	37	215	610	18920	108
15	1000	110	152	610	18920	76
16	2330	260	104	610	18920	52

Table 4: Initial conditions of model compartments for the olive groves used in model calibration and validation.

Olive field	H	N	R_S	R_I	P	V_S	V_I	C_S	C_0	C_1	C_2	C_3	C_4	C_5
	kg ha^{-1}				Insects ha^{-1}			Trees ha^{-1}						
Calibration fields														
1	550	720	70	8	250,000	0	0	27	31	12	8	0	0	0
2	550	240	25	3	250,000	0	0	9	53	13	13	0	0	0
3	550	240	25	3	250,000	0	0	13	42	21	8	0	0	0
4	550	240	25	3	250,000	0	0	19	47	23	5	0	0	0
5	550	240	25	3	250,000	0	0	0	48	6	3	0	0	0
Validation fields														
6	550	240	25	3	250,000	0	0	0	39	54	5	0	0	0
7	550	240	25	3	250,000	0	0	0	9	55	12	0	0	0
8	550	240	25	3	250,000	0	0	0	6	44	33	9	0	0
9	550	480	50	5	250,000	0	0	0	15	49	29	6	0	0
10	550	240	25	3	250,000	0	0	0	75	48	14	0	0	0
11	550	240	25	3	250,000	0	0	0	15	37	19	0	0	0
12	550	240	25	3	250,000	0	0	0	23	38	11	5	0	0
13	550	240	25	3	250,000	0	0	0	129	75	11	0	0	0
14	550	240	25	3	250,000	0	0	0	106	23	23	0	0	0
15	550	720	70	8	250,000	0	0	0	47	47	10	0	0	0
16	550	1680	170	18	250,000	0	0	0	47	47	10	0	0	0

5

Two simplified mathematical models for the spread of *Xf* in olive trees

In the previous chapter, we developed a model that is very accurate from the biological point of view. However, its complexity prevents us from studying its well-posedness. In this chapter, we develop two simplified versions of the model of Ch. 4, which can be explored from a mathematical point of view. A third model, more complex than these ones, will be presented and studied in Chapter 6.

In more detail, this chapter combines a short mathematical background with two compartmental models developed within the BeXyl project. In the opening subsection, we recall some useful mathematical notions.

We then introduce a first model with eight compartments (four plant and four insect compartments), in which the pathogen is not yet present. This model is used to formalise the idea of dynamic vector preference: we prescribe fixed preference parameters, describing the fraction of vectors that would choose each plant type in an ideal situation where all hosts are equally available, and we then let the effective contact frequencies evolve in time according to the changing availability of the different plant types. In this way, we can quantify how the interplay between preference and host availability shapes the distribution of vector feeding events.

The second model, still formulated as a system of ordinary differential equations, focuses on crop plants and vectors only, with three crop compartments and two vector compartments. Here the bacterium is reintroduced and crop plants are split into susceptible and two infected classes, so that we can describe the disease progression within the crop. This model is specifically designed to investigate how different parameters influence the long-time (asymptotic) proportion of infected crops and infectious vectors.

These models are exploratory precursors of the model presented in the next chapter, which will account both for the dynamics induced by vector preferences, combined with host availability, and for how disease spread varies as a consequence of these mechanisms.

5.1 Background Theorems and Definitions

5.1.1 Lyapunov stability and its first criterion

Consider the system of autonomous differential equations

$$\dot{\mathbf{x}}(t) = \mathbf{F}(\mathbf{x}(t)), \tag{5.1}$$

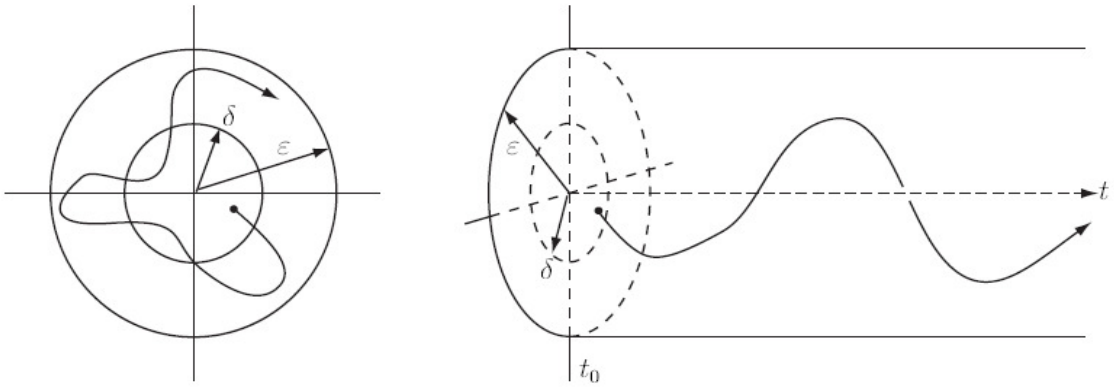


Figure 37: Visual example for a better understanding of the definition of a Lyapunov stable equilibrium point. If every trajectory of points starting inside the inner circle is entirely confined within the bigger circle, the center of the circles is a stable equilibrium point for Lyapunov. Source: [56]

where $\mathbf{x}(t) \in \mathcal{D} \subseteq \mathbb{R}^n$ and $\mathbf{F} : \mathcal{D} \to \mathbb{R}^n$ is continuously differentiable, and a point $\tilde{\mathbf{x}}$ such that $\mathbf{F}(\tilde{\mathbf{x}}) = \mathbf{0}$ is an equilibrium point for the system. We say that:

- $\tilde{\mathbf{x}}$ is *Lyapunov stable* if for every neighborhood U of $\tilde{\mathbf{x}}$ there exists a neighborhood $V \subseteq U$ such that orbits starting from points inside V remain confined in U for all $t \geq 0$. Equivalently, if $\forall \epsilon > 0 \ \exists \ \delta = \delta(\epsilon) > 0$ such that $\|\mathbf{x}(0) - \tilde{\mathbf{x}}\| < \delta \implies \|\mathbf{x}(t) - \tilde{\mathbf{x}}\| < \epsilon, \ \forall t \geq 0$.

- $\tilde{\mathbf{x}}$ is said to be *attractive* if there exists a neighborhood U of $\tilde{\mathbf{x}}$ such that for every orbit $\mathbf{x}(t)$ starting from a point inside U:

$$\lim_{t \to +\infty} \mathbf{x}(t) = \tilde{\mathbf{x}}.$$

  The largest neighborhood U for which this occurs is called the *basin of attraction.*

- $\tilde{\mathbf{x}}$ is said to be *asymptotically stable* if it is stable and attractive.
  I.e., if there exists $\delta > 0$ such that $\|\mathbf{x}(0) - \tilde{\mathbf{x}}\| < \delta \implies \lim_{t \to +\infty} \mathbf{x}(t) = \tilde{\mathbf{x}}$.

- $\tilde{\mathbf{x}}$ is said to be *exponentially stable* if there exist $\alpha, \beta, \delta > 0$ such that
  $\|\mathbf{x}(0) - \tilde{\mathbf{x}}\| < \delta \implies \|\mathbf{x}(t) - \tilde{\mathbf{x}}\| \leq \alpha \|\mathbf{x}(0) - \tilde{\mathbf{x}}\| e^{-\beta t}, \quad \forall t \geq 0$.

- $\tilde{\mathbf{x}}$ is said to be *unstable* if there exists a neighborhood U of $\tilde{\mathbf{x}}$ such that, for every neighborhood V of $\tilde{\mathbf{x}}$ with $V \subseteq U$, there exist an initial condition $\mathbf{x}_0 \in V$ and a corresponding trajectory $\mathbf{x}(t)$, with $\mathbf{x}(0) = \mathbf{x}_0$, such that $\mathbf{x}(t) \notin U$ for some $t \geq 0$.

Now, given Eq. (5.1), with $\tilde{\mathbf{x}}$ an equilibrium point, the linearization of the system in its neighborhood is obtained by considering the perturbed trajectory:

$$\mathbf{x}(t) = \tilde{\mathbf{x}} + \delta\mathbf{x}(t),$$

and substituting it into the equation:

$$\dot{\mathbf{x}} = \dot{\delta\mathbf{x}} = \mathbf{F}(\tilde{\mathbf{x}} + \delta\mathbf{x}(t)) = \mathbf{F}(\tilde{\mathbf{x}}) + \left.\frac{\partial \mathbf{F}}{\partial \mathbf{x}^\top}\right|_{\mathbf{x}=\tilde{\mathbf{x}}} \delta\mathbf{x} + \mathcal{O}(\|\delta\mathbf{x}\|^2).$$

Then, neglecting terms of order higher than the first, the linear differential system

$$\dot{\mathbf{v}} = A(\tilde{\mathbf{x}})\mathbf{v}, \text{with } A(\tilde{\mathbf{x}}) = \left.\frac{\partial \mathbf{F}}{\partial \mathbf{x}^\top}\right|_{\mathbf{x}=\tilde{\mathbf{x}}}$$

is the linearization of system (5.1).

Lyapunov's first criterion of stability establishes that:

- if the equilibrium point $\mathbf{v} = \mathbf{0}$ of the linearized system $\dot{\mathbf{v}} = A(\tilde{\mathbf{x}})\mathbf{v}$ is asymptotically stable, then $\tilde{\mathbf{x}}$ is an asymptotically stable equilibrium point of the non-linear system (5.1);
- if $\mathbf{v} = 0$ is unstable, then $\tilde{\mathbf{x}}$ is an unstable point of the non-linear system (5.1);
- if $\mathbf{v} = 0$ is stable but not asymptotically stable, then nothing can be concluded about the point $\tilde{\mathbf{x}}$ for the non-linear system (5.1).

5.1.2 Lyapunov's theorem

Lyapunov's theorem is one of the most powerful and widely used tools in the stability analysis of dynamical systems. Named after the Russian mathematician Aleksandr Mikhailovich Lyapunov, who formulated it in 1892, the theorem provides a criterion for determining the stability of an equilibrium point without solving the system's differential equation.

The theorem concerns autonomous dynamical systems described by the differential equation (5.1), for which $\mathbf{x} = \mathbf{0}$ is an equilibrium point. The stability of this point can be determined through a Lyapunov function $L(\mathbf{x}(t))$, which must meet the following conditions:

- $L(\mathbf{x})$ is positive definite, meaning $L(\mathbf{x}) > 0$ for all $\mathbf{x} \neq \mathbf{0}$ and $L(\mathbf{0}) = \mathbf{0}$.
- The time derivative of L, given by $\dot{L}(\mathbf{x}(t)) = \nabla_x L(\mathbf{x}(t)) \cdot \mathbf{F}(\mathbf{x}(t))$, is negative semidefinite, i.e., $\dot{L}(\mathbf{x}) \leq 0$ for all $\mathbf{x} \in \mathbb{R}^n$.

The theorem is particularly useful as it allows for the assertion of system stability without necessarily knowing the system's solutions. It is employed in various fields such as control engineering, physics, biology, and economics to analyse the stability of dynamical systems modelled through differential equations.

Depending on the behaviour of $\dot{L}(\mathbf{x})$, the theorem distinguishes between:

- **Asymptotic Stability:** If $\dot{L}(\mathbf{x})$ is negative definite ($\dot{L}(\mathbf{x}) < 0$ for all $\mathbf{x} \neq \mathbf{0}$), then the equilibrium point is asymptotically stable.
- **Neutral Stability:** If $\dot{L}(\mathbf{x})$ is negative semidefinite but not definitively negative (there exists $\mathbf{x} \neq \mathbf{0}$ such that $\dot{L}(\mathbf{x}) = \mathbf{0}$), the equilibrium point is stable but not necessarily attractive.

Despite its utility, Lyapunov's theorem has limitations: e.g., a challenge lies in the selection or construction of a suitable Lyapunov function, which is not always possible for all dynamical systems. Despite this, Lyapunov's theorem is a fundamental tool in the stability analysis of dynamical systems, offering a rigorous and powerful methodology for ensuring the safety and reliability of dynamic models in many scientific and engineering applications.

5.1.3 Fixed Point Method

The fixed point method is a fundamental technique in numerical analysis for approximating the roots of a function. A point x is considered a fixed point for f if $x = f(x)$. The basic idea is to transform a problem of finding roots into a problem of finding a fixed point. To apply the fixed point method, one reformulates the original equation $g(x) = 0$ into $x = f(x)$, ensuring that the right-hand side function f is well-defined and continuous on the chosen interval. The iterative scheme is then given by:

$$x_{n+1} = f(x_n),$$

where x_n is the approximation at the nth iteration. The process is repeated until the change between successive iterations is within a predefined tolerance, indicating convergence to a fixed point.

For the method to converge, the function f should satisfy specific conditions:

- f should be continuous on the interval of interest.
- The derivative $f'(x)$ should exist and satisfy $|f'(x)| < 1$ for all x in the interval, ensuring that the function is a contraction mapping.

These conditions help ensure that the sequence generated by the iterative process converges to a unique fixed point within the interval.

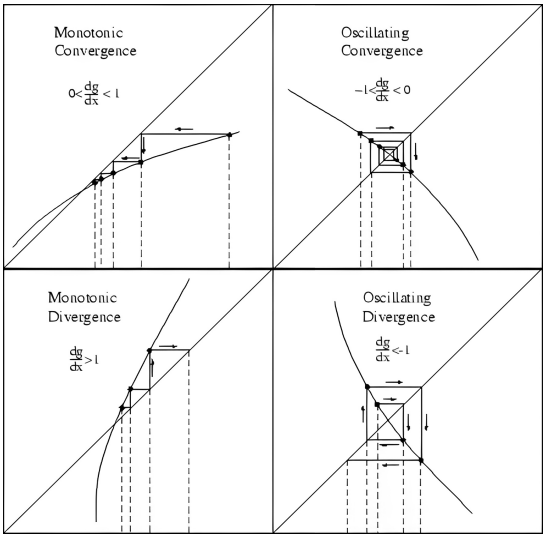


Figure 38: Behaviours of the progression of an applied Fixed Point Method depending on the derivative of the function within a neighborhood of the solution.
Source: www.ilovemethods.blogspot.com

The fixed point method can be particularly useful in computing equilibrium points of ordinary differential equations (ODEs).

This approach is particularly useful in non-linear dynamics, where analytical solutions are intractable, but numerical approximations can provide significant insights into the system's behaviour at its equilibrium states.

5.2 First simplified Model

5.2.1 Introduction

In this model the epidemiological component of system (4.1) is suppressed and vectors interact with plants only through feeding preferences. The resulting formulation is a system of eight ordinary differential equations without delay terms. It focuses on the feedback between host availability and vector redistribution among plant types.

From a biological viewpoint, we distinguish four plant classes: herbaceous vegetation (H), non-susceptible hosts (N), reservoir plants (R), and crop plants (C). Herbaceous, non-susceptible and reservoir vegetation are assumed to undergo logistic-type growth with a carrying capacity, while crop biomass is taken as constant in time. On the vector side, we model a single physiological stage (adults) and split the vector population into four compartments V_H, V_N, V_R, and V_C, representing the number of vectors currently located on plants of type H, N, R, and C, respectively.

In this setting there is no pathogen and no distinction between susceptible and in-

fected plants or vectors. The aim of this model is therefore not to reproduce disease dynamics, but to isolate and analyse the *preference functions* that govern how vectors distribute themselves among the available plant types, as a function of plant biomass and intrinsic palatability parameters. This provides a controlled framework to understand how landscape composition and plant quality shape vector pressure on crops, independently of infection processes.

5.2.2 Model #1: structure and derivation

The state variables of Model #1 are

$$H(t),\ N(t),\ R(t),\ C(t),\ V_H(t),\ V_N(t),\ V_R(t),\ V_C(t),$$

and represent, respectively, the biomasses (per unit area) of herbaceous, non-susceptible, reservoir and crop vegetation, and the numbers of adult vectors currently present on each of these four plant types.

For notational convenience, we now omit the explicit dependence on time and write $H, N, R, C, V_H, V_N, V_R, V_C$ in place of $H(t), N(t), R(t), C(t), V_H(t), V_N(t), V_R(t), V_C(t)$. The temporal evolution of these variables is described by the equations

$$\dot{H} = -m_H \cdot H + g_H \cdot H \cdot \left(1 - \frac{H}{K_H}\right), \tag{5.2}$$

$$\dot{N} = -m_N \cdot N + g_N \cdot N \cdot \left(1 - \frac{N}{K_N}\right), \tag{5.3}$$

$$\dot{R} = -m_R \cdot R + g_R \cdot R \cdot \left(1 - \frac{R}{K_R}\right), \tag{5.4}$$

$$\dot{C} = 0, \tag{5.5}$$

$$\dot{V}_H = -m_V \cdot V_H + f \cdot V_H + P_H \cdot (V_N + V_R + V_C) - (1 - P_H) \cdot V_H, \tag{5.6}$$

$$\dot{V}_N = -m_V \cdot V_N + f \cdot V_N + P_N \cdot (V_H + V_R + V_C) - (1 - P_N) \cdot V_N, \tag{5.7}$$

$$\dot{V}_R = -m_V \cdot V_R + f \cdot V_R + P_R \cdot (V_H + V_N + V_C) - (1 - P_R) \cdot V_R, \tag{5.8}$$

$$\dot{V}_C = -m_V \cdot V_C + f \cdot V_C + P_C \cdot (V_H + V_N + V_R) - (1 - P_C) \cdot V_C, \tag{5.9}$$

endowed with initial conditions

$$\begin{aligned} &H(0) = H_0, \quad N(0) = N_0, \quad R(0) = R_0, \quad C(0) = C_0, \\ &V_H(0) = V_{H0}, \quad V_N(0) = V_{N0}, \quad V_R(0) = V_{R0}, \quad V_C(0) = V_{C0}. \end{aligned} \tag{5.10}$$

Plant dynamics. The first three equations describe the dynamics of the herbaceous, non-susceptible and reservoir vegetation. For each $X \in \{H, N, R\}$ we have

$$\dot{X} = -m_X \cdot X + g_X \cdot X \cdot \left(1 - \frac{X}{K_X}\right),$$

where $m_X \geq 0$ is the per capita mortality (or loss) rate, $g_X \geq 0$ is the intrinsic growth rate, and $K_X > 0$ is a carrying capacity that limits biomass growth. This is a logistic-type equation with an additional constant mortality term. The crop compartment C is assumed to have constant biomass over the time horizon of interest, so that

$$\dot{C} = 0, \qquad C(t) \equiv C_0.$$

Vector dynamics. The vector population is split into four sub-populations according to the plant type on which individuals are currently feeding. For each $X \in \{H, N, R, C\}$, the variable $V_X(t)$ represents the number of adult vectors present on plants of type X at time t.

Vectors are subject to three processes:

- a mortality rate $m_V \geq 0$;
- reproduction at per capita rate $f \geq 0$, applied uniformly to all vector compartments;
- redistribution among plant types, driven by the preference functions P_X.

For instance, in the equation for V_H, the term $P_H(V_N + V_R + V_C)$ represents the influx of vectors arriving on herbaceous vegetation from the other plant types, proportional to the total number of vectors currently not on H and to the preference for H, while the term $(1 - P_H)V_H$ represents the outflow of vectors leaving H towards other plant types. Analogous interpretations hold for the equations of V_N, V_R and V_C.

Preference functions. The preference functions P_X encode the relative attractiveness

of each plant type $X \in \{H, N, R, C\}$ to vectors. They are defined by

$$\begin{aligned}
P_H &= \frac{\dfrac{p_H \cdot H}{\lambda + H}}{\dfrac{p_H \cdot H}{\lambda + H} + \dfrac{p_N \cdot N}{\lambda + N} + \dfrac{p_R \cdot R}{\lambda + R} + \dfrac{p_C \cdot C}{\lambda + C}}, \\
P_N &= \frac{\dfrac{p_N \cdot N}{\lambda + N}}{\dfrac{p_H \cdot H}{\lambda + H} + \dfrac{p_N \cdot N}{\lambda + N} + \dfrac{p_R \cdot R}{\lambda + R} + \dfrac{p_C \cdot C}{\lambda + C}}, \\
P_R &= \frac{\dfrac{p_R \cdot R}{\lambda + R}}{\dfrac{p_H \cdot H}{\lambda + H} + \dfrac{p_N \cdot N}{\lambda + N} + \dfrac{p_R \cdot R}{\lambda + R} + \dfrac{p_C \cdot C}{\lambda + C}}, \\
P_C &= \frac{\dfrac{p_C \cdot C}{\lambda + C}}{\dfrac{p_H \cdot H}{\lambda + H} + \dfrac{p_N \cdot N}{\lambda + N} + \dfrac{p_R \cdot R}{\lambda + R} + \dfrac{p_C \cdot C}{\lambda + C}}.
\end{aligned} \tag{5.11}$$

Here $p_X \in (0, 1]$ is a constant weight representing the maximal preference for plant type X when it is abundantly available, with

$$p_H + p_N + p_R + p_C = 1, \tag{5.12}$$

while $\lambda \geq 0$ is a "half-saturation" constant controlling how fast the preference saturates with increasing biomass. The Monod-type structure (see 4.6.1) captures the idea that preference increases with biomass. By construction, $0 \leq P_X \leq 1$ and

$$P_H + P_N + P_R + P_C = 1, \tag{5.13}$$

so that the preference P_X can be interpreted as time-dependent fractions of the vector population allocating their feeding activity to each plant type. If $\lambda = 0$ we define $P_H = p_H$, $P_N = p_N$, $P_R = p_R$, and $P_C = p_C$.

5.2.3 Analysis of Model #1

We aim to analyse existence, uniqueness, and continuous dependence on initial data of the Cauchy problem (5.2)-(5.10). Qualitative behaviour of the solution will emerge during the analysis.

Lemma 5.1 (Plant dynamics: explicit solutions and non-negativity)**.** *Let $X(t)$ denote any of the plant compartments $H(t)$, $N(t)$, or $R(t)$ in system (5.2)–(5.10), and consider the scalar Cauchy problem*

$$\dot{X}(t) = -m_X \cdot X(t) + g_X \cdot X(t) \cdot \Big(1 - \frac{X(t)}{K_X}\Big), \qquad X(t_0) = X_0 \geq 0, \tag{5.14}$$

with parameters $g_X \geq 0$, $K_X > 0$, $m_X \geq 0$, and set

$$M := \max\{X_0, K_X\}.$$

Then:

1. *There exists a unique global solution $X \in C^1([t_0, +\infty); \mathbb{R})$ of (5.14).*
2. *If $g_X > 0$ and $g_X \neq m_X$, setting $r_X := g_X - m_X$ and $a_X := g_X/K_X$, the solution is given explicitly by*

$$X(t) = \frac{1}{\dfrac{a_X}{r_X} + \Big(\dfrac{1}{X_0} - \dfrac{a_X}{r_X}\Big)e^{-r_X(t-t_0)}}, \qquad t \geq t_0,\ X_0 > 0. \tag{5.15}$$

   If $g_X = m_X > 0$, then

$$X(t) = \frac{1}{\dfrac{g_X}{K_X}(t - t_0) + \dfrac{1}{X_0}}, \qquad t \geq t_0,\ X_0 > 0. \tag{5.16}$$

   If $g_X = 0$, then

$$X(t) = X_0 e^{-m_X(t-t_0)}, \qquad t \geq t_0,\ X_0 > 0. \tag{5.17}$$

   In all cases, the formula extends continuously to $X_0 = 0$ by $X(t) \equiv 0$.

3. *For every $X_0 \geq 0$ the solution satisfies*

$$0 \leq X(t) \leq M \quad \text{for all } t \geq t_0.$$

   In particular

$$X_0 = 0 \implies X(t) \equiv 0, \qquad X_0 > 0 \implies 0 < X(t) \leq M \text{ for all } t \geq t_0,$$

   and if $0 \leq X_0 \leq K_X$ then $0 \leq X(t) \leq K_X$ for all $t \geq t_0$.

Moreover, the crop compartment satisfies $\dot{C}(t) = 0$, $C(t_0) = C_0 \geq 0$, so that $C(t) \equiv C_0 \geq 0$ for all $t \geq t_0$.

Proof. We first note that the right-hand side of (5.14) is a polynomial in X, hence it is locally Lipschitz on $\mathbb{R}$. By the Cauchy–Lipschitz theorem, for any $X_0 \in \mathbb{R}$ there exists a unique maximal solution $X \in C^1(I;\mathbb{R})$ on some interval I containing t_0. We now prove (2) and (3); the boundedness in (3) will then imply that $I = [t_0, +\infty)$, thus completing (1).

Proof of (2). If $g_X > 0$ and $g_X \neq m_X$, rewriting (5.14) as

$$\dot{X} = r_X X - a_X X^2, \qquad r_X = g_X - m_X,\ a_X = \frac{g_X}{K_X},$$

one recognises the logistic equation. The standard Bernoulli reduction (or direct separation of variables) yields (5.15) for $X_0 > 0$, and the expression extends continuously to $X_0 = 0$ by setting $X(t) \equiv 0$.

If $g_X = m_X > 0$, (5.14) reduces to

$$\dot{X} = -\frac{g_X}{K_X} X^2,$$

which is separable and gives (5.16) for $X_0 > 0$, extended continuously to $X_0 = 0$ by $X \equiv 0$. If $g_X = 0$, (5.14) reduces to $\dot{X} = -m_X X$, whose solution is (5.17), again extended continuously to $X_0 = 0$ by $X \equiv 0$. This proves (2).

Proof of (3). If $X_0 = 0$, then in all parameter cases the explicit solutions in (2) reduce to $X(t) \equiv 0$ for $t \geq t_0$, and clearly $0 \leq X(t) \leq M$.

Assume now $X_0 > 0$. We first show that $X(t) > 0$ for all $t \geq t_0$.

- If $g_X = 0$, then (5.17) gives $X(t) > 0$.
- If $g_X = m_X > 0$, then (5.16) gives

  $$X(t) = \frac{1}{\dfrac{g_X}{K_X}(t - t_0) + \dfrac{1}{X_0}},$$

  and the denominator is strictly positive for all $t \geq t_0$, hence $X(t) > 0$.
- If $g_X > 0$ and $g_X \neq m_X$, denote by $D(t)$ the denominator in (5.15):

  $$D(t) = \frac{a_X}{r_X} + \Big(\frac{1}{X_0} - \frac{a_X}{r_X}\Big) e^{-r_X (t - t_0)} = \frac{a_X}{r_X}\Big(1 - e^{-r_X (t - t_0)}\Big) + \frac{1}{X_0} e^{-r_X (t - t_0)}.$$

  If $r_X > 0$, then $\frac{a_X}{r_X} > 0$ and $1 - e^{-r_X (t - t_0)} \geq 0$, so the first term is non-negative, and the second term is strictly positive. If $r_X < 0$, then $\frac{a_X}{r_X} < 0$ and $1 - e^{-r_X (t - t_0)} \leq 0$, so again the first term is non-negative and the second term strictly positive. In both cases $D(t) > 0$ for all $t \geq t_0$, hence $X(t) = 1/D(t) > 0$.

Thus, for $X_0 > 0$ we have $X(t) > 0$ for every $t \geq t_0$.

We now show the upper bound $X(t) \leq M$.

- If $g_X = 0$ or $g_X = m_X > 0$, the explicit formulas (5.17)–(5.16) clearly give a non-increasing solution in t, so

$$0 < X(t) \leq X_0 \leq M \quad \text{for all } t \geq t_0.$$

- If $g_X > 0$ and $g_X \neq m_X$, from (5.14) we can write

$$\dot{X}(t) = -m_X X(t) + g_X X(t)\Big(1 - \frac{X(t)}{K_X}\Big).$$

  For every $X \geq K_X$ we have $1 - X/K_X \leq 0$, hence

$$\dot{X}(t) \leq -m_X X(t) \leq 0 \quad \text{whenever } X(t) \geq K_X.$$

  Thus, if $X_0 \geq K_X$ the solution is non-increasing from t_0 on and $X(t) \leq X_0 = M$ for all $t \geq t_0$. If instead $0 < X_0 < K_X$ and there existed $t_1 > t_0$ with $X(t_1) > K_X$, by continuity we could define

$$t^* := \inf\{t \geq t_0 : X(t) = K_X\},$$

  so that $X(t) \leq K_X$ on $[t_0, t^*]$ and $X(t^*) = K_X$. But then $\dot{X}(t^*) \leq 0$ by the above inequality, which contradicts the fact that X should cross the level K_X upwards at t^*. Hence $X(t) \leq K_X \leq M$ for all $t \geq t_0$ also in this case.

Summarising, for $X_0 > 0$ we have

$$0 < X(t) \leq M \quad \text{for all } t \geq t_0,$$

and together with the case $X_0 = 0$ this yields (3). The special case $0 \leq X_0 \leq K_X$ follows immediately, since then $M = K_X$.

Finally, since $0 \leq X(t) \leq M$ for all t in the maximal interval I and the right-hand side of (5.14) is locally Lipschitz on bounded sets, the solution can be extended beyond any finite endpoint of I. Therefore $I = [t_0, +\infty)$ and (1) holds. For the crop compartment we have $\dot{C} = 0$ and $C(t_0) = C_0 \geq 0$, so $C(t) \equiv C_0 \geq 0$ for all $t \geq t_0$. □

5.2.4 Local existence and uniqueness of solution

We begin by introducing the abstract formulation of the Cauchy problem (5.2)-(5.10).

Let $t_0 \geq 0$ be a given initial time and $T > t_0$ a finite final time. We denote by

$$J = (t_0, T)$$

the corresponding time interval. The initial values for the plant and vector compartments are

$$H_0,\ N_0,\ R_0,\ C_0,\ V_{H0},\ V_{N0},\ V_{R0},\ V_{C0} \in [0, +\infty),$$

with the plant biomasses not all simultaneously zero, i.e.

$$H_0 + N_0 + R_0 + C_0 > 0.$$

We collect the state variables into the vector

$$\mathbf{x}(t) = \begin{bmatrix} H(t) \\ N(t) \\ R(t) \\ C(t) \\ V_H(t) \\ V_N(t) \\ V_R(t) \\ V_C(t) \end{bmatrix}, \qquad \mathbf{x}_0 = \begin{bmatrix} H_0 \\ N_0 \\ R_0 \\ C_0 \\ V_{H0} \\ V_{N0} \\ V_{R0} \\ V_{C0} \end{bmatrix}. \tag{5.18}$$

For notational convenience, we define the denominator of the preference functions as

$$\Sigma(t) = \frac{p_H \cdot H(t)}{\lambda + H(t)} + \frac{p_N \cdot N(t)}{\lambda + N(t)} + \frac{p_R \cdot R(t)}{\lambda + R(t)} + \frac{p_C \cdot C(t)}{\lambda + C(t)}, \tag{5.19}$$

so that the time-dependent preference functions can be written as

$$P_H(t) = \frac{\dfrac{p_H \cdot H(t)}{\lambda + H(t)}}{\Sigma(t)}, \quad P_N(t) = \frac{\dfrac{p_N \cdot N(t)}{\lambda + N(t)}}{\Sigma(t)}, \quad P_R(t) = \frac{\dfrac{p_R \cdot R(t)}{\lambda + R(t)}}{\Sigma(t)}, \quad P_C(t) = \frac{\dfrac{p_C \cdot C(t)}{\lambda + C(t)}}{\Sigma(t)}. \tag{5.20}$$

We introduce the non-linear vector function $\mathbf{f} : \mathbb{R}^8 \to \mathbb{R}^8$ by

$$\mathbf{f}(\mathbf{x}(t)) = \begin{bmatrix} -m_H \cdot H + g_H \cdot H \cdot \left(1 - \dfrac{H}{K_H}\right) \\ -m_N \cdot N + g_N \cdot N \cdot \left(1 - \dfrac{N}{K_N}\right) \\ -m_R \cdot R + g_R \cdot R \cdot \left(1 - \dfrac{R}{K_R}\right) \\ 0 \\ -m_V \cdot V_H + f \cdot V_H + P_H \cdot (V_N + V_R + V_C) - (1 - P_H) \cdot V_H \\ -m_V \cdot V_N + f \cdot V_N + P_N \cdot (V_H + V_R + V_C) - (1 - P_N) \cdot V_N \\ -m_V \cdot V_R + f \cdot V_R + P_R \cdot (V_H + V_N + V_C) - (1 - P_R) \cdot V_R \\ -m_V \cdot V_C + f \cdot V_C + P_C \cdot (V_H + V_N + V_R) - (1 - P_C) \cdot V_C \end{bmatrix}, \tag{5.21}$$

where the components P_H, P_N, P_R, P_C are given by (5.20) if $\lambda > 0$, are equal to p_H, p_N, p_R, p_C if $\lambda = 0$. The coefficients $p_H, p_N, p_R, p_C \in (0, 1]$ are given fixed values that simulate the probability of an insect feeding on one type of a plant, rather than another, in the event of having any type of plant completely available, being probabilities we have $p_H + p_N + p_R + p_C = 1$. For clarity, in (5.21) we have omitted the explicit dependence on t in the state variables and in the preferences.

With this notation, the Cauchy problem (5.2)-(5.10) can be written in compact form as

$$\begin{cases} \dot{\mathbf{x}}(t) = \mathbf{f}(\mathbf{x}(t)), \quad \forall t \in J, \\ \mathbf{x}(t_0) = \mathbf{x}_0 \end{cases} \tag{5.22}$$

Notice that $\mathbf{f}$ is autonomous.

Theorem 5.2 (Local existence and uniqueness for Model #1)**.** *Let $A \subset \mathbb{R}^8$ be an open, bounded, connected set such that $\mathbf{x}_0 \in A$. Assume that the initial data $\mathbf{x}_0$ in* (5.18) *are non-negative and such that $H_0 + N_0 + R_0 + C_0 > 0$, assume that the parameters satisfy $g_X \geq 0$, $K_X > 0$, $m_X \geq 0$ (for $X \in \{H, N, R\}$), $m_V \geq 0$, $f \geq 0$, $p_H, p_N, p_R, p_C \in (0, 1]$, with $p_H + p_N + p_R + p_C = 1, \lambda \geq 0$. Then there exists $\delta > 0$, depending on the set A, and a unique solution $\mathbf{x} : [t_0 - \delta, t_0 + \delta] \to A$, with $\mathbf{x} : t \mapsto \mathbf{x}(t)$, $\mathbf{x}(t_0) = \mathbf{x}_0$ of the Cauchy problem* (5.22)*. Moreover, $\mathbf{x} \in C^1([t_0 - \delta, t_0 + \delta])$.*

Proof. We distinguish the cases $\lambda = 0$ and $\lambda > 0$.

Case $\lambda = 0$.

By assumption, when $\lambda = 0$ the preference functions are defined as

$$P_X(t) \equiv p_X, \qquad X \in \{H, N, R, C\},$$

so they are constant in time and independent of the state variables. In particular, no quotient appears in the definition of the vector function $\mathbf{f}$, and the last equations of the system (5.2) - (5.10) reduces to linear ODEs with constant coefficients.

For the plant compartments H, N, R the equations are unaffected by the value of λ, and Lemma 5.1 provides, for each $X \in \{H, N, R\}$, a unique global solution $X(t)$ of class $C^1([t_0, +\infty); \mathbb{R})$, given explicitly by (5.15)–(5.17). Moreover $C(t) \equiv C_0$ for all $t \geq t_0$.

For the vectors compartments, set

$$V(t) := V_H(t) + V_N(t) + V_R(t) + V_C(t).$$

Summing the four equations for V_H, V_N, V_R, V_C in (5.2) we obtain

$$\dot{V}(t) = (f - m_V)\, V(t), \qquad V(t_0) = V_0 := V_{H0} + V_{N0} + V_{R0} + V_{C0},$$

so

$$V(t) = V_0\, \mathrm{e}^{(f - m_V)(t - t_0)}, \qquad t \geq t_0. \tag{5.23}$$

For each $X \in \{H, N, R, C\}$, using $P_X \equiv p_X$ we rewrite the equation for V_X as

$$\dot{V}_X = -m_V V_X + f V_X + p_X(V - V_X) - (1 - p_X)V_X = (f - m_V - 1)\, V_X + p_X\, V(t),$$

with $V_X(t_0) = V_{X0} \geq 0$. Inserting (5.23) gives a linear ODE whose explicit solution is

$$V_X(t) = \big(V_{X0} - p_X V_0\big)\, \mathrm{e}^{(f - m_V - 1)(t - t_0)} + p_X V_0\, \mathrm{e}^{(f - m_V)(t - t_0)}, \qquad t \geq t_0. \tag{5.24}$$

Formula (5.24) holds for all $X \in \{H, N, R\}$ with the corresponding preference weight p_X and initial value V_{X0}.

Collecting Lemma 5.1, and (5.24), we obtain an explicit C^1 function $\mathbf{x} : [t_0, +\infty) \to \mathbb{R}^8$ that satisfies the Cauchy problem (5.22) and is uniquely determined by the initial datum $\mathbf{x}_0$. In particular, local existence and uniqueness in a neighbourhood of t_0 hold in the case $\lambda = 0$.

Case $\lambda > 0$.

$X(t) \geq 0$ for $X \in \{H, N, R, C\}$ (Lemma 5.1), and $\lambda > 0 \implies \Sigma(t)$, defined in (5.19), is well defined; hence P_X, with $X \in \{H, N, R, C\}$, are well defined too; and $\mathbf{f} \in C^0(\mathbb{R}^8)$. Now, we compute the Jacobian matrix of $\mathbf{f}$. Recalling that $V = V_C + V_H + V_N + V_R$ and stating that every partial derivative not written is equal to 0, we have

$$\begin{aligned}
\frac{\partial f_1}{\partial x_1} &= -m_H + g_H - \frac{2 g_H \cdot H}{K_H}, \\
\frac{\partial f_2}{\partial x_2} &= -m_N + g_N - \frac{2 g_N \cdot N}{K_N}, \\
\frac{\partial f_3}{\partial x_3} &= -m_R + g_R - \frac{2 g_R \cdot R}{K_R}.
\end{aligned}$$

$$\frac{\partial f_5}{\partial x_1} = \frac{p_H \cdot V \cdot \lambda}{(H+\lambda)^2 \cdot \Sigma}\left[1 - \frac{H \cdot p_H}{(H+\lambda)\cdot\Sigma}\right] \qquad \frac{\partial f_6}{\partial x_1} = -\frac{N \cdot \lambda \cdot p_N \cdot p_H \cdot V}{(N+\lambda)\cdot(H+\lambda)^2 \cdot \Sigma^2}$$

$$\frac{\partial f_5}{\partial x_2} = -\frac{H \cdot \lambda \cdot p_H \cdot p_N \cdot V}{(H+\lambda)\cdot(N+\lambda)^2 \cdot \Sigma^2} \qquad \frac{\partial f_6}{\partial x_2} = \frac{p_N \cdot V \cdot \lambda}{(N+\lambda)^2 \cdot \Sigma}\left[1 - \frac{N \cdot p_N}{(N+\lambda)\cdot\Sigma}\right]$$

$$\frac{\partial f_5}{\partial x_3} = -\frac{H \cdot \lambda \cdot p_H \cdot p_R \cdot V}{(H+\lambda)\cdot(R+\lambda)^2 \cdot \Sigma^2} \qquad \frac{\partial f_6}{\partial x_3} = -\frac{N \cdot \lambda \cdot p_N \cdot p_R \cdot V}{(N+\lambda)\cdot(R+\lambda)^2 \cdot \Sigma^2}$$

$$\frac{\partial f_5}{\partial x_4} = -\frac{H \cdot \lambda \cdot p_H \cdot p_C \cdot V}{(H+\lambda)\cdot(C+\lambda)^2 \cdot \Sigma^2} \qquad \frac{\partial f_6}{\partial x_4} = -\frac{N \cdot \lambda \cdot p_N \cdot p_C \cdot V}{(N+\lambda)\cdot(C+\lambda)^2 \cdot \Sigma^2}$$

$$\frac{\partial f_5}{\partial x_5} = f - m_V + \frac{H \cdot p_H}{(H+\lambda)\cdot\Sigma} - 1 \qquad \frac{\partial f_6}{\partial x_5} = \frac{N \cdot p_N}{(N+\lambda)\cdot\Sigma}$$

$$\frac{\partial f_5}{\partial x_6} = \frac{H \cdot p_H}{(H+\lambda)\cdot\Sigma} \qquad \frac{\partial f_6}{\partial x_6} = f - m_V + \frac{N \cdot p_N}{(N+\lambda)\cdot\Sigma} - 1$$

$$\frac{\partial f_5}{\partial x_7} = \frac{H \cdot p_H}{(H+\lambda)\cdot\Sigma} \qquad \frac{\partial f_6}{\partial x_7} = \frac{N \cdot p_N}{(N+\lambda)\cdot\Sigma}$$

$$\frac{\partial f_5}{\partial x_8} = \frac{H \cdot p_H}{(H+\lambda)\cdot\Sigma} \qquad \frac{\partial f_6}{\partial x_8} = \frac{N \cdot p_N}{(N+\lambda)\cdot\Sigma}$$

$$\frac{\partial f_7}{\partial x_1} = -\frac{R \cdot \lambda \cdot p_R \cdot p_H \cdot V}{(R+\lambda)\cdot(H+\lambda)^2 \cdot \Sigma^2} \qquad \frac{\partial f_8}{\partial x_1} = -\frac{C \cdot \lambda \cdot p_C \cdot p_H \cdot V}{(C+\lambda)\cdot(H+\lambda)^2 \cdot \Sigma^2}$$

$$\frac{\partial f_7}{\partial x_2} = -\frac{R \cdot \lambda \cdot p_R \cdot p_N \cdot V}{(R+\lambda)\cdot(N+\lambda)^2 \cdot \Sigma^2} \qquad \frac{\partial f_8}{\partial x_2} = -\frac{C \cdot \lambda \cdot p_C \cdot p_N \cdot V}{(C+\lambda)\cdot(N+\lambda)^2 \cdot \Sigma^2}$$

$$\frac{\partial f_7}{\partial x_3} = \frac{p_R \cdot V \cdot \lambda}{(R+\lambda)^2 \cdot \Sigma}\left[1 - \frac{R \cdot p_R}{(R+\lambda)\cdot\Sigma}\right] \qquad \frac{\partial f_8}{\partial x_3} = -\frac{C \cdot \lambda \cdot p_C \cdot p_R \cdot V}{(C+\lambda)\cdot(R+\lambda)^2 \cdot \Sigma^2}$$

$$\frac{\partial f_7}{\partial x_4} = -\frac{R \cdot \lambda \cdot p_R \cdot p_C \cdot V}{(R+\lambda)\cdot(C+\lambda)^2 \cdot \Sigma^2} \qquad \frac{\partial f_8}{\partial x_4} = \frac{p_C \cdot V \cdot \lambda}{(C+\lambda)^2 \cdot \Sigma}\left[1 - \frac{C \cdot p_C}{(C+\lambda)\cdot\Sigma}\right]$$

$$\frac{\partial f_7}{\partial x_5} = \frac{R \cdot p_R}{(R+\lambda)\cdot\Sigma} \qquad \frac{\partial f_8}{\partial x_5} = \frac{C \cdot p_C}{(C+\lambda)\cdot\Sigma}$$

$$\frac{\partial f_7}{\partial x_6} = \frac{R \cdot p_R}{(R+\lambda)\cdot\Sigma} \qquad \frac{\partial f_8}{\partial x_6} = \frac{C \cdot p_C}{(C+\lambda)\cdot\Sigma}$$

$$\frac{\partial f_7}{\partial x_7} = f - m_V + \frac{R \cdot p_R}{(R+\lambda)\cdot\Sigma} - 1 \qquad \frac{\partial f_8}{\partial x_7} = \frac{C \cdot p_C}{(C+\lambda)\cdot\Sigma}$$

$$\frac{\partial f_7}{\partial x_8} = \frac{R \cdot p_R}{(R+\lambda)\cdot\Sigma} \qquad \frac{\partial f_8}{\partial x_8} = f - m_V + \frac{C \cdot p_C}{(C+\lambda)\cdot\Sigma} - 1$$

Because any $\lambda + X > 0$ for any $t \in J$ and for $X \in \{H, N, R, C\}$, and because $\Sigma(t) > 0 \, \forall t \geq t_0$ (at least one plant compartment solution is strictly positive for any $t \in J$), all the partial derivatives are well defined and continuous $\forall \mathbf{x} \in \mathbb{R}^8$. This implies that $\mathbf{f}$ is locally Lipschitz on any compact of $\mathbb{R}^8$. Then the thesis follows by applying the Cauchy-Lipschitz theorem (see, e.g., [10]). □

5.2.5 Global existence and uniqueness of the solution of Model #1

Let us now analyse the behaviour of our ODE system in order to establish the existence and uniqueness of a global solution on J.

Lemma 5.3 (Vector dynamics: non-negativity and bounds)**.** *If there exists a solution of* (5.22) *on an interval $I \subseteq J$, then*

1. *the total vector population $V(t) = V_H(t) + V_N(t) + V_R(t) + V_C(t)$ satisfies*

$$\dot{V}(t) = (f - m_V)\, V(t), \qquad V(t_0) = V_0 := V_{H0} + V_{N0} + V_{R0} + V_{C0}, \tag{5.25}$$

   hence

$$V(t) = V_0\, \mathrm{e}^{(f-m_V)(t-t_0)} \geq 0 \quad \textit{for all } t \geq t_0. \tag{5.26}$$

2. *Each vector compartment remains non-negative for all t in the existence interval, and is bounded above by the total population:*

$$0 \leq V_X(t) \leq V(t) \quad \textit{for all } t \geq t_0, \quad X \in \{H, N, R, C\}.$$

Proof. Summing the four equations for V_H, V_N, V_R, V_C in (5.2), and recalling (5.13), we obtain,

$$\dot{V}(t) = (f - m_V)V(t), \qquad V(t_0) = V_0,$$

which yields (5.26). In particular, if $V_0 \geq 0$ then $V(t) \geq 0$ for all $t \geq t_0$.

Next we prove that each component V_X remains non-negative. Using the identity

$$V(t) = V_H(t) + V_N(t) + V_R(t) + V_C(t),$$

and the form of the right-hand side in (5.2), one can rewrite, for any $X \in \{H, N, R, C\}$,

$$\dot{V}_X(t) = (f - m_V - 1)\, V_X(t) + P_X(t)\, V(t), \tag{5.27}$$

where $P_X(t) \in [0, 1]$ for all $t \geq t_0$ and $P_H + P_N + P_R + P_C \equiv 1$.

Fix $X \in \{H, N, R, C\}$ and assume by contradiction that there exists $t^* > t_0$ such that $V_X(t^*) < 0$. By continuity and the initial condition $V_{X0} \geq 0$, we can define

$$\tau := \inf\{t > t_0 \,:\, V_X(t) = 0\},$$

so that $t_0 \leq \tau < t^*$, $V_X(\tau) = 0$ and $V_X(t) > 0$ for all $t \in [t_0, \tau)$. From (5.26) we have $V(t) \geq 0$ for all $t \geq t_0$, and in particular $V(\tau) \geq 0$. Evaluating (5.27) at $t = \tau$ we obtain

$$\dot{V}_X(\tau) = (f - m_V - 1)\, V_X(\tau) + P_X(\tau)\, V(\tau) = P_X(\tau)\, V(\tau) \geq 0,$$

since $P_X(\tau) \in [0, 1]$ and $V(\tau) \geq 0$. Thus, at the first time τ when V_X reaches the value 0, its time derivative is non-negative. By uniqueness of solutions for (5.27), this implies

that V_X cannot cross the hyperplane $\{V_X = 0\}$ from positive to negative values, which contradicts the assumption that $V_X(t^*) < 0$. Therefore

$$V_X(t) \geq 0 \quad \text{for all } t \geq t_0 \text{ and for any } X \in \{H, N, R, C\}.$$

Hence we can finally state:

$$0 \leq V_X(t) \leq V(t) \quad \text{for all } t \geq t_0, \quad X \in \{H, N, R, C\}.$$

□

Theorem 5.4. *Under the same assumptions of the Theorem 5.2, the Cauchy problem* (5.22) *admits a unique solution defined for all* $t \in J$*. Moreover, each component of the solution is non-negative and bounded* $\forall t \in J$*.*

Proof. Let $\widetilde{X} = \sup_{t \in J} X(t) < +\infty$, $X \in \{H, N, R\}$, by Lemma 5.1, and $\widetilde{V} = \sup_{t \in J} V(t) < +\infty$ by Lemma 5.3. Then set $A := (0, \widetilde{H}) \times (0, \widetilde{N}) \times (0, \widetilde{R}) \times \{C_0\} \times (0, \widetilde{V})^4$. By using the same arguments of Theorem 5.2, the thesis follows. □

5.2.6 Equilibrium points and Jacobian analysis

To analyse the long–time behaviour of the system, we first compute its equilibrium points, namely, states for which $\mathbf{f}(\mathbf{x}(t)) = \mathbf{0}$. An equilibrium point $\bar{\mathbf{x}} = (\bar{H}, \bar{N}, \bar{R}, \bar{C}, \bar{V}_H, \bar{V}_N, \bar{V}_R, \bar{V}_C)$ is therefore characterised by the conditions

$$\begin{cases} \bar{H} = 0 \ \text{ or } \ \bar{H} = \left(1 - \dfrac{m_H}{g_H}\right) K_H, \\ \bar{N} = 0 \ \text{ or } \ \bar{N} = \left(1 - \dfrac{m_N}{g_N}\right) K_N, \\ \bar{R} = 0 \ \text{ or } \ \bar{R} = \left(1 - \dfrac{m_R}{g_R}\right) K_R, \\ \bar{C} = C_0, \\ \bar{V}_H = \dfrac{(\bar{V}_N + \bar{V}_R + \bar{V}_C)\, \bar{P}_H}{m_V - f - \bar{P}_H + 1}, \\ \bar{V}_N = \dfrac{(\bar{V}_H + \bar{V}_R + \bar{V}_C)\, \bar{P}_N}{m_V - f - \bar{P}_N + 1}, \\ \bar{V}_R = \dfrac{(\bar{V}_H + \bar{V}_N + \bar{V}_C)\, \bar{P}_R}{m_V - f - \bar{P}_R + 1}, \\ \bar{V}_C = \dfrac{(\bar{V}_H + \bar{V}_N + \bar{V}_R)\, \bar{P}_C}{m_V - f - \bar{P}_C + 1}, \end{cases} \tag{5.28}$$

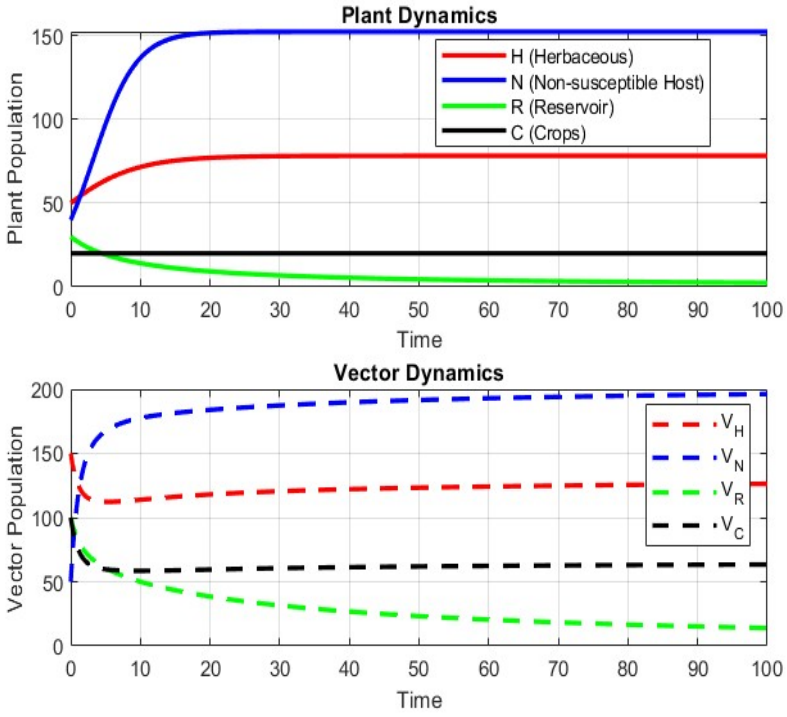


Figure 39: A solution of the simplified BeXyl Model 1.
Source: BeXyl Model

where the equilibrium preference weights $\bar{P}_X$ are defined in terms of the plant equilibrium as follows:

$$\bar{\Sigma} := \frac{p_H \bar{H}}{\lambda + \bar{H}} + \frac{p_N \bar{N}}{\lambda + \bar{N}} + \frac{p_R \bar{R}}{\lambda + \bar{R}} + \frac{p_C \bar{C}}{\lambda + \bar{C}}, \tag{5.29}$$

and

$$\begin{aligned} \bar{P}_H &:= \frac{\dfrac{p_H \bar{H}}{\lambda + \bar{H}}}{\bar{\Sigma}}, \quad \bar{P}_N := \frac{\dfrac{p_N \bar{N}}{\lambda + \bar{N}}}{\bar{\Sigma}}, \\ \bar{P}_R &:= \frac{\dfrac{p_R \bar{R}}{\lambda + \bar{R}}}{\bar{\Sigma}}, \quad \bar{P}_C := \frac{\dfrac{p_C \bar{C}}{\lambda + \bar{C}}}{\bar{\Sigma}}. \end{aligned} \tag{5.30}$$

By construction $0 \leq \bar{P}_X \leq 1$ for all $X \in \{H, N, R, C\}$, and $\bar{P}_H + \bar{P}_N + \bar{P}_R + \bar{P}_C = 1$.

We remark that, while the plant equilibria can be determined in closed form by solving three decoupled scalar equations, the situation is more involved for the vector equilibria. Indeed, the equilibrium relations for $\bar{V}_H, \bar{V}_N, \bar{V}_R, \bar{V}_C$ are mutually coupled, so that each component appears in the definition of the others. As a consequence, there are no explicit expressions for $(\bar{V}_H, \bar{V}_N, \bar{V}_R, \bar{V}_C)$, and hence these quantities cannot but be computed numerically solving the associated fixed–point problem via a simple fixed–point iteration scheme.

To investigate the stability properties of the equilibria, we rely on the Jacobian matrix of the vector field $\mathbf{f}$, whose entries $\partial f_i / \partial x_j$ have been computed in the previous subsection. Evaluating the Jacobian matrix at a given equilibrium point $\bar{\mathbf{x}}$ and analysing the spectrum of the linearised system, we can characterise local stability in the sense of Lyapunov, according to the general framework recalled in Subsection 5.1.1.

Since plant dynamics are not directly influenced by the vector compartments and their equilibrium values can be determined analytically, we first make a short digression on the stability of the plant equilibria. Restricting attention to the four plant variables (H, N, R, C), each equation depends only on the corresponding compartment and on fixed parameters. The Jacobian matrix associated with this reduced subsystem is therefore diagonal,

$$J = \begin{bmatrix} \dfrac{\partial \dot{H}}{\partial H} & 0 & 0 & 0 \\ 0 & \dfrac{\partial \dot{N}}{\partial N} & 0 & 0 \\ 0 & 0 & \dfrac{\partial \dot{R}}{\partial R} & 0 \\ 0 & 0 & 0 & \dfrac{\partial \dot{C}}{\partial C} \end{bmatrix},$$

with $\frac{\partial \dot{C}}{\partial C} = 0$, since the crop compartment C is constant.

By symmetry, it is enough to discuss the compartment H; the same arguments apply to N and R with the obvious changes in notation. Recall that

$$\frac{\partial \dot{H}}{\partial H} = -m_H + g_H\Big(1 - \frac{2H}{K_H}\Big),$$

hence the eigenvalue associated with the linearisation in the H-direction is

$$\lambda_H(H) = -m_H + g_H\Big(1 - \frac{2H}{K_H}\Big).$$

Equilibrium subcase 1:
$\bar{H} = 0$.
In this subcase $\lambda_H = g_H - m_H$, hence

$$\begin{cases} m_H > g_H & \Longrightarrow \bar{H} \text{ is locally stable,} \\ m_H < g_H & \Longrightarrow \bar{H} \text{ is unstable.} \end{cases}$$

Equilibrium subcase 2:
$\bar{H} = (1 - m_H/g_H)K_H$.
In this subcase $\lambda_H = m_H - g_H$, hence

$$\begin{cases} m_H < g_H & \Longrightarrow \bar{H} \text{ is locally stable,} \\ m_H > g_H & \Longrightarrow \bar{H} \text{ is unstable.} \end{cases}$$

In the limit case $m_H = g_H$, the two equilibria identified above coalesce at $\bar{H} = 0$, and the linearisation yields $\lambda_H = 0$. To settle stability we resort to a Lyapunov argument. When $m_H = g_H$, the equation reduces to

$$\dot{H} = -\frac{m_H}{K_H} H^2.$$

On the biologically relevant invariant set $\{H \geq 0\}$, we consider the Lyapunov candidate

$$L(H) = \frac{1}{2} H^2,$$

which is positive definite with respect to $\bar{H} = 0$. Its derivative along trajectories is

$$\dot{L}(H) = H\dot{H} = -\frac{m_H}{K_H} H^3 \leq 0 \quad \text{for all } H \geq 0,$$

and $\dot{L}(H) = 0$ if and only if $H = 0$. Thus $\dot{L}$ is negative definite on $\{H \geq 0\}$. By Lyapunov's stability theorem (Theorem 5.1.2), we conclude that the equilibrium $\bar{H} = 0$ is asymptotically stable (though not exponentially stable, since solutions decay like $1/t$ as $t \to +\infty$) for the reduced one-dimensional dynamics of H.

The same reasoning applies to the compartments N and R, leading to analogous stability conditions expressed in terms of the corresponding parameters m_N, g_N and m_R, g_R.

The corresponding time evolution of the plant compartments in the three parameter regimes $g_X > m_X$, $g_X = m_X$ and $g_X < m_X$ is illustrated in Figure 41. In particular, the plots in Figure 41 visualise how the balance between growth and decline determines whether plant biomass converges to zero or to a positive equilibrium.

Vector equilibria and the regime $m_X \geq g_X$. As discussed above, once a plant equilibrium $(\bar{H}, \bar{N}, \bar{R}, \bar{C})$ is fixed, the equilibrium values of the vector compartments $(\bar{V}_H, \bar{V}_N, \bar{V}_R, \bar{V}_C)$ are determined by the linear relations in (5.28), whose coefficients depend on the plant equilibrium only through the preference weights $\bar{P}_X$ defined in (5.29)–(5.30). In general, these four equations are mutually coupled: each component $\bar{V}_X$ appears in the definition of the others. For this reason closed–form expressions for $(\bar{V}_H, \bar{V}_N, \bar{V}_R, \bar{V}_C)$ are not particularly transparent, and in practice we compute vector equilibria numerically by solving the corresponding fixed–point problem (see Section 5.1.3).

There is, however, a parameter regime in which the structure of the vector equilibria can be described explicitly and yields some qualitative insight. Assume that

$$m_X \geq g_X \quad \text{for } X \in \{H, N, R\},$$

so that, as shown in the previous subsection, the only biologically relevant plant equilibrium is

$$\bar{H} = \bar{N} = \bar{R} = 0, \qquad \bar{C} = C_0 > 0.$$

In this case the preference weights reduce to

$$\bar{P}_H = \bar{P}_N = \bar{P}_R = 0, \qquad \bar{P}_C = 1,$$

and the vector dynamics simplify considerably. The equations for the vector compartments become

$$\begin{aligned}
\dot{V}_H &= (f - m_V - 1)\, V_H, \\
\dot{V}_N &= (f - m_V - 1)\, V_N, \\
\dot{V}_R &= (f - m_V - 1)\, V_R, \\
\dot{V}_C &= (f - m_V)\, V_C + V_H + V_N + V_R,
\end{aligned}$$

while the total vector population $V(t)$ satisfies $\dot{V}(t) = (f - m_V)\, V(t)$.

We now distinguish three subcases according to the sign of $f - m_V$.

Case $f > m_V$. Here $\dot{V} = (f - m_V)V$ with $f - m_V > 0$, so that $V(t) = V_0\, \mathrm{e}^{(f - m_V)(t - t_0)}$ grows exponentially unless $V_0 = 0$. The only equilibrium is the trivial extinction state

$$\bar{V}_H = \bar{V}_N = \bar{V}_R = \bar{V}_C = 0,$$

which is unstable. In particular, no nontrivial bounded vector equilibrium exists in this parameter regime.

Case $f < m_V$. In this case $\dot{V} = (f - m_V)V$ with $f - m_V < 0$, hence $V(t) \to 0$ as $t \to +\infty$. From the linear system above it follows that each compartment $V_X(t)$ decays exponentially to zero, so that the unique vector equilibrium is again the extinction state

$$\bar{V}_H = \bar{V}_N = \bar{V}_R = \bar{V}_C = 0,$$

which is now asymptotically stable. Together with the condition $m_X \geq g_X$ for $X \in \{H, N, R\}$, this implies that the only equilibrium of the full system is

$$(\bar{H}, \bar{N}, \bar{R}, \bar{C}, \bar{V}_H, \bar{V}_N, \bar{V}_R, \bar{V}_C) = (0, 0, 0, C_0, 0, 0, 0, 0),$$

and every trajectory with non-negative initial data converges to this state as $t \to +\infty$.

Case $f = m_V$. When $f = m_V$ the total vector population $V(t)$ is conserved in time, whereas the redistribution among compartments is still driven by the preference weights. In the present regime $m_X \geq g_X$ for $X \in \{H, N, R\}$, we have $\bar{P}_C = 1$ and therefore

$$\dot{V}_H = -V_H, \qquad \dot{V}_N = -V_N, \qquad \dot{V}_R = -V_R, \qquad \dot{V}_C = V_H + V_N + V_R.$$

Solving explicitly, we obtain

$$V_H(t) = V_{H0}\, \mathrm{e}^{-(t-t_0)}, \quad V_N(t) = V_{N0}\, \mathrm{e}^{-(t-t_0)}, \quad V_R(t) = V_{R0}\, \mathrm{e}^{-(t-t_0)},$$

and

$$V_C(t) = V_{C0} + (V_{H0} + V_{N0} + V_{R0})\big(1 - \mathrm{e}^{-(t-t_0)}\big),$$

so that

$$\lim_{t\to+\infty} V_H(t) = \lim_{t\to+\infty} V_N(t) = \lim_{t\to+\infty} V_R(t) = 0,$$

and

$$\lim_{t\to+\infty} V_C(t) = V_0.$$

In other words, in the long run all vectors concentrate on the crops, and the whole initial vector population V_0 is asymptotically supported on the compartment V_C, as illustrated in Figure 40.

From the equilibrium viewpoint, when $f = m_V$ and $(\bar{H}, \bar{N}, \bar{R}, \bar{C}) = (0, 0, 0, C_0)$ the system admits a one-parameter family of vector equilibria of the form

$$\bar{V}_H = \bar{V}_N = \bar{V}_R = 0, \qquad \bar{V}_C = V(0) \geq 0.$$

Each such equilibrium is Lyapunov stable but not asymptotically stable in the full state space, since trajectories starting with a different total population converge to a different point on the same one-dimensional manifold of equilibria. For a given initial condition, however, the dynamics select the unique equilibrium with $\bar{V}_C = V_0$, towards which the solution converges.

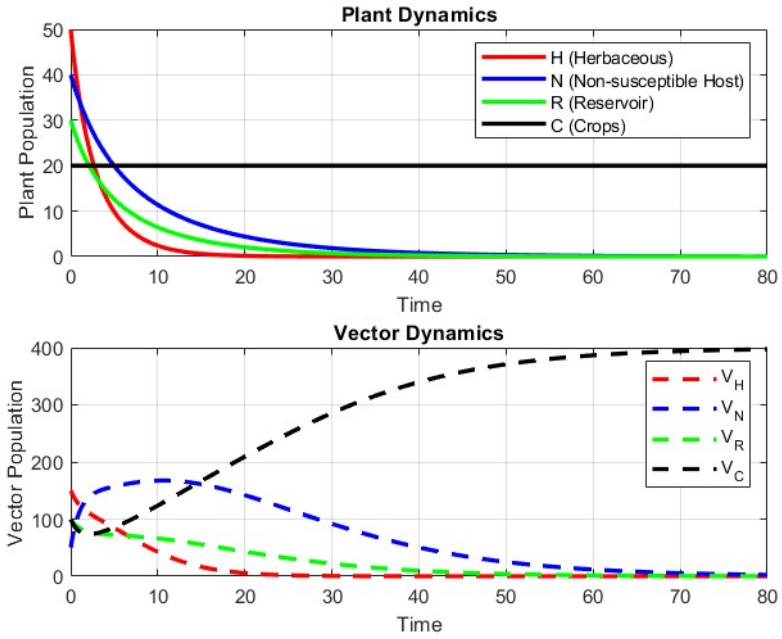


Figure 40: Solution of the Model #1 with $m_X \geq g_X$ and $m_V = f$ computed solving (5.2)-(5.10) with an adaptive fourth–fifth order Runge–Kutta method.

5.3 Second simplified Model

5.3.1 Introduction

The second simplified formulation of the BeXyl model explicitly accounts for the presence of the disease, while still retaining a structure simple enough to allow a rigorous mathematical analysis. In contrast to the full BeXyl framework, which includes several plant types and life stages of the vector, here we restrict the description to the core components that directly drive pathogen spread within the crop compartments.

This reduced structure is designed to isolate and highlight the feedbacks between vector infection and the progression of disease severity in the crop.

In the following subsection we introduce the ODE system, specify the biological assumptions underlying each term, and set the notation that will be used for the subsequent qualitative analysis.

5.3.2 Model #2: structure and derivation

The state variables of Model #2 are

$$C_s(t),\ C_0(t),\ C_1(t),\ V_s(t),\ V_i(t),$$

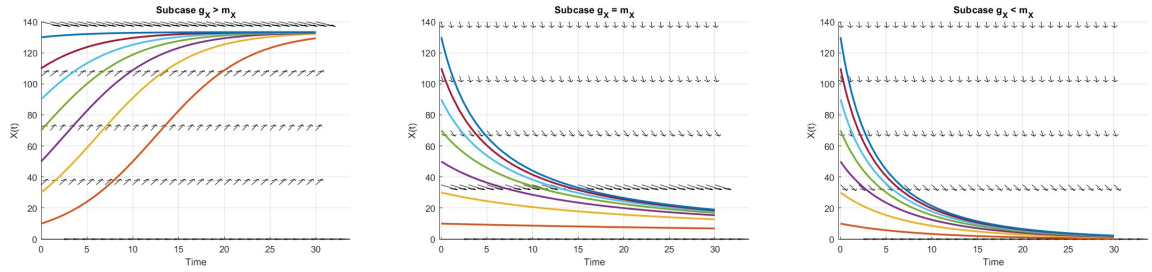


Figure 41: Model #1. Trends in plant-related compartments as a function of the balance between growth (g_X) and decline (m_X), as analytically proven. Numerical solutions were computed using an adaptive fourth–fifth order Runge–Kutta method.

and represent, respectively, the densities (per unit area) of susceptible crop plants, mildly infected crop plants (infection level 0), severely infected crop plants (infection level 1), susceptible vectors, and infected vectors.

For notational convenience, we omit the explicit dependence on time and write C_s, C_0, C_1, V_s, V_i in place of $C_s(t), C_0(t), C_1(t), V_s(t), V_i(t)$. The temporal evolution of these variables is described by the equations

$$\dot{C}_s = -i_C\, C_s\, V_i + r_{C_0}\, C_0 + c\, C_1, \tag{5.31}$$

$$\dot{C}_0 = i_C\, C_s\, V_i - r_{C_0}\, C_0 - d\, C_0\, V_i + r_{C_1}\, C_1, \tag{5.32}$$

$$\dot{C}_1 = d\, C_0\, V_i - r_{C_1}\, C_1 - c\, C_1, \tag{5.33}$$

$$\dot{V}_s = -a\,(p_0\, C_0 + p_1\, C_1)\, V_s + h\, V_i - m_V\, V_s^2 + f\,(V_s + V_i), \tag{5.34}$$

$$\dot{V}_i = a\,(p_0\, C_0 + p_1\, C_1)\, V_s - h\, V_i - m_V\, V_i^2, \tag{5.35}$$

endowed with initial conditions

$$\begin{aligned} &C_s(0) = C_{s0}, \quad C_0(0) = C_{00}, \quad C_1(0) = C_{10}, \\ &V_s(0) = V_{s0}, \quad V_i(0) = V_{i0}, \end{aligned} \tag{5.36}$$

where all initial data are assumed to be non-negative.

Crop dynamics. The crop population is partitioned into three epidemiological classes: susceptible plants C_s, mildly infected plants C_0 (level 0), and severely infected plants C_1 (level 1). The parameter $i_C \geq 0$ is the infection coefficient, and the term

$$i_C\, C_s\, V_i$$

represents the variation of susceptible and mildly infected crops due to encounters between infected vectors and susceptible crops. It is responsible for the transfer of plants from C_s to C_0.

Infection progression and recovery are modelled as follows. The parameter $d \geq 0$ is the disease progression rate: the term

$$d\, C_0\, V_i$$

represents the variation of mildly and severely infected crops due to infected vectors which accelerate disease deterioration. It is responsible for the transfer of plants from C_0 to C_1. The parameters $r_{C_0} \geq 0$ and $r_{C_1} \geq 0$ are recovery rates: r_{C_0} governs regression from level 0 back to the susceptible class, while r_{C_1} governs regression from level 1 back to level 0. Accordingly, the terms $r_{C_0} C_0$ and $r_{C_1} C_1$ redistribute biomass along the chain

$$C_s \longleftrightarrow C_0 \longleftrightarrow C_1.$$

External management actions are represented by the parameter $c \geq 0$, which models removal and replacement of severely infected plants. The term cC_1 appears with opposite sign in the equations for C_1 and C_s, expressing the assumption that biomass removed from the severely infected class is instantaneously replaced by healthy crop, for instance through replanting. This modelling choice ensures that external control does not alter the total crop biomass.

Summing the three crop equations yields

$$\frac{d}{dt}(C_s + C_0 + C_1) = 0,$$

so that the total crop density $C_{\text{tot}} := C_s(t) + C_0(t) + C_1(t)$ is conserved in time and remains equal to its initial value $C_{\text{tot}}(0) = C_{s0} + C_{00} + C_{10}$.

Vector dynamics. The vector population is divided into susceptible and infected individuals, with state variables V_s and V_i, respectively. The parameter $a \geq 0$ is the acquisition rate: when a susceptible vector feeds on an infected crop, it acquires the pathogen and moves from V_s to V_i. The effective force of infection experienced by vectors is proportional to the weighted sum

$$p_0\, C_0 + p_1\, C_1,$$

where $p_0, p_1 \in [0, 1]$ are preference parameters that describe how likely (they are in fact probabilities) a vector is to land on a mildly infected plant (C_0) versus a severely infected plant (C_1). Including susceptible crops, an additional preference probability p_s for C_s would be introduced so that $p_0 + p_1 + p_s = 1$; in the present setting we only focus on infected crops, and therefore assume $p_0 + p_1 \leq 1$. The terms

$$-a(p_0 C_0 + p_1 C_1) V_s \quad \text{and} \quad a(p_0 C_0 + p_1 C_1) V_s$$

thus represent, respectively, the loss of susceptible vectors due to acquisition and the corresponding gain in the infected compartment.

Infected vectors may lose infectivity at rate $h \geq 0$, for instance due to pathogen clearance or loss of detectable infection. The term hV_i appears with positive sign in the state equation for V_s and negative sign in the state equation for V_i, modelling the transition from V_i to V_s.

Demographic processes are described by the parameters $f \geq 0$ and $m_V \geq 0$. The fertility term

$$f(V_s + V_i)$$

represents the birth of new susceptible vectors, assumed to be proportional to the total vector population. Density dependent mortality is incorporated through the quadratic terms

$$-m_V V_s^2, \qquad -m_V V_i^2,$$

which model crowding-induced mortality acting separately on susceptible and infected vectors.

5.3.3 Local existence and uniqueness of solutions

We now introduce the abstract formulation of the Cauchy problem associated with Model #2 and prove its local well-posedness.

Let $t_0 \geq 0$ be a given initial time and $T > t_0$ a finite final time, and set $J = (t_0, T)$. The initial values for the crop and vector compartments are $C_{s0},\ C_{00},\ C_{10},\ V_{s0},\ V_{i0} \in [0, +\infty)$. We collect the state variables into the vector

$$\mathbf{x}(t) = \begin{bmatrix} C_s(t) \\ C_0(t) \\ C_1(t) \\ V_s(t) \\ V_i(t) \end{bmatrix}, \qquad \mathbf{x}_0 = \begin{bmatrix} C_{s0} \\ C_{00} \\ C_{10} \\ V_{s0} \\ V_{i0} \end{bmatrix}. \tag{5.37}$$

The non-linear vector function $\mathbf{f} : \mathbb{R}^5 \to \mathbb{R}^5$ is defined by (omitting time dependence)

$$\mathbf{f}(\mathbf{x}(t)) = \begin{bmatrix} -i_C\, C_s\, V_i + r_{C_0}\, C_0 + c\, C_1 \\ i_C\, C_s\, V_i - r_{C_0}\, C_0 - d\, C_0\, V_i + r_{C_1}\, C_1 \\ d\, C_0\, V_i - r_{C_1}\, C_1 - c\, C_1 \\ -a\,(p_0 C_0 + p_1 C_1) V_s + h V_i - m_V V_s^2 + f(V_s + V_i) \\ a\,(p_0 C_0 + p_1 C_1) V_s - h V_i - m_V V_i^2 \end{bmatrix}. \tag{5.38}$$

The Cauchy problem associated with Model #2 can thus be written in compact form as

$$\begin{cases} \dot{\mathbf{x}}(t) = \mathbf{f}(\mathbf{x}(t)), \quad t \in J, \\ \mathbf{x}(t_0) = \mathbf{x}_0. \end{cases} \tag{5.39}$$

We assume that the parameters satisfy

$$\begin{aligned} &i_C, r_{C_0}, r_{C_1}, c, d, a, h, m_V, f \ \geq 0, \\ &0 \leq p_0, p_1 \leq 1, \qquad p_0 + p_1 \leq 1, \end{aligned} \tag{5.40}$$

which are biologically natural conditions on infection, recovery, control, disease progression, acquisition, healing, mortality, fertility rates, and preference weights.

Theorem 5.5 (Local existence and uniqueness for Model #2)**.** *Let $A \subset \mathbb{R}^5$ be an open, bounded, connected set such that $\mathbf{x}_0 \in A$. Assume that the initial data $\mathbf{x}_0$ are non-negative, and that the parameters satisfy* (5.40)*. Then there exists $\delta > 0$, with δ depending on A, and a unique function*

$$\mathbf{x} : [t_0 - \delta, t_0 + \delta] \to A, \qquad \mathbf{x} \in C^1([t_0 - \delta, t_0 + \delta]),$$

such that $\mathbf{x}(t_0) = \mathbf{x}_0$ and $\mathbf{x}$ solves the Cauchy problem (5.39) *on $[t_0 - \delta, t_0 + \delta]$. Moreover, the solution depends continuously on the initial data $\mathbf{x}_0$.*

Proof. The system (5.38) is autonomous and every component of $\mathbf{f}$ is a polynomial in the variables C_s, C_0, C_1, V_s, V_i, with coefficients depending only on the parameters. In particular,

$$\mathbf{f} \in C^\infty(\mathbb{R}^5),$$

so all its first-order partial derivatives are continuous.

Let $A \subset \mathbb{R}^5$ be open, bounded and connected, with $\mathbf{x}_0 \in A$. Since A is bounded and the partial derivatives $\partial_{x_j} f_i$ are continuous on A, they are bounded there. Hence $\mathbf{f}$ is locally Lipschitz on any compact subset K of $\mathbb{R}^5$. It is sufficient to take K such that $A \subset K$ and $\mathbf{f}$ is Lipschitz on A.

By the Cauchy–Lipschitz theorem for ODEs (see, e.g., [10]), there exists $\delta > 0$ and a unique solution

$$\mathbf{x} \in C^1([t_0 - \delta, t_0 + \delta])$$

of (5.39) such that $\mathbf{x}(t_0) = \mathbf{x}_0$ and $\mathbf{x}(t) \in A$ for all $t \in [t_0 - \delta, t_0 + \delta]$. The same theorem also ensures continuous dependence of the solution on initial data. □

5.3.4 Global existence and uniqueness of the solution of Model #2

We now analyse the behaviour of the ODE system in order to establish the existence and uniqueness of a global solution and to characterise the qualitative properties of the trajectories.

Lemma 5.6 (Crop dynamics: conservation, positivity and bounds)**.** *If there exists a locally unique solution of* (5.39) *on an interval $I \subseteq J$, with initial data $C_{s0}, C_{00}, C_{10} \geq 0$, then each crop compartment remains non-negative and is bounded from above by the total crop density:*

$$0 \leq C_k(t) \leq C_{\text{tot}}(t_0) \quad \textit{for all } t \in I, \quad k \in \{s, 0, 1\}.$$

Proof. To prove non-negativity, we use an invariance argument for the non-negative orthant. Suppose that at some time $t^* \in I$ one of the crop variables vanishes while all others are non-negative.

If $C_s(t^*) = 0$ and $C_0(t^*), C_1(t^*) \geq 0$, then from (5.31) we have

$$\dot{C}_s(t^*) = -i_C C_s(t^*) V_i(t^*) + r_{C_0} C_0(t^*) + c C_1(t^*) = r_{C_0} C_0(t^*) + c C_1(t^*) \geq 0.$$

If $C_0(t^*) = 0$ and $C_s(t^*), C_1(t^*) \geq 0$, then

$$\dot{C}_0(t^*) = i_C C_s(t^*) V_i(t^*) - r_{C_0} C_0(t^*) - d C_0(t^*) V_i(t^*) + r_{C_1} C_1(t^*) = i_C C_s(t^*) V_i(t^*) + r_{C_1} C_1(t^*) \geq 0.$$

If $C_1(t^*) = 0$ and $C_s(t^*), C_0(t^*) \geq 0$, then

$$\dot{C}_1(t^*) = d C_0(t^*) V_i(t^*) - r_{C_1} C_1(t^*) - c C_1(t^*) = d C_0(t^*) V_i(t^*) \geq 0.$$

In all cases, at any point where a component C_k attains the value 0 while the others are non-negative, its time derivative is non-negative. By continuity and uniqueness of solutions, this implies that none of the components C_s, C_0, C_1 can cross from non-negative to negative values. Since they are initially non-negative, they remain so on I.

Finally, because $C_s, C_0, C_1 \geq 0$ and their sum is constant and equal to $C_{\text{tot}}(t_0)$, each component satisfies $C_k(t) \leq C_{\text{tot}}(t_0)$ for all $t \in I$. □

Lemma 5.7 (Vector dynamics: non-negativity and bounds)**.** *If there exists a locally unique solution of* (5.39) *on an interval $I \subseteq J$, with initial data $V_{s0}, V_{i0} \geq 0$. Then, for all $t \in I$,*

1. *$V_s(t) \geq 0$ and $V_i(t) \geq 0$;*
2. *there exists a constant $M > 0$, depending only on the parameters and on V_{s0}, V_{i0}, such that*
$$0 \leq V_s(t),\, V_i(t) \leq M \qquad \text{for all } t \in I.$$

Proof. Let $t^* \in I$ be such that $V_s(t^*) = 0$ and $V_i(t^*) \geq 0$. From (5.34) we obtain

$$\dot{V}_s(t^*) = -a(p_0 C_0 + p_1 C_1) V_s(t^*) + h V_i(t^*) - m_V V_s^2(t^*) + f\big(V_s(t^*) + V_i(t^*)\big) = (h+f)\, V_i(t^*) \geq 0.$$

Hence, at any time where V_s touches zero, its derivative is non-negative, so V_s cannot cross the hyperplane $\{V_s = 0\}$ from non-negative to negative values. Since $V_s(t_0) = V_{s0} \geq 0$ and V_s is continuous, it follows that $V_s(t) \geq 0$ for all $t \in I$.

The same argument applies to V_i. If $V_i(t^*) = 0$ and $V_s(t^*) \geq 0$, then

$$\dot{V}_i(t^*) = a(p_0 C_0 + p_1 C_1) V_s(t^*) - h V_i(t^*) - m_V V_i^2(t^*) = a(p_0 C_0 + p_1 C_1) V_s(t^*) \geq 0,$$

so V_i cannot become negative either. Summing the equations (5.34) for V_s and (5.35) V_i yields

$$\dot{V}(t) = -m_V\big(V_s^2(t) + V_i^2(t)\big) + f\,V(t). \tag{5.41}$$

Using the inequality

$$V_s(t)^2 + V_i(t)^2 \;\geq\; \frac{1}{2}\big(V_s(t) + V_i(t)\big)^2 = \frac{1}{2}V^2(t),$$

we obtain, for $m_V > 0$,

$$\dot{V}(t) \leq f\,V(t) - \frac{m_V}{2}\,V(t)^2 =: g\big(V(t)\big). \tag{5.42}$$

Let Y be the solution of the logistic Cauchy problem

$$\begin{cases} Y'(t) = g\big(Y(t)\big) = fY(t) - \dfrac{m_V}{2}Y^2(t), \\ Y(t_0) = V(t_0) = V_{s0} + V_{i0} \geq 0. \end{cases}$$

The solution reads (for $f \neq 0$)

$$Y(t) = \frac{f\,Y(t_0)\,e^{f(t-t_0)}}{f + \dfrac{m_V}{2}\,Y(t_0)\big(e^{f(t-t_0)} - 1\big)},$$

and (for $f = 0$)

$$Y(t) = \frac{Y(t_0)}{1 + \dfrac{m_V}{2}\,Y(t_0)\,(t - t_0)},$$

which is anyway globally defined and bounded from above by the maximum between the carrying capacity $2f/m_V$ and $Y(t_0)$. Moreover, g is continuous and locally Lipschitz, so we can apply a scalar comparison theorem for differential inequalities (see, e.g., [97]): from (5.42) and $V(t_0) = Y(t_0)$ it follows that

$$V(t) \leq Y(t) \leq \frac{2f}{m_V} \qquad \text{for all } t \in I.$$

If instead $m_V = 0$, the identity (5.41) reduces to

$$\dot{V}(t) = f\,V(t),$$

with solution

$$V(t) = V(t_0)\,e^{f(t-t_0)},$$

which is finite for all finite t.

In both cases, there exists a constant $M > 0$ such that $0 \leq V(t) \leq M$ for all $t \in I$. Since now we have $0 \leq V_s(t), V_i(t)$ and by definition $V_s(t), V_i(t) \leq V(t)$, we obtain

$$0 \leq V_s(t),\, V_i(t) \leq M \qquad \forall t \in I.$$

□

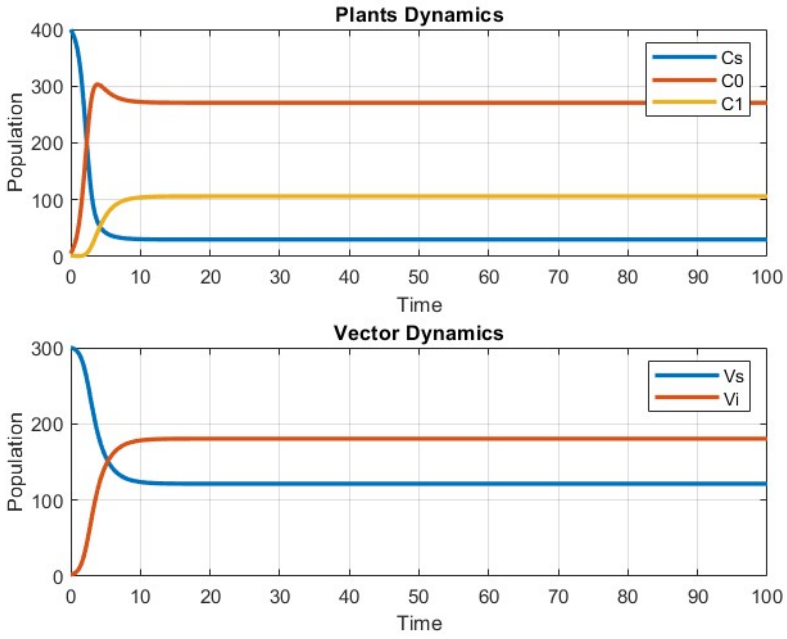


Figure 42: An example of a Model #2 solution

Theorem 5.8 (Global existence, uniqueness, and bounds for Model #2)**.** *Under the same assumptions as in Theorem 5.5, the Cauchy problem* (5.39) *admits a unique solution defined for all* $t \in J$*. Moreover, each component of the solution is non-negative and bounded* $\forall t \in J$*.*

Proof. The proof follows directly from Theorem 5.5, Lemma 5.6, and Lemma 5.7. □

5.3.5 Equilibrium points and Jacobian analysis

To investigate the long-term behaviour of Model #2 we study the equilibrium points of system (5.39), i.e., solutions

$$\bar{\mathbf{x}} = (\bar{C}_s, \bar{C}_0, \bar{C}_1, \bar{V}_s, \bar{V}_i)$$

satisfying

$$\mathbf{f}(\bar{\mathbf{x}}(t)) = \mathbf{0},$$

where $\mathbf{f}$ is defined in (5.38).

As observed above, the crop dynamics conserve the total crop biomass,

$$C_{\text{tot}} := C_s(t) + C_0(t) + C_1(t) \equiv C_{s0} + C_{00} + C_{10},$$

so that at any equilibrium point we must have

$$\bar{C}_s + \bar{C}_0 + \bar{C}_1 = C_{\text{tot}}. \tag{5.43}$$

In particular, the three crop equations are not independent: at equilibrium any two of them imply the third.

Disease-free equilibrium. A biologically relevant equilibrium is the disease-free configuration, characterised by the absence of infection in the crop and in the vector population. Setting

$$\bar{C}_0 = 0, \qquad \bar{C}_1 = 0, \qquad \bar{V}_i = 0,$$

equations (5.31)-(5.33) reduce to

$$\dot{C}_s = 0, \qquad \dot{C}_0 = 0, \qquad \dot{C}_1 = 0,$$

and, for the vectors,

$$\dot{V}_s = -m_V \bar{V}_s^2 + f\bar{V}_s, \qquad \dot{V}_i = -h\bar{V}_i - m_V \bar{V}_i^2.$$

Hence any equilibrium with

$$\bar{C}_s = C_{\text{tot}}, \quad \bar{C}_0 = 0, \quad \bar{C}_1 = 0, \quad \bar{V}_i = 0, \quad \bar{V}_s \in \{0,\, f/m_V\} \text{ (if } m_V > 0) \tag{5.44}$$

is disease-free. In the parameter regimes of interest, we assume the presence of a resident vector population and focus on the equilibrium with

$$\bar{V}_s = \frac{f}{m_V}, \qquad \bar{V}_i = 0,$$

when $m_V > 0$ and $f > 0$.

Endemic equilibria. Endemic equilibria, where a positive fraction of crop plants and vectors are infected, correspond to solutions with

$$\bar{C}_0 > 0, \quad \bar{C}_1 > 0, \quad \bar{V}_i > 0.$$

Using the conservation law (5.43) to eliminate $\bar{C}_s = C_{\text{tot}} - \bar{C}_0 - \bar{C}_1$, the three crop equations at equilibrium reduce to the two independent relations

$$0 = i_C\,(C_{\text{tot}} - \bar{C}_0 - \bar{C}_1)\,\bar{V}_i - r_{C_0}\,\bar{C}_0 - d\,\bar{C}_0\,\bar{V}_i + r_{C_1}\,\bar{C}_1, \tag{5.45}$$

$$0 = d\,\bar{C}_0\,\bar{V}_i - (r_{C_1} + c)\,\bar{C}_1, \tag{5.46}$$

coupled with the two equations for vector

$$0 = -a(p_0\bar{C}_0 + p_1\bar{C}_1)\,\bar{V}_s + h\,\bar{V}_i - m_V\,\bar{V}_s^2 + f(\bar{V}_s + \bar{V}_i), \tag{5.47}$$

$$0 = a(p_0\bar{C}_0 + p_1\bar{C}_1)\,\bar{V}_s - h\,\bar{V}_i - m_V\,\bar{V}_i^2. \tag{5.48}$$

For $\bar{V}_i > 0$ the third crop equation (5.46) gives

$$\bar{C}_1 = \frac{d\,\bar{V}_i}{r_{C_1} + c}\,\bar{C}_0,$$

which can be substituted into (5.45), (5.47) and (5.48). The resulting algebraic system in the three unknowns $(\bar{C}_0, \bar{V}_s, \bar{V}_i)$ is non-linear and does not admit a closed-form solution.

In practice, for a given parameter set we solve the steady-state system (5.45)–(5.48) numerically by a quasi-Newton method (MATLAB function `fsolve`). At each iteration we enforce the crop conservation constraint (5.43), so that the numerical equilibrium automatically satisfies $\bar{C}_s + \bar{C}_0 + \bar{C}_1 = C_{\text{tot}}$. This yields an approximation of endemic equilibria $\bar{\mathbf{x}}$ with prescribed numerical tolerance.

Jacobian matrix and local stability. To assess the local stability of an equilibrium $\bar{\mathbf{x}}$, we linearise system (5.39) around $\bar{\mathbf{x}}$ and compute the Jacobian matrix

$$\mathcal{J}_{\mathbf{f}}(\bar{\mathbf{x}}) = \left[\frac{\partial f_i}{\partial x_j}(\bar{\mathbf{x}})\right]_{i,j=1}^{5}, \quad \bar{\mathbf{x}} = (\bar{C}_s, \bar{C}_0, \bar{C}_1, \bar{V}_s, \bar{V}_i).$$

From (5.38), the entries of $\mathcal{J}_{\mathbf{f}}$ are

$$\mathcal{J}_{\mathbf{f}}(\mathbf{x}) = \begin{pmatrix} -i_C V_i & r_{C_0} & c & 0 & -i_C C_s \\ i_C V_i & -r_{C_0} - dV_i & r_{C_1} & 0 & i_C C_s - dC_0 \\ 0 & dV_i & -(r_{C_1} + c) & 0 & dC_0 \\ 0 & -ap_0 V_s & -ap_1 V_s & -a(p_0 C_0 + p_1 C_1) - 2m_V V_s + f & h + f \\ 0 & ap_0 V_s & ap_1 V_s & a(p_0 C_0 + p_1 C_1) & -h - 2m_V V_i \end{pmatrix}.$$

Evaluating $\mathcal{J}_{\mathbf{f}}$ at a given equilibrium point $\bar{\mathbf{x}}$ and computing its eigenvalues λ_k allows us to classify the equilibrium:

- if $\mathrm{Re}(\lambda_k) < 0$ for all $k = 1, \ldots, 5$, the equilibrium is locally asymptotically stable;
- if at least one eigenvalue has positive real part, the equilibrium is unstable.

5.3.6 A visual–numerical validation

We now analyse how a specific parameter influences a key outcome of Model no. 2, namely the proportion of severely infected crops at equilibrium. Let $\bar{C}_1$ denote the equilibrium value of the compartment C_1. Since the total crop biomass is conserved, the quantity of interest is the equilibrium fraction

$$\Pi := \frac{\bar{C}_1}{C_{\text{tot}}},$$

which measures the percentage of severely infected crops in the long run.

To isolate the role of the crop infection rate i_C, we fix all the other parameters and, in particular, we neglect vector mortality and fertility, vector healing, and external control actions (setting $m_V = f = h = c = 0$). Under these assumptions the steady-state equations can be solved explicitly. If V_{tot} denotes the (constant) total vector density, the equilibrium fraction of severely infected crops is

$$\Pi(i_C) = \frac{V_{\text{tot}}^2 \, d \, i_C}{V_{\text{tot}}^2 d \, i_C + V_{\text{tot}} i_C r_{C_1} + r_{C_0} r_{C_1}},$$

which is a rational function of i_C with a linear denominator.

To validate this explicit formula against the full dynamical system, we compute, for each value of i_C in a biologically meaningful range, the long-time limit $C_1(t)/C_{\text{tot}}$ from numerical simulations of (5.39), and compare it with $\Pi(i_C)$. In Figure 43 the blue circles represent the numerically computed equilibrium fractions, while the red continuous curve corresponds to the analytical expression $\Pi(i_C)$. The two curves are almost indistinguishable over the whole range of i_C, and both display the expected hyperbolic behaviour. This close agreement provides a visual–numerical validation of the analytical relationship between the crop infection rate and the final proportion of severely infected plants, as well as a consistency check for the numerical implementation of Model no. 2.

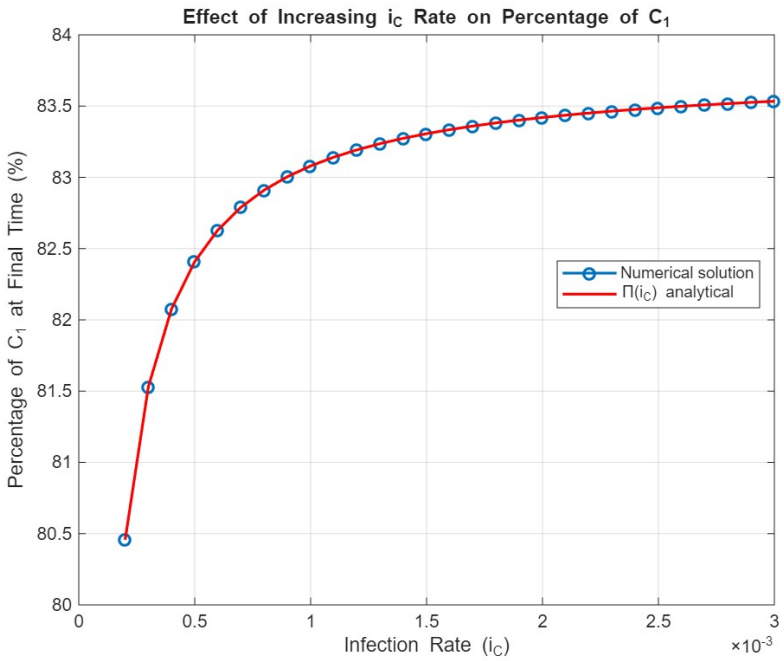


Figure 43: Effect of the crop infection rate i_C on the proportion of severely infected crops. Blue circles: numerical approximation of $C_1(t)/C_{\text{tot}}$ at large times t, close to the numerical equilibrium, obtained by solving (5.39) for different values of i_C. Red curve: analytical equilibrium fraction $\Pi(i_C)$. All curves are computed with $d = 1.3 \times 10^{-4}$, $r_{C_0} = 2.53 \times 10^{-1}$ and $r_{C_1} = 1.26 \times 10^{-1}$. The overlap between numerics and theory results provides a visual–numerical validation of the model.

6

A mathematical model with host preference for the spread of *Xf* in olive trees

In the previous chapter we presented two preliminary, simplified mathematical models of the *Xf* formulations of the BeXyl model, mainly with the purpose of clarifying the biological mechanisms to be modelled and of testing the numerical framework on reduced dynamics. Those versions, however, did not yet include a rigorous treatment of vector host preference, nor a full mathematical analysis of the resulting structures. In this chapter we close that gap and introduce the complete epidemiological ODE model in which vector feeding behaviour is made explicit and is allowed to depend on the current availability and infection status of the plant compartments.

Vector preferences are, to date, only partially accounted for in most plant epidemiology models: they are either fixed as constant weights, or they are embedded implicitly in transmission coefficients, so that their ecological role cannot be disentangled from the other processes. Here we adopt a different standpoint: we model preference as a dynamic, state–dependent mechanism that redistributes vector pressure among reservoir vegetation, crop hosts, infected plants and non-susceptible vegetation. This choice makes it possible to quantify how a change in landscape composition or in plant symptom expression may immediately translate into a change in transmission, something that current models seldom address.

From a mathematical viewpoint, this chapter represents a qualitative step forward with respect to the previous ones: starting from the biologically motivated ODE system, we prove existence, uniqueness, non-negativity and boundedness of solutions under assumptions on data, we characterize invariant sets induced by plant conservation, and we show how equilibria can be computed and tested for stability analysis. In this way, the model becomes not just a simulation tool, but a framework that can be interrogated, compared and, in later sections, coupled with management scenarios.

The content of this chapter is the result of a collaboration with Igor Daniel Weber, Paola Gervasio, Anna Simonetto, and Gianni Gilioli of the University of Brescia, DICATAM, Brescia, Italy, and has been submitted to the scientific journal *Bulletin of Mathematical Biology*.

6.1 Introduction

Diseases mediated by insect vectors are of particular concern in agriculture because their dynamics are governed by non-trivial interactions between hosts, pathogens, and mobile vectors within heterogeneous landscapes [66, 43]. Understanding the transmission dynamics of these pathogens requires addressing a highly complex system, for which mathematical modelling within a landscape ecology framework provides an essential approach. Such models offer a powerful means to disentangle the underlying processes, allowing researchers to assess how host distribution, vector behaviour, and spatial heterogeneity influence the course and outcomes of epidemics.

Several modelling approaches have been applied to vector–borne plant diseases. Compartmental models (e.g., susceptible-infectious-recovered - SIR) provide analytical clarity and allow estimation of epidemic thresholds [27]. However, they rely on the assumption of homogeneous mixing, which overlooks spatial heterogeneity. Network-based models represent fields or host patches as nodes linked by vector–mediated transmission pathways, making them well suited to fragmented landscapes [41]. They require accurate empirical parameterisation of connectivity. Agent-based models (ABMs) capture fine-scale heterogeneity and complex interactions by simulating individuals as autonomous agents [23, 36], but they are computationally demanding and often lack generality. Stochastic models account for randomness in vector movement and transmission [31], providing key insights into invasion probabilities and extinction risks, yet they are analytically intractable and computationally intensive.

Among the modelling approaches available, compartmental models based on ordinary differential equations (ODEs) have proven particularly versatile for capturing vector–plant–pathogen dynamics (see [72], [82], and [99]). Simplified formulations have provided analytical thresholds for pathogen persistence [91], whereas hybrid ODE–PDE frameworks have facilitated sensitivity analyses and scenario exploration [87]. Collectively, these studies underscore the central role of ODE-based models in bridging biological, ecological, and management perspectives, establishing them as a cornerstone of predictive epidemiology for vector–borne plant pathogens.

Building on this foundation, our model advances the compartmental framework by introducing dynamic host-preference functions, which explicitly account for behaviour-driven transmission. This extension provides novel insights into how vector behaviour modulates epidemic trajectories, thereby enhancing our capacity to predict and control the spread of vector–borne plant diseases.

Motivated by these considerations, we develop and rigorously analyse a deterministic compartmental model, formulated as a system of non-linear ODEs, to describe the epidemiological dynamics of a generic plant–pathogen–vector system. The model explicitly incorporates the vector population, susceptible host plants (including both cultivated species and non-cultivated reservoirs), and non-susceptible vegetation acting as alternative feeding resources.

A key innovation of our framework lies in the incorporation of preference-driven dynamics into the host–vector–pathogen interaction. Host selection is represented as a non-neutral behavioural trait that actively modulates transmission and shapes spatio-temporal disease patterns. Preferences are captured through dynamically updated weight functions responsive to host availability, thereby providing a mechanistic and biologically grounded description of adaptive vector behaviour. This formulation reveals how host preference can either amplify or mitigate disease spread, highlighting opportunities for management strategies based on habitat manipulation, such as the use of decoy plants or competitive ground covers.

From a mathematical perspective, the model is shown to be well-posed under broad and biologically plausible assumptions. We establish existence, uniqueness, and non-negativity of solutions, and derive analytical bounds that confine system trajectories within invariant, biologically meaningful regions.

By integrating mathematical precision with ecological realism, the framework provides a robust tool for both qualitative understanding and quantitative forecasting of vector–borne plant disease dynamics. Its applicability is demonstrated through a case study of *X. fastidiosa* outbreaks in olive agroecosystems in Apulia, capturing key interactions among vectors, hosts, and landscape structure.

The paper is structured as follows: Section 6.2 introduces the ODE model and the underlying biological assumptions; Section 6.3 develops the mathematical analysis (existence, uniqueness, non-negativity, boundedness, and local stability of equilibria); Section 6.4 presents the case study and parameterisation for the *Xylella*–olive system; Section 6.5 reports the numerical simulations, including scenarios that mimic management strategies; finally, Section 6.6 concludes with a discussion and outlines future developments.

6.2 Model structure and derivation

In this study, we investigate how vector host preferences influence the spread of phytopathogenic agents within agroecosystems. To this end, we formulate a compartmental epidemiological model that describes the dynamics of a vector–borne plant disease. The model captures the interactions among four major ecological components: i) reservoir host plants, ii) crop host plants (both represented as dynamic state variables), iii) non-susceptible host plants, included as a fixed parameter representing alternative feeding sources, and iv) insect vectors, modelled by considering only the infective life stage responsible for pathogen acquisition and transmission. Except for the non-susceptible hosts, each component is divided into susceptible and infected compartments, which are modelled with a system of six coupled non-linear ODEs that describe the temporal dynamics of the following time-dependent state variables: $R_s, R_i, C_s, C_i, V_s, V_i$. These variables denote, respectively, susceptible and infected reservoir plants, susceptible and infected crop plants, and susceptible and infected vectors. All compartment values are

expressed as average densities per unit area.

6.2.1 Reservoir plant dynamics

Reservoir plants act as long-term sources of infection. Their dynamics are governed by standard infection-recovery processes. Susceptible reservoir plants R_s become infected at a rate proportional to the density of infected vectors V_i, modulated by a transmission parameter i_R and the preference function P_{R_s}, which expresses the dynamically updated feeding preference of vectors for susceptible reservoir plants. Infected reservoir plants R_i may recover over time at a constant rate r_R, re-entering the susceptible class. These dynamics are described by the following equations:

$$\begin{aligned} \dot{R}_s &= -i_R \cdot P_{R_s} \cdot V_i + r_R \cdot R_i, \\ \dot{R}_i &= i_R \cdot P_{R_s} \cdot V_i - r_R \cdot R_i, \end{aligned} \tag{6.1}$$

The preference function P_{R_s} is defined as:

$$P_{R_s} = \frac{p_R \cdot R_s}{p_R \cdot R_s + p_R \cdot R_i + p_{C_s} \cdot C_s + p_{C_i} \cdot C_i + p_N \cdot N}, \tag{6.2}$$

where the coefficients p_R, p_{C_s}, p_{C_i} and $p_N \in (0, 1]$, are constant in time vector preference weights for each plant class (reservoirs, susceptible crops, infected crops, non-susceptible hosts, respectively), while N denotes the constant number of non-susceptible hosts (e.g., non-host vegetation or physically inaccessible plants). Notice that the preference P_{R_s} dynamically adapts to variations in plant population densities, thereby modulating vector behaviour and the resulting infection pressure. A single parameter p_R is used for both susceptible and infected reservoirs, under the assumption that infection does not substantially alter reservoir plant phenology. Consequently, vectors cannot differentiate between healthy and infected reservoir plants, and their feeding preference is assumed to be identical in both cases.

6.2.2 Crop plant dynamics

Crop plants represent economically valuable hosts that are vulnerable to infection. Similar to reservoir plants, their dynamics follow standard infection-recovery processes. Susceptible crop plants C_s become infected at a rate proportional to the density of infected vectors V_i, modulated by a transmission parameter i_C and the preference function P_{C_s}. Infected crop plants C_i may recover over time at a constant rate r_C, re-entering the susceptible class. The governing equations for crops are:

$$\begin{aligned} \dot{C}_s &= -i_C \cdot P_{C_s} \cdot V_i + r_C \cdot C_i, \\ \dot{C}_i &= i_C \cdot P_{C_s} \cdot V_i - r_C \cdot C_i. \end{aligned} \tag{6.3}$$

Here, P_{C_s} is the dynamically updated feeding preference of vectors for susceptible crop plants, and is defined as:

$$P_{C_s} = \frac{p_{C_s} \cdot C_s}{p_R \cdot R_s + p_R \cdot R_i + p_{C_s} \cdot C_s + p_{C_i} \cdot C_i + p_N \cdot N}. \tag{6.4}$$

This definition ensures that the feeding preference P_{C_s} adapts continuously to the state of the plant community, and thereby influences the infection of crop compartments.

6.2.3 Vector dynamics

Vector insects are responsible for acquiring and transmitting the pathogen while feeding on host plants and reservoirs. The vector population is split into susceptible individuals V_s and infected individuals V_i, whose dynamics are driven by acquisition, loss of infectivity, natural birth, and mortality.

Susceptible vectors V_s become infected through feeding on infected plants (specifically infected reservoir or infected crop hosts) with constant acquisition rate a and time-dependent preference functions P_{C_i} and P_{R_i}.

Similarly to P_{R_s}, P_{R_i} represents the preference of vectors for infected reservoir plants and is defined as

$$P_{R_i} = \frac{p_R \cdot R_i}{p_R \cdot R_s + p_R \cdot R_i + p_{C_s} \cdot C_s + p_{C_i} \cdot C_i + p_N \cdot N}, \tag{6.5}$$

while P_{C_i} is defined as

$$P_{C_i} = \frac{p_{C_i} \cdot C_i}{p_R \cdot R_s + p_R \cdot R_i + p_{C_s} \cdot C_s + p_{C_i} \cdot C_i + p_N \cdot N}, \tag{6.6}$$

and represents the dynamic feeding preference of vectors for infected crop plants.

Infected vectors V_i may lose infectivity at a constant rate i_{reg}, returning to the susceptible class. Additionally, all vectors are subject to birth and death processes. Birth occurs at a constant per capita rate f on the total vector population $(V_s + V_i)$, while death follows a quadratic density-dependent term with constant mortality rate m_V.

The resulting equations governing vector dynamics are:

$$\begin{aligned} \dot{V}_s &= -a(P_{C_i} + P_{R_i})V_s + i_{\text{reg}} \cdot V_i - m_V(V_s^2 + V_i \cdot V_s) + f(V_s + V_i), \\ \dot{V}_i &= a(P_{C_i} + P_{R_i})V_s - i_{\text{reg}} \cdot V_i - m_V(V_i^2 + V_i \cdot V_s). \end{aligned} \tag{6.7}$$

This formulation captures both the behavioural influence of host preference and the ecological constraints regulating vector population size and composition.

6.3 Analysis of the system with preferences

In this section, we first prove the local solution's existence, uniqueness, and non-negativity under suitable assumptions on the initial data. We then extend the analysis to show that the solution exists and is unique globally in time, while staying non-negative.

6.3.1 Local existence and uniqueness of the solutions

Let T be a finite positive real value, $J = (t_0, T)$ the time interval of simulation, and $R_{s_0}, R_{i_0}, C_{s_0}, C_{i_0}, V_{s_0}, V_{i_0}$ the initial values of the state variables $R_s(t)$, $R_i(t)$, $C_s(t)$, $C_i(t)$, $V_s(t)$, $V_i(t)$, respectively, for any $t \in J$. We define the state variable vector $\mathbf{x}(t)$ at time $t \in J$ and the initial vector $\mathbf{x_0}$ as

$$\mathbf{x}(t) = \begin{bmatrix} R_s(t) \\ R_i(t) \\ C_s(t) \\ C_i(t) \\ V_s(t) \\ V_i(t) \end{bmatrix}, \quad \mathbf{x_0} = \begin{bmatrix} R_{s_0} \\ R_{i_0} \\ C_{s_0} \\ C_{i_0} \\ V_{s_0} \\ V_{i_0} \end{bmatrix}. \tag{6.8}$$

Then we define the non-linear vector function

$$\mathbf{f}(\mathbf{x}(t)) = \begin{bmatrix} -i_R \cdot P_{R_s} \cdot V_i + r_R \cdot R_i \\ i_R \cdot P_{R_s} \cdot V_i - r_R \cdot R_i \\ -i_C \cdot P_{C_s} \cdot V_i + r_C \cdot C_i \\ i_C \cdot P_{C_s} \cdot V_i - r_C \cdot C_i \\ -a(P_{C_i} + P_{R_i})V_s + i_{\text{reg}} \cdot V_i - m_V(V_s^2 + V_i \cdot V_s) + f(V_s + V_i), \\ a(P_{C_i} + P_{R_i})V_s - i_{\text{reg}} \cdot V_i - m_V \cdot V_i(V_s + V_i) \end{bmatrix}, \tag{6.9}$$

where P_{R_s}, P_{R_i}, P_{C_s}, and P_{C_i} are defined in (6.2), (6.5), (6.4), and (6.6) respectively, and represent the time-dependent vector preferences for reservoirs and hosts. For the sake of clarity, we have written R_s instead of $R_s(t)$ and similarly for all the other state variables and preference functions. The coefficients $p_R, p_{C_s}, p_{C_i}, p_N \in (0, 1]$ are given fixed values that simulate the probability of an insect feeding on one type of plant rather than another in the event of having any type of plant completely available.

The Cauchy problem:

$$\begin{cases} \dot{\mathbf{x}}(t) = \mathbf{f}(\mathbf{x}(t)) \quad \forall t \in J \\ \mathbf{x}(t_0) = \mathbf{x}_0, \end{cases} \tag{6.10}$$

represents the abstract form of equations (6.1), (6.3), (6.7), completed with initial conditions.

Lemma 6.1. *Let the initial amount P_0 of all plant compartments (excluding the non-susceptible hosts N) be strictly positive, i.e.,*

$$P_0 = R_{s_0} + R_{i_0} + C_{s_0} + C_{i_0} > 0.$$

Then, for all $t \in J$, the total amount of plants (even excluding N) obtained solving (6.10) is conserved in time, i.e.,

$$R_s(t) + R_i(t) + C_s(t) + C_i(t) = P_0. \tag{6.11}$$

Proof. Note that the sum of each pair of ODEs in (6.1) and (6.3), associated with any plant compartments (reservoirs and crops, respectively), is null, i.e.,

$$\dot{R}_s(t) + \dot{R}_i(t) = 0, \qquad \dot{C}_s(t) + \dot{C}_i(t) = 0.$$

Thus,

$$\dot{R}_s + \dot{R}_i + \dot{C}_s + \dot{C}_i = 0, \tag{6.12}$$

which, combined with the initial conditions, implies the stated conservation law. □

Notice that the total amounts of reservoir plants and crop plants are conserved over time. We thus introduce the constant total amount of reservoirs and crops, respectively.

$$R_0 = R(t) = R_s(t) + R_i(t), \qquad C_0 = C(t) = C_s(t) + C_i(t), \quad \forall t \in J. \tag{6.13}$$

The model only allows transitions between susceptible and infected states, governed by the number of infected insects, vector preferences for plants, infection and recovery rates, and the current amount of each compartment.

Lemma 6.2. *Let the initial amount P_0 of all plant compartments (excluding the non-susceptible hosts N) be strictly positive. Moreover, let the coefficients $p_R, p_{C_s}, p_{C_i}, p_N$ be in $(0, 1]$.*

Then the denominator of the preference functions P_{R_s}, P_{R_i}, P_{C_s}, P_{C_i}, remains strictly positive for all $t \in J$, i.e.,

$$d(t) = p_R \cdot R_s(t) + p_R \cdot R_i(t) + p_{C_s} \cdot C_s(t) + p_{C_i} \cdot C_i(t) + p_N \cdot N > 0. \tag{6.14}$$

Proof. Let $\tilde{p} = \min\{p_R, p_{C_s}, p_{C_i}, p_N\} > 0$. Then, by using (6.11), we have the estimate

$$d(t) \geq \tilde{p} \cdot (R_s(t) + R_i(t) + C_s(t) + C_i(t) + N) = \tilde{p} \cdot (P_0 + N) > 0$$

for all $t \in J$. □

Theorem 6.3. *Let $A \subset \mathbb{R}^6$ be an open, bounded, connected set such that $\mathbf{x}_0 \in A$. Assume that R_{s_0}, R_{i_0}, C_{s_0}, C_{i_0}, V_{s_0}, and V_{i_0} are non-negative values with the first four not simultaneously null; $i_R, i_C, r_R, r_C, a, i_{reg}, m_V, f, N$ are non-negative values; p_R, p_{C_s}, p_{C_i}, $p_N \in (0,1]$ with $2p_R + p_{C_s} + p_{C_i} + p_N = 1$. Then there exists $\delta > 0$, depending on A, and a unique solution $\mathbf{x} : [t_0 - \delta, t_0 + \delta] \to A$ with $\mathbf{x} : t \mapsto \mathbf{x}(t)$, $\mathbf{x}(t_0) = \mathbf{x}_0$ of the Cauchy problem (6.10). Moreover, $\mathbf{x} \in C^1([t_0 - \delta, t_0 + \delta])$.*

Proof. The given hypotheses allow us to apply Lemmas 6.1 and 6.2. It follows that the denominator d of the preference functions is strictly positive for any $t \in J$ and this ensures that $\mathbf{f}$ is continuous on $\mathbb{R}^6$. Now, we compute the Jacobian matrix of $\mathbf{f}$. For greater clarity, we hide the dependence on t and express the derivatives $\frac{\partial f_i}{\partial x_j}$ in terms of the state variables $R_s, R_i, C_s, C_i, V_s, V_i$ and d (the latter is defined in (6.14)). We have:

$$\frac{\partial f_1}{\partial x_1} = \frac{i_R \cdot p_R \cdot V_i \,(p_R \cdot R_s - d)}{d^2} \qquad \frac{\partial f_1}{\partial x_2} = r_R + \frac{i_R \cdot p_R^2 \cdot R_s \cdot V_i}{d^2}$$
$$\frac{\partial f_2}{\partial x_1} = \frac{i_R \cdot p_R \cdot V_i \,(d - p_R \cdot R_s)}{d^2} \qquad \frac{\partial f_2}{\partial x_2} = -\frac{i_R \cdot p_R^2 \cdot R_s \cdot V_i}{d^2} - r_R$$
$$\frac{\partial f_3}{\partial x_1} = \frac{i_C \cdot p_{C_s} \cdot p_R \cdot C_s \cdot V_i}{d^2} \qquad \frac{\partial f_3}{\partial x_2} = \frac{i_C \cdot p_{C_s} \cdot p_R \cdot C_s \cdot V_i}{d^2}$$
$$\frac{\partial f_4}{\partial x_1} = -\frac{i_C \cdot p_{C_s} \cdot p_R \cdot C_s \cdot V_i}{d^2} \qquad \frac{\partial f_4}{\partial x_2} = -\frac{i_C \cdot p_{C_s} \cdot p_R \cdot C_s \cdot V_i}{d^2}$$
$$\frac{\partial f_5}{\partial x_1} = \frac{a \cdot p_R \cdot V_s \,(p_R \cdot R_i + p_{C_i} \cdot C_i)}{d^2} \qquad \frac{\partial f_5}{\partial x_2} = \frac{a \cdot p_R \cdot V_s \,(p_R \cdot R_i + p_{C_i} \cdot C_i - d)}{d^2}$$
$$\frac{\partial f_6}{\partial x_1} = -\frac{a \cdot p_R \cdot V_s \,(p_R \cdot R_i + p_{C_i} \cdot C_i)}{d^2} \qquad \frac{\partial f_6}{\partial x_2} = \frac{a \cdot p_R \cdot V_s \,(d - p_{C_i} \cdot C_i - p_R \cdot R_i)}{d^2}$$

$$\frac{\partial f_1}{\partial x_3} = \frac{i_R \cdot p_R \cdot p_{C_s} \cdot R_s \cdot V_i}{d^2} \qquad \frac{\partial f_1}{\partial x_4} = \frac{i_R \cdot p_R \cdot p_{C_i} \cdot R_s \cdot V_i}{d^2}$$
$$\frac{\partial f_2}{\partial x_3} = -\frac{i_R \cdot p_R \cdot p_{C_s} \cdot R_s \cdot V_i}{d^2} \qquad \frac{\partial f_2}{\partial x_4} = -\frac{i_R \cdot p_R \cdot p_{C_i} \cdot R_s \cdot V_i}{d^2}$$
$$\frac{\partial f_3}{\partial x_3} = \frac{i_C \cdot p_{C_s} \cdot V_i \,(p_{C_s} \cdot C_s - d)}{d^2} \qquad \frac{\partial f_3}{\partial x_4} = \frac{i_C \cdot p_{C_s} \cdot p_{C_i} \cdot C_s \cdot V_i}{d^2} + r_C$$
$$\frac{\partial f_4}{\partial x_3} = \frac{i_C \cdot p_{C_s} \cdot V_i \,(d - p_{C_s} \cdot C_s)}{d^2} \qquad \frac{\partial f_4}{\partial x_4} = -\frac{i_C \cdot p_{C_s} \cdot p_{C_i} \cdot C_s \cdot V_i}{d^2} - r_C$$
$$\frac{\partial f_5}{\partial x_3} = \frac{a \cdot p_{C_s} \cdot V_s \,(p_R \cdot R_i + p_{C_i} \cdot C_i)}{d^2} \qquad \frac{\partial f_5}{\partial x_4} = \frac{a \cdot p_{C_i} \cdot V_s \,(p_R \cdot R_i + p_{C_i} \cdot C_i - d)}{d^2}$$
$$\frac{\partial f_6}{\partial x_3} = -\frac{a \cdot p_{C_s} \cdot V_s \,(p_R \cdot R_i + p_{C_i} \cdot C_i)}{d^2} \qquad \frac{\partial f_6}{\partial x_4} = \frac{a \cdot p_{C_i} \cdot V_s \,(d - p_R \cdot R_i - p_{C_i} \cdot C_i)}{d^2}$$

$$
\begin{aligned}
&\frac{\partial f_1}{\partial x_5} = 0 && \frac{\partial f_1}{\partial x_6} = -\frac{i_R \cdot p_R \cdot R_s}{d} \\
&\frac{\partial f_2}{\partial x_5} = 0 && \frac{\partial f_2}{\partial x_6} = \frac{i_R \cdot p_R \cdot R_s}{d} \\
&\frac{\partial f_3}{\partial x_5} = 0 && \frac{\partial f_3}{\partial x_6} = -\frac{i_C \cdot p_{C_s} \cdot C_s}{d} \\
&\frac{\partial f_4}{\partial x_5} = 0 && \frac{\partial f_4}{\partial x_6} = \frac{i_C \cdot p_{C_s} \cdot C_s}{d} \\
&\frac{\partial f_5}{\partial x_5} = f - \frac{a\left(p_R \cdot R_i + p_{C_i} \cdot C_i\right)}{d} - m_V\left(2V_s + V_i\right) && \frac{\partial f_5}{\partial x_6} = i_{\text{reg}} + f - m_V \cdot V_s \\
&\frac{\partial f_6}{\partial x_5} = \frac{a\left(p_R \cdot R_i + p_{C_i} \cdot C_i\right)}{d} - m_V \cdot V_i && \frac{\partial f_6}{\partial x_6} = -(i_{\text{reg}} + 2m_V \cdot V_i + m_V \cdot V_s)
\end{aligned}
$$

Because $d(t) > 0$ for any $t \in J$ all the partial derivatives $\frac{\partial f_i}{\partial x_j}$ are well defined and continuous $\forall\, \mathbf{x} \in \mathbb{R}^6$. This implies that $\mathbf{f}$ is locally Lipschitz on any compact of $\mathbb{R}^6$. Then the thesis follows by applying the Cauchy-Lipschitz theorem (see, e.g., [10]). □

6.3.2 Global existence and uniqueness of the solutions

Let us now analytically evaluate the behaviour of our ODEs system to guarantee the existence and uniqueness of the global solution on J.

Before proceeding with the detailed proof, we note that although the primary goal is to prove the global non-negativity and boundedness of the solutions, the analysis will also reveal explicit lower and upper bounds within which the solutions must evolve. These bounds characterize the admissible region in the state space where the solutions are biologically and mathematically feasible.

Lemma 6.4. *Let* $\mathbf{x}$ *and* $\mathbf{f}$ *be defined in (6.8) and (6.9), respectively. If* $x_i(t) = 0$ *and* $x_j(t) \geq 0\, \forall j \neq i$, *then* $\dot{x}_i(t) \geq 0$, $\forall\, t > t_0$ *for which the solution* $\mathbf{x}(t)$ *of the Cauchy problem (6.10) exists.*

Proof. We analyse each equation $\dot{x}_i(t) = f_i(t, \mathbf{x}(t))$ of (6.10) under the assumption that the corresponding variable x_i is zero, while all others remain non-negative.

If there exists a time t such that $R_s(t) = 0$, then $P_{R_s}(t) = 0$, hence $\dot{x}_1(t) = \dot{R}_s(t) = r_R \cdot R_i(t) = r_R \cdot x_2(t) \geq 0$.

We proceed similarly with the other equations.

If $R_i(t) = 0$, then $-r_R \cdot R_i(t) = 0$ and the term $i_R \cdot P_{R_s}(t) \cdot V_i(t) \geq 0$. Thus $\dot{x}_2(t) = \dot{R}_i(t) \geq 0$.

If $C_s(t) = 0$, then $P_{C_s}(t) = 0$, and thus $\dot{x}_3(t) = \dot{C}_s(t) = r_C \cdot C_i(t) \geq 0$.

If $C_i(t) = 0$, then $-r_C \cdot C_i(t) = 0$, and $i_C \cdot P_{C_s}(t) \cdot V_i(t) \geq 0$. Thus $\dot{x}_4(t) = \dot{C}_i(t) \geq 0$.

If $V_s(t) = 0$, then all terms involving $V_s(t)^2$ or $V_s(t)$ vanish. Thus $\dot{x}_5(t) = \dot{V}_s(t) = i_{\text{reg}} \cdot V_i(t) + f \cdot V_i(t) \geq 0$.

If $V_i(t) = 0$, all terms involving $V_i(t)^2$ or $V_i(t)$ vanish. Thus $\dot{x}_6(t) = \dot{V}_i(t) = a(P_{C_i}(t) + P_{R_i}(t))V_s(t) \geq 0$. □

Theorem 6.5. *The solution* $\mathbf{x}(t)$ *of the problem (6.10) remains non-negative* $\forall t \in [t_0 - \delta, t_0 + \delta]$*, where* δ *has been introduced in Theorem 6.3.*

Proof. We proceed by contradiction. Suppose there exists a time $t^* \in (t_0, t_0 + \delta)$ such at least one component x_i of $\mathbf{x}$ is negative at time t^*.

Define

$$\bar{T} := \inf \{t > t_0 : x_i(t) \leq 0 \text{ for some } i \in \{1, \ldots, 6\}\}.$$

Because the solution $\mathbf{x}(t)$ is continuous (by Theorem 6.3) and the initial conditions are non-negative, at least one component $x_i(\bar{T}) = 0$, while all the others are non-negative.

Thus, by Lemma 6.4, we have $\dot{x}_i(\bar{T}) \geq 0$.

This implies that x_i cannot decrease and go below zero in a right neighborhood of $\bar{T}$, contradicting the existence of t^*.

Therefore, every component of $\mathbf{x}(t)$ remains non-negative for all $t \geq t_0$. □

Lemma 6.6. *If there exists a solution of (6.10) on an interval* $I \subseteq J$*, then* $V_s(t)$ *and* $V_i(t)$ *are bounded on* I*.*

Proof. We define

$$V(t) = V_s(t) + V_i(t)$$

and sum the two equations in (6.7). By hiding the dependence on t for simplicity, we obtain

$$\begin{aligned}\dot{V} = \dot{V}_s + \dot{V}_i &= -a(P_{C_i} + P_{R_i})V_s + i_{\text{reg}}V_i - m_V(V_s^2 + V_s \cdot V_i) + f(V_s + V_i) \\ &\quad + a(P_{C_i} + P_{R_i})V_s - i_{\text{reg}}V_i - m_V(V_i^2 + V_i \cdot V_s) \\ &= f(V_s + V_i) - m_V(V_s^2 + 2V_s \cdot V_i + V_i^2) = f \cdot V - m_V \cdot V^2.\end{aligned}$$

The equation $\dot{V} = f \cdot V - m_V \cdot V^2$, is a classical logistic equation with carrying capacity f/m_V. It can be solved analytically (see, e.g., [74]), provided that it is endowed with the initial conditions $V(t_0) = V_0$.

When $f \neq 0$, its explicit solution reads

$$V(t) = \frac{f \cdot V_0 \cdot e^{f(t-t_0)}}{f + m_V \cdot V_0\big(e^{f(t-t_0)} - 1\big)}, \tag{6.15}$$

and describes the logistic dynamics of the total vector population with intrinsic growth rate f and density-dependent mortality rate m_V. We recall that both m_V and f are non-negative parameters.

Let's start analyzing the case with $m_V \neq 0$. If $V_0 > f/m_V$, then V decreases asymptotically to the carrying capacity value $K = f/m_V > 0$; if $V_0 < f/m_V$, V grows asymptotically to K; while if $V_0 = f/m_V, V = V_0 = K \ \forall t > 0$. So, if $V_0 \geq 0$, we proved that $V(t)$ remains non-negative and bounded $\forall\, t > t_0$.

On the other hand, if mortality m_V is zero, which is a plausible scenario, then

$$V(t) = V_0\, e^{f(t-t_0)}, \tag{6.16}$$

i.e., the total number of insects grows exponentially, but it remains finite at finite times.

If, instead, $f = 0$ and $m_V \neq 0$, then

$$V(t) = \frac{V_0}{1 + m_V \cdot V_0 \cdot (t - t_0)}, \tag{6.17}$$

i.e., the total number of insects decreases and tends to zero.

Provided that the solution of system (6.10) exists at time $t > t_0$, thanks to Theorem 6.5, it holds that both $V_s(t)$ and $V_i(t)$ are non-negative. Because the solution $V(t)$ is bounded for any $t > t_0$, we conclude that $V_s(t)$ and $V_i(t)$ are individually bounded at time t . □

Lemma 6.7. *If there exists a solution of (6.10) on an interval $I \subseteq J$, then $R_s(t)$, $R_i(t)$, $C_s(t)$, and $C_i(t)$ are bounded on I.*

Proof. Each plant compartment $R_s(t)$, $R_i(t)$, $C_s(t)$, and $C_i(t)$ has been proved to be non-negative for every $t \in I$, thanks to Theorem 6.5. Because the total number of reservoir plants $R(t) = R_s(t) + R_i(t)$ and crop plants $C(t) = C_s(t) + C_i(t)$ remains constant for every $t \in I$, each of these variables remains bounded between 0 and the corresponding initial total amount of plants, R_0 or C_0, respectively. □

Now we can state the global existence and uniqueness theorem.

Theorem 6.8. *Under the same assumptions of Theorem 6.3, the Cauchy problem (6.10) admits a unique solution defined for all $t \in J$. Moreover, each component of the solution is non-negative and bounded in time.*

Proof. Let $\widetilde{X} = \sup_{t \in J} X(t) < +\infty$, $X \in \{R_s, R_i, C_s, C_i\}$, by Lemma 6.7, and $\widetilde{V} = \sup_{t \in J} V(t) < +\infty$ by Lemma 6.6. Then set $A := (0, \widetilde{R}_s) \times (0, \widetilde{R}_i) \times (0, \widetilde{C}_s) \times (0, \widetilde{C}_i) \times (0, \widetilde{V})^2$. By using the same arguments of Theorem 6.3, and by Theorem 6.5, the thesis follows. □

6.3.3 State variable bounds induced by initial data

We now determine some intervals in which the state variables of the problem (6.10) lie, only starting from the initial conditions and the problem parameters.

Analysis of reservoirs.

If $R_{s_0} = R_{i_0} = 0$, then $R(t) = R_0 = 0\ \forall t \in J$. Consequently, $R_s(t) = R_i(t) = 0$, for every $t \in J$ (we recall that they are always non-negative thanks to Theorem 6.5).

When instead, at least one between R_{s_0} and R_{i_0} is non-zero, the lowest possible solution R_s over the time interval is obtained in the worst-case scenario, i.e., when $\dot{R}_s$ is as negative as possible. This occurs when $P_{R_s}(t) = 1\ \forall t \in J$, which implies $R_i(t) = 0\,\forall t \in J$, so that $\dot{R}_s = -i_R V_i$. Whenever $P_{R_s} < 1$ it holds

$$\dot{R}_s \geq -i_R \cdot V_i.$$

By comparison theorems for ODEs (see [30]), we then have:

$$R_s(t) \geq R_{s_0} - i_R \int_{t_0}^{t} V_i(s)\, ds.$$

In particular, since $V_i(t)$ is non-negative, continuous and bounded on J, it holds

$$R_s(t) \geq R_{s_0} - i_R(t - t_0) \cdot \sup_{t \in J} V_i(t),$$

where $\sup_{t \in J} V_i(t)$ depends on the values of the parameters m_V, f, and the initial vector population $V_0 = V_{s_0} + V_{i_0}$. The following statements are derived from the concepts and results presented in Lemma 6.6, Lemma 6.7, and Theorem 6.3.

When $f = 0$ and $m_V \neq 0$, or when both $f \neq 0$ and $m_V \neq 0$ with $V_0 > \frac{f}{m_V}$, then $\sup_{t \in J} V_i(t) = V_0$ and, thanks to (6.13),

$$\max\{0, R_{s_0} - i_R V_0 (t - t_0)\} \leq R_s(t) \leq R_0 \quad \text{for any } t \in J. \tag{6.18}$$

When $m_V = 0$ and $f \neq 0$, since no a priori upper bound on $V_i(t)$ can be established, we have

$$0 \leq R_s(t) \leq R_0 \quad \text{for any } t \in J. \tag{6.19}$$

Finally, when $f \neq 0$, $m_V \neq 0$, and $V_0 \leq \frac{f}{m_V}$, we have $\sup_{t \in J} V_i(t) = f/m_V$ and

$$\max\left\{0, R_{s_0} - i_R \cdot \frac{f}{m_V}(t - t_0)\right\} \leq R_s(t) \leq R_0 \quad \text{for any } t \in J. \tag{6.20}$$

Now, we estimate the bounds for $R_i(t)$. Proceeding as above, observing that the first term in the right-hand side of $(6.1)_2$ is always non-negative, the worst-case scenario for R_i is $\dot{R}_i = -r_R R_i$, which occurs when the product $i_R P_{R_s} V_i = 0$.

In all the other cases, we have

$$\dot{R}_i \geq -r_R \cdot R_i.$$

Since $R_i(t) \geq 0$ for all $t \in J$, applying comparison theorems [30], this inequality yields:

$$R_i(t) \geq R_{i_0} \cdot e^{-r_R(t-t_0)} \quad \text{for any } t \in J.$$

Thus, recalling Lemma 6.1, we obtain the final estimate for the infected reservoirs solution

$$R_{i_0} \cdot e^{-r_R(t-t_0)} \leq R_i(t) \leq R_0 \quad \text{for all } t \in J. \tag{6.21}$$

Analysis of crops.

The previous considerations, made for the reservoir compartments R_s and R_i, also apply to the crop compartments C_s and C_i, since the functional form of the two ODEs couples is the same. Thus, resuming the corresponding cases (6.18), (6.19), and (6.20), we state

$$\max\left\{0, C_{s_0} - i_C \cdot (t-t_0) \sup_{t \in J} V_i(t)\right\} \leq C_s(t) \leq C_0 \quad \text{for any } t \in J, \tag{6.22}$$

and

$$C_{i_0} \cdot e^{-r_C(t-t_0)} \leq C_i(t) \leq C_0 \quad \text{for all } t \in J. \tag{6.23}$$

Analysis of vector compartments.

To derive a lower bound on $V_s(t)$, we estimate the worst-case scenario for $(6.7)_1$ by neglecting all non-negative contributions, i.e., we discard the recovery term $i_{\text{reg}} \cdot V_i$ and the birth term $f(V_s + V_i)$. Additionally, we assume maximal preference $P_{C_i} + P_{R_i} = 1$. Under these assumptions, we obtain the inequality:

$$\dot{V}_s \geq -a \cdot V_s - m_V(V_s^2 + V_i \cdot V_s).$$

If $m_V \neq 0$ and $V_0 = V_s(t_0) + V_i(t_0) > \frac{f}{m_V}$, in view of the analysis done in the proof of Lemma 6.6, $V(t) = V_s(t) + V_i(t)$ is a decreasing function, thus $-(V_s^2 + V_s \cdot V_i) \geq -V_0^2$ for any $t \in J$.

If $m_V \neq 0$ and $V_0 \leq \frac{f}{m_V}$, then $V(t)$ is an increasing function whose values belong to the interval $[V_0, \frac{f}{m_V})$, thus $-(V_s^2 + V_s \cdot V_i) \geq -\left(\frac{f}{m_V}\right)^2$.

In both cases, we obtain a linear differential inequality of the form

$$\dot{V}_s \geq -a \cdot V_s - m_V \cdot C,$$

where $C = \max\left\{V_0^2, (\frac{f}{m_V})^2\right\}$. Because the solution of $\dot{y} = -a \cdot y - m_V \cdot C$ with initial condition $y(t_0) = y_0$ reads $y(t) = y_0 + \frac{m_V \cdot C}{a} e^{-a(t-t_0)} - \frac{m_V \cdot C}{a}$, by comparison theorems [30], the susceptible vector population satisfies

$$\max\left\{0, (V_{s_0} + \frac{m_V \cdot C}{a})e^{-a(t-t_0)} - \frac{m_V \cdot C}{a}\right\} \leq V_s(t) \leq \sqrt{C} \quad \text{for all } t \in J. \tag{6.24}$$

If instead $m_V = 0$, the worst-case scenario is $\dot{V}_s \geq -a \cdot V_s$, thus by applying standard comparison theorems [30], it holds that $V_s(t) \geq V_{s_0} \cdot e^{-a(t-t_0)})$. Notice that now the maximum of $V_s(t)$ cannot be expressed a priori in terms of the initial conditions and parameters alone; however, we can exploit the fact that $V_s(t) + V_i(t) = V_0 \cdot e^{f \cdot t}$ (see (6.16)), thus

$$V_{s_0} \cdot e^{-a(t-t_0)} \leq V_s(t) \leq V_0 \cdot e^{f \cdot t} \quad \text{for all } t \in J. \tag{6.25}$$

We conclude this section by analyzing the infected vector compartment $V_i(t)$. In this case, the worst-case scenario

$$\dot{V}_i \geq -i_{\text{reg}} \cdot V_i - m_V(V_i^2 + V_i \cdot V_s)$$

is obtained by neglecting the positive term in the right-hand side of $(6.7)_2$. By applying the same arguments as in the case of $V_s(t)$, we obtain that: if $m_V \neq 0$, then

$$\max\left\{0, (V_{i_0} + \frac{m_V \cdot V_0^2}{i_{\text{reg}}})e^{-i_{\text{reg}}(t-t_0)} - \frac{m_V \cdot V_0^2}{i_{\text{reg}}}\right\} \leq V_i(t) \leq V_0 \quad \text{for all } t \in J, \tag{6.26}$$

otherwise:

$$V_{i_0} \cdot e^{-i_{\text{reg}}(t-t_0)} \leq V_i(t) \leq V_0 \cdot e^{f \cdot t} \quad \text{for all } t \in J. \tag{6.27}$$

6.3.4 Equilibrium points and Jacobian analysis

To analyse the long-term behaviour of the system (6.10), we compute the equilibrium points, i.e., the solutions of $\mathbf{f}(t, \mathbf{x}(t)) = \mathbf{0}$. The equilibrium points $\bar{\mathbf{x}} = (\bar{R}_s, \bar{R}_i, \bar{C}_s, \bar{C}_i, \bar{V}_s, \bar{V}_i)$ satisfy the system:

$$\begin{cases}
\bar{R}_s = \dfrac{r_R \cdot \bar{R}_i \left(p_R \cdot \bar{R}_i + p_{C_s} \cdot \bar{C}_s + p_{C_i} \cdot \bar{C}_i + p_N \cdot N\right)}{p_R \left(i_R \cdot \bar{V}_i - r_R \cdot \bar{R}_i\right)} \\
\bar{R}_i = \dfrac{-r_R \left(p_R \cdot \bar{R}_s + p_{C_s} \cdot \bar{C}_s + p_{C_i} \cdot \bar{C}_i + p_N \cdot N\right) \pm \sqrt{r_R^2 \left(p_R \cdot \bar{R}_s + p_{C_s} \cdot \bar{C}_s + p_{C_i} \cdot \bar{C}_i + p_N \cdot N\right)^2 + 4 r_R \cdot p_R^2 \cdot i_R \cdot \bar{R}_s \cdot \bar{V}_i}}{2 p_R \cdot r_R} \\
\bar{C}_s = \dfrac{r_C \cdot \bar{C}_i \left(p_R \cdot \bar{R}_s + p_R \cdot \bar{R}_i + p_{C_i} \cdot \bar{C}_i + p_N \cdot N\right)}{p_{C_s} \left(i_C \cdot \bar{V}_i - r_C \cdot \bar{C}_i\right)} \\
\bar{C}_i = \dfrac{-r_C \left(p_R \cdot \bar{R}_s + p_R \cdot \bar{R}_i + p_{C_s} \cdot \bar{C}_s + p_N \cdot N\right) \pm \sqrt{r_C^2 \left(p_R \cdot \bar{R}_s + p_R \cdot \bar{R}_i + p_{C_s} \cdot \bar{C}_s + p_N \cdot N\right)^2 + 4 r_C \cdot p_{C_s} \cdot p_{C_i} \cdot i_C \cdot \bar{C}_s \cdot \bar{V}_i}}{2 p_{C_i} \cdot r_C} \\
\bar{V}_s = \dfrac{f - m_V \cdot \bar{V}_i - \frac{a}{d}\left(p_{C_i} \cdot \bar{C}_i + p_R \cdot \bar{R}_i\right) \pm \sqrt{\left[f - m_V \cdot \bar{V}_i - \frac{a}{d}\left(p_{C_i} \cdot \bar{C}_i + p_R \cdot \bar{R}_i\right)\right]^2 + 4 m_V \cdot \bar{V}_i \left(i_{\text{reg}} + f\right)}}{2 m_V} \\
\bar{V}_i = \dfrac{-i_{\text{reg}} - m_V \cdot \bar{V}_s \pm \sqrt{\left(i_{\text{reg}} + m_V \cdot \bar{V}_s\right)^2 + 4 m_V \cdot \bar{V}_s \frac{a}{d}\left(p_{C_i} \cdot \bar{C}_i + p_R \cdot \bar{R}_i\right)}}{2 m_V}
\end{cases} \tag{6.28}$$

where

$$\bar{d} = p_R \cdot \bar{R}_s + p_R \cdot \bar{R}_i + p_{C_s} \cdot \bar{C}_s + p_{C_i} \cdot \bar{C}_i + p_N \cdot N.$$

Due to the implicit form of (6.28), its solution cannot be computed analytically. Thus, we apply an iterative quasi-Newton method (in particular, we used MATLAB function fsolve) and compute an accurate numerical approximation of the equilibrium points $\bar{\mathbf{x}}$ under biologically realistic parameters up to a tolerance $\epsilon = 10^{-6}$. To preserve the biological constraint that the total number of host plants remains constant over time, we rescale the susceptible and infected subpopulations at each iteration so that their sum remains equal to the initial total.

Once an equilibrium point is obtained numerically, we analyse its local stability by linearizing the system at equilibrium. Specifically, we evaluate the Jacobian matrix $\mathcal{J}_{\mathbf{f}}(\bar{\mathbf{x}}) = [\frac{\partial f_i}{\partial x_i}(\bar{\mathbf{x}})]$, whose components are defined inside the proof of Theorem 6.3. Its entries express the sensitivity of the state variables to small perturbations on data.

The analysis of the eigenvalues λ_i of $\mathcal{J}_{\mathbf{f}}(\bar{\mathbf{x}})$ sheds light on the local stability, more precisely, if $Re(\lambda_i) < 0$ for any $i = 1, \ldots, 6$, the equilibrium is locally asymptotically stable (see, e.g., [18, Ch.4]) for formal definitions of local stability and uniqueness), otherwise it is unstable. Moreover, linearization provides theoretical insight into the dynamics near equilibrium points. Indeed, denoting by

$\|\mathcal{J}_{\mathbf{f}}((\bar{\mathbf{x}}))\| = \sqrt{\lambda_{\max}(\mathcal{J}_{\mathbf{f}}((\bar{\mathbf{x}}))^T \mathcal{J}_{\mathbf{f}}((\bar{\mathbf{x}})))}$ the spectral norm of the Jacobian at the equilibrium point $(\bar{\mathbf{x}})$, if $\|\mathcal{J}_{\mathbf{f}}((\bar{\mathbf{x}}))\| < 1$, then Banach's fixed-point theorem ensures that the equilibrium point is locally unique and attracting (see [7]).

For the initial conditions $R_{s_0} = 213$, $R_{i_0} = 53$, $C_{s_0} = 107$, $C_{i_0} = 27$, $V_{s_0} = 58800$, and $V_{i_0} = 1200$, and using the parameter values reported in Table 5, the quasi-Newton method converges to the following equilibrium point:

$\bar{R}_s = 38.13, \bar{R}_i = 227.87, \bar{C}_s = 34.77, \bar{C}_i = 99.24, \bar{V}_s = 13928.51, \bar{V}_i = 44571.49.$

The obtained results agree with the asymptotic values of the solution of problem (6.10). All the eigenvalues of the Jacobian matrix evaluated at this point have non-positive real parts, indicating a marginally stable equilibrium. The spectral norm of the Jacobian is approximately 0.0525, thus, we can state that this equilibrium point is locally unique.

6.4 Model Applications

The proposed model was applied to the epidemiological context of *X. fastidiosa* outbreaks in olive groves in the Apulia region, Southern Italy.

Transmission probabilities from infected vectors to both olive trees (i_C) and reservoir plants (i_R) were assumed to be equal. The value was defined based on laboratory data from Cornara et al. [53], and further calibrated through preliminary simulation trials, resulting in a daily transmission rate of 3.49×10^{-4} day^{-1}. This parameter incorporates plant susceptibility and failed infection attempts during vector–host interactions. The

recovery rates of infected olive trees (r_C) and reservoir plants (r_R) were assumed to be equal, due to the absence of specific data for Olive Quick Decline Syndrome (OQDS). Nonetheless, recognizing that not all new infections persist, due to plant immune responses or unfavourable environmental conditions, such as vessel occlusion or suboptimal vector–host interactions, a daily recovery rate of 0.005 day^{-1} was considered biologically plausible. The rate of vector acquisition from infected plants was parameterized using experimental observations of *Philaenus spumarius* (Hemiptera: Aphrophoridae) feeding on naturally infected olive trees, as reported by Bodino et al. [84], Cavalieri et al. [63], Cornara et al. [53]. The resulting mean acquisition rate was estimated as 0.078 day^{-1}.

The density-dependent vector mortality rate (m_V) was set to 10^{-7}, corresponding to a carrying capacity of approximately 1000 individuals per square meter, based on maximum observed population densities of *P. spumarius* in European ecosystems (see [17]). The vector birth rate (f) was derived from fecundity estimates provided by Silva and Rodrigues [45], and defined as 0.00585 $\text{vectors}^{-1}\cdot\text{day}^{-1}$. To account for the univoltine life cycle of *P. spumarius*, in which adult populations are renewed annually and no vertical transmission of the bacteria from the parents to the offspring, a constant infectivity loss rate (i_{reg}) was implemented to reset the proportion of infected vectors. This parameter was set to 0.00588 day^{-1}, corresponding to an average adult lifespan of 170 days under Apulian environmental conditions ([99], [62]).

Vector host preference parameters ($p_N, p_R, p_{C_s}, p_{C_i}$) were estimated using monitoring data of adult *P. spumarius* across different vegetation types such as olive trees, herbaceous vegetation, and woody shrubs [62, 63]. The average proportion of vectors observed on each plant type was used to define the corresponding preference parameters, as summarized in Table 5. In particular, the preference for infected olive trees was set to half that for not infected olive trees, in order to account for their reduced suitability and attractiveness due to symptom expression (see [34]).

A numerical analysis was carried out to explore how vector preferences for infected crop plants influence the epidemic dynamics. Specifically, the ratio of vector preference for susceptible and infected crops (p_{C_s}/p_{C_i}) was varied between 1 and 10, simulating decreasing levels of vector preference for infected plants. This can represent different levels of symptom severity of infected plants, which can alter their attractiveness to vectors. For each scenario, the equilibrium proportions of infected crops and infected vectors were computed. Similarly, the effect of vector preference for non-susceptible vegetation (p_N) was assessed by varying this parameter from 0.1 to 0.8. The dynamics of crop and vector infection prevalence were tracked at seven distinct time points to evaluate both the magnitude and the rate of epidemic progression toward equilibrium.

The impact of four management strategies on the epidemiological dynamics of *X. fastidiosa* in olive systems was also investigated through numerical simulations (see Table 5): (1) chemical and biological vector control, (2) *X. fastidiosa* control in infected olive trees, (3) the adoption of resistant or tolerant olive cultivars, (4) ground cover

management. Each strategy was modelled through specific modifications to the system's parameters.

Chemical and biological vector control (e.g., pesticides including those with deterrent or repellent effects on vector feeding behaviour) was implemented in the model as an increase in vector mortality rate and a decrease in transmission-related parameters, particularly the biting rate and thus the probabilities of vector acquisition and crop inoculation.

Control actions targeting *X. fastidiosa* within-host plants—including antimicrobial applications, biocontrol agents, or treatments promoting plant immune responses—were modelled as increasing the recovery rate of infected crops and reducing the acquisition and inoculation probabilities.

The use of resistant or tolerant olive cultivars was incorporated via a reduction in the inoculation probability from infected vectors, a decrease in crop attractiveness to vectors (see [103]), and an increase in the crop recovery rate.

Finally, ground cover management, including practices such as soil tillage, mowing, or the introduction of non-preferred cover crops, was assumed to reduce the vector birth rate (e.g., lower availability or suitability of substrates for oviposition, and negative effect on fecundity and preimaginal survival), increase vector mortality (e.g., altering microhabitats or exposing vectors to unfavourable conditions), and lower preference for ground vegetation, as reflected by a reduced p_N, associated with non-susceptible host plants.

To assess the influence of each management strategy, numerical simulations were performed by simultaneously varying two of the affected parameters across a defined range, spanning from the baseline scenario (i.e., absence of control) to the maximum effect achievable by the corresponding intervention. In each simulation set, the third parameter associated with the strategy was held constant to isolate the effects of the two other varying parameters under investigation. For every combination of parameter values, the model was run to equilibrium, and the resulting proportions of infected crops and infected vectors at the asymptotic steady state were recorded as outcome variables.

Simulations were conducted using a representative area unit of one hectare, populated with 100 olive trees (100 trees $\cdot$ ha^{-1}) and an initial infection prevalence of 1%. Reservoir vegetation was assumed to be composed of 20 plants in total, being 15 susceptible and 5 initially infected. The density of non-susceptible host vegetation was set to 120 units, representing a combination of ground cover plants, shrubs, and trees. Specifically, it was assumed that ground cover vegetation occupied the entire hectare surface, presenting a biomass equivalent to that of olive trees, while the shrubs and trees were assumed to be present in a similar density as the reservoir vegetation (i.e., 20 plant units). The initial vector population was set to 5 adult insects per square meter, in line with estimates by [64], resulting in a total of 50,000 susceptible vectors and 100 initially infected individuals.

Table 5: Baseline parameter values used in the epidemiological model, along with the ranges explored under the implementation of management strategies (values shown in brackets). Parameters influenced by control strategies are marked with a "x" in the corresponding column: (1) Vector control, (2) *X. fastidiosa* control within infected olive trees, (3) Adoption of resistant or tolerant olive cultivars, and (4) Ground cover management.

Par.	Description	Baseline value	Tested range	Man. strategies			
				1	2	3	4
i_R	Inoculation rate of reservoir plants	3.49×10^{-4}					
i_C	Inoculation rate of olive trees	3.49×10^{-4}	$[10^{-5}, 3.49 \times 10^{-4}]$	✗	✗	✗	
r_R	Disease recovery rate of reservoir plants	5×10^{-3}					
r_C	Disease recovery rate of olive trees	5×10^{-3}	$[5 \times 10^{-3}, 10^{-1}]$		✗	✗	
a	Vector acquisition rate	7.79×10^{-2}	$[10^{-3}, 7.79 \times 10^{-2}]$	✗	✗		
m_V	Density-dependent vector mortality rate	10^{-7}	$[10^{-7}, 10^{-6}]$	✗	✗		✗
f	Vector birth rate	5.85×10^{-3}	$[10^{-4}, 5.85 \times 10^{-3}]$	✗			
i_{reg}	Infection regression rate from vectors	5.88×10^{-3}					
p_N	Preference for non-susceptible hosts	3.983×10^{-1}	$[10^{-3}, 3.983 \times 10^{-1}]$				✗
p_R	Preference for reservoir plants	2.215×10^{-1}					
p_{C_s}	Preference for susceptible olive trees	1.058×10^{-1}	$[10^{-2}, 1.058 \times 10^{-1}]$				✗
p_{C_i}	Preference for infected olive trees	5.29×10^{-2}	$[5 \times 10^{-3}, 5.29 \times 10^{-2}]$				✗

6.5 Numerical Simulations

The model simulation results, obtained using the baseline parameter values, are shown in Figure 44. In this scenario, the number of infected olive and reservoir plants reached equilibrium within the second year of simulation, stabilizing at approximately 80% and 95% infection prevalence, respectively. The total vector population gradually increased, reaching a maximum density of approximately 6 individuals per square meter, of which approximately 50% were infected at equilibrium.

Analysis of vector preference for infected olive trees revealed that lower attractiveness of infected hosts resulted in reduced infection prevalence in both olives and vectors, with vector infection levels showing greater sensitivity to this parameter (Figure 45). The decrease in prevalence tended to stabilize when the preference ratio p_{C_s}/p_{C_i} was higher than four. This limited response is likely due to the continued availability of infected reservoir vegetation, which sustained vector acquisition of the pathogen despite reduced interaction with infected crop hosts.

A higher attractiveness of the vector population for non-susceptible hosts contributed to a reduction in the infection prevalence of both olive trees and vectors (Figure 46). For values of p_N above 0.3, the prevalence dynamics required a longer period to reach the asymptotic equilibrium (at $t = 1000$), indicating a slower epidemiological progression.

Vector control strategies that combined a reduced capacity a of vectors to acquire *X. fastidiosa* with increased vector mortality m_V emerged as among the most effective

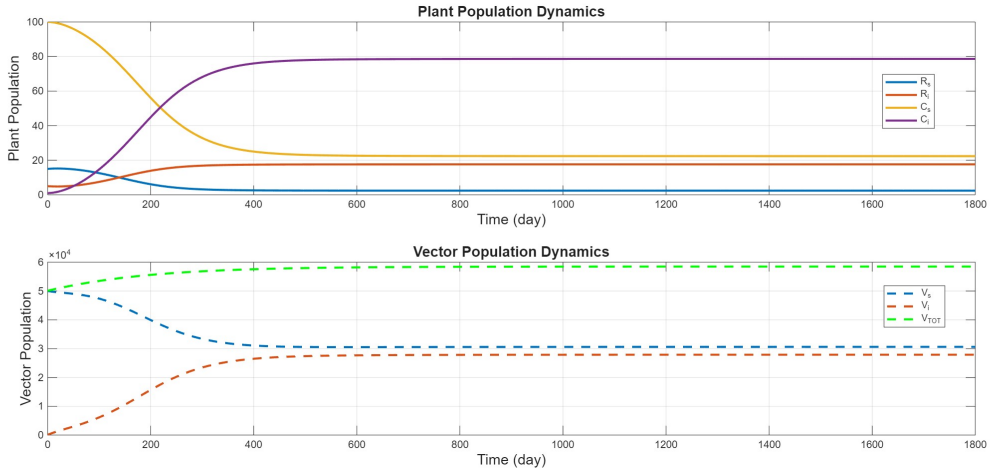


Figure 44: Baseline model simulation of *Xylella fastidiosa* epidemiological dynamics in olive grove agroecosystems in Apulia, Italy; the upper plot shows the dynamics of olive trees and reservoir vegetation compartments, while the lower one illustrates the vector population dynamics

measures for limiting disease spread, resulting in equilibrium infection levels in olive trees falling below its initial prevalence of 1% (Figure 47a and 47c). Interestingly, the prevalence of infected vectors was less sensitive to variations in the inoculation rate i_C than to changes in the acquisition rate (a), as indicated by the near-vertical isolines in Figure 47f.

X. fastidiosa control strategies that increase the recovery rate r_C of infected olive trees, when combined with reduced efficiency of bacterial acquisition by vectors a or lower inoculation success i_C, were highly effective in limiting infection prevalence among olive trees (equilibrium prevalence below 0.01; Figure 48b, 48c). In contrast, the prevalence of infected vectors was only marginally affected by the combined effect of increased recovery and reduced inoculation rates (Figure 48f), as vectors could still acquire the bacterium from infected reservoir plants.

The combined effect of increased recovery and reduced vector preference for olive trees, achieved through the adoption of resistant or tolerant cultivars (Figure 49b), produced outcomes comparable to those obtained by combining increased recovery with reduced inoculation efficiency (Figure 49c). Notably, although the use of resistant or tolerant cultivars reduced the proportion of infected crops and the overall availability of inoculum, it had a limited impact on the prevalence of infected vectors (Figure 49d–49f), since this strategy does not impair the ability of vectors to acquire the bacterium from infected reservoir plants.

Ground cover management significantly reduced the prevalence of infection in both

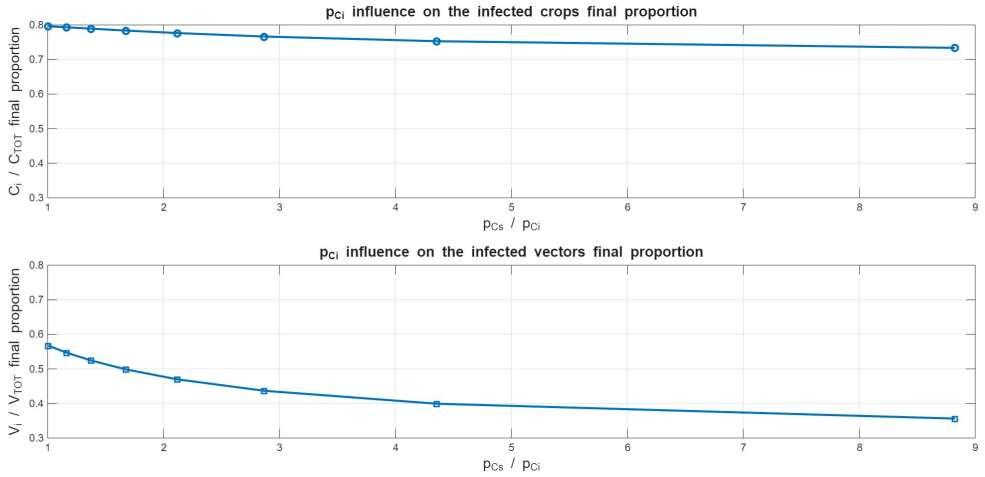


Figure 45: Effect of increasing rates of p_{C_s} per p_{C_i} in the prevalence of infected olive trees (upper plot) and vectors (bottom plot) at the asymptotic equilibrium

olive trees and vectors when it led to higher vector mortality and lower birth rates (Figures 50a, 50d). In contrast, the isolated effect of a reduced birth rate alone had a limited influence on epidemic dynamics. Furthermore, sowing less-preferred ground cover vegetation-that is, reducing p_N-may unintentionally increase infection prevalence if the selected species fail to promote a reduction in vector populations (Figures 50b, 50e), as vectors may then concentrate their activity on olive and reservoir plants.

6.6 Discussion and conclusion

We have proposed a compartmental model to describe the epidemiological dynamics of a vector–borne plant disease, explicitly incorporating vector–host preference patterns. The resulting system of non-linear ODEs has been thoroughly analysed under biologically meaningful assumptions, and several fundamental mathematical properties were rigorously established, demonstrating the robustness and reliability of the model.

We proved the local and global existence and uniqueness of solutions of the Cauchy problem, ensuring that the model is well-posed and its predictions are mathematically sound. The system preserves non-negativity and boundedness of all state variables over time, guaranteeing consistency with biological realism. Moreover, explicit bounds derived from initial conditions provide analytical insight into the long-term behaviour of the system.

Jacobian-based analyses around equilibrium points, together with spectral criteria, reinforce the internal consistency of the model and allow characterization of local stability in relation to biologically relevant parameters. The incorporation of preference-driven

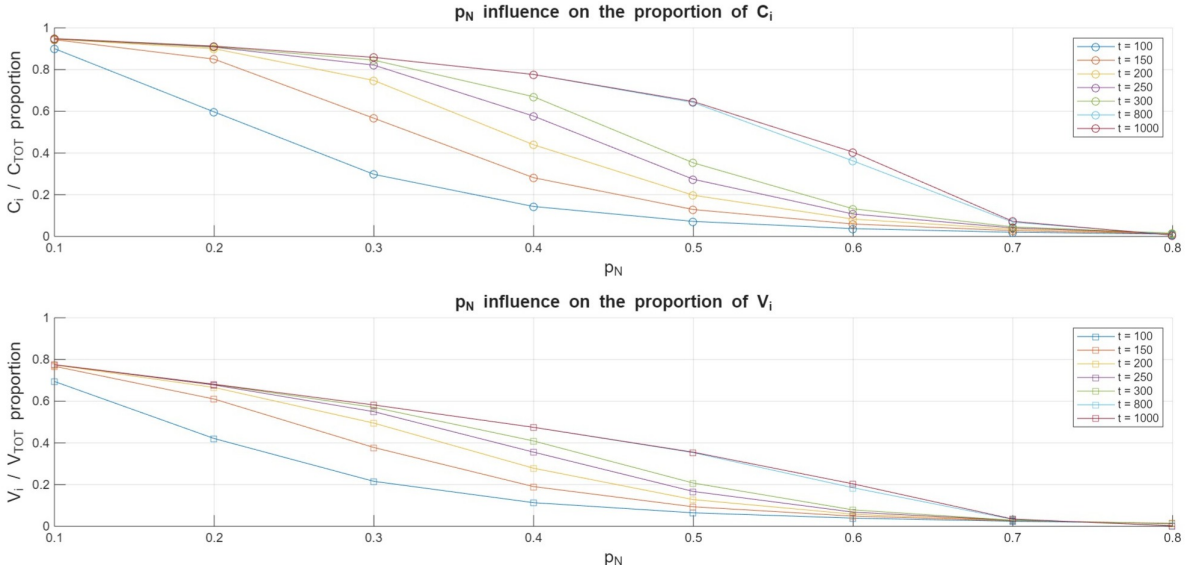


Figure 46: Effect of increasing rates of p_N in the prevalence of infected olive trees (upper plot) and vectors (bottom plot) at different time points until the asymptotic equilibrium at t = 1000

dynamics has been successfully integrated into a coherent and stable mathematical framework.

These analytical results not only validate the model theoretically but also lay the foundation for future developments. The model already supports meaningful biological applications and can serve as a base for extensions, such as the formulation of optimal control strategies. Overall, it constitutes a reliable quantitative framework for describing vector–host–pathogen interactions in agroecosystems and predicting the associated epidemiological dynamics.

From the model application to the *X. fastidiosa* case study, numerical simulations provided valuable information on the role of vector–host plant interactions in shaping the epidemiological dynamics in olive agroecosystems. Lower vector preferences for infected olive trees showed limited effectiveness in reducing crop infection when attractive, infectious reservoir vegetation remained available in the landscape, a finding consistent with [42].

Moreover, the availability of highly preferred non-susceptible vegetation significantly slowed epidemic progression and reduced infection prevalence at equilibrium. These results support the hypothesis that agroecosystems where vectors can find alternative non-host plants can reduce vector–olive contact rates and control pathogen transmission (see [101]). For resistant or tolerant cultivars, plant attractiveness to vectors emerged as a key trait influencing infection dynamics, especially when combined with lower infection rates and higher recovery capacities. However, simulation results indicated that management strategies focusing exclusively on protecting the crop host may have limited impact

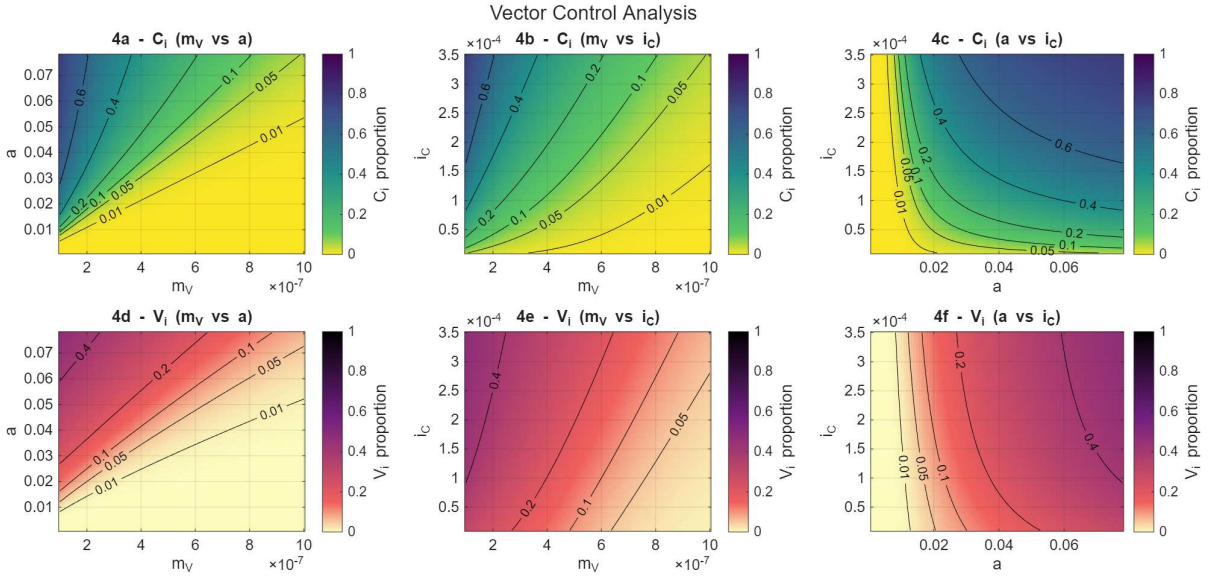


Figure 47: Effect of vector control measures on the prevalence of infected olive trees (upper plots) and vectors (bottom plots) at the asymptotic equilibrium; the impact was assessed through pairwise combinations of parameters affected by vector control: (m_V, a) - plots a and d, (m_V, i_C) - plots b and e, and (a, i_C) - plots c and f

on the prevalence of infected vectors. This pattern arises from the persistent presence of infected reservoir vegetation, which continues to serve as a source of bacterial inoculum for the vector population.

Incorporating dynamic host preferences into the model provides a nuanced understanding of vector–host interactions and their impact on disease spread. This framework highlights that management strategies directly targeting *X. fastidiosa* within the plant can be considerably more effective when combined with an understanding of vector behaviour.

Overall, our framework highlights how vector–host interactions and landscape composition shape the dynamics of vector–borne plant diseases. By capturing the interplay between vector behaviour, host susceptibility, and agroecosystem structure, it provides insights for developing integrated management strategies that enhance both disease control and the resilience of agricultural landscapes.

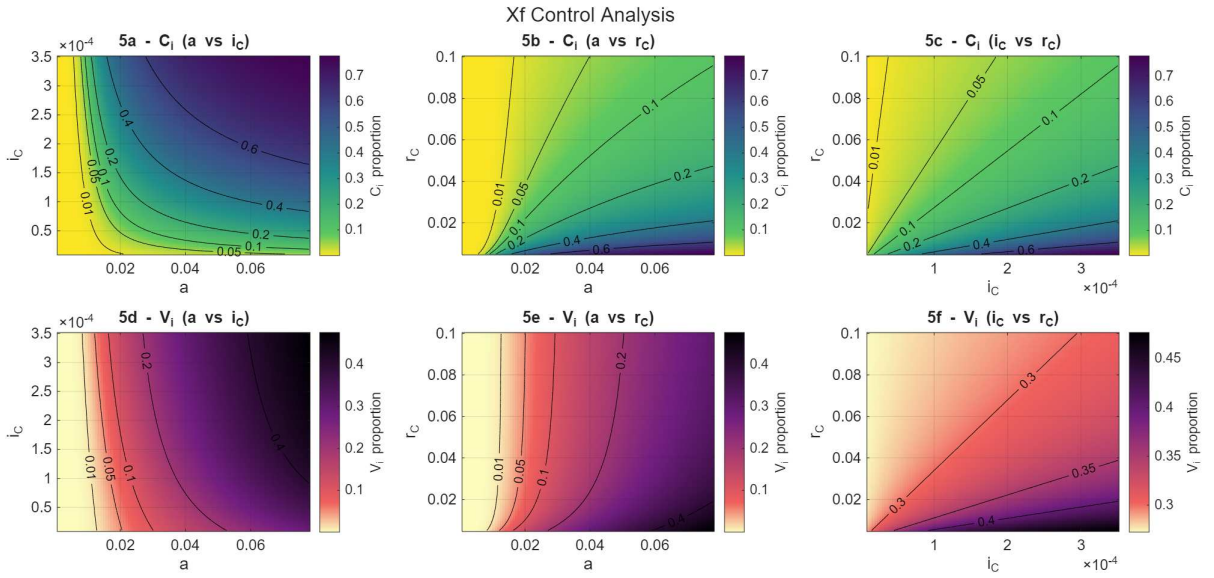


Figure 48: Effect of *Xylella fastidiosa (Xf)* control measures targeting infected olive trees on the prevalence of infection in olive trees (upper plots) and vectors (bottom plots) at the asymptotic equilibrium; the impact was assessed through pairwise combinations of parameters affected by *Xf* control: (a, i_C) - plots a and d, (a, r_C) - plots b and e, and (i_C, r_C) - plots c and f

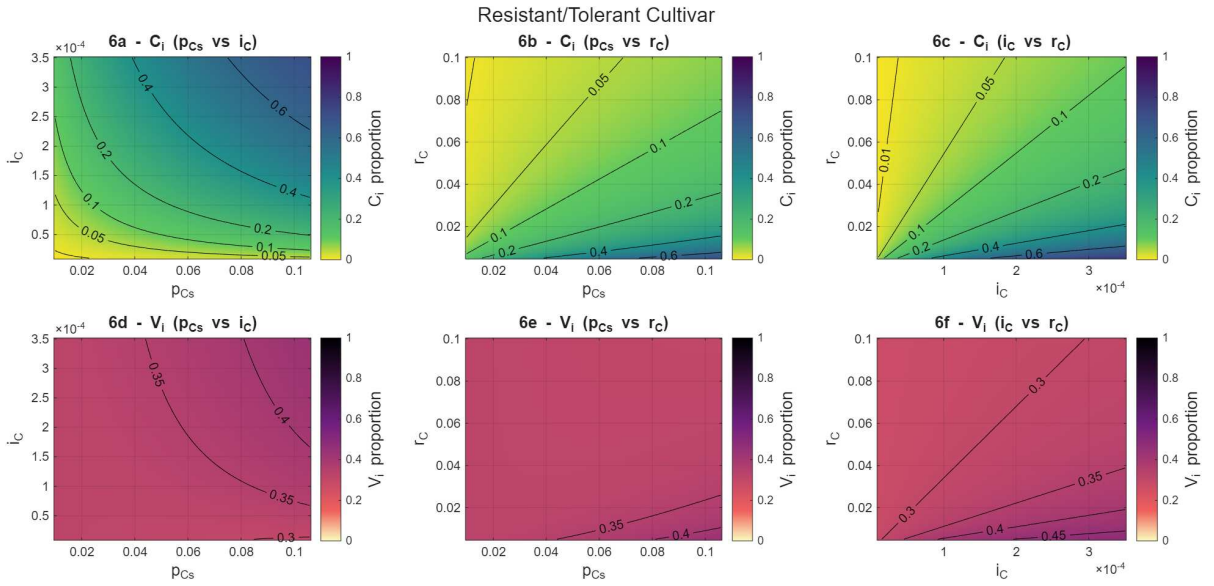


Figure 49: Effect of the adoption of resistant or tolerant olive cultivars on the prevalence of infection in olive trees (upper plots) and vectors (bottom plots) at the asymptotic equilibrium; the impact was assessed versus pairwise combinations of parameters affected by cultivar resistance or tolerance: (p_{C_s}, i_C) - plots a and d, (p_{C_s}, r_C) - plots b and e, and (i_C, r_C) - plots c and f)

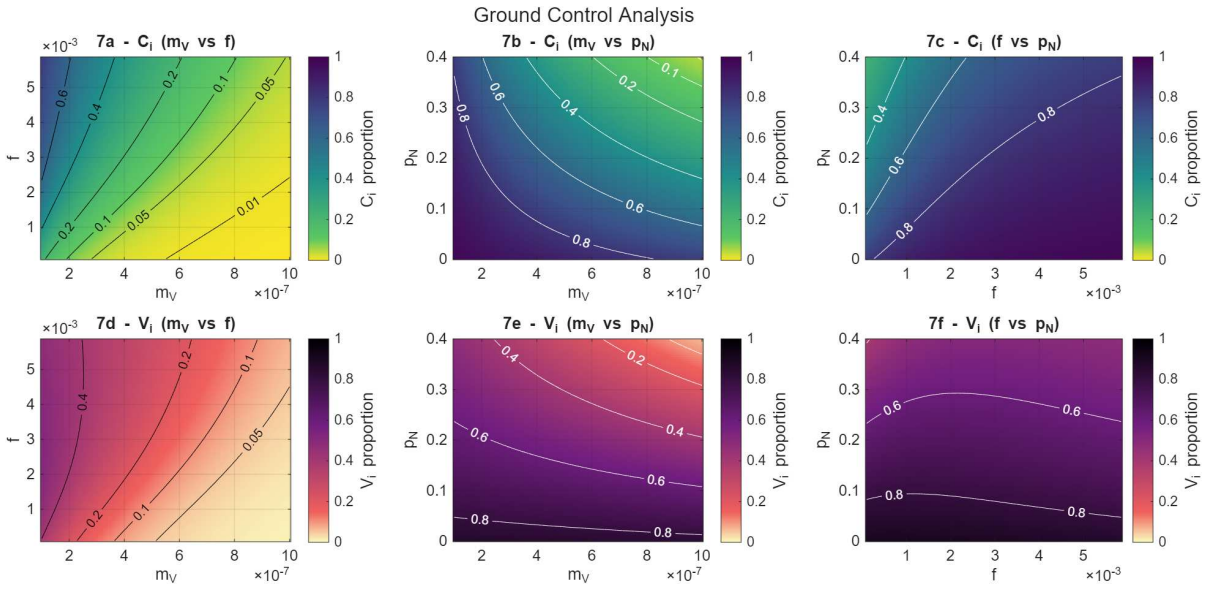


Figure 50: Effect of ground cover management on the prevalence of infection in olive trees (upper plots) and vectors (bottom plots) at the asymptotic equilibrium; the impact was assessed through pairwise combinations of parameters affected by ground control: (m_V, f) - plots a and d, (m_V, p_N) - plots b and e, and (f, p_N) - plots c and f

7

Coupled Kolmogorov model for bacterial spread in grapevine

In this chapter, we consider and analyse a mathematical model recently proposed by G. Gilioli [106] and presented in its preliminary form at the 14th conference of the European Foundation for Plant Pathology (2–5 June 2025, Uppsala, Sweden). This model aims to describe how a bacterial population spreads inside the conducting tissues of a plant, with a specific focus on grapevine. Indeed, in Northern Italy, for instance, *Xylella fastidiosa* has begun to seriously affect grapevine, and understanding how the bacterial load moves between different parts of the plant may help identify, e.g., when it is more effective to prune infected branches. Since branches and roots are in continuous physiological communication, a model that tracks the bacterial load in both compartments and captures their mutual influence can provide actionable information for management.

To represent this bio–epidemiological situation, we adopt a pair of Kolmogorov-type evolution equations, one for the distribution of bacterial load in the branches and one for the roots. The key modelling feature is that the transport component in each equation does not depend only on time and bacterial load coordinate, but also on the solution of the *other* equation. In other words, the flux in the branches is modulated by the current bacterial state of the roots, and vice versa. This two-way coupling reflects the biological exchange between the two plant compartments and yields a model with good descriptive and predictive capabilities. Some illustrative results and qualitative behaviours produced by this coupled formulation will be reported in Section 7.6.

From the mathematical viewpoint, our strategy is the following. In Section 7.2 we first study a linear, decoupled version of the Kolmogorov system and prove existence and uniqueness of weak solutions. We then use these results to treat the fully coupled non-linear problem in Section 7.3. In Section 7.5 we describe the discretisation scheme adopted for the numerical approximation, while the last Section 7.6 reports the numerical results for a representative test case.

Main modelling assumptions and scope. The system that is the core of this model is built to represent within-host spread of a xylem-limited bacterium by combining two interacting plant compartments (branches and roots) and describing, in each of them, the heterogeneity of infection levels through a continuous bacterial-load coordinate. The variable $x \in \Omega$ is interpreted as the $\log_{10}$ (bacterial load), restricted to a bounded interval $\Omega = (x_{\min}, x_{\max})$ that represents biologically meaningful lower and upper limits (from virtually uninfected tissue to a carrying-capacity regime). The unknowns $\phi_B(t, x)$ and $\phi_R(t, x)$ are non-negative density distributions of biomass with respect to x, so that

$\phi_{(\cdot)}(t,x)\,dx$ measures the amount of tissue whose load lies in $(x, x+dx)$.

The terms S_B and S_R encode the net drift of bacterial load in each compartment (growth, regression and translocation effects). The key modelling hypothesis is the two-way coupling: bacteria can move bidirectionally through the connected xylem network, allowing both upward transport from roots to branches and vice-versa. A constant diffusion coefficient $\mu > 0$ is included as a phenomenological variability term acting on the bacterial-load axis. Boundary conditions are imposed to prevent artificial gain/loss of biomass through the extremes of Ω. Pruning is treated as an impulsive removal of branch biomass at prescribed times, while regrowth can be represented by a source term G_B over a springtime interval. Although Kolmogorov forward equations are widely used in structured-population modelling, here they are transferred to within-host plant infection dynamics through a coupled formulation.

To the best of our knowledge, within-plant models for *Xylella fastidiosa* do not typically adopt a coupled Kolmogorov formulation in which the bacterial load is the structuring variable and roots and branches interact through their current load distributions. Accordingly, the modelling hypotheses appear to be new in this specific context.

The analysis carried out in this chapter was made possible thanks to the valuable contribution of Prof. Alessandro Giacomini (Università degli Studi di Brescia).

7.1 The mathematical model

Let $\Omega = (x_{\min}, x_{\max}) \subset \mathbb{R}$ be an interval and (t_0, T) a time interval. The variable $x \in \Omega$ represents the exponent of the bacterial load. Let $\phi_B(t,x)\,dx$ and $\phi_R(t,x)\,dx$ denote the amount of branches and roots, respectively, in biomass which have a bacterial load between x and $x+dx$ at time t. Given the functional forms $S_B(t,x,\phi_R)$, $S_R(t,x,\phi_B)$, and

$$M_B(t,x) \geq 0, \quad G_B(t,x) \geq 0, \quad \mu > 0, \quad \phi_{B,0}(x) \geq 0, \quad \phi_{R,0}(x) \geq 0,$$

we seek $\phi_B(t,x)$ and $\phi_R(t,x)$ on $(t,x) \in (t_0,T) \times \Omega$, solution to the following system

$$\begin{cases} \partial_t \phi_B(t,x) + \partial_x H_B(t,x,\phi_B,\phi_R) + M_B(t,x)\,\phi_B(t,x) = G_B(t,x) & \text{in } \Omega \times (t_0,T), \\ \partial_t \phi_R(t,x) + \partial_x H_R(t,x,\phi_R,\phi_B) = 0 & \text{in } \Omega \times (t_0,T), \\ \phi_B(t_0,x) = \phi_{B,0}(x), \qquad \phi_R(t_0,x) = \phi_{R,0}(x) & \text{in } \Omega, \\ H_B(t,x,\phi_B,\phi_R) = 0, \qquad H_R(t,x,\phi_R,\phi_B) = 0 & \text{on } \partial\Omega \times (t_0,T), \end{cases} \tag{7.1}$$

where

$$H_B(t,x,\phi_B,\phi_R) := S_B(t,x,\phi_R)\,\phi_B - \mu\,\partial_x \phi_B,$$
$$H_R(t,x,\phi_R,\phi_B) := S_R(t,x,\phi_B)\,\phi_R - \mu\,\partial_x \phi_R,$$

are the total fluxes (advective + diffusive).

Without loss of generality, we set $t_0 = 0$ by a time shift. Hence all statements below are given on $(0, T)$ with initial condition at $t = 0$. Here S_B and S_R denote the advective transport coefficients in branches and roots, respectively, M_B is the (non-negative) mortality rate in the branches, G_B is an external source term in the branches, and $\mu > 0$ is the (constant) diffusion coefficient in the bacterial–load variable.

7.2 Existence and Uniqueness (decoupled case, branches)

In this section, we analyse the case in which the coefficients S_B and S_R depend only on time and bacterial-load coordinate x, but are independent of the unknown functions ϕ_B and ϕ_R. The resulting system is decoupled and then, each equation can be studied independently. We focus on the branches equation, since it is the most complete one; the analysis for the roots equation can be carried out similarly, bearing in mind that both the mortality term and the right-hand side are identically zero. We follow the classical analysis of Evans (Chapter 7, [32]).

Fix the interval $\Omega = (x_{\min}, x_{\max}) \subset \mathbb{R}$ and the finite time horizon $T > 0$. Define $Q_T := (0, T) \times \Omega$. For simplicity we get rid of the subindex B from the equation $(7.1)_1$, thus we look for $\phi = \phi(t, x) \equiv \phi_B(t, x)$ solution of the linear PDE in *divergence form*

$$\partial_t \phi + \partial_x\big(S(t, x)\, \phi - \mu\, \partial_x \phi\big) + M(t, x)\, \phi = G(t, x) \quad \text{in } Q_T, \tag{7.2}$$

endowed with the *no–conormal–flux* boundary condition

$$S(t, x)\, \phi(t, x) - \mu\, \partial_x \phi(t, x) = 0 \qquad \text{on } (0, T) \times \partial\Omega, \tag{7.3}$$

and initial datum

$$\phi(0, x) = \phi_0(x) \qquad \text{in } \Omega. \tag{7.4}$$

Assumptions. We assume

$$\mu > 0, \quad S \in L^\infty(Q_T), \quad M \in L^\infty(Q_T),\ M \geq 0, \tag{7.5}$$

and

$$G \in L^2\big(0, T; L^2(\Omega)\big), \qquad \phi_0 \in L^2(\Omega). \tag{7.6}$$

Remark 7.1 (On the sign of M). In the model, M represents mortality, hence we assume $M \geq 0$ and $M \in L^\infty(Q_T)$. From the analytical viewpoint, the existence of a solution and the a priori estimates only require $M \in L^\infty(Q_T)$ with no sign condition. We keep $M \geq 0$ to reflect the modelling choice (birth/gain terms are treated separately via G).

Remark 7.2 (Notation convention). To simplify our formulas, from now on we will simply write L^2, H^1, $(H^1)^*$ instead of $L^2(\Omega)$, $H^1(\Omega)$, $(H^1)^*(\Omega)$ ($(H^1)^*(\Omega)$ denotes the dual space of $H^1(\Omega)$). Thus, for example, the inner product $(\cdot, \cdot)_{L^2}$ will be that of $L^2(\Omega)$

and $\langle\cdot,\cdot\rangle_{(H^1)^*,H^1}$ will denote the duality between $(H^1)^*(\Omega)$ and $H^1(\Omega)$. Moreover, we write $L^p_t X_x := L^p(0,T;X)$ for Bochner spaces: e.g. $L^2_t L^2_x = L^2(0,T;L^2(\Omega))$ and $L^2_t H^1_x = L^2(0,T;H^1(\Omega))$. The norm is $\|u\|_{L^pX} = \big(\int_0^T \|u(t)\|_X^p\,dt\big)^{1/p}$.

Whenever these spaces are referred to a set different from Ω, we will write it explicitly.

Bilinear form and weak solution

For almost every $t \in (0,T)$ we define the bilinear form

$$\mathcal{B}[\phi, v; t] := \int_\Omega \Big(\mu\,\partial_x\phi\,\partial_x v \;-\; S(t,x)\,\phi\,\partial_x v \;+\; M(t,x)\,\phi\,v\Big)\,dx, \qquad \phi, v \in H^1. \tag{7.7}$$

By multiplying (7.2) by $v \in H^1$ and integrating by parts in x, and imposing (7.3), we get

$$\int_\Omega \partial_t\phi\,v\,dx \;+\; \mathcal{B}[\phi, v; t] \;=\; \int_\Omega G\,v\,dx. \tag{7.8}$$

Definition 7.3 (Weak solution)**.** We say that ϕ is a weak solution of (7.2)–(7.4) if

$$\phi \in L^2_t H^1_x, \qquad \partial_t\phi \in L^2_t (H^1_x)^*, \tag{7.9}$$

and for almost every $t \in (0,T)$ and every $v \in H^1$ the identity

$$\langle \partial_t\phi(t), v\rangle_{(H^1)^*,H^1} + \mathcal{B}[\phi(t), v; t] \;=\; (G(t), v)_{L^2}, \tag{7.10}$$

holds, with initial condition $\phi(0) = \phi_0 \in L^2$.

Remark 7.4. In the weak identities and estimates that pass to the limit we will use the duality $\langle\cdot,\cdot\rangle_{(H^1)^*,H^1}$. In the Galerkin approximations, since the terms involved belong to L^2, we will identify $\langle\cdot,\cdot\rangle = (\cdot,\cdot)_{L^2}$ only to exploit the orthonormality of the basis and obtain, for example, $(\partial_t\phi_m, \phi_m)_{L^2} = \frac{1}{2}\frac{d}{dt}\|\phi_m\|^2_{L^2}$.

Theorem 7.5 ([32] Lions–Magenes in H^1–L^2–$(H^1)^*$)**.** *Let $\Omega \subset \mathbb{R}$ be bounded and $T > 0$. If*

$$\phi \in L^2_t H^1_x \qquad \text{and} \qquad \partial_t\phi \in L^2_t (H^1_x)^*,$$

then the following properties hold:

1. *$\phi \in C([0,T]; L^2)$;*
2. *the map $t \mapsto \|\phi(t)\|^2_{L^2}$ is absolutely continuous and, for almost every $t \in [0,T]$,*

$$\frac{d}{dt}\|\phi(t)\|^2_{L^2} = 2\,\big\langle \partial_t\phi(t),\, \phi(t)\big\rangle_{(H^1)^*,H^1}; \tag{7.11}$$

3. *there exists $C = C(T,\Omega) > 0$ such that*

$$\max_{0\le t\le T} \|\phi(t)\|_{L^2} \;\le\; C\Big(\,\|\phi\|_{L^2_t H^1_x} + \|\partial_t\phi\|_{L^2_t (H^1_x)^*}\Big). \tag{7.12}$$

Galerkin approximations

Let $\{w_k\}_{k\geq 1} \subset H^1$ be a family of functions orthonormal in L^2 and orthogonal in H^1 (for instance the eigenfunctions of the Laplacian with homogeneous Neumann b.c.). For $m \in \mathbb{N}$ we seek $\phi_m : [0,T] \to H^1$ such that

$$\phi_m(t) = \sum_{k=1}^{m} d_m^k(t)\, w_k, \tag{7.13}$$

whose coefficients $d_m^k(t)$ satisfy the initial conditions

$$d_m^k(0) = (\phi_0, w_k)_{L^2} \qquad (k = 1, \dots, m), \tag{7.14}$$

and the equations, for $k = 1, \dots, m$,

$$(\partial_t \phi_m(t), w_k)_{L^2} + \mathcal{B}[\phi_m(t), w_k; t] = (G(t), w_k)_{L^2} \quad \text{for every } t \in [0,T]. \tag{7.15}$$

Denoting by $V_m = \operatorname{span}\{w_1, \dots, w_m\}$, $\phi_m \in V_m$ is the Galerkin solution of problem (7.2) - (7.4).

Remark 7.6 (Choice of the Galerkin basis). In the weak formulation with homogeneous conormal flux condition the natural choice of the space is H^1; therefore we can use as a basis the eigenfunctions of the Laplacian with Neumann b.c., which form an orthonormal basis of L^2 and are dense in H^1. It is in fact not necessary that the eigenfunctions satisfy the boundary conditions on the flux; this is satisfied by the limit solution.

Theorem 7.7 (Construction of the Galerkin approximations)**.** *For every $m \in \mathbb{N}$ there exists a unique function*

$$\phi_m : [0,T] \to V_m, \qquad \phi_m(t) = \sum_{k=1}^{m} d_m^k(t)\, w_k,$$

whose coefficients $d_m^k(t)$ satisfy the initial conditions (7.14) *and the Galerkin identity* (7.15) *for almost every $t \in [0,T]$.*

Proof. Since the w_k do not depend on t, for every j we have, in the sense of distributions,

$$(\partial_t \phi_m(t), w_j)_{L^2} \;=\; \frac{d}{dt}\,(\phi_m(t), w_j)_{L^2} \;=\; \frac{d}{dt}(d_m^j)(t).$$

It follows that, for almost every t,

$$\partial_t \phi_m(t) = \sum_{k=1}^{m} \frac{d}{dt}(d_m^k)(t)\, w_k. \tag{7.16}$$

Taking the L^2 inner product with w_j we obtain

$$(\partial_t \phi_m(t), w_j)_{L^2} \;=\; \sum_{k=1}^{m} \frac{d}{dt}(d_m^k)(t)\,(w_k, w_j)_{L^2}. \tag{7.17}$$

Since $\{w_j\}$ is orthonormal in L^2, we have $(w_k, w_j)_{L^2} = \delta_{kj}$ and therefore

$$(\partial_t \phi_m(t), w_k)_{L^2} \;=\; \frac{d}{dt}(d_m^k)(t) \qquad \text{for almost every } t \in (0,T). \tag{7.18}$$

(A posteriori, from the ODE system we deduce that, for every $k = 1, \dots, m$, the (d_m^k) are absolutely continuous in $[0,T]$, hence the equality actually holds for every t.)

The bilinear term instead produces the coefficients

$$e^{k\ell}(t) := \mathcal{B}[w_\ell, w_k; t] = \int_\Omega \Big(\mu\, \partial_x w_\ell \partial_x w_k - S(t,x)\, w_\ell\, \partial_x w_k + M(t,x)\, w_\ell\, w_k \Big)\, dx \tag{7.19}$$

. Rewriting (7.15) with (7.18)–(7.19) we obtain the ODE system

$$\begin{gathered} \frac{d}{dt}(d_m^k)(t) + \sum_{\ell=1}^{m} e^{k\ell}(t)\, d_m^\ell(t) = f^k(t), \qquad f^k(t) := (G(t), w_k)_{L^2}, \\ \text{with initial conditions (7.14)}, \end{gathered} \tag{7.20}$$

for almost every $t \in [0,T]$, which, by the classical theory of ordinary differential equations, admits a unique absolutely continuous solution on $[0,T]$. □

Lemma 7.8 (Bessel inequality)**.** *Let $\{w_k\}_{k\ge 1}$ be orthonormal in L^2. Then, for every $f \in L^2$ and every m,*

$$\sum_{k=1}^{m} |(f, w_k)_{L^2}|^2 \le \|f\|_{L^2}^2.$$

We now need an energy estimate, uniform in m, for the Galerkin solutions ϕ_m. This estimate must control in time the L^2 norm and the diffusive contribution, with constants depending only on μ, $\|S\|_{L^\infty(Q_T)}$, $\|M\|_{L^\infty(Q_T)}$, T and Ω. This control will then be used to obtain compactness (Aubin–Lions), pass to the limit in the weak formulation, and then conclude existence and uniqueness.

Theorem 7.9 (Energy estimates for the Galerkin approximations)**.** *Under the same assumptions and notation of Theorem 7.7, there exists $C > 0$, independent of m, such that*

$$\max_{0\le t\le T} \|\phi_m(t)\|_{L^2} \;+\; \|\phi_m\|_{L_t^2 H_x^1} \;+\; \|\partial_t \phi_m\|_{L_t^2 (H_x^1)^*} \;\le\; C\Big(\|\phi_0\|_{L^2} + \|G\|_{L_t^2 L_x^2} \Big).$$

Proof. We test (7.15) with w_k, multiply by $d_m^k(t)$ and sum over $k = 1, \dots, m$. Using (7.13) we obtain, for almost every $t \in (0,T)$,

$$(\partial_t \phi_m(t), \phi_m(t))_{L^2} + \mathcal{B}[\phi_m(t), \phi_m(t); t] = (G(t), \phi_m(t))_{L^2}. \tag{7.21}$$

Since $(\partial_t \phi_m, \phi_m)_{L^2} = \frac{1}{2}\frac{d}{dt}\|\phi_m\|_{L^2}^2$, we have

$$\frac{1}{2}\frac{d}{dt}\|\phi_m\|_{L^2}^2 + \mathcal{B}[\phi_m, \phi_m; t] = (G, \phi_m)_{L^2}. \tag{7.22}$$

For the transport term, by Cauchy–Schwarz and Young inequalities (with $\varepsilon = \mu$),

$$\left| \int_\Omega S\, \phi_m\, \partial_x \phi_m \right| \le \|S\|_{L^\infty(Q_T)}\, \|\phi_m\|_{L^2}\, \|\partial_x \phi_m\|_{L^2} \le \frac{\mu}{2}\|\partial_x \phi_m\|_{L^2}^2 + \frac{\|S\|_{L^\infty(Q_T)}^2}{2\mu}\, \|\phi_m\|_{L^2}^2. \tag{7.23}$$

Since $M \ge 0$, it follows that

$$\mathcal{B}[\phi_m, \phi_m; t] \ge \frac{\mu}{2}\|\partial_x \phi_m\|_{L^2}^2 - \frac{\|S\|_{L^\infty(Q_T)}^2}{2\mu}\, \|\phi_m\|_{L^2}^2. \tag{7.24}$$

Moreover $(G, \phi_m)_{L^2} \le \frac{1}{2}\|G\|_{L^2}^2 + \frac{1}{2}\|\phi_m\|_{L^2}^2$. Substituting (7.24) into (7.22) we obtain

$$\frac{d}{dt}\|\phi_m\|_{L^2}^2 + \mu\, \|\partial_x \phi_m\|_{L^2}^2 \le C_1\, \|\phi_m\|_{L^2}^2 + \|G\|_{L^2}^2, \tag{7.25}$$

with $C_1 := 1 + \frac{\|S\|_{L^\infty(Q_T)}^2}{\mu}$. Set

$$\eta(t) := \|\phi_m(t)\|_{L^2}^2, \qquad \xi(t) := \|G(t)\|_{L^2}^2; \tag{7.26}$$

then (7.25) implies

$$\frac{d}{dt}\eta(t) \le C_1\, \eta(t) + \xi(t) \qquad \text{for almost every } t \in (0,T). \tag{7.27}$$

By the differential form of Grönwall's inequality (see [15]),

$$\eta(t) \le e^{C_1 t}\left(\eta(0) + \int_0^t \xi(s)\, ds \right) \qquad (0 \le t \le T). \tag{7.28}$$

From the initial data $d_m^k(0) = (\phi_0, w_k)_{L^2}$ and from Bessel's inequality (Lemma 7.8) it follows that

$$\eta(0) = \|\phi_m(0)\|_{L^2}^2 = \sum_{k=1}^{m} |(\phi_0, w_k)_{L^2}|^2 \le \|\phi_0\|_{L^2}^2.$$

Hence we obtain the uniform estimate *(with $C = e^{C_1 T}$)*

$$\max_{t\in[0,T]} \|\phi_m(t)\|_{L^2}^2 \;\le\; C\Big(\|\phi_0\|_{L^2}^2 + \|G\|_{L_t^2 L_x^2}^2\Big). \tag{7.29}$$

Integrating (7.25) over $(0,T)$ we get

$$\|\phi_m(T)\|_{L^2}^2 - \|\phi_m(0)\|_{L^2}^2 + \mu\int_0^T \|\partial_x\phi_m(t)\|_{L^2}^2\,dt \;\le\; C_1\int_0^T \|\phi_m(t)\|_{L^2}^2\,dt + \int_0^T \|G(t)\|_{L^2}^2\,dt. \tag{7.30}$$

Since $\|\phi_m(T)\|_{L^2}^2 \ge 0$ and, again by Bessel, $\|\phi_m(0)\|_{L^2}^2 \le \|\phi_0\|_{L^2}^2$, we deduce

$$\mu\int_0^T \|\partial_x\phi_m(t)\|_{L^2}^2\,dt \;\le\; C_1\int_0^T \|\phi_m(t)\|_{L^2}^2\,dt + \|G\|_{L_t^2 L_x^2}^2 + \|\phi_0\|_{L^2}^2. \tag{7.31}$$

From the uniform estimate (7.29) we have, absorbing T into the constant C,

$$\int_0^T \|\phi_m(t)\|_{L^2}^2\,dt \le T\sup_{t\in[0,T]}\|\phi_m(t)\|_{L^2}^2 \le C\big(\|\phi_0\|_{L^2}^2 + \|G\|_{L_t^2 L_x^2}^2\big).$$

Substituting this estimate in (7.31) and absorbing μ into the constant C, we conclude

$$\int_0^T \|\partial_x\phi_m(t)\|_{L^2}^2\,dt \;\le\; C\Big(\|\phi_0\|_{L^2}^2 + \|G\|_{L_t^2 L_x^2}^2\Big). \tag{7.32}$$

Now fix $v \in H^1$ with $\|v\|_{H^1} \le 1$ [6]
and write

$$v = v^1 + v^2, \qquad v^1 \in \operatorname{span}\{w_1,\dots,w_m\} = V_m, \qquad (v^2, w_k)_{L^2} = 0 \;\; (k = 1,\dots,m).$$

Since $\{w_k\}$ is orthogonal in H^1, we have $\|v^1\|_{H^1} \le \|v\|_{H^1} \le 1$.

Since, for a.e. $t \in [0,T]$, $\partial_t\phi_m(t) \in V_m \subset H^1 \subset L^2$,

$$\langle \partial_t\phi_m(t), v\rangle_{(H^1)^*,H^1} = (\partial_t\phi_m(t), v)_{L^2} = (\partial_t\phi_m(t), v^1)_{L^2},$$

because $(\partial_t\phi_m(t), v^2)_{L^2} = 0$.

From the Galerkin identity (7.15) (valid for every $v^1 \in V_m$) we deduce

$$\big\langle \partial_t\phi_m(t),\, v\big\rangle_{(H^1)^*,H^1} = \big(\partial_t\phi_m(t),\, v\big)_{L^2} = (G(t), v^1)_{L^2} - \mathcal{B}[\phi_m(t), v^1; t] \text{ for a.e. } t \in [0,T]. \tag{7.33}$$

[6] without loss of generality, because by definition $\|f\|_{(H^1)^*} = \sup_{\|w\|_{H^1}\le 1} |\langle f, w\rangle_{(H^1)^*,H^1}|$; given $v \neq 0$ we normalize $\hat v := v/\|v\|_{H^1}$ and $|\langle f, v\rangle| = \|v\|_{H^1}|\langle f, \hat v\rangle|$

For the source term,

$$|(G(t), v^1)_{L^2}| \;\le\; \|G(t)\|_{L^2}\,\|v^1\|_{L^2} \;\le\; C\,\|G(t)\|_{L^2}\,\|v^1\|_{H^1} \;\le\; C\,\|G(t)\|_{L^2},$$

where we used the continuous embedding $H^1 \hookrightarrow L^2$.
For the bilinear term, from the continuity of $\mathcal{B}$ on $H^1 \times H^1$,

$$|\mathcal{B}[\psi, v; t]| \le C\,\|\psi\|_{H^1}\,\|v\|_{H^1} \qquad \forall\, \psi, v \in H^1, \tag{7.34}$$

we get

$$|\mathcal{B}[\phi_m(t), v^1; t]| \;\le\; C\,\|\phi_m(t)\|_{H^1}\,\|v^1\|_{H^1}.$$

Putting the two previous estimates together and using $\|v^1\|_{H^1} \le 1$ we obtain, for almost every $t \in [0,T]$,

$$|\langle \partial_t \phi_m(t), v\rangle| \le C\Big(\|G(t)\|_{L^2} + \|\phi_m(t)\|_{H^1}\Big). \tag{7.35}$$

Taking the sup over all $v \in H^1(\Omega)$ with $\|v\|_{H^1} \le 1$ (definition of the norm in $(H^1)^*$) we conclude

$$\|\partial_t \phi_m(t)\|_{(H^1)^*} \le C\Big(\|G(t)\|_{L^2} + \|\phi_m(t)\|_{H^1}\Big). \tag{7.36}$$

Squaring (7.36) and integrating in $t \in (0,T)$, we have

$$\int_0^T \|\partial_t \phi_m(t)\|^2_{(H^1)^*}\,dt \;\le\; C\int_0^T \Big(\|G(t)\|^2_{L^2} + \|\phi_m(t)\|^2_{H^1}\Big)\,dt.$$

Applying the energy estimates (7.29)–(7.32) (which uniformly control both $\|\phi_m\|_{L^2_t H^1_x}$ and $\sup_t \|\phi_m(t)\|_{L^2}$) we get

$$\int_0^T \|\partial_t \phi_m(t)\|^2_{(H^1)^*}\,dt \le C\Big(\|\phi_0\|^2_{L^2} + \|G\|^2_{L^2_t L^2_x}\Big). \tag{7.37}$$

From (7.29) and (7.32) we get

$$\begin{aligned}\|\phi_m\|^2_{L^2_t H^1_x} &= \int_0^T \big(\|\phi_m(t)\|^2_{L^2} + \|\partial_x \phi_m(t)\|^2_{L^2}\big)\,dt \\ &\le T \max_{t\in[0,T]} \|\phi_m(t)\|^2_{L^2} \;+\; \int_0^T \|\partial_x \phi_m(t)\|^2_{L^2}\,dt \;\le\; C\Big(\|\phi_0\|^2_{L^2} + \|G\|^2_{L^2_t L^2_x}\Big).\end{aligned}$$

Moreover, by (7.37),

$$\|\partial_t \phi_m\|^2_{L^2_t (H^1_x)^*} \;\le\; C\Big(\|\phi_0\|^2_{L^2} + \|G\|^2_{L^2_t L^2_x}\Big).$$

Taking the square root in the three estimates (and renaming the constant), we obtain the claim:

$$\max_{0\le t\le T}\|\phi_m(t)\|_{L^2} \;+\; \|\phi_m\|_{L^2_tH^1_x} \;+\; \|\partial_t\phi_m\|_{L^2_t(H^1_x)^*} \;\le\; C\Big(\|\phi_0\|_{L^2}+\|G\|_{L^2_tL^2_x}\Big).$$

□

Theorem 7.10 (Existence and uniqueness)**.** *There exists a unique weak solution of problem* (7.2)–(7.4) *such that:*

$$\max_{0\le t\le T}\|\phi(t)\|_{L^2} \;+\; \|\phi\|_{L^2_tH^1_x} \;+\; \|\partial_t\phi\|_{L^2_t(H^1_x)^*} \;\le\; C\Big(\|\phi_0\|_{L^2}+\|G\|_{L^2_tL^2_x}\Big). \tag{7.38}$$

Proof. From the energy estimates (7.29)–(7.32) and from the estimate on the time derivative (7.37), the sequence of Galerkin solutions $\{\phi_m\}$ is bounded in $L^2_tH^1_x$ and $\{\partial_t\phi_m\}$ is bounded in $L^2_t(H^1_x)^*$. Therefore there exist a subsequence (not relabelled) and a function ϕ such that

$$\phi_m \rightharpoonup \phi \;\text{ in } L^2_tH^1_x, \qquad \partial_t\phi_m \rightharpoonup \partial_t\phi \;\text{ in } L^2_t(H^1_x)^*. \tag{7.39}$$

Fix an integer N and choose a test function of the form

$$v(t)=\sum_{k=1}^{N} d^k(t)\,w_k, \qquad d^k\in C^1([0,T]). \tag{7.40}$$

For $m\ge N$, multiplying the Galerkin identity (7.15) by $d^k(t)$, summing over $k=1,\dots,N$ and integrating in t we obtain

$$\int_0^T\Big(\langle\partial_t\phi_m(t),v(t)\rangle_{(H^1)^*,H^1}+\mathcal{B}[\phi_m(t),v(t);t]\Big)\,dt \;=\; \int_0^T(G(t),v(t))_{L^2}\,dt. \tag{7.41}$$

Thanks to the weak convergences (7.39) and to the continuity of the bilinear form $\mathcal{B}$ on $H^1\times H^1$, by passing to the limit as $m\to\infty$ in (7.41) we get

$$\int_0^T\Big(\langle\partial_t\phi(t),v(t)\rangle_{(H^1)^*,H^1}+\mathcal{B}[\phi(t),v(t);t]\Big)\,dt \;=\; \int_0^T(G(t),v(t))_{L^2}\,dt. \tag{7.42}$$

The previous identity has been obtained first for test functions of the form (7.40). Since $\mathrm{span}\{w_k\}$ is dense in H^1 and $C^1([0,T])$ is dense in $L^2(0,T)$, finite sums $\sum_{k=1}^N d^k(t)w_k$ with $d^k\in C^1([0,T])$ are dense in $L^2(0,T;H^1)$. Moreover, the maps

$$v\mapsto\int_0^T\langle\partial_t\phi(t),v(t)\rangle\,dt, \qquad v\mapsto\int_0^T\mathcal{B}[\phi(t),v(t);t]\,dt, \qquad v\mapsto\int_0^T(G(t),v(t))_{L^2}\,dt$$

are continuous linear functionals on $L^2(0,T;H^1)$ (by Cauchy–Schwarz and the continuity of $\mathcal{B}$ in (7.34)). Hence the identity extends, by density, to every $v \in L^2(0,T;H^1)$. Taking in particular $v \in C^1([0,T];H^1)$ and approximating it with functions of the form (7.40), we may integrate by parts in t and obtain the formula below.

$$\int_0^T \Big(- \langle \phi(t), \partial_t v(t) \rangle_{(H^1)^*,H^1} + \mathcal{B}[\phi(t), v(t); t] \Big)\, dt = \int_0^T (G(t), v(t))_{L^2}\, dt + (\phi(0), v(0)) - (\phi(T), v(T)). \tag{7.43}$$

By choosing $v(T) = 0$ we finally get

$$\int_0^T \Big(- \langle \phi(t), \partial_t v(t) \rangle_{(H^1)^*,H^1} + \mathcal{B}[\phi(t), v(t); t] \Big)\, dt \;=\; \int_0^T (G(t), v(t))_{L^2}\, dt + (\phi(0), v(0)). \tag{7.44}$$

By density of $C^1([0,T];H^1)$ in $L^2(0,T;H^1)$ and continuity in v of all the functionals involved, identity (7.44) extends to every $v \in L^2(0,T;H^1)$.
We now have to prove that the limit solution ϕ satisfies the initial condition (7.4).
Repeating the same steps starting from (7.41), for ϕ_m instead of ϕ, with the same $v \in C^1([0,T];H^1(\Omega))$ and $v(T) = 0$, we get

$$\int_0^T \Big(- \langle \phi_m(t), \partial_t v(t) \rangle_{(H^1)^*,H^1} + \mathcal{B}[\phi_m(t), v(t); t] \Big)\, dt = \int_0^T (G(t), v(t))_{L^2}\, dt + (\phi_m(0), v(0)).$$

Passing to the limit, using (7.39) and the fact that $\phi_m(0) = \sum_{k=1}^m (\phi_0, w_k) w_k \to \phi_0$ in L^2 (by completeness of the orthonormal basis $\{w_k\}$), we obtain $(\phi(0), v(0)) = (\phi_0, v(0))$ for every $v(0) \in H^1$, that is, $\phi(0) = \phi_0$ in L^2.

Consequently, ϕ satisfies Definition 7.3; in particular, by Theorem 7.5 we have $\phi \in C([0,T];L^2)$. Moreover, using the convergences in (7.39) we can pass to the limit in the energy estimates (7.29)–(7.32) and (7.37). In this way we obtain that there exists a constant $C > 0$, depending only on μ, $\|S\|_{L^\infty(Q_T)}$, $\|M\|_{L^\infty(Q_T)}$, T and Ω, such that the weak solution ϕ of (7.2)–(7.4) satisfies the uniform bound (7.38).

We shall use this estimate in the analysis of the non-linear coupled problem.

Now let ϕ_1, ϕ_2 be weak solutions with the same data; then $w := \phi_1 - \phi_2$ satisfies (7.10) with $G \equiv 0$ and $w(0) = 0$. Taking $v = w$ in (7.10) we get, for almost every $t \in [0,T]$,

$$\frac{1}{2}\frac{d}{dt}\|w\|_{L^2}^2 + \mathcal{B}[w, w; t] = 0. \tag{7.45}$$

And using (7.24) with ϕ_m replaced by w,

$$\frac{d}{dt}\|w\|_{L^2}^2 \le \frac{\|S\|_{L^\infty(Q_T)}^2}{\mu}\, \|w\|_{L^2}^2, \tag{7.46}$$

and by Grönwall and $w(0) = 0$ it follows that $w \equiv 0$, hence the uniqueness of the weak solution. □

7.3 Analysis of the non-linear coupled problem

Let us consider problem (7.1). We make the following assumptions on the data:

1. $\mu > 0, \quad M_B \in L^\infty(Q_T)$, $M_B \geq 0, \quad G_B \in L^2_t L^2_x, \quad \phi_{B,0}, \phi_{R,0} \in L^2(\Omega)$.

2. (Non-linear transport operators) We are given two operators

$$\mathcal{S}_B,\ \mathcal{S}_R : L^2_t L^2_x \longrightarrow L^2_t L^2_x$$

such that:

(i) $\mathcal{S}_B$ and $\mathcal{S}_R$ are continuous with respect to the $L^2_t L^2_x$ norm;

(ii) there exists a constant $S_* > 0$ such that, for every $\phi \in L^2_t L^2_x$,

$$\|\mathcal{S}_B(\phi)\|_{L^\infty(Q_T)} \leq S_*, \qquad \|\mathcal{S}_R(\phi)\|_{L^\infty(Q_T)} \leq S_*.$$

Define the normed space

$$X := \{u \in L^2_t H^1_x :\ \partial_t u \in L^2_t (H^1_x)^*\}, \qquad \|u\|^2_X := \|u\|^2_{L^2_t H^1_x} + \|u_t\|^2_{L^2_t (H^1_x)^*},$$

and $\mathbb{X} := X \times X$. It holds that $\mathbb{X}$ is a Hilbert space. Given $(\psi_B, \psi_R) \in \mathbb{X}$, define the operator $\mathcal{T} : \mathbb{X} \to \mathbb{X}$ such that $(\phi_B, \phi_R) = \mathcal{T}(\psi_B, \psi_R)$ is the unique weak solution of the *linear problem*

$$\begin{cases} \partial_t \phi_B + \partial_x\big(\mathcal{S}_B(\psi_R)\,\phi_B - \mu\,\partial_x \phi_B\big) + M_B\,\phi_B = G_B & \text{in } \Omega \times (0,T), \\ \partial_t \phi_R + \partial_x\big(\mathcal{S}_R(\psi_B)\,\phi_R - \mu\,\partial_x \phi_R\big) = 0 & \text{in } \Omega \times (0,T), \\ \mathcal{S}_B(\psi_R)\,\phi_B - \mu\,\partial_x \phi_B = 0 & \text{on } \partial\Omega \times (0,T), \\ \mathcal{S}_R(\psi_B)\,\phi_R - \mu\,\partial_x \phi_R = 0 & \text{on } \partial\Omega \times (0,T), \\ \phi_B(0,x) = \phi_{B,0}(x), \qquad \phi_R(0,x) = \phi_{R,0}(x) & \text{in } \Omega. \end{cases} \tag{7.47}$$

Given (ψ_B, ψ_R), existence and uniqueness of (ϕ_B, ϕ_R) follow from the linear case studied in Sec. 7.2.

Observe that if the system (7.1) admits a solution (ϕ_B, ϕ_R), then, by construction, it satisfies

$$(\phi_B, \phi_R) = \mathcal{T}(\phi_B, \phi_R),$$

that is, (ϕ_B, ϕ_R) is a fixed point of $\mathcal{T}$. The aim of the next subsection is therefore to show that $\mathcal{T}$ admits at least one fixed point.

Continuity of the operator $\mathcal{T}$

We now address the continuity of the operator $\mathcal{T}$. Let $\{(\psi_B^n, \psi_R^n)\}_{n\in\mathbb{N}}$ be a sequence in $\mathbb{X}$ such that

$$(\psi_B^n, \psi_R^n) \longrightarrow (\psi_B, \psi_R) \quad \text{strongly in } \mathbb{X} \quad \text{as } n \to \infty.$$

Since $H^1(\Omega)$ is continuously embedded into $L^2(\Omega)$, this implies, in particular,

$$(\psi_B^n, \psi_R^n) \longrightarrow (\psi_B, \psi_R) \quad \text{strongly in } (L_t^2 L_x^2)^2.$$

For notational simplicity, in the proofs below, we carry out the detailed estimates only for the branches equation, that is for ϕ_B. The roots equation for ϕ_R has exactly the same structure (with the exception of the growth and mortality terms G and M, whose absence would only simplify the subsequent steps of the proof), so the same arguments apply to ϕ_R and we do not repeat them.

The branches components ϕ_B^n and ϕ_B solve the linear equations:

$$\begin{cases} \partial_t \phi_B^n + \partial_x\big(\mathcal{S}_B(\psi_R^n)\,\phi_B^n - \mu\,\partial_x \phi_B^n\big) + M_B\,\phi_B^n = G_B & \text{in } \Omega\times(0,T), \\ \mathcal{S}_B(\psi_R^n)\,\phi_B^n - \mu\,\partial_x\phi_B^n = 0 & \text{on } \partial\Omega\times(0,T), \\ \phi_B^n(0,x) = \phi_{B,0}(x) & \text{in } \Omega. \end{cases} \tag{7.48}$$

$$\begin{cases} \partial_t \phi_B + \partial_x\big(\mathcal{S}_B(\psi_R)\,\phi_B - \mu\,\partial_x \phi_B\big) + M_B\,\phi_B = G_B & \text{in } \Omega\times(0,T), \\ \mathcal{S}_B(\psi_R)\,\phi_B - \mu\,\partial_x\phi_B = 0 & \text{on } \partial\Omega\times(0,T), \\ \phi_B(0,x) = \phi_{B,0}(x) & \text{in } \Omega. \end{cases} \tag{7.49}$$

Adding to both sides of $(7.48)_1$ the term $\partial_x\big(\mathcal{S}_B(\psi_R)\,\phi_B^n\big)$, and then moving $\partial_x\big(\mathcal{S}_B(\psi_R^n)\,\phi_B^n\big)$ to the right-hand side, we can write:

$$\partial_t \phi_B^n + \partial_x\big(\mathcal{S}_B(\psi_R)\,\phi_B^n - \mu\,\partial_x\phi_B^n\big) + M_B\,\phi_B^n = G_B - \partial_x\big((\mathcal{S}_B(\psi_R^n) - \mathcal{S}_B(\psi_R))\,\phi_B^n\big). \tag{7.50}$$

The weak formulations of $(7.49)_1$ and (7.50) amount to

$$\int_\Omega \partial_t\phi_B\, v\,dx - \int_\Omega \big(\mathcal{S}_B(\psi_R)\,\phi_B - \mu\,\partial_x\phi_B\big)\,\partial_x v\,dx + \int_\Omega M_B\,\phi_B\, v\,dx = \int_\Omega G_B\, v\,dx, \tag{7.51}$$

and

$$\begin{aligned} &\int_\Omega \partial_t\phi_B^n\, v\,dx - \int_\Omega \big(\mathcal{S}_B(\psi_R)\,\phi_B^n - \mu\,\partial_x\phi_B^n\big)\,\partial_x v\,dx + \int_\Omega M_B\,\phi_B^n\, v\,dx \\ &\qquad = \int_\Omega G_B\, v\,dx - \int_\Omega (\mathcal{S}_B(\psi_R^n) - \mathcal{S}_B(\psi_R))\,\phi_B^n\,\partial_x v\,dx. \end{aligned} \tag{7.52}$$

Subtracting (7.51) from (7.52), we obtain

$$\begin{aligned}\int_\Omega \partial_t(\phi_B^n - \phi_B)\, v\, dx - \int_\Omega \big(\mathcal{S}_B(\psi_R)\,(\phi_B^n - \phi_B) - \mu\,\partial_x(\phi_B^n - \phi_B)\big)\,\partial_x v\, dx \\ + \int_\Omega M_B\,(\phi_B^n - \phi_B)\, v\, dx = \int_\Omega (\mathcal{S}_B(\psi_R^n) - \mathcal{S}_B(\psi_R))\,\phi_B^n\,\partial_x v\, dx.\end{aligned} \tag{7.53}$$

We now introduce the difference variable

$$v_B^n := \phi_B^n - \phi_B, \text{ such that } v_B^n(0,\cdot) = 0 \text{ in } \Omega.$$

With this notation, (7.53) can be rewritten as

$$\begin{aligned}\int_\Omega \partial_t v_B^n\, v\, dx - \int_\Omega \big(\mathcal{S}_B(\psi_R)\, v_B^n - \mu\,\partial_x v_B^n\big)\,\partial_x v\, dx + \int_\Omega M_B\, v_B^n\, v\, dx \\ = \int_\Omega (\mathcal{S}_B(\psi_R^n) - \mathcal{S}_B(\psi_R))\,\phi_B^n\,\partial_x v\, dx,\end{aligned} \tag{7.54}$$

for every $v \in H^1(\Omega)$ and almost every $t \in (0,T)$.

Arguing as in the linear case, we now take $v = v_B^n(t)$ in (7.54). For almost every $t \in (0,T)$ this gives

$$\begin{aligned}\int_\Omega \partial_t v_B^n\, v_B^n\, dx - \int_\Omega \Big(\mathcal{S}_B(\psi_R)\, v_B^n - \mu\,\partial_x v_B^n\Big)\partial_x v_B^n\, dx + \int_\Omega M_B\,(v_B^n)^2\, dx \\ = \int_\Omega (\mathcal{S}_B(\psi_R^n) - \mathcal{S}_B(\psi_R))\,\phi_B^n\,\partial_x v_B^n\, dx,\end{aligned}$$

and thus

$$\begin{aligned}\frac{1}{2}\frac{d}{dt}\|v_B^n(t)\|_{L^2}^2 + \mu\|\partial_x v_B^n(t)\|_{L^2}^2 - \int_\Omega \mathcal{S}_B(\psi_R)\, v_B^n\,\partial_x v_B^n\, dx + \int_\Omega M_B\,(v_B^n)^2\, dx \\ = \int_\Omega (\mathcal{S}_B(\psi_R^n) - \mathcal{S}_B(\psi_R))\,\phi_B^n\,\partial_x v_B^n\, dx.\end{aligned} \tag{7.55}$$

The third term on the left-hand side can be estimated as in the linear problem:

$$\left|\int_\Omega \mathcal{S}_B(\psi_R)\, v_B^n\,\partial_x v_B^n\, dx\right| \le \frac{\mu}{2}\|\partial_x v_B^n(t)\|_{L^2}^2 + \frac{S_*}{2\mu}\|v_B^n(t)\|_{L^2}^2 \tag{7.56}$$

Now we estimate the new right-hand side of (7.55), for almost every $t \in (0,T)$, by Cauchy–Schwarz and Young's inequality with parameter $\varepsilon = \mu/2$. We have

$$\left| \int_\Omega (\mathcal{S}_B(\psi_R^n) - \mathcal{S}_B(\psi_R))\, \phi_B^n\, \partial_x v_B^n\, dx \right| \le \left\| (\mathcal{S}_B(\psi_R^n) - \mathcal{S}_B(\psi_R))\, \phi_B^n \right\|_{L^2} \|\partial_x v_B^n(t)\|_{L^2} \\ \le \frac{\mu}{4} \|\partial_x v_B^n(t)\|_{L^2}^2 + \frac{1}{\mu} \left\| (\mathcal{S}_B(\psi_R^n) - \mathcal{S}_B(\psi_R))\, \phi_B^n \right\|_{L^2}^2. \tag{7.57}$$

Here we used the L^∞ bound for $\mathcal{S}_B$.
Using (7.56) and (7.57) in (7.55), recalling that $M_B \ge 0$, we find

$$\frac{d}{dt}\|v_B^n(t)\|_{L^2}^2 + \frac{\mu}{2}\|\partial_x v_B^n(t)\|_{L^2}^2 \le \frac{S_*}{\mu} \|v_B^n(t)\|_{L^2}^2 + \frac{2}{\mu} \left\| (\mathcal{S}_B(\psi_R^n) - \mathcal{S}_B(\psi_R))\, \phi_B^n \right\|_{L^2}^2,$$

Integrating in time over $(0,T)$, applying Grönwall's inequality exactly working as in the proof of Theorem 7.9 (from (7.25) to the end of the proof), and recalling that $v_B^n(0,x) = 0$ in Ω, we obtain

$$\|v_B^n\|_{L_t^2 H_x^1} + \|\partial_t v_B^n\|_{L_t^2 (H_x^1)^*} \le C \left\| (\mathcal{S}_B(\psi_R^n) - \mathcal{S}_B(\psi_R))\, \phi_B^n \right\|_{L_t^2 L_x^2}, \tag{7.58}$$

where $C > 0$ only depends on μ, the uniform bound on $\mathcal{S}_B$, $\|M_B\|_{L^\infty(Q_T)}$, T and Ω, and is independent of n.
Now, we prove that

$$\left\| (\mathcal{S}_B(\psi_R^n) - \mathcal{S}_B(\psi_R))\, \phi_B^n \right\|_{L_t^2 L_x^2} \longrightarrow 0 \text{ when } n \to \infty. \tag{7.59}$$

First, by assumption on $\mathcal{S}_B$ we have

$$\mathcal{S}_B(\psi_R^n) \to \mathcal{S}_B(\psi_R) \quad \text{strongly in } L_t^2 L_x^2.$$

In particular, possibly extracting a further subsequence,

$$\mathcal{S}_B(\psi_R^n)(t,x) \to \mathcal{S}_B(\psi_R)(t,x) \quad \text{for a.e. } (t,x) \in Q_T. \tag{7.60}$$

From the second assumptions on $\mathcal{S}_B$, we have

$$\|\mathcal{S}_B(\psi_R^n) - \mathcal{S}_B(\psi_R)\|_{L^\infty(Q_T)} \le 2\mathcal{S}_* \qquad \text{for all } n.$$

By applying the linear a priori estimate (7.38) to problems (7.48) and (7.49), we obtain uniform bounds for ϕ_B^n and ϕ_B in X. Hence, from these bounds and the Aubin–Lions compactness theorem 2.6, the sequence ϕ_B^n is relatively compact in $L_t^2 L_x^2$, so, up to a subsequence, $\phi_B^n \to \phi_B$ strongly in $L_t^2 L_x^2$.

We now write

$$\phi_B^n = (\phi_B^n - \phi_B) + \phi_B$$

and apply the triangle inequality:

$$\begin{aligned}\left\|\left(\mathcal{S}_B(\psi_R^n)-\mathcal{S}_B(\psi_R)\right)\phi_B^n\right\|_{L_t^2L_x^2} &\le \left\|\left(\mathcal{S}_B(\psi_R^n)-\mathcal{S}_B(\psi_R)\right)(\phi_B^n-\phi_B)\right\|_{L_t^2L_x^2}\\ &\quad+\left\|\left(\mathcal{S}_B(\psi_R^n)-\mathcal{S}_B(\psi_R)\right)\phi_B\right\|_{L_t^2L_x^2}\\ &= I_{1,n}+I_{2,n}.\end{aligned}$$

For the first term we use the uniform bound $||\mathcal{S}_B(\psi_R^n)||_\infty \le \mathcal{S}_*$ and $||\mathcal{S}_B(\psi_R)||_\infty \le \mathcal{S}_*$:

$$I_{1,n} \le \|\mathcal{S}_B(\psi_R^n)-\mathcal{S}_B(\psi_R)\|_{L^\infty(Q_T)}\,\|\phi_B^n-\phi_B\|_{L_t^2L_x^2} \le 2\mathcal{S}_*\,\|\phi_B^n-\phi_B\|_{L_t^2L_x^2} \longrightarrow 0.$$

For $I_{2,n}$ we write

$$I_{2,n}^2 = \int_0^T\int_\Omega \left|\mathcal{S}_B(\psi_R^n(t,x))-\mathcal{S}_B(\psi_R(t,x))\right|^2|\phi_B(t,x)|^2\,dx\,dt.$$

By (7.60) the integrand converges pointwise to zero. Moreover,

$$\left|\mathcal{S}_B(\psi_R^n)-\mathcal{S}_B(\psi_R)\right|^2|\phi_B|^2 \le 4\mathcal{S}_*^2\,|\phi_B|^2 \quad \text{in } Q_T,$$

and $4\mathcal{S}_*^2\,|\phi_B|^2$ is integrable since $\phi_B \in L_t^2L_x^2$. Therefore, by the dominated convergence Theorem 2.1.6, $I_{2,n}\to 0$.
Combining the two limits we conclude that

$$\left\|\left(\mathcal{S}_B(\psi_R^n)-\mathcal{S}_B(\psi_R)\right)\phi_B^n\right\|_{L_t^2L_x^2} \longrightarrow 0, \text{ as } n\to\infty$$

so that, from (7.58) we have

$$v_B^n \to 0 \quad \text{in } L_t^2H_x^1 \quad \text{and} \quad \partial_t v_B^n \to 0 \quad \text{in } L_t^2(H_x^1)^*,$$

which implies

$$\phi_B^n \to \phi_B \quad \text{in } L_t^2H_x^1 \text{ and } \partial_t\phi_B^n \to \partial_t\phi_B \text{ in } L_t^2(H_x^1)^*.$$

Repeating the same argument for the roots equation $(7.47)_2$, we obtain

$$\phi_R^n \to \phi_R \quad \text{in } L_t^2H_x^1 \text{ and } \partial_t\phi_R^n \to \partial_t\phi_R \text{ in } L_t^2(H_x^1)^*.$$

Hence, in the product space we have

$$\mathcal{T}(\psi_B^n,\psi_R^n) = (\phi_B^n,\phi_R^n) \longrightarrow (\phi_B,\phi_R) = \mathcal{T}(\psi_B,\psi_R) \quad \text{strongly in } \mathbb{X},$$

which shows the continuity of $\mathcal{T}$ on $\mathbb{X}$.

7.3.1 Existence of a solution via Schauder's fixed-point theorem

By the estimate (7.38) for the linear problem, there exists $R > 0$ such that, for every $(\psi_B, \psi_R) \in \mathbb{X}$, we have

$$\mathcal{T}(\psi_B, \psi_R) \in \overline{B}_R.$$

In particular,

$$\mathcal{T}(\overline{B}_R) \subset \overline{B}_R.$$

The map $\mathcal{T}$ is also compact on $\mathbb{X}$, i.e. it has a relatively compact range. Indeed, if (ψ_B^n, ψ_R^n) is bounded in $\mathbb{X}$, then exists a subsequence $(\psi_B^{n_k}, \psi_R^{n_k})$ and $(\psi_B, \psi_R) \in \mathbb{X}$ such that

$$\begin{cases} \psi_B^n \rightharpoonup \psi_B & \text{in } L_t^2 H_x^1, \\ \partial_t \psi_B^n \rightharpoonup \partial_t \psi_B & \text{in } L_t^2 (H_x^1)^*, \end{cases} \qquad \begin{cases} \psi_R^n \rightharpoonup \psi_R & \text{in } L_t^2 H_x^1, \\ \partial_t \psi_R^n \rightharpoonup \partial_t \psi_R & \text{in } L_t^2 (H_x^1)^*. \end{cases}$$

By the Aubin–Lions compactness theorem (Theorem 2.6) we then obtain the strong convergence

$$(\psi_B^{n_k}, \psi_R^{n_k}) \longrightarrow (\psi_B, \psi_R) \quad \text{in } (L_t^2 L_x^2)^2. \tag{7.61}$$

The previous subsection entails

$$\mathcal{T}(\psi_B^{n_k}, \psi_R^{n_k}) \longrightarrow \mathcal{T}(\psi_B, \psi_R) \quad \text{in } \mathbb{X}.$$

as (7.61) was the key property used for the continuity of $\mathcal{T}$.

All the hypotheses of Schauder's fixed-point theorem (Theorem 2.4) are now satisfied, hence $\mathcal{T}$ admits at least one fixed point $(\phi_B, \phi_R) \in \overline{B}_R$.

By construction, (ϕ_B, ϕ_R) is a weak solution of the coupled problem (7.1). Finally, by the Lions–Magenes Theorem 7.5 we have

$$\phi_B, \phi_R \in C([0, T]; L^2(\Omega)),$$

and the a priori estimate (7.38) holds for this solution.

7.4 The S–ϕ relationship — two options

We now present two concrete choices for the transport functions S_B, S_R. Both constructions are designed so as to fit the structural assumptions on the non-linear operators $\mathcal{S}_B, \mathcal{S}_R$ stated above (continuity $\mathcal{S}_B, \mathcal{S}_R : L_t^2 L_x^2 \to L_t^2 L_x^2$ and a uniform L^∞ bound).

Modelling assumptions: We consider

- a continuous and bounded function $\sigma : \mathbb{R} \to \mathbb{R}$, named *saturation function*;

- two measurable and essentially bounded functions $c_B, c_R : Q_T \to \mathbb{R}$, named *background coefficients*;
- a kernel $K \in L^1(\Omega)$, with $K \geq 0$, and $\int_\Omega K(x)\,dx = 1$.

The unknowns ϕ_B and ϕ_R represent amount of biomass, therefore the biologically meaningful regime corresponds to

$$\phi_B(t,x) \geq 0, \qquad \phi_R(t,x) \geq 0 \quad \text{for a.e. } (t,x) \in Q_T.$$

In particular, if a weak solution were to take negative values (even for a short time or on a set of positive measure), it would no longer be acceptable from the modelling viewpoint, as it would lose its biological interpretation. In such a case the simulation is stopped.

Both options below give rise to operators $\mathcal{S}_B, \mathcal{S}_R$ satisfying the assumptions in the coupled existence theorem.

Option A. Here S "reads" from ϕ only the *fraction* of branches or roots above a prescribed threshold x_c. The larger this fraction, the stronger the transport; the effect is then saturated through the function σ. For $\phi_B, \phi_R \in L^2(Q_T)$ we define, for almost every $t \in (0,T)$,

$$P_R(t) = \frac{\displaystyle\int_{x \geq x_c} \phi_R(t,x)\,dx}{\displaystyle\int_\Omega \phi_R(t,x)\,dx + \varepsilon}, \qquad P_B(t) = \frac{\displaystyle\int_{x \geq x_c} \phi_B(t,x)\,dx}{\displaystyle\int_\Omega \phi_B(t,x)\,dx + \varepsilon},$$

with a fixed $\varepsilon > 0$ preventing division by zero. Then, we set

$$\begin{aligned} S_B(t,x,\phi_R) &= c_B(t,x) + \sigma(P_R(t))\,, \\ S_R(t,x,\phi_B) &= c_R(t,x) + \sigma(P_B(t))\,. \end{aligned}$$

Biological reading: transport in the branches increases when the fraction of roots with high bacterial load grows; similarly S_R responds to the "high-load" fraction in the branches.

Option B: non-local coupling in x (convolution). Here S depends on a *local-in-x average* of ϕ obtained via a kernel $K \in L^1(\Omega)$, $K \geq 0$, $\int_\Omega K = 1$ (e.g. a Gaussian kernel $K(\xi) = \frac{1}{\sqrt{2\pi}\,\ell}\, e^{-\frac{\xi^2}{2\ell^2}}$, with standard deviation $\ell > 0$). For $\phi_B, \phi_R \in L^2(Q_T)$ we set

$$(\mathcal{K}\phi_R)(t,x) = \int_\Omega K(x-y)\,\phi_R(t,y)\,dy, \qquad (\mathcal{K}\phi_B)(t,x) = \int_\Omega K(x-y)\,\phi_B(t,y)\,dy,$$

and define

$$\begin{aligned} S_B(t,x,\phi_R) &= c_B(t,x) + \sigma((\mathcal{K}\phi_R)(t,x))\,, \\ S_R(t,x,\phi_B) &= c_R(t,x) + \sigma((\mathcal{K}\phi_B)(t,x))\,. \end{aligned}$$

Biological reading: transport in a given bacterial-load level x responds to the density of plant biomass ϕ near x (the kernel K sets how "near"). Again the response is saturated by σ.

Analytical note. In both options S_B and S_R satisfy the assumptions given at the beginning of Section 7.3.

Option A.

By construction $0 \le P_R^{\phi_R}(t) \le 1$ for a.e. t, hence $P_R^{\phi_R} \in L^\infty(0,T) \subset L^2(0,T)$.
Let $(\phi_R^n)_{n\in\mathbb{N}} \subset L^2(Q_T)$ be a sequence such that

$$\phi_R^n \to \phi_R \quad \text{in } L^2(Q_T),$$

with $\phi_R^n \ge 0$ a.e. in Q_T for every n. Passing to a subsequence (not relabelled), we may assume that

$$\phi_R^n \to \phi_R \quad \text{a.e. in } Q_T.$$

For a.e. $t \in (0,T)$ the maps $x \mapsto \phi_R^n(t,x)$ belong to $L^2(\Omega)$; by the inclusion theorem for Lebesgue spaces, namely the continuous embedding $L^2(\Omega) \hookrightarrow L^1(\Omega)$, we have

$$\left| \int_\Omega \phi_R^n(t,x)\,dx \right| \le |\Omega|^{1/2}\, \|\phi_R^n(t,\cdot)\|_{L^2(\Omega)},$$

and similarly for ϕ_R. Hence, for a.e. t the quantities

$$\int_{x\ge x_c} \phi_R^n(t,x)\,dx, \qquad \int_\Omega \phi_R^n(t,x)\,dx$$

are finite, so $P_R^{\phi^n}(t) := P_R^{\phi_R^n}(t)$ is well defined and satisfies $0 \le P_R^{\phi^n}(t) \le 1$.
Moreover, for a.e. $t \in (0,T)$,

$$\left| \int_{x\ge x_c} \big(\phi_R^n - \phi_R\big)(t,x)\,dx \right| \le |\Omega|^{1/2}\, \|\phi_R^n(t,\cdot) - \phi_R(t,\cdot)\|_{L^2(\Omega)},$$

and the same estimate holds with the integral over Ω. Squaring and integrating in t we obtain

$$\int_0^T \left| \int_{x\ge x_c} \big(\phi_R^n - \phi_R\big)(t,x)\,dx \right|^2 dt \le |\Omega|\, \|\phi_R^n - \phi_R\|^2_{L^2(Q_T)} \longrightarrow 0,$$

and analogously for the integrals over Ω. Hence, up to a further subsequence, for a.e. t the numerators and denominators in $P_R^{\phi^n}(t)$ converge to those in $P_R^{\phi}(t)$, so

$$P_R^{\phi^n}(t) \longrightarrow P_R^{\phi}(t) \qquad \text{for a.e. } t \in (0,T),$$

with the uniform bound $0 \le P_R^{\phi^n}(t) \le 1$. Therefore, by the dominated convergence theorem in t,

$$P_R^{\phi^n} \longrightarrow P_R^{\phi} \quad \text{in } L^2(0,T).$$

Since σ is continuous and bounded, the sequence $\sigma\big(P_R^{\phi^n}\big)$ converges to $\sigma\big(P_R^{\phi}\big)$ in $L^2(0,T)$ again by dominated convergence; adding the bounded term c_B we obtain

$$\mathcal{S}_B(\phi_R^n) \to \mathcal{S}_B(\phi_R) \quad \text{in } L^2(Q_T).$$

An entirely analogous argument applies to $\mathcal{S}_R$.

Option B.
For $K \in L^1(\Omega)$, Young's inequality for convolutions gives

$$\|\mathcal{K}(\phi_R^n - \phi_R)\|_{L^2(Q_T)} \le \|K\|_{L^1(\Omega)}\, \|\phi_R^n - \phi_R\|_{L^2(Q_T)}.$$

Hence, if $\phi_R^n \to \phi_R$ in $L^2(Q_T)$, then $\mathcal{K}\phi_R^n \to \mathcal{K}\phi_R$ in $L^2(Q_T)$. By continuity and boundedness of σ and by dominated convergence, $\sigma(\mathcal{K}\phi_R^n) \to \sigma(\mathcal{K}\phi_R)$ in $L^2(Q_T)$, and therefore $\mathcal{S}_B(\phi_R^n) \to \mathcal{S}_B(\phi_R)$ in $L^2(Q_T)$. The reasoning for $\mathcal{S}_R$ is identical.

Moreover, in both options the uniform bound on c_B, c_R and on σ implies a uniform $L^\infty(Q_T)$ bound on S_B and S_R, as required.

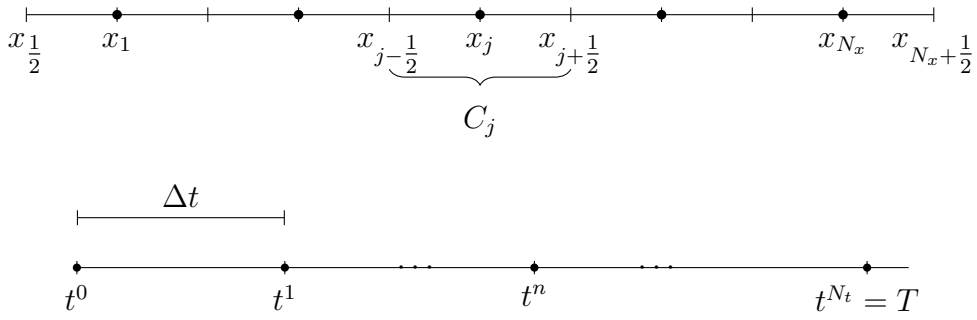
7.5 Discretisation

Let $\bar{\Omega} = [x_{\min}, x_{\max}]$ be partitioned into N_x cells of width $\Delta x = (x_{\max} - x_{\min})/N_x$.

We denote by $x_{j+\frac{1}{2}} = x_{\min} + j\,\Delta x$ $(j = 0, \dots, N_x)$ the interfaces between cells, i.e., $C_j = (x_{j-1/2}, x_{j+1/2})$, and by

$$x_j = \tfrac{1}{2}\big(x_{j-\frac{1}{2}} + x_{j+\frac{1}{2}}\big) = x_{\min} + \Big(j - \tfrac{1}{2}\Big)\Delta x, \quad j = 1, \dots, N_x,$$

the center of the cell C_j.



The time interval is split into N_t steps of size $\Delta t = T/N_t$ and set $t^n = n\Delta t$ for $n = 0, \dots, N_t$. For each cell C_j and any time t^n, we define the cell averages by, for $j = 1, \dots, N_x$,

$$\phi_{B,j}^n \approx \frac{1}{\Delta x}\int_{x_{j-\frac{1}{2}}}^{x_{j+\frac{1}{2}}} \phi_B(t^n, x)\, dx, \qquad \phi_{R,j}^n \approx \frac{1}{\Delta x}\int_{x_{j-\frac{1}{2}}}^{x_{j+\frac{1}{2}}} \phi_R(t^n, x)\, dx.$$

The transport velocities at the interfaces are made explicit at time t^n as:

$$\begin{aligned} S^n_{B,j+\frac{1}{2}} &:= \frac{S_B(t^n, x_j, \phi^n_{R,j}) + S_B(t^n, x_{j+1}, \phi^n_{R,j+1})}{2}, \\ S^n_{R,j+\frac{1}{2}} &:= \frac{S_R(t^n, x_j, \phi^n_{B,j}) + S_R(t^n, x_{j+1}, \phi^n_{B,j+1})}{2}, \end{aligned} \tag{7.62}$$

then, we consider an *upwind* flux–splitting:

$$S^{n,+}_{(\cdot),j+\frac{1}{2}} = \max\big(S^n_{(\cdot),j+\frac{1}{2}}, 0\big), \qquad S^{n,-}_{(\cdot),j+\frac{1}{2}} = \min\big(S^n_{(\cdot),j+\frac{1}{2}}, 0\big).$$

The total numerical flux (advective+diffusive) at $x_{j+\frac{1}{2}}$ is

$$\boxed{H^{n+1}_{(\cdot),j+\frac{1}{2}} = S^{n,+}_{(\cdot),j+\frac{1}{2}}\, \phi^{n+1}_{(\cdot),j} + S^{n,-}_{(\cdot),j+\frac{1}{2}}\, \phi^{n+1}_{(\cdot),j+1} - \mu\, \frac{\phi^{n+1}_{(\cdot),j+1} - \phi^{n+1}_{(\cdot),j}}{\Delta x}}. \tag{7.63}$$

Integrating over C_j and using the implicit Euler scheme in time, the discretisation of Equations $(7.1)_{1,2}$ reads: for $j = 2, \dots, N_x - 1$

$$\phi^{n+1}_{B,j} - \phi^n_{B,j} + \frac{\Delta t}{\Delta x}\Big(H^{n+1}_{B,j+\frac{1}{2}} - H^{n+1}_{B,j-\frac{1}{2}}\Big) + \Delta t\, M^{n+1}_{B,j}\, \phi^{n+1}_{B,j} = \Delta t\, G^{n+1}_{B,j}, \tag{7.64}$$

$$\phi^{n+1}_{R,j} - \phi^n_{R,j} + \frac{\Delta t}{\Delta x}\Big(H^{n+1}_{R,j+\frac{1}{2}} - H^{n+1}_{R,j-\frac{1}{2}}\Big) = 0. \tag{7.65}$$

By substituting (7.63) in (7.64) and (7.65), we obtain a tridiagonal system

$$A^{n+1}_{(\cdot)}\, \boldsymbol{\phi}^{n+1}_{(\cdot)} = \boldsymbol{f}^{n+1}_{(\cdot)}, \tag{7.66}$$

where

$$\boldsymbol{\phi}^{n+1}_B = \begin{bmatrix} \phi^{n+1}_{B,1} \\ \phi^{n+1}_{B,2} \\ \vdots \\ \phi^{n+1}_{B,N_x} \end{bmatrix}, \qquad \boldsymbol{\phi}^{n+1}_R = \begin{bmatrix} \phi^{n+1}_{R,1} \\ \phi^{n+1}_{R,2} \\ \vdots \\ \phi^{n+1}_{R,N_x} \end{bmatrix}.$$

For $j = 2, \dots, N_x - 1$, the non-null entries of the matrix A_B and right-hand side of $\boldsymbol{f}^{n+1}_B$ read

$$\begin{aligned} A_B(j, j-1) &= -\frac{\Delta t}{\Delta x}\Big(S^{n,+}_{B,j-\frac{1}{2}} + \frac{\mu}{\Delta x}\Big), \\ A_B(j, j) &= 1 + \frac{\Delta t}{\Delta x}\left(S^{n,+}_{B,j+\frac{1}{2}} - S^{n,-}_{B,j-\frac{1}{2}} + \frac{2\mu}{\Delta x}\right) + \Delta t\, M^{n+1}_{B,j}, \\ A_B(j, j+1) &= \frac{\Delta t}{\Delta x}\Big(S^{n,-}_{B,j+\frac{1}{2}} - \frac{\mu}{\Delta x}\Big), \\ f^{n+1}_{B,j} &= \phi^n_{B,j} + \Delta t\, G^{n+1}_{B,j}. \end{aligned} \tag{7.67}$$

Similarly, for $j = 2, \ldots, N_x - 1$ the non-null entries of the matrix A_R and of the right-hand side $\boldsymbol{f}_R^{n+1}$ are

$$\begin{aligned} A_R(j, j-1) &= -\frac{\Delta t}{\Delta x}\Big(S^{n,+}_{R,j-\frac{1}{2}} + \frac{\mu}{\Delta x}\Big), \\ A_R(j, j) &= 1 + \frac{\Delta t}{\Delta x}\left(S^{n,+}_{R,j+\frac{1}{2}} - S^{n,-}_{R,j-\frac{1}{2}} + \frac{2\mu}{\Delta x}\right), \\ A_R(j, j+1) &= \frac{\Delta t}{\Delta x}\Big(S^{n,-}_{R,j+\frac{1}{2}} - \frac{\mu}{\Delta x}\Big), \\ f^{n+1}_{R,j} &= \phi^n_{R,j}. \end{aligned} \tag{7.68}$$

For what concerns no–conormal–flux boundary conditions, i.e. $H^{n+1}_{(\cdot),\frac{1}{2}} = H^{n+1}_{(\cdot),N_x+\frac{1}{2}} = 0$, we have:

Left end $j = 1$:

$$\begin{aligned} A_{(\cdot)}(1,1) &= 1 + \frac{\Delta t}{\Delta x}\Big(S^{n,+}_{(\cdot),\frac{3}{2}} + \frac{\mu}{\Delta x}\Big) + \Delta t\, M^{n+1}_{(\cdot),1}, \\ A_{(\cdot)}(1,2) &= \frac{\Delta t}{\Delta x}\Big(S^{n,-}_{(\cdot),\frac{3}{2}} - \frac{\mu}{\Delta x}\Big), \\ f^{n+1}_{B,1} &= \phi^n_{B,1} + \Delta t\, G^{n+1}_{B,1}, \qquad f^{n+1}_{R,1} = \phi^n_{R,1}. \end{aligned} \tag{7.69}$$

Right end $j = N_x$:

$$\begin{aligned} A_{(\cdot)}(N_x, N_x-1) &= -\frac{\Delta t}{\Delta x}\Big(S^{n,+}_{(\cdot),N_x-\frac{1}{2}} + \frac{\mu}{\Delta x}\Big), \\ A_{(\cdot)}(N_x, N_x) &= 1 + \frac{\Delta t}{\Delta x}\Big(-S^{n,-}_{(\cdot),N_x-\frac{1}{2}} + \frac{\mu}{\Delta x}\Big) + \Delta t\, M^{n+1}_{(\cdot),N_x}, \\ f^{n+1}_{B,N_x} &= \phi^n_{B,N_x} + \Delta t\, G^{n+1}_{B,N_x}, \qquad f^{n+1}_{R,N_x} = \phi^n_{R,N_x}. \end{aligned} \tag{7.70}$$

7.5.1 Positivity correction (post–processing)

Let $\varepsilon > 0$ be a numerical tolerance (for example $\varepsilon = 10^{-14}$). $\boldsymbol{\phi}^{n+1}$ denotes either $\boldsymbol{\phi}_B^{n+1}$ or $\boldsymbol{\phi}_R^{n+1}$ solution of (7.66), we apply the following conservative left-to-right correction:

1. **Interior cells + first cell** ($j = 1, \ldots, N_x - 1$).

$$\begin{aligned} \text{if } \ \phi_j^{n+1} < -\varepsilon: \quad & \phi_{j+1}^{n+1} \ \leftarrow \ \phi_{j+1}^{n+1} + \phi_j^{n+1}, \qquad \phi_j^{n+1} \ \leftarrow \ 0, \\ \text{if } \ -\varepsilon \le \phi_j^{n+1} < 0: \quad & \phi_j^{n+1} \ \leftarrow \ 0 \quad \text{(numerical noise)}. \end{aligned}$$

2. **Right boundary check** ($j = N_x$). If $\phi_{N_x}^{n+1} < -\varepsilon$, let $d := \phi_{N_x}^{n+1} (< 0)$ and $p := \phi_{N_x-1}^{n+1}$, then:

- if $|p| \leq \varepsilon$: we *stop* the execution (pathological case: no reservoir on the left);
- if $p + d \geq -\varepsilon$: we absorb the deficit into the penultimate node and set the last one to zero,
$$\phi_{N_x-1}^{n+1} \leftarrow p + d, \qquad \phi_{N_x}^{n+1} \leftarrow 0,$$
and, if needed, we truncate $\phi_{N_x-1}^{n+1}$ to 0 when it falls into $(-\varepsilon, 0)$;
- otherwise: we *stop* the execution (the deficit would exceed the capacity of the penultimate node, thus losing conservativity).

This procedure preserves exactly the mass $\sum_{j=1}^{N_x} \phi_j^{n+1}$ as long as the deficit can be transferred inside the domain or absorbed by the penultimate node; in the cases in which this is not possible, the code is deliberately stopped to diagnose the anomaly.

7.5.2 Special case: pruning

When a *total pruning* occurs, we do not model it with a normal mortality term, but as an impulsive external event. At the corresponding time step we directly impose (the vector $\boldsymbol{\phi}^{n+1}$ denotes either $\boldsymbol{\phi}_B^{n+1}$ or $\boldsymbol{\phi}_R^{n+1}$, solution of (7.66))

$$\boldsymbol{\phi}^{n+1} \equiv \mathbf{0}.$$

This choice is motivated by the structure of the numerical scheme. In the code, mortality enters through an implicit term of the form

$$\phi_j^{n+1} - \phi_j^n + \Delta t\, M_j^{n+1}\, \phi_j^{n+1} = 0,$$

so that, in absence of transport and sources,

$$\phi_j^{n+1} = \frac{\phi_j^n}{1 + \Delta t\, M_j^{n+1}}.$$

Hence, even taking M_j^{n+1} very large, a single time step would only reduce each cell by a factor $\frac{1}{1+\Delta t\, M_j^{n+1}}$, but would not set it exactly to zero. Biologically, however, a total pruning corresponds to the instantaneous removal of all biomass in the affected compartment. To represent this effect correctly at the discrete level, it is therefore necessary to override the implicit update at the pruning time and enforce the direct zeroing of the profile $\boldsymbol{\phi}$.

7.6 Epidemiological model of *Xylella fastidiosa* infection in vineyards

The eco-epidemiological model introduced in the previous sections has been presented and discussed at the 14th Conference of the European Foundation for Plant Pathology (2–5 June 2025, Uppsala, Sweden). It is a mechanistic tool to explore the risk of *Xylella fastidiosa* introduction and spread in vineyards. Below, we report the abstract submitted for that event; in the following figures we also show some of the numerical results obtained from the model simulations. This work is the result of a collaboration with Igor Daniel Weber, Anna Simonetto, Paola Gervasio, Gianni Gilioli of the University of Brescia, DICATAM, Brescia, Italy; and Juan Antonio Navas-Cortés of the Institute for Sustainable Agriculture (IAS), Spanish National Research Council (CSIC), Córdoba, Spain.

Xylella fastidiosa Wells (1987) (Proteobacteria: Xanthomonadaceae) is a xylem-limited bacterium that infects over 600 plant species, including several economically important crops. Native to the Americas, *X. fastidiosa* subsp. *fastidiosa* (*Xff*) has caused severe losses in the U.S. grapevine industry as the causative agent of Pierce's Disease (PD). Since the detection of this subspecies in Mallorca Island (Spain) in 2016, concerns about its impact on European viticulture have escalated, highlighting a critical gap in epidemiological tools needed for risk assessment and to guide management strategies.

The *Xff* epidemiological system is complex, driven by interactions among the pathogen, insect vectors, and host plants, further modulated by abiotic factors such as temperature and water stress. To address this complexity, we developed an eco-epidemiological model to simulate *Xff* disease dynamics in vineyards by integrating physiological and ecological processes. The model incorporates key system components: herbaceous plants (hosts for vector immature stages), non-susceptible woody plants (vector food sources), reservoir plants (infection sources for vectors), grapevines (structured into compartments based on disease progression, including infectious asymptomatic plants), and vectors (categorized into immature, uninfected adult, and infected adult stages). Model parameters were derived from published laboratory and field data. Model calibration was performed based on a case study of an *Xff* outbreak in Southern Europe.

This model represents a significant step forward in understanding *Xff* epidemiology, providing valuable insights into the potential risk faced by wine-growing regions in Europe. Furthermore, it provides a critical foundation for designing effective strategies to prevent and mitigate the establishment and spread of this pathogen in vineyards.

To obtain the results presented at the conference, and reported in Figs. 52 and 53, we used the following parameter values and functional forms. For brevity, we do not report them in full detail here. The diffusion coefficient μ was set to 10^{-5}, whereas the functions S_B and S_R are defined as follows:

$$S_B(t,x) = \frac{r_{S_B}\, r(T(t))}{\ln(10)} \left(1 - \frac{10^x}{K}\right) + \frac{i_V(t)}{K\, \ln(10)\, 10^x},$$

where

- $r(T(t))$ is called *bacterial growth function*;
- r_{S_B} is called *branches suitability coefficient for bacterial growth*;
- K is the maximum bacterial load;
- $i_V(t)$ is the function that models the infection due to inoculum from vectors,

and,

$$S_R(t,x) = \frac{r_{S_R}\, r(T(t))}{\ln(10)} \left(1 - \frac{10^x}{K}\right) - \frac{m_c(T(t))}{\ln(10)},$$

where

- r_{S_R} is called *roots suitability coefficient for bacterial growth*;
- $m_c(T(t))$ is the bacterial disease regression rate function due to cold during the winter period.

The mortality function M_B is defined as follows: it is identically zero throughout the years and acts only on the pruning days (once a year), when it removes all branches. The function G_B, instead, acts in spring by generating new branches over a given time interval, making their distribution follow the profile of the roots solution during that period.

Concerning the total domain and initial data, we take the bacterial load variable x (in $\log_{10}$ scale) in the interval $\Omega = [-12, 7]$, divided into $N_x = 500$ steps, and we consider a time horizon of 5 years, which in the simulations is discretised with a time step $\Delta t = 1\,\mathrm{h}$ (i.e. $N_t = 5 \times 8760$ time steps). The initial distribution in branches is set to zero, $\Phi_{B0}(x) \equiv 0$, whereas the initial distribution in roots, $\Phi_{R0}(x)$, is chosen as a Gaussian profile in $\log_{10}$–bacterial load with mean $\bar{x} = -2$ and standard deviation $\varsigma = 0.5$, truncated to the interval $[-7, 3]$ and renormalized so that

$$\int_{-7}^{3} \Phi_{R0}(x)\, dx = 100.$$

Simulation results. Figure 52 shows the time evolution of the distribution of bacterial loads in roots (left) and branches (right). In the roots, the infection persists over the whole five–year horizon and the distribution slowly drifts towards higher bacterial

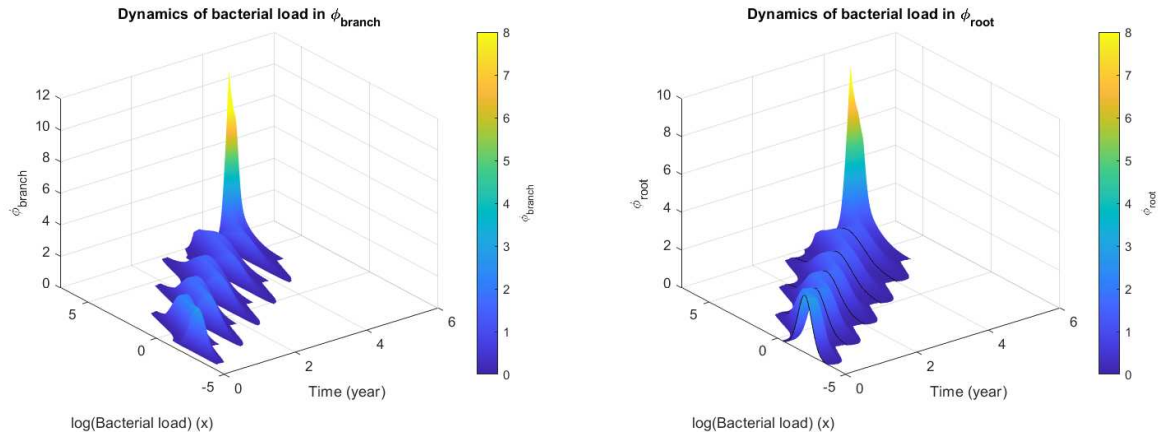


Figure 51: Three-dimensional view of the coupled solutions under the *Oakland (USA)* temperature forcing (five-year horizon). Compared with the warmer-site simulation (Manacor), both compartments display lower bacterial-load levels on average and reduced seasonal peaks, supporting the intended temperature-dependent behaviour of the model. Left: branches; right: roots. Horizontal axes: time (years) and bacterial load coordinate $x = \log_{10}(\text{bacterial load})$; vertical axis (and colour): biomass density ϕ.

loads, despite winter cold effects encoded in $S_R(t)$. In the branches, instead, the distribution is reset every winter by pruning and each spring the newly formed branches are reinfected from the roots, generating recurrent seasonal peaks. Figure 53 provides a three–dimensional view of the same solutions.

The numerical experiments confirm that the model responds consistently to climatic forcing through the temperature-dependent growth/regression mechanisms. In the warmer-site simulation (Manacor), the coupled system produces a progressive drift of the root distribution towards higher bacterial-load levels and recurrent seasonal peaks in the branches after spring regrowth, as clearly visible in Figures 52–53. When the same model is driven by temperature data from a colder location (Oakland), the solutions remain on average shifted towards lower load levels and display markedly reduced seasonal peaks in both compartments (Figure 51). These differences in simulated bacterial dynamics are in agreement with empirical observations of infection dynamics under different temperature conditions: warmer growing seasons favour a faster drift of biomass towards higher load levels, whereas colder conditions (and stronger winter regression) hinder the accumulation of high loads and promote persistence in moderate-to-low levels. Moreover, the two-compartment coupling remains visible in both cases: roots act as a reservoir sustaining reinfection of branches; whereas under colder forcing the magnitude of this effect is smaller, leading to systematically weaker branch excursions (compare Figure 51 with Figure 53).

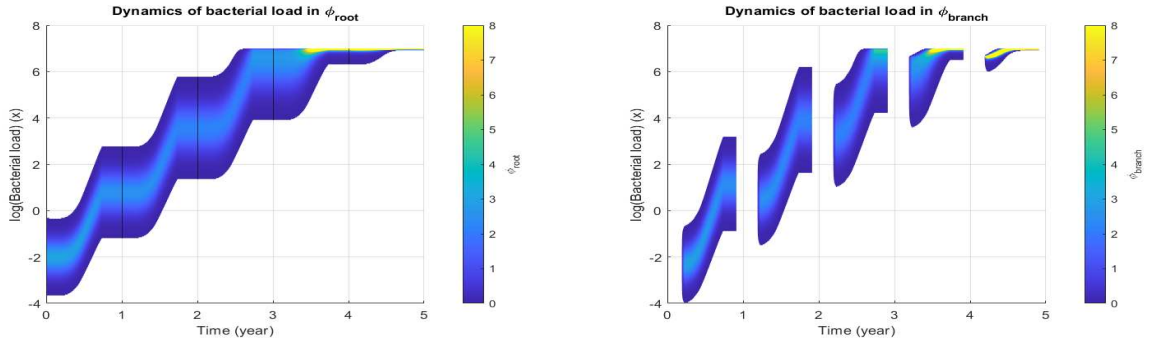


Figure 52: Two dimensional time evolution of the bacterial-load distributions simulated for the grapevine model under the *Manacor (Mallorca, Spain)* temperature forcing (five-year horizon). Horizontal axis: time; vertical axis: bacterial load coordinate $x = \log_{10}(\text{bacterial load})$; colour: biomass density ϕ. Left: roots; right: branches. Interruptions in the branches panel are due to seasonal pruning and subsequent spring regrowth.

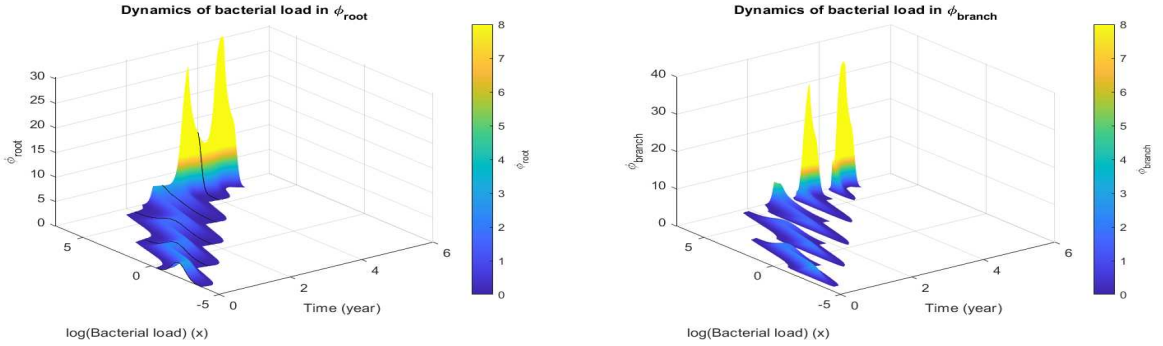


Figure 53: Three-dimensional view of the coupled solutions under the *Manacor (Mallorca, Spain)* temperature forcing (five-year horizon). Horizontal axes: time and bacterial load coordinate $x = \log_{10}(\text{bacterial load})$; vertical axis (and colour): biomass density ϕ. Left: roots; right: branches. Interruptions in the branches panel are due to seasonal pruning and subsequent spring regrowth.

List of Figures

1 Spodoptera frugiperda - Larva. Source: website *www.agro.genica.com.* 18
2 Spodoptera frugiperda States Distribution Map - 2021. Source: website *www.eppo.int.* 18
3 Spodoptera frugiperda - Adult. Source: website *www.defrentealcampo.com.* . 19
4 Spodoptera frugiperda damage. Source: website *www.entomologytoday.org.* . . 19
5 Erasmoneura vulnerata. Source: website *www.BugGuide.net.* 20
6 Foliage lesions (light green stains) and Erasmoneura vulnerata excrement (black spots). Source: website *www.alpineentomology.net.* 20
7 Adult *Philaenus spumarius* (meadow spittlebug) on a leaf, dorsal view. Source: website *www.idtools.dpi.nsw.gov.* 21
8 *Xylella fastidiosa* under the electron microscope. Source: *www.denia.com.* 22
9 *Xylella fastidiosa* damage in Puglia - Italy. Source: *www.terraevita.edagricole.it.* 22
10 Example of output solution from Entomonlib for a phenological model in which emergence functions are defined over a one-year time span for 3 consecutive generations. The 4th stage is the adult one. Source: Entomonlib. 26
11 Nodes and control volumes in the interval [0,1]. 29
12 An example of temperature plots. Source: Entomonlib. 35
13 Another example of a temperature plot. Source: Entomonlib. 36
14 Development rate functions determined from data (chosen function type: Brière). Source: Entomonlib. 37
15 A visual comparison of an Entomonlib abundance solution (blue line) and the related target data (red asterisks). Source: Entomonlib. 37
16 A Brière function cut in its negative values. Source: [78]. 39
17 The quadratic with constant exterior branches function. Source: Entomonlib. . 40
18 The 3branches function. Source: Entomonlib. 41
19 The Euler beta distribution. Source: www.en.wikipedia.org. 43
20 A Bieri distribution. Source: Entomonlib. 44
21 The Gamma distribution. Source: www.en.wikipedia.org. 45
22 Source: Entomonlib. 46
23 Simulated population dynamics (insects $/m^2$) of *P. spumarius* life stages in Liguria, Northern Italy, used as an example of model validation. Red asterisks represent field monitoring data for $N3$–$N5$ nymphal stages, and grey dots represent field monitoring data for adult stages, converted to insects per square meter. 53

24 Schematic representation of the eco-epidemiological model framework. Rectangles represent vegetation compartments, while circles denote vector compartments. Solid black arrows denote vegetation dynamics, demographic processes, and transitions between compartments. Red arrows depict vector—host plant interactions that determine vector acquisition (dotted arrows) from infectious plants and inoculation events (dashed arrows) by infected vectors. Grey arrows are vector–host plant interactions that do not involve pathogen transmission. Definitions of model compartments and functions are provided in Table 1. . . 59
25 Average weekly temperatures (°C) over the five-year simulation period (2015–2019) in olive groves used for model calibration and validation in the Apulia region, Italy. Each panel corresponds to a different calibration site. The black lines represent the mean weekly temperatures, while the shaded grey areas indicate the range between average weekly maximum and minimum temperatures. 65
26 Average weekly available soil water (mm, black lines, left y-axis) and weekly cumulative precipitation (mm, blue bars, right y-axis) over the five-year simulation period (2015-2019) in olive groves used for model calibration and validation in the Apulia region, Italy. 66
27 Trends of infection over five years (2015–2019) at the five calibration sites. Lines represent the simulated percentage of olive trees in each disease stage, while points indicate observed field data in the *Xf*-infected area of Lecce province (Zarco-Tejada et al., 2018 [61], 2021 [90]). C_S–C_1: Asymptomatic olives; C_2: $>$ 0–25% canopy with desiccated branches; C_3: $>$ 25–50%; C_4: $>$ 50–75%; and C_5: $>$ 75% canopy with desiccated branches or fully desiccated trees. 68
28 Trends of infection over five years (2015–2019) at the validation sites. Lines represent the simulated percentage of olive trees in each disease stage, while points indicate observed field data in the *Xf*-infected area of Lecce province (Zarco-Tejada et al., 2018 [61], 2021 [90]). C_S–C_1: Asymptomatic olives; C_2: $>$ 0–25% canopy with desiccated branches; C_3: $>$ 25–50%; C_4: $>$ 50–75%; and C_5: $>$ 75% canopy with desiccated branches or fully desiccated trees. 69
29 Simulated dynamics of non-crop vegetation and vectors over a five-year period in one of the 16 simulated olive groves in the Apulia region, Italy. Panels show (a) herbaceous vegetation biomass, (b) biomass of non-susceptible shrubs and trees, (c) biomass of the reservoir vegetation (R_S – susceptible, R_I – infected; R– overall), and (d) vector populations (P – preimaginal insects, V_S – non-infected adults; V_I – infected adults). 70
30 Simulated herbaceous biomass dynamics (H) (kg ha^{-1}) over five-year period (2015-2019) in olive groves used for model calibration (a) and validation (b) in the Apulia region, Italy. 71

31 Simulated biomass dynamics of non-susceptible shrubs and trees (N) (kg ha^{-1}) over five-year period (2015-2019) in olive groves used for model calibration (a) and validation (b) in the Apulia region, Italy. 72
32 Simulated biomass dynamics of non-infected (R_S), infected (R_I) and total reservoir (R) (kg ha^{-1}) over five-year period (2015-2019) in olive groves used for model calibration (a) and validation (b) in the Apulia region, Italy. 73
33 Simulated number of preimaginal stage (P), and non-infected (V_S) and infected (V_I) adult stages of *Philaenus spumarius* over five-year period (2015-2019) in olive groves used for model calibration (a) and validation (b) in the Apulia region, Italy. 74
34 Peak prevalence (%) of infected *P. spumarius* adults over five-year period (2015-2019) in olive groves used for model calibration (a) and validation (b) in the Apulia region, Italy. 75
35 Percentage (%) of olive trees in each disease stage over a five-year period (2015-2019) in olive groves used for model calibration (a) and validation (b) in the Apulia region, Italy. Lines represent the simulated dynamics, while points represent the observed dynamics from field data in the Xf-infected area of Lecce province. C_S: non-infected olive trees;C_0: infected but non-infectious asymptomatic trees; C_1: infectious asymptomatic trees; and C_2–C_5: symptomatic trees. 76
36 The Monod equation (the unit of measure could vary depending on the application topic. Source: www.cs.montana.edu. 78
37 Visual example for a better understanding of the definition of a Lyapunov stable equilibrium point. If every trajectory of points starting inside the inner circle is entirely confined within the bigger circle, the center of the circles is a stable equilibrium point for Lyapunov. Source: [56] 94
38 Behaviours of the progression of an applied Fixed Point Method depending on the derivative of the function within a neighborhood of the solution. Source: www.ilovemethods.blogspot.com 97
39 A solution of the simplified BeXyl Model 1. Source: BeXyl Model 110
40 Solution of the Model #1 with $m_X \geq g_X$ and $m_V = f$ computed solving (5.2)-(5.10) with an adaptive fourth–fifth order Runge–Kutta method. 115
41 Model #1. Trends in plant-related compartments as a function of the balance between growth (g_X) and decline (m_X), as analytically proven. Numerical solutions were computed using an adaptive fourth–fifth order Runge–Kutta method. 116
42 An example of a Model #2 solution 122

43 Effect of the crop infection rate i_C on the proportion of severely infected crops. Blue circles: numerical approximation of $C_1(t)/C_{\text{tot}}$ at large times t, close to the numerical equilibrium, obtained by solving (5.39) for different values of i_C. Red curve: analytical equilibrium fraction $\Pi(i_C)$. All curves are computed with $d = 1.3 \times 10^{-4}$, $r_{C_0} = 2.53 \times 10^{-1}$ and $r_{C_1} = 1.26 \times 10^{-1}$. The overlap between numerics and theory results provides a visual–numerical validation of the model. 126
44 Baseline model simulation of *Xylella fastidiosa* epidemiological dynamics in olive grove agroecosystems in Apulia, Italy; the upper plot shows the dynamics of olive trees and reservoir vegetation compartments, while the lower one illustrates the vector population dynamics 145
45 Effect of increasing rates of p_{C_s} per p_{C_i} in the prevalence of infected olive trees (upper plot) and vectors (bottom plot) at the asymptotic equilibrium 146
46 Effect of increasing rates of p_N in the prevalence of infected olive trees (upper plot) and vectors (bottom plot) at different time points until the asymptotic equilibrium at t = 1000 147
47 Effect of vector control measures on the prevalence of infected olive trees (upper plots) and vectors (bottom plots) at the asymptotic equilibrium; the impact was assessed through pairwise combinations of parameters affected by vector control: (m_V, a) - plots a and d, (m_V, i_C) - plots b and e, and (a, i_C) - plots c and f 148
48 Effect of *Xylella fastidiosa (Xf)* control measures targeting infected olive trees on the prevalence of infection in olive trees (upper plots) and vectors (bottom plots) at the asymptotic equilibrium; the impact was assessed through pairwise combinations of parameters affected by *Xf* control: (a, i_C) - plots a and d, (a, r_C) - plots b and e, and (i_C, r_C) - plots c and f 149
49 Effect of the adoption of resistant or tolerant olive cultivars on the prevalence of infection in olive trees (upper plots) and vectors (bottom plots) at the asymptotic equilibrium; the impact was assessed versus pairwise combinations of parameters affected by cultivar resistance or tolerance: (p_{C_s}, i_C) - plots a and d, (p_{C_s}, r_C) - plots b and e, and (i_C, r_C) - plots c and f) 150
50 Effect of ground cover management on the prevalence of infection in olive trees (upper plots) and vectors (bottom plots) at the asymptotic equilibrium; the impact was assessed through pairwise combinations of parameters affected by ground control: (m_V, f) - plots a and d, (m_V, p_N) - plots b and e, and (f, p_N) - plots c and f 150

51 Three-dimensional view of the coupled solutions under the *Oakland (USA)* temperature forcing (five-year horizon). Compared with the warmer-site simulation (Manacor), both compartments display lower bacterial-load levels on average and reduced seasonal peaks, supporting the intended temperature-dependent behaviour of the model. Left: branches; right: roots. Horizontal axes: time (years) and bacterial load coordinate $x = \log_{10}(\text{bacterial load})$; vertical axis (and colour): biomass density ϕ. 176
52 Two dimensional time evolution of the bacterial-load distributions simulated for the grapevine model under the *Manacor (Mallorca, Spain)* temperature forcing (five-year horizon). Horizontal axis: time; vertical axis: bacterial load coordinate $x = \log_{10}(\text{bacterial load})$; colour: biomass density ϕ. Left: roots; right: branches. Interruptions in the branches panel are due to seasonal pruning and subsequent spring regrowth. 177
53 Three-dimensional view of the coupled solutions under the *Manacor (Mallorca, Spain)* temperature forcing (five-year horizon). Horizontal axes: time and bacterial load coordinate $x = \log_{10}(\text{bacterial load})$; vertical axis (and colour): biomass density ϕ. Left: roots; right: branches. Interruptions in the branches panel are due to seasonal pruning and subsequent spring regrowth. 177

List of Tables

1 Summary of model state variables and functions of the overall Eco-epidemiological model. 61

2 Intervals of bacterium titre [$\log(B^j)$, CFU(Colony Forming Units) ml^{-1}] for each compartment of infected olive trees (C_0–C_5), and the central values of bacterium titre intervals assumed for estimating the vector acquisition rates. . 82

3 Carrying capacities of non-susceptible shrubs and trees (K^N) and reservoir plants (K^R), total number of olive trees, and semi-saturation of the Monod functional response (λ^H, λ^N, λ^{R_S}, λ^{R_I}, and λ^{C_S} to λ^{C_5}) assumed for each host plant compartment across all simulated olive groves. 91

4 Initial conditions of model compartments for the olive groves used in model calibration and validation. 92

5 Baseline parameter values used in the epidemiological model, along with the ranges explored under the implementation of management strategies (values shown in brackets). Parameters influenced by control strategies are marked with a "x" in the corresponding column: (1) Vector control, (2) *X. fastidiosa* control within infected olive trees, (3) Adoption of resistant or tolerant olive cultivars, and (4) Ground cover management. 144

Bibliography

[1] W. O. Kermack and A. G. McKendrick. "A Contribution to the Mathematical Theory of Epidemics". In: *Proceedings of the Royal Society of London. Series A* 115.772 (1927), pp. 700–721.

[2] J. Schauder. "Der Fixpunktsatz in Funktionalräumen". In: *Studia Mathematica* 2.1 (1930), pp. 171–180.

[3] W. O. Kermack and A. G. McKendrick. "Contributions to the Mathematical Theory of Epidemics. II.—The Problem of Endemicity". In: *Proceedings of the Royal Society of London. Series A* 138.834 (1932), pp. 55–83.

[4] J. Monod. "The Growth of Bacterial Cultures". In: *Annual Review of Microbiology* 3 (1949), pp. 371–394.

[5] J.-L. Lions. *Quelques méthodes de résolution des problèmes aux limites non linéaires*. French. Chap. I, §5, Thm. 5.1 (Aubin–Lions), p. 58. Paris: Dunod; Gauthier–Villars, 1969.

[6] W. Witsack. "Experimentell-ökologische Untersuchungen über Dormanz-Formen von Zikaden (Homoptera, Auchenorrhyncha). 2. Zur Ovarial-Parapause und obligatorischen Embryonal-Diapause von *Philaenus spumarius* (L.) (Aphrophoridae)". German. In: *Zoologische Jahrbücher. Abteilung für Systematik, Ökologie und Geographie der Tiere* 100 (1973), pp. 517–562.

[7] W. Rudin. *Principles of Mathematical Analysis*. 3rd. 1221 Avenue of the Americas, New York: McGraw-Hill, 1976.

[8] A. N. Sparks. "A review of the biology of the fall armyworm". In: *The Florida Entomologist* 62.2 (1979), pp. 82–87.

[9] T. L. Wagner, H.-I. Wu, P. J. H. Sharpe, R. M. Schoolfield, and R. N. Coulson. "Modeling Insect Development Rates: a Literature Review and Application of a Biophysical Model". In: *Annals of the Entomological Society of America* 77.2 (1984), pp. 208–220.

[10] H. Amann. *Ordinary Differential Equations: An Introduction to Nonlinear Analysis*. Vol. 13. De Gruyter Studies in Mathematics. Berlin, Germany: De Gruyter, 1990.

[11] I. Györi. "Some mathematical aspects of modelling cell population dynamics". In: *Computers & Mathematics with Applications* 20.4 (1990), pp. 127–138.

[12] W. Yan and D. H. Wallace. "A Model of Photoperiod × Temperature Interaction Effects on Plant Development". In: *Critical Reviews in Plant Sciences* 15.1 (1996), pp. 63–96.

[13] B. L. Hill and A. H. Purcell. "Populations of *Xylella fastidiosa* in plants required for transmission by an efficient vector". In: *Phytopathology* 87.12 (1997), pp. 1197–1201.

[14] R. G. Allen, L. S. Pereira, D. Raes, and M. Smith. *Crop Evapotranspiration: Guidelines for Computing Crop Water Requirements*. FAO Irrigation and Drainage Paper 56. Rome: FAO, 1998.

[15] R. Howard. *The Gronwall Inequality*. Lecture notes, University of South Carolina. 1998.

[16] J. W. Chapman, T. Williams, A. Escribano, P. Caballero, R. D. Cave, and D. Goulson. "Fitness consequences of cannibalism in the fall armyworm, *Spodoptera frugiperda*". In: *Behavioral Ecology* 10.3 (1999), pp. 298–303.

[17] S. Yurtsever. "On the Polymorphic Meadow Spittlebug, Philaenus spumarius (L.) (Homoptera: Cercopidae)". In: *Turkish Journal of Zoology* 24.4 (2000), pp. 447–460.

[18] H. K. Khalil. *Nonlinear Systems*. 3rd ed. Upper Saddle River, NJ: Prentice Hall, 2002.

[19] D. G. McCall and G. J. Bishop-Hurley. "A pasture growth model for use in a whole-farm dairy production model". In: *Agricultural Systems* 76.3 (2003), pp. 1183–1205.

[20] E. Pebesma. "Multivariable geostatistics in S: the gstat package". In: *Computers & Geosciences* 30.7 (2004), pp. 683–691.

[21] R. P. P. Almeida, C. Wistrom, B. L. Hill, J. Hashim, and A. H. Purcell. "Vector transmission of *Xylella fastidiosa* to dormant grape". In: *Plant Disease* 89.4 (2005), pp. 419–424.

[22] E. Dufrêne, H. Davi, C. François, G. Le Maire, V. Le Dantec, and A. Granier. "Modelling carbon and water cycles in a beech forest. Part I: Model description and uncertainty analysis on modelled NEE". In: *Ecological Modelling* 185.2–4 (2005), pp. 407–436.

[23] M. J. Keeling and K. T. D. Eames. "Networks and epidemic models". In: *Journal of the Royal Society Interface* 2 (2005), pp. 295–307.

[24] M. Kottek, J. Grieser, C. Beck, B. Rudolf, and F. Rubel. "World Map of the Köppen–Geiger Climate Classification Updated". In: *Meteorologische Zeitschrift* 15.3 (2006), pp. 259–263.

[25] S. Rossi, A. Deslauriers, T. Anfodillo, and V. Carraro. "Evidence of threshold temperatures for xylogenesis in conifers at high altitudes". In: *Oecologia* 152 (2007), pp. 1–12.

[26] Q. Alfio, S. Fausto, and G. Paola. *Calcolo scientifico*. Springer, 2008.

[27] F. van den Bosch, N. McRoberts, F. van den Berg, and L. V. Madden. "The basic reproduction number of plant pathogens: matrix approaches to complex dynamics". In: *Phytopathology* 98.2 (2008), pp. 239–249.

[28] M. P. Daugherty and R. P. P. Almeida. "Estimating *Xylella fastidiosa* transmission parameters: decoupling sharpshooter number and feeding period". In: *Entomologia Experimentalis et Applicata* 132.1 (2009), pp. 84–92.

[29] A. J. Romera, D. G. McCall, J. M. Lee, and M. G. Agnusdei. "Improving the McCall herbage growth model". In: *New Zealand Journal of Agricultural Research* 52.4 (2009), pp. 477–494.

[30] M. Budinčević. "A Comparison Theorem of Differential Equations". In: *Novi Sad Journal of Mathematics* 40.1 (2010), pp. 55–56.

[31] N. J. Cunniffe and C. A. Gilligan. "Invasion, persistence and control in epidemic models for plant pathogens: the effect of host demography". In: *Journal of the Royal Society Interface* 7.44 (2010), pp. 439–451.

[32] L. C. Evans. *Partial Differential Equations*. 2nd ed. Vol. 19. Graduate Studies in Mathematics. §5.9.2, Thm. 3 (case $V = H^1$, $H = L^2$, $V' = (H^1)^*$), p. 287. Providence, RI: American Mathematical Society, 2010.

[33] H. Brezis. *Functional Analysis, Sobolev Spaces and Partial Differential Equations*. New York: Springer, 2011.

[34] M. P. Daugherty, A. Rashed, R. P. P. Almeida, and T. M. Perring. "Vector preference for hosts differing in infection status: sharpshooter movement and *Xylella fastidiosa* transmission". In: *Ecological Entomology* 36.6 (2011), pp. 654–662.

[35] J. H. Lieth, M. M. Meyer, K.-H. Yeo, and B. C. Kirkpatrick. "Modeling Cold Curing of Pierce's Disease in *Vitis vinifera* 'Pinot Noir' and 'Cabernet Sauvignon' Grapevines in California". In: *Phytopathology* 101.12 (2011), pp. 1492–1500.

[36] L. Roques, S. Soubeyrand, and J. Y. Rousselet. "A statistical-reaction–diffusion approach for analyzing expansion processes". In: *Journal of Theoretical Biology* 274.1 (2011), pp. 43–51.

[37] T. Tao. *An Introduction to Measure Theory*. Vol. 126. Graduate Studies in Mathematics. Open-access lecture notes available on the author's webpage. Providence, RI: American Mathematical Society, 2011.

[38] M. Saponari, D. Boscia, F. Nigro, and G. P. Martelli. "Identification of DNA sequences related to *Xylella fastidiosa* in oleander, almond and olive trees exhibiting leaf scorch symptoms in Apulia (Southern Italy)". In: *Journal of Plant Pathology* 94 (2013). Disease Note, p. 688.

[39] Q. Sun, Y. Sun, M. A. Walker, and J. M. Labavitch. "Vascular occlusions in grapevines with Pierce's disease make disease symptom development worse". In: *Plant Physiology* 161 (2013), pp. 1529–1541.

[40] S.-J. Jeong and D. Medvigy. "Macroscale prediction of autumn leaf coloration throughout the continental United States". In: *Global Ecology and Biogeography* 23.11 (2014), pp. 1245–1254.

[41] M. Shaw and M. Pautasso. "Networks and plant disease management: concepts and applications". In: *Annual Review of Phytopathology* 52 (2014), pp. 477–493.

[42] A. R. Zeilinger and M. P. Daugherty. "Vector preference and host defense against infection interact to determine disease dynamics". In: *Oikos* 123 (2014), pp. 613–622.

[43] N. J. Cunniffe, R. O. Stutt, R. E. DeSimone, T. R. Gottwald, and C. A. Gilligan. "Optimising and communicating options for the control of invasive plant disease when there is epidemiological uncertainty". In: *PLOS Computational Biology* 11.4 (2015).

[44] M. Pasalodos-Tato, R. Ruiz-Peinado, M. del Río, and G. Montero. "Shrub biomass accumulation and growth rate models to quantify carbon stocks and fluxes for the Mediterranean region". In: *European Journal of Forest Research* 134.3 (2015), pp. 537–553.

[45] S. E. Silva and A. S. B. Rodrigues. "Differential survival and reproduction in colour forms of *Philaenus spumarius* give new insights to the study of its balanced polymorphism". In: *Ecological Entomology* 40.6 (2015), pp. 759–766.

[46] I. E. Ben Moussa, V. Mazzoni, F. Valentini, T. Yaseen, D. Lorusso, S. Speranza, M. Digiaro, L. Varvaro, R. Krugner, and A. M. D'Onghia. "Seasonal fluctuations of sap-feeding insect species infected by *Xylella fastidiosa* in Apulian olive groves of Southern Italy". In: *Journal of Economic Entomology* 109.4 (2016), pp. 1512–1518.

[47] L. Bosso, M. Di Febbraro, G. Cristinzio, A. Zoina, and D. Russo. "Shedding light on the effects of climate change on the potential distribution of *Xylella fastidiosa* in the Mediterranean basin". In: *Biological Invasions* 18.6 (2016), pp. 1759–1768.

[48] G. Gilioli, S. Pasquali, and E. Marchesini. "A modelling framework for pest population dynamics and management: An application to the grape berry moth". In: *Ecological Modelling* 320 (2016), pp. 348–357.

[49] G. Goergen, P. L. Kumar, S. B. Sankung, A. Togola, and M. Tamo. "*Spodoptera frugiperda* (J. E. Smith) (Lepidoptera: Noctuidae) in Sub-Saharan Africa: A First Report and Its Potential for Spread and Damage". In: *PLOS ONE* 11.10 (2016).

[50] P. Jia, L. Lu, X. Chen, J. Chen, L. Guo, X. Yu, and Q. Liu. "A climate-driven mechanistic population model of Aedes albopictus with diapause". In: *Parasites & Vectors* 9 (2016), p. 175.

[51] A. Brunori, F. Dini, C. Cantini, G. Sala, T. La Mantia, T. Caruso, F. P. Marra, C. Trotta, L. Nasini, L. Regni, and P. Proietti. "Biomass and volume modeling in Olea europaea L. cv "Leccino"". In: *Trees* 31 (2017), pp. 1859–1874.

[52] D. Cornara, M. Saponari, A. R. Zeilinger, A. de Stradis, D. Boscia, G. Loconsole, D. Bosco, G. P. Martelli, R. P. P. Almeida, and F. Porcelli. "Spittlebugs as vectors of *Xylella fastidiosa* in olive orchards in Italy". In: *Journal of Pest Science* 90.2 (2017), pp. 521–530.

[53] D. Cornara, V. Cavalieri, C. Dongiovanni, G. Altamura, F. Palmisano, D. Bosco, F. Porcelli, R. P. P. Almeida, and M. Saponari. "Transmission of *Xylella fastidiosa* by naturally infected *Philaenus spumarius* (Hemiptera: Aphrophoridae) to different host plants". In: *Journal of Applied Entomology* 141.1-2 (2017), pp. 80–87.

[54] M. Saponari, D. Boscia, G. Altamura, G. Loconsole, S. Zicca, G. D'Attoma, M. Morelli, F. Palmisano, A. Saponari, D. Tavano, et al. "Isolation and pathogenicity of *Xylella fastidiosa* associated with olive quick decline syndrome in Apulia, Italy". In: *Scientific Reports* 7 (2017).

[55] D. Cornara, D. Bosco, and A. Ferères. "*Philaenus spumarius*: when an old acquaintance becomes a new threat to European agriculture". In: *Journal of Pest Science* 91.3 (2018), pp. 957–972.

[56] M. Khudaydus and W. Kallel. "Stability of Switched Systems in Sense of Lyapunov Theorems". In: (2018).

[57] D. G. Montezano, A. Specht, D. R. Sosa-Gómez, V. F. Roque-Specht, J. C. Sousa-Silva, S. V. Paula-Moraes, J. A. Peterson, and T. E. Hunt. "Host plants of *Spodoptera frugiperda* (Lepidoptera: Noctuidae)". In: *African Entomology* 26.2 (2018), pp. 286–300.

[58] J. Rapicavoli, B. Ingel, B. Blanco-Ulate, D. Cantu, and C. Roper. "*Xylella fastidiosa*: an examination of a re-emerging plant pathogen". In: *Molecular Plant Pathology* 19.4 (2018), pp. 786–800.

[59] A. Sicard, A. R. Zeilinger, M. Vanhove, T. E. Schartel, D. J. Beal, M. P. Daugherty, and R. P. P. Almeida. "*Xylella fastidiosa*: Insights into an emerging plant pathogen". In: *Annual Review of Phytopathology* 56 (2018), pp. 181–202.

[60] S. Soubeyrand, P. de Jerphanion, O. Martin, M. Saussac, C. Manceau, P. Hendrikx, and C. Lannou. "Inferring pathogen dynamics from temporal count data: the emergence of *Xylella fastidiosa* in France is probably not recent". In: *New Phytologist* 219.2 (2018), pp. 824–836.

[61] P. J. Zarco-Tejada, C. Camino, P. S. A. Beck, R. Calderón, A. Hornero, R. Hernández-Clemente, T. Kattenborn, M. Montes-Borrego, L. Susca, M. Morelli, V. González-Dugo, and J. A. Navas-Cortés. "Previsual symptoms of *Xylella fastidiosa* infection revealed in spectral plant-trait alterations". In: *Nature Plants* 4.7 (2018), pp. 432–439.

[62] N. Bodino, V. Cavalieri, C. Dongiovanni, E. Plazio, M. A. Saladini, A. Simonetto, S. Volani, G. Fumarola, M. Di Carolo, F. Porcelli, M. Saponari, and D. Bosco. "Phenology, seasonal abundance and stage-structure of spittlebug (Hemiptera: Aphrophoridae) populations in olive groves in Italy". In: *Scientific Reports* 9 (2019), p. 17725.

[63] V. Cavalieri, G. Altamura, G. Fumarola, M. Di Carolo, M. Saponari, D. Cornara, D. Bosco, and C. Dongiovanni. "Transmission of *Xylella fastidiosa* subspecies pauca sequence type 53 by different insect species". In: *Insects* 10.10 (2019), p. 324.

[64] F. Di Serio, N. Bodino, V. Cavalieri, S. Demichelis, M. Di Carolo, C. Dongiovanni, G. Fumarola, G. Gilioli, E. Guerrieri, U. Picciotti, E. Plazio, F. Porcelli, M. Saladini, M. Salerno, A. Simonetto, D. Tauro, S. Volani, S. Zicca, and D. Bosco. "Collection of data and information on biology and control of vectors of *Xylella fastidiosa*". In: *EFSA Supporting Publications* 16 (2019), EN–1628.

[65] C. Duso, G. Zanettin, F. Pavan, and A. Pozzebon. "Investigations on the grape leafhopper *Erasmoneura vulnerata* (Fitch) in north-eastern Italy". In: *Insects* 10.2 (2019), p. 44.

[66] EFSA Panel on Plant Health. "Update of the Scientific Opinion on the risks to plant health posed by *Xylella fastidiosa* in the EU territory". In: *EFSA Journal* 17.5 (2019), e05665.

[67] A. Fierro, A. Liccardo, and F. Porcelli. "A lattice model to manage the vector and the infection of *Xylella fastidiosa* on olive trees". In: *Scientific Reports* 9 (2019), p. 44997.

[68] M. Godefroid, A. Cruaud, J.-C. Streito, J.-Y. Rasplus, and J.-P. Rossi. "Xylella fastidiosa: climate suitability of European continent". In: *Scientific Reports* 9.1 (2019), p. 8844.

[69] M. Jeger and C. Bragard. "The epidemiology of *Xylella fastidiosa*: a perspective on current knowledge and framework to investigate plant host–vector–pathogen interactions". In: *Phytopathology* 109.2 (2019), pp. 200–210.

[70] Y. Lou, K. Liu, D. He, D. Gao, and S. Ruan. "Modelling diapause in mosquito population growth". In: *Journal of Mathematical Biology* 78.7 (2019), pp. 2259–2288.

[71] M. Saponari, A. Giampetruzzi, G. Loconsole, D. Boscia, and P. Saldarelli. "*Xylella fastidiosa* in olive in Apulia, Italy: where we stand". In: *Phytopathology* 109.2 (2019), pp. 175–186.

[72] M. Brunetti, V. Capasso, M. Montagna, and E. Venturino. "A mathematical model for *Xylella fastidiosa* epidemics in the Mediterranean regions. Promoting good agronomic practices for their effective control". In: *Ecological Modelling* 432 (2020), p. 109204.

[73] M. Castellini, A. M. Stellacci, M. Mastrangelo, F. Caputo, and L. M. Manici. "Estimating the Soil Hydraulic Functions of Some Olive Orchards: Soil Management Implications for Water Saving in Soils of Salento Peninsula (Southern Italy)". In: *Agronomy* 10.2 (2020), p. 177.

[74] N. Cufaro Petroni, S. De Martino, and S. De Siena. "Logistic and theta-logistic models in population dynamics: general analysis and exact results". In: *Journal of Physics A: Mathematical and Theoretical* 53.44 (2020).

[75] A. Hornero, R. Hernández-Clemente, P. R. J. North, P. S. A. Beck, D. Boscia, J. A. Navas-Cortés, and P. J. Zarco-Tejada. "Monitoring the incidence of *Xylella fastidiosa* infection in olive orchards using ground-based evaluations, airborne imaging spectroscopy and Sentinel-2 time series through 3-D radiative transfer modelling". In: *Remote Sensing of Environment* 236 (2020).

[76] Q. Liu, S. Piao, M. Campioli, M. Gao, Y. H. Fu, K. Wang, Y. He, X. Li, and I. A. Janssens. "Modeling leaf senescence of deciduous tree species in Europe". In: *Global Change Biology* 26.7 (2020), pp. 4104–4118.

[77] Á. López-Bernal, O. García-Tejera, L. Testi, F. Orgaz, and F. J. Villalobos. "Studying and modelling winter dormancy in olive trees". In: *Agricultural and Forest Meteorology* 280 (2020).

[78] L. Rossini. "Development of stochastic models for plant protection". PhD thesis. 2020.

[79] K. Schneider, W. van der Werf, M. Cendoya, M. Mourits, J. A. Navas-Cortés, A. Vicent, et al. "Impact of *Xylella fastidiosa* subspecies pauca in European olives". In: *Proceedings of the National Academy of Sciences* 117.17 (2020), pp. 9250–9259.

[80] S. M. White, J. A. Navas-Cortés, J. M. Bullock, D. Boscia, and D. S. Chapman. "Estimating the epidemiology of emerging *Xylella fastidiosa* outbreaks in olives". In: *Plant Pathology* 69.9 (2020), pp. 1403–1413.

[81] S. Aniţa, V. Capasso, and S. Scacchi. "Controlling the spatial spread of a *Xylella* epidemic". In: *Bulletin of Mathematical Biology* 83.4 (2021), p. 32.

[82] S. Avosani, P. Franceschi, M. Ciolli, V. Verrastro, and V. Mazzoni. "Vibrational playbacks and microscopy to study the signalling behaviour and female physiology of *Philaenus spumarius*". In: *Journal of Applied Entomology* 145.6 (2021), pp. 518–529.

[83] N. Bodino, V. Cavalieri, C. Dongiovanni, E. Plazio, S. Volani, M. A. Saladini, F. Porcelli, D. Bosco, M. G. Pansa, A. Simonetto, et al. "Dispersal of the meadow spittlebug *Philaenus spumarius* in olive groves and its relevance for *Xylella fastidiosa* epidemiology". In: *Envi-*

ronmental Entomology 50.6 (2021), pp. 1367–1379.

[84] N. Bodino, V. Cavalieri, M. Pegoraro, G. Altamura, F. Canuto, S. Zicca, G. Fumarola, R. P. P. Almeida, M. Saponari, C. Dongiovanni, and D. Bosco. "Temporal dynamics of the transmission of *Xylella fastidiosa* subsp. *pauca* by *Philaenus spumarius* to olive plants". In: *Entomologia Generalis* 41.5 (2021), pp. 463–480.

[85] F. Gambella, L. Bianchini, M. Cecchini, G. Egidi, A. Ferrara, L. Salvati, A. Colantoni, and D. Morea. "Moving toward the north? The spatial shift of olive groves in Italy". In: *Agricultural Economics – Czech* 67.4 (2021), pp. 129–135.

[86] G. Gilioli, P. Colli, M. Colturato, P. Gervasio, and G. Sperandio. "A nonlinear model for stage-structured population dynamics with nonlocal density-dependent regulation: An application to the fall armyworm moth". In: *Mathematical Biosciences* 335 (2021).

[87] L. Martin, A. Rousseau, J. Godoy, and J.-B. Burie. "Equilibrium and sensitivity analysis of a spatio-temporal host-vector epidemic model". In: *Mathematics and Computers in Simulation* 185 (2021), pp. 534–556.

[88] O. Martin, Y. Fernandez-Diclo, J. Coville, and S. Soubeyrand. "Equilibrium and sensitivity analysis of a spatio-temporal host–vector epidemic model". In: *Nonlinear Analysis: Real World Applications* 57 (2021).

[89] M. Morente, D. Cornara, A. Moreno, and A. Fereres. "Parapause breakage as a key step for the continuous indoor rearing of *Philaenus spumarius*". In: *Journal of Applied Entomology* 145.10 (2021), pp. 1062–1067.

[90] P. J. Zarco-Tejada, T. Poblete, C. Camino, V. Gonzalez-Dugo, R. Calderon, A. Hornero, R. Hernandez-Clemente, M. Román-Écija, M. P. Velasco-Amo, B. B. Landa, P. S. A. Beck, M. Saponari, D. Boscia, and J. A. Navas-Cortés. "Divergent abiotic spectral pathways unravel pathogen stress signals across species". In: *Nature Communications* 12.1 (2021), p. 6088.

[91] N. Bazarra, Á. Calsina, and J. Pinyol. "Analysis of a mathematical model arising in plant disease epidemiology". In: *Mathematics* 10.13 (2022), p. 2292.

[92] M. De Pascali, M. Vergine, C. Negro, D. Greco, F. Vita, E. Sabella, L. De Bellis, and A. Luvisi. "*Xylella fastidiosa* and drought stress in olive trees: a complex relationship mediated by soluble sugars". In: *Biology* 11.1 (2022), p. 112.

[93] O. Dombrowski, C. Brogi, H.-J. Hendricks Franssen, D. Zanotelli, and H. Bogena. "CLM5-FruitTree: a new sub-model for deciduous fruit trees in the Community Land Model (CLM5)". In: *Geoscientific Model*

Development 15 (2022), pp. 5167–5193.

[94] A. Giménez-Romero, J. Galván, M. Montesinos, J. Bauzà, M. Godefroid, A. Fereres, J. J. Ramasco, M. A. Matías, and E. Moralejo. "Global predictions for the risk of establishment of Pierce's disease of grapevines". In: *Communications Biology* 5.1 (2022), p. 1389.

[95] M. Godefroid and J. M. Durán. "Composition of landscape impacts the distribution of the main vectors of *Xylella fastidiosa* in southern Spain". In: *Journal of Applied Entomology* 146 (2022), pp. 666–675.

[96] N. Bodino, A. Simonetto, C. Dongiovanni, V. Cavalieri, M. Di Carolo, G. Gilioli, D. Bosco, and M. Saponari. "Bioecological traits of spittlebugs and their implications for the epidemiology and control of the *Xylella fastidiosa* epidemic in Apulia". In: *Scientific Reports* 13.1, 13062 (2023).

[97] F. Boyer. *Ordinary Differential Equations*. Lecture notes, Université de Toulouse. 2023.

[98] A. Didevarasl, J. M. Costa Saura, D. Spano, P. Deiana, R. L. Snyder, M. Mulas, G. Nieddu, S. Zelasco, M. Santona, and A. Trabucco. "Modeling Phenological Phases across Olive Cultivars in the Mediterranean". In: *Plants* 12.18 (2023), p. 3181.

[99] G. Gilioli, A. Simonetto, M. Colturato, N. Bazarra, J. R. Fernández, M. G. Naso, D. Boscia, D. Bosco, C. Dongiovanni, A. Maiorano, O. Mosbach-Schulz, J. A. Navas Cortés, and M. Saponari. "An eco-epidemiological model supporting rational disease management of *Xylella fastidiosa*. An application to the outbreak in Apulia (Italy)". In: *Ecological Modelling*, 110226 (2023).

[100] A. Giménez-Romero, E. Moralejo, and M. A. Matías. "A compartmental model for *Xylella fastidiosa* diseases with explicit vector seasonal dynamics". In: *Phytopathology* 113 (2023), pp. 1686–1696.

[101] S. Avosani, R. Nieri, V. Mazzoni, C. Zippari, M. L. Vitale, V. Verrastro, S. Germinara, T. F. Döring, D. Cornara, G. Anfora, Z. Hamouche, E. Tarasco, I. D'Isita, G. Belusic, A. Fereres, and V. Thompson. "Intruding into a conversation: how behavioral manipulation could support management of *Xylella fastidiosa* and its insect vectors". In: *Journal of Pest Science* 97 (2024), pp. 17–33.

[102] M. Cendoya, A. Navarro-Quiles, A. López-Quílez, A. Vicent, and D. Conesa. "An individual-based spatial epidemiological model for the spread of plant diseases". In: *Journal of Agricultural, Biological and Environmental Statistics* (2024). Online first.

[103] D. Cornara, V. Zaffaroni-Caorsi, Z. Hamouche, S. Avosani, G. Cavallo, V. Verrastro, C. Lago, A. Trani, A. De Stradis, R. P. P. Almeida, and A. Fereres. "Host finding and probing behavior by *Philaenus spumarius* on

olive varieties with a different degree of susceptibility to *Xylella fastidiosa*". In: *Journal of Pest Science* 97.4 (2024), pp. 2101–2113.

[104] G. Gilioli, A. Simonetto, I. D. Weber, P. Gervasio, G. Sperandio, D. Bosco, N. Bodino, C. Dongiovanni, M. Di Carolo, V. Cavalieri, M. Saponari, and D. Boscia. "A model for predicting the phenology of *Philaenus spumarius*". In: *Scientific Reports* 14.1, 8137 (2024).

[105] C. M. Wallis and Z. Gorman. "Pre-inoculation water deficit effects on grapevine physiology, *Xylella fastidiosa* titers, and Pierce's disease progression". In: *BMC Research Notes* 17.1, 119 (2024).

[106] G. Gilioli. Personal communication. 2025.

Thanks

My deepest gratitude goes to Professor Paola Gervasio, who took charge of and cared for my scientific journey with unfailing patience, expertise, and professionalism.

I am also sincerely grateful to Igor Daniel Weber for all the time we shared—at any hour of the day and night—trying to give shape and substance to the models we worked on with commitment and passion.

A special thank you goes to my parents, Luisella Paganelli and Orazio Bertoldi, who support me in every way they can, across my many passions and professions; without their help this PhD would never even have existed.

A huge thank you to Teresa Frassine for her constant support and unfailing willingness to help me whenever I was in need.

My thanks go as well to all my friends, who have been beacons of calm and joy in busy and demanding times.

I am also grateful to all the professors and researchers who accompanied me along this path—among them Anna Simonetto, Gianni Gilioli and Alessandro Giacomini—from whom I have often, and gladly, learned a lot.

I also wish to thank Alessandro Musesti for all his methodological advice and for being, over many years, an instructive presence in my life on many very different fronts.

I am indebted to the E. Fermi High School in Salò and to the Italian state for allowing me to live this adventure with a reasonable degree of financial stability.

A general thank you to all my Tramps: souls, personalities, stories, and skills, all extremely diverse, that make my musical life even more worth living, giving me the energy and enthusiasm to pursue, despite the enormous commitment required for organization and various bureaucracies, a second profession that has remained unchanged in its passionate aspect. And this warmth and positive energy overflow like a raging river also in my ability to be passionate as a behavioural pattern in life, including towards mathematics.

Finally, my heartfelt thanks go to mathematics itself: what began as a "school subject I happen to be good at" has become, together with music, a long-standing companion, from which I do not expect to part ways any time.